

STABILITY OF MICRO- AND MACROSCOPIC
TRAFFIC FLOW MODELS ON THE TRANSITION
FROM CIRCULAR ROAD TO INFINITE LANE

Dissertation with the aim of achieving a doctoral degree at the
Faculty of Mathematics, Informatics and Natural Sciences

Department of Mathematics
of Universität Hamburg

submitted by Hannes von Allwörden

Hamburg, 2020

Accepted as dissertation by the Department of Mathematics of Universität Hamburg based on the evaluations by:

Prof. Dr. Ingenuin Gasser (Universität Hamburg)

Prof. Dr. Jens Struckmeier (Universität Hamburg)

Prof. Dr. Simone Göttlich (Universität Mannheim)

Date of the oral defense: June 4, 2020

Acknowledgements

This work would not have been possible without the help of numerous people and it would not be complete without a big thank you to all of them.

My supervisors Ingenuin Gasser and Jens Struckmeier as well as my panel chair Jörn Behrens have given me the opportunity to work on this project and guided me in a way that let a lot of room for the development of my own ideas. Especially the countless discussions with Ingenuin throughout the last years have been invaluable in terms of insights and feedback. Bodo Werner has triggered this research by pointing out some numerical phenomena and open questions in a stimulating paper. His ideas and code have helped me a lot to get started on this topic.

In spring 2019 I gained many new perspectives and insights during a visit to Gabor Orosz and his research group in Ann Arbor. This and other journeys would not have been possible without the generous funding by the Department of Mathematics and MIN Graduate School.

The faculty members, colleagues and fellow PhD-students at the department liberally shared thoughts, hints, and literature recommendations, coffee and lunch as well as joy and, at times, frustration. I appreciate the great working atmosphere and the time we spent working and studying together.

And finally, I have been blessed with unlimited support, confidence, encouragement, and love from my family and partner.

Abstract

Mathematical models of traffic flow have been successfully used to describe, understand and predict congestion, behaviour at bottlenecks, and other phenomena. Models for single-lane vehicular traffic are often formulated either “microscopically” as systems of ordinary differential equations, trying to capture the dynamics at the level of a single vehicle, or “macroscopically” as (systems of) partial differential equations, describing e.g. car density and flow velocity. For microscopic models of a finite number of cars on a ring road, detailed stability and bifurcation analysis can be done. In this way it can be explained why and how a slight variation of circumstances like mean density, reaction time, or driving behaviour can lead to an abrupt change from smoothly flowing traffic to congestion. It may be suspected that the fact that the information about a driver’s decisions influences his actions at a later point of time by travelling from vehicle to vehicle upstream around the circle might lead to unrealistic effects. If, however, an open road of infinite length is considered instead, the situation becomes more involving mathematically.

The aim of this dissertation is to study how stability properties of traffic flow models change on the transition from circular road to infinite lane and from microscopic to macroscopic description. Prior applications of the concepts of convective and absolute instability to microscopic models are reviewed. These results are compared to those obtained for related macroscopic models. The notions of transient and remnant instability, well-known from partial differential equations, are introduced for microscopic models by considering their behaviour under certain exponentially weighted norms.

Analysis of car-following models on the circular road has shown that periodic solutions corresponding to stop-and-go-waves may emerge from Hopf bifurcations and can be numerically continued through parameter space, sometimes even into regions for which the quasi-stationary solutions are locally stable. We examine how these solutions behave and how they move with respect to different reference frames when the ring is opened and the number of cars is infinite.

Contents

1	Introduction	1
1.1	Motivation	1
1.2	Preceding work	5
1.2.1	Convective/absolute instability	5
1.2.2	Shift-invariant solutions	6
1.3	Research questions	6
I	Set-up	9
2	Microscopic car-following models	9
2.1	Definitions and assumptions	10
2.2	Special solutions	14
2.2.1	Existence of nearby solutions	15
2.2.2	Linearisation	16
2.3	Examples	17
3	Micro-macro link	21
3.1	History	21
3.2	Continuous microscopic car-following models	22
3.3	Densities	24
3.3.1	Definitions	25
3.3.2	Headway-density relationships	26
3.3.3	Continuity equations	29
3.4	Numerics for macroscopic equations	30
3.4.1	Finite differences	30
3.4.2	Finite volume	32
3.5	Examples	32

II	Quasistationary solutions	39
4	Stability	39
4.1	Microscopic models	39
4.1.1	Linear stability in terms of Toeplitz and Laurent operators	39
4.1.2	Different frames of reference	45
4.1.3	Acceleration models with a single leader	46
4.1.4	Lyapunov arguments	47
4.2	Macroscopic models	50
4.2.1	Linearisation	50
4.2.2	Characteristic polynomial and string stability	52
4.3	Examples	54
5	Linear analysis of jam behaviour	61
5.1	Historical overview	61
5.2	Convective and absolute instability	63
5.2.1	Macroscopic models	63
5.2.2	Microscopic models	70
5.2.3	Drawbacks	73
5.3	Transient and remnant instability	74
5.3.1	Macroscopic models	74
5.3.2	Microscopic models	75
5.4	Examples	78
5.4.1	Reaction-diffusion equations	78
5.4.2	Traffic flow models	84

III	Shift-invariant solutions	93
6	Finding solutions	93
6.1	Periodic solutions	93
6.1.1	Circular road	93
6.1.2	Infinite lane	96
6.2	Heteroclinic solutions	99
6.3	Examples	101
7	Stability and jam behaviour	113
7.1	Floquet multipliers and exponents	113
7.1.1	Circular road	113
7.1.2	Infinite lane	114
7.2	Convective/absolute instability	117
7.3	Examples	118
8	Discussion and Outlook	125
8.1	Discussion	125
8.2	Outcome and applicability	129
8.3	Open questions	130
	Bibliography	133
	Nomenclature	141
	Appendices	145
A	Additional figures	145
B	Bifurcation analysis	147
B.1	Circular road	147
B.2	Delay system	148
C	Summary of main results	151
D	Publications derived from this dissertation	153
E	Declaration	155

Chapter 1

Introduction

1.1 Motivation

In everyday life we frequently face the situation that our options for travelling from A to B are confined to narrow channels by practicability, economical reason, or law. Often, these connections also have to be shared with many others. From highways over bicycle lanes to the queue at the supermarket counter, this is true for almost any mode of transportation. Even ships at sea and planes in the air typically move along more or less strictly defined paths in spite of their apparent freedom (Fig. 1.1(c)). This is far from being a genuinely human phenomenon: Many wild animals tend to create and adhere to fixed trails as well, be it for harvesting, carving out their territory or annual migrations (cf. LEWIS 2013), and are sometimes arguably better at it than humans, as in the case of ants (Fig. 1.1(b)), who seem to effectively avoid congestion on their roads (cf. HÖNICKE et al. 2015).

Since the development of the automobile, individual vehicular traffic has become the dominating means of transport and continues to grow in most parts of the world. In spite of its benefits, this created a range of problems including congestion (Fig. 1.1(a)), air pollution, noise etc., not to mention its significant contribution to CO₂ emissions and the impending climate change. This demonstrates the necessity to not only reduce the number of vehicles and our dependency on fossil fuels, but also to improve our understanding and control of traffic flow mechanisms on all levels. Historically, research in this direction started with the early works by GREENSHIELDS (1935) and PIPES (1953), the development of the famous LWR model by LIGHTHILL and WHITHAM (1955) and RICHARDS (1956), works by CHANDLER et al. (1958), GREENBERG (1959), HERMAN et al. (1959), and others. Since then, a tremendous amount of research has been done by a very diverse community of engineers, physicists, mathematicians, and others, mostly from the point of view of differential equations and dynamical systems and with the aim of modelling and describing central phenomena. For a historical overview, see e.g. the articles KLAR et al. (1996), BRACKSTONE and McDONALD (1999), NAGEL et al. (2003), BELLOMO and DOGBE (2011), WAGENINGEN-KESSELS et al. (2015), as well as the introductory textbooks on the subject by KERNER (2004), TREIBER and KESTING (2013), ELEFTERIADOU (2013), and KESSELS (2019).

More recently, a different perspective is added by the increasing development of electronic safety devices and attempts towards (partial) automation of vehicular traffic. For road vehicles, this may range from safety systems (e.g. anti-lock braking system, electronic stability control) over various kinds of cruise control systems to connected and automated vehicles (CAVs) equipped to exchange information with other vehicles digitally and/or drive autonomously to some extent (see e.g. SPERLING 2018). These technologies are usually developed and investigated under the aspect

of optimal control (see e.g. MIUCIC 2019).

As common with new technologies, many expectations and fears are tied to these developments. This may e.g. be observed in the public discussion concerning the tests of a self-driving minibus prototype in Hamburg (Fig. 1.2(b)).

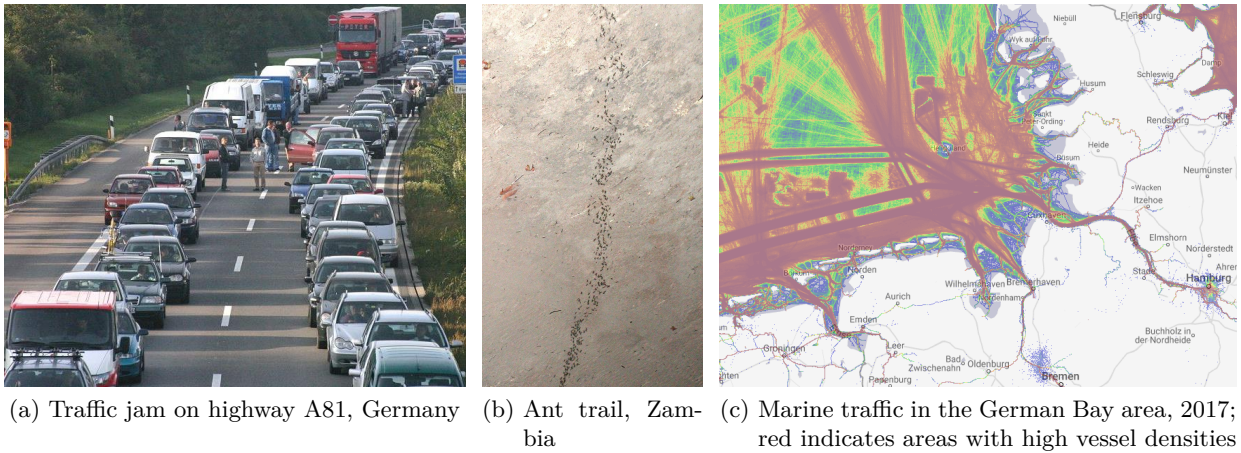
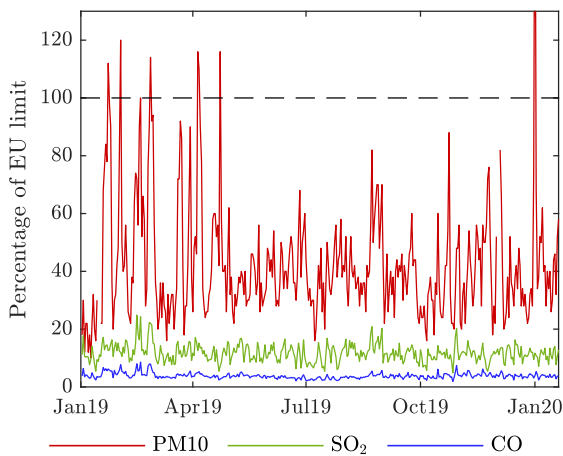


Figure 1.1: Examples of traffic systems with different agents and dimensionality ¹



(a) Air pollution at Max Brauer Allee, Hamburg. Due to high concentrations of particulate matter (PM), access restrictions have been imposed in 2018



(b) In a project led by HOCHBAHN, automated minibusses are tested in semi-autonomous mode in the HafenCity area of Hamburg, Germany

Figure 1.2: Problems and perspectives related to the development of traffic flow ²

A feature common to the situations mentioned above and of vehicular traffic in particular is that they may be described as multi-agent systems with anisotropic interaction and distributed control,

¹ (a) photograph by Alexander Blum
 (b) photograph by http://www.fourmilab.ch/images/eclipse_2001/africaimages.html
 (c) marine traffic data obtained from <https://www.marinetraffic.com/en/ais/>

² (a) data obtained from <https://luft.hamburg.de/clp/max-brauer-allee-ii-aktuelle-messdaten/>
 (b) project HEAT: <https://www.hochbahn.de/hochbahn/hamburg/en/home/projects>



Figure 1.3: Circular road experiments are a popular tool to study collective effects of driving behaviour under controlled conditions

where avoidance of collisions is desirable. While the direction may not be rigidly restricted, certain one-dimensional paths exist that are preferable.

In its most basic form, this can be modelled as a single, homogeneous string of agents. Of course, depending on the setting, effects like heterogeneity of the agents, dependencies of space and time, the number of lanes, overtaking, intersections with other roads etc. may have to be taken into account for a more accurate model.

As long as the situation is dominated by the interactions between the agents and no exterior influences such as road curvature, slopes or bottlenecks are present, we intuitively expect the agents to move at a constant common velocity such that they are at rest relative to each other. This behaviour obviously minimises the energy consumption and stress caused by acceleration and deceleration.

However, even if each agent is able to follow his predecessor without amplifying the small mistakes that will inevitably occur, homogeneous flow conditions may break down in a string of agents seemingly “out of nowhere”. This central phenomenon is often referred to as “phantom traffic jam”.

For empirical research under controlled conditions, ring road experiments are a popular tool (Fig. 1.3). In this setup, it has been demonstrated that phantom traffic jams occur (SUGIYAMA et al. 2008), and how they may be avoided by the introduction of CAVs (STERN et al. 2018). Other modes of transport such as bicycles have been explored by ring-road experiments as well (GAVRIILIDOU et al. 2019).

However, it is unclear how closely the results of such experiments resemble features of real traffic and what may be considered as an artefact of the “unphysical” boundary conditions. This is true for mathematical models as well but here, without having to worry about car rental costs or finding appropriate test tracks, we have the freedom to explore arbitrarily and even infinite numbers of vehicles on an open road as an alternative (Fig. 1.4).

In this context, there are several interesting questions related to phantom traffic jams:

- For a parameter-dependent traffic flow model, which parameters will let a small perturbation develop into a jam? How do the boundaries between parameter regions depend upon the

setting?

- How fast does the breakup spread? Where does it go? This of course depends on the frame of reference: Typically, our idea of the emergence of a phantom traffic jam is that of a chain reaction where each driver’s reaction is slightly stronger than its predecessor’s. The perturbation is thus amplified as it moves upstream through the string of vehicles, converse to the direction in which they are driving. It may only travel in downstream direction if the anisotropy is sufficiently small, i.e. if the drivers are influenced by what is happening behind them. From the perspective of a person standing at the side of the road, the terms up- and downstream do have a different meaning which is related to the drivers’ view by their equilibrium velocity: An observer at rest will perceive the perturbation as moving upstream if it is communicated from preceding to following car quicker than they are passing him by.
- How can the emerging inhomogeneous solutions be characterised? Typically, we expect some form of stop-and-go-solutions, i.e. oscillating behaviour with rapid transitions between phases of relatively fast and slow movement. Their actual shape may depend strongly on the setting: While a small number of vehicles on a ring road may quickly converge to a stable periodic solution (Fig. 1.4(a)), the inhomogeneous solution will stay local on the infinite lane and may be characterised by a sequence of jumps between different states with high and low velocity (Fig. 1.4(b)).

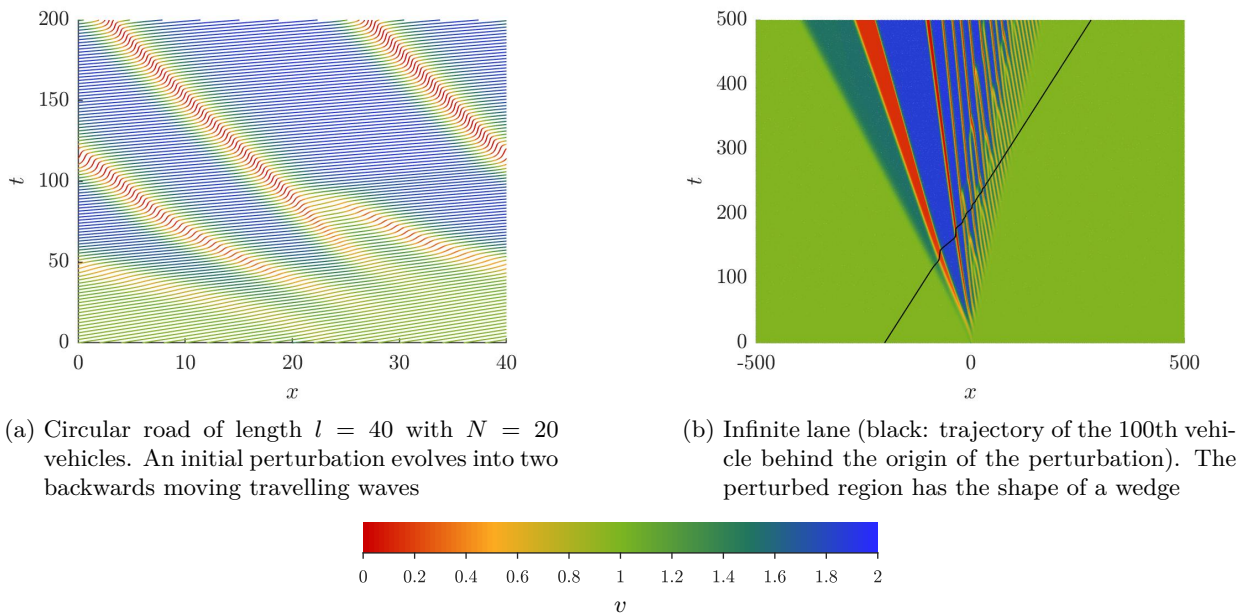


Figure 1.4: Evolution of a small perturbation to an initially homogeneous flow on a ring road and an infinite lane with colour-coded velocity (simulation of the Bando model with $a = 1$, $h_e = 2$)

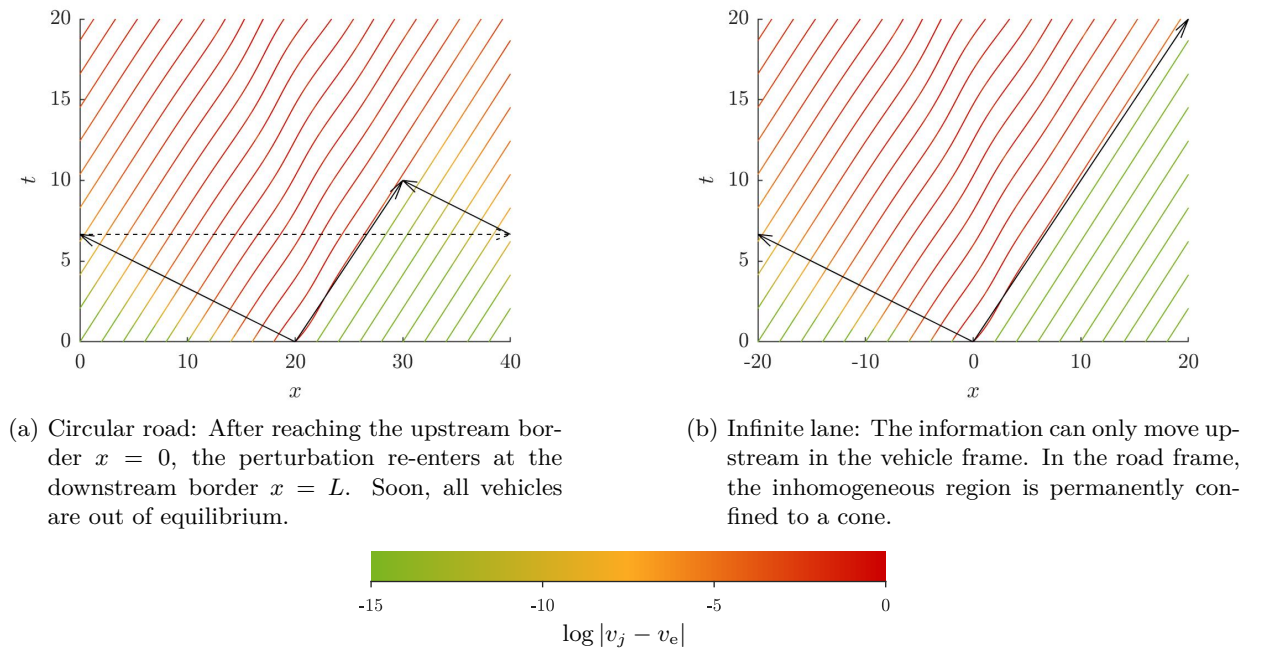


Figure 1.5: Detail from Fig. 1.4: Direct comparison of the transition to inhomogeneity with colour-coded deviation from equilibrium velocity. The arrows indicate the spread of the initially localised perturbation

1.2 Preceding work

1.2.1 Convective/absolute instability

The notions of convective and absolute instability have been studied in a traffic flow context by MITARAI and NAKANISHI (1999), WARD and WILSON (2011), and TREIBER and KESTING (2011). MITARAI and NAKANISHI discuss one particular microscopic model without much theoretical detail and determine the boundary between convectively upstream- and absolutely unstable homogeneous flow solutions.

TREIBER and KESTING use the group velocity to approximate the speed of a perturbation in a microscopic- and a related macroscopic model. The results are used in an attempt to dismiss the critique of “2nd order models” in DAGANZO (1995). They also evaluate empirical data and come to the conclusion that convectively downstream- and absolute instability seem not to occur.

WARD and WILSON consider a more general framework of microscopic car-following models on the infinite lane with a leading car, where the perturbation is localised. They use an inductive argument and derive a rather complex set of necessary conditions.

The notions of transient- and remnant instability are introduced for partial differential equations (PDEs) in SANDSTED and SCHEEL (2000) and shown to be preferable to those of convective- and absolute instability in some contexts.

1.2.2 Shift-invariant solutions

Periodic solutions of microscopic car-following models have been studied in detail by GASSER et al. (2004) and OROSZ et al. (2004a). Recently, also TOMOEDA et al. (2018) and KISS et al. (2019) have made interesting contributions on the subject. To our knowledge, the transition to the infinite lane has not been discussed in detail so far. Some of the results we are going to present on this issue are currently under review in VON ALLWÖRDEN and GASSER (submitted 2018).

1.3 Research questions

In this thesis, we are therefore going to address the following questions:

1. String stability
 - (a) How are the stability properties for microscopic traffic flow models in the different settings related?
 - (b) How are the spectra of microscopic models on the infinite lane related to those of “linked” macroscopic models?
2. Convective/Absolute instability
 - (a) What is the connection between the notions of convective instability employed by MITARAI and NAKANISHI (1999) and WARD and WILSON (2011)?
 - (b) Do related macroscopic models show similar convective/absolute stability behaviour? If so, in which sense?
 - (c) How can the concepts of remnant/transient instability be applied to microscopic traffic flow models?
3. Periodic solutions
 - (a) How can the periodic solutions found on the circular road be parametrised and completed as solutions on the infinite lane?
 - (b) How can we calculate stability properties of periodic solutions on the infinite lane?
 - (c) Can we distinguish between convectively and absolutely unstable periodic solutions?

The structure of the thesis closely resembles these questions:

In Part I, we state basic definitions and assumptions for microscopic traffic flow models (Chapter 2) and show how to systematically derive sequences of related macroscopic models (Chapter 3).

Part II is dedicated to homogeneous flow solutions, particularly the questions of when and how fast they break down. After reviewing the stability analysis (Chapter 4) we compare and extend approaches for convective/absolute instability in micro- and macroscopic settings (Chapter 5).

In Part III we discuss how to find and parametrise shift-invariant solutions on the infinite lane (Chapter 6). Afterwards we discuss their stability and convective/absolute behaviour (Chapter 7).

Several examples are worked out at the end of each chapter. Throughout the text, the Bando model is used as an illustrative example that connects the different parts. Despite its simplicity, this model has been demonstrated to show a wealth of phenomena that also occur in other, more elaborate traffic flow models; its relevance for traffic flow theory can be compared to that of *Drosophila melanogaster* to genetics.

Finally, the obtained results are discussed and an outlook for further research is given (Chapter 8).

I Set-up

Chapter 2

Microscopic car-following models

Over the years, a multitude of different models have been proposed to describe traffic flow. We refer to BELLOMO and DOGBE (2011) and WAGENINGEN-KESSELS et al. (2015) for an overview of the historical development and connections to other model classes. The paper by PIPES (1953) with the model

$$\dot{v}_j = a(v_{j-1} - v_j) \quad (2.1)$$

is maybe the first example of a microscopic traffic model.

Due to the sheer number of models it is necessary to look for frameworks that allow to address multiple models simultaneously. This of course requires a balance between the strive for generality, including as many models as possible, on one hand, and the necessity to be concrete enough to allow meaningful conclusions on the other.

The concept of “car-following”- or “follow the leader” models has proved to be very useful to this end. A general overview of car-following models is given in BRACKSTONE and McDONALD (1999) and AGHABAYK et al. (2015). The important subclass of optimal velocity models is reviewed in LAZAR et al. (2016).

Unfortunately, the terms “car-following” and “follow the leader” are used in a slightly ambiguous meaning in the literature. For example, the early paper GAZIS et al. (1961) specifically regards the delay differential equation

$$\dot{v}_j(t) = a \frac{v_j(t)^{\alpha_1}}{(x_{j-1}(t-\tau) - x_j(t-\tau))^{\alpha_2}} (v_{j-1}(t-\tau) - v_j(t-\tau)) \quad (2.2)$$

with parameters $\alpha_{1,2}$ as a follow-the-leader model, while the more recent works by WILSON and WARD (2011) and TREIBER and KESTING (2013) consider car-following models as second-order ordinary differential equations of the form

$$\dot{v}_j(t) = a(x_{j-1}(t) - x_j(t), v_j(t), v_{j-1}(t)), \quad (2.3)$$

where the acceleration is given by a function a of the headway and the velocities of both the own and the preceding vehicle with relatively weak constraints.

Recently, technological advance has put a focus on systems that allow an exchange of information with nearby vehicles beyond the direct leader.

In the following, we will therefore consider a variant of a general car-following framework similar to the ones presented in WILSON and WARD (2011) and TREIBER and KESTING (2013) that enables us to study interactions with an interval of leading and following vehicles and puts special emphasis on the underlying “road topology”.

The latter will be used as an umbrella term to refer to the different set-ups we are interested in, i.e. circular road and open road with or without a leading and a last car. Strictly speaking this is a slight misnomer since in our model it is not the road but the index set and the boundary condition that are making the difference.

2.1 Definitions and assumptions

In real life, a road is characterised by a multitude of features. Mathematically, it may be described as a curve embedded in a space \mathcal{X} which is at least \mathbb{R}^3 , possibly augmented by further information including width, number of lanes, quality, legal regulations etc. Some aspects, like speed limits or traffic lights, may even be changing with time on a scale relevant for traffic flow dynamics. The road network in a certain area may be modelled as a directed graph, again with additional information at the nodes describing the properties of road intersections.

In order to be able to study car following without the effects caused by road intersections, we need to consider either a closed loop or an infinitely long open road without any on- or offramps. Both situations can be modelled as a, possibly periodic, curve $\mathcal{R} : \mathbb{R} \rightarrow \mathcal{X}$. Consequently, we may perform our calculations on \mathbb{R} regardless of the setting and map to the “true” space afterwards. Therefore, for a vehicle j at time t , we will write its position as $x_j(t) \in \mathbb{R}$. Sometimes, in order to emphasise the fact that the vehicle positions may be thought of as a function of j and t , we may also write $x(j, t)$ instead of $x_j(t)$. For nontrivial traffic flow dynamics, vehicle j needs to be part of a set J with more than one element.

We make the following assumptions:

Assumption 2.1

1. Except for at most one vehicle $j^* \in J$, each vehicle j has a direct preceder $j' \in J$ with $x_j < x_{j'}$.
2. Each car is the preceder of at most one other car.
3. For two vehicles $j, j' \in J$, there is a unique distance $n \in \mathbb{N}$ such that j is the n -th preceder of j' or vice versa.

Implicitly, we have also already suggested the assumption of time-independence of the indices:

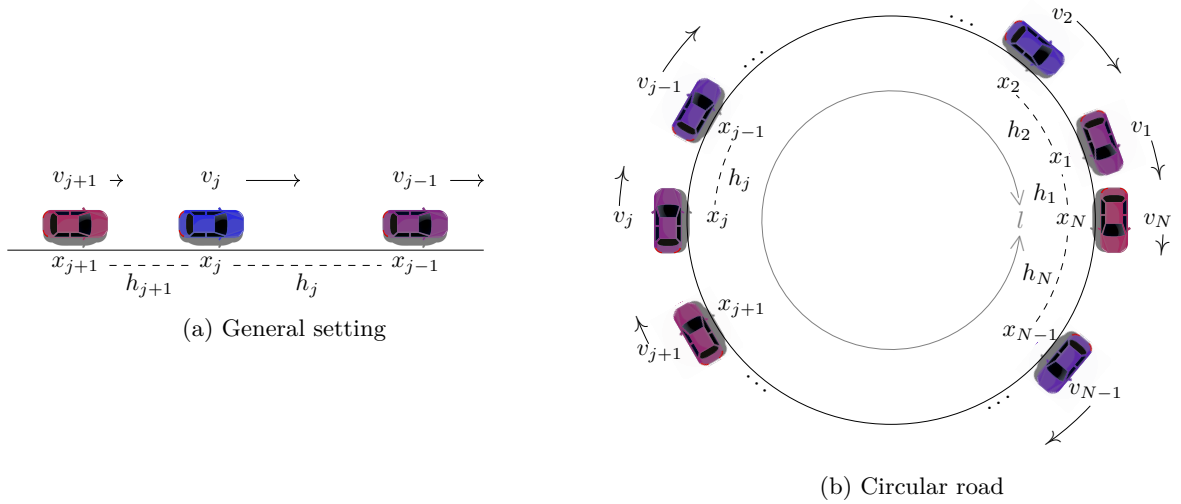


Figure 2.1: Setup and notation for microscopic car-following models

Assumption 2.2 J and the order of the positions x_j are time-independent, i.e. there is no overtaking, adding or removal of vehicles, etc.

From the Peano Axioms we see that under these assumptions, J is isomorphic to one of the sets \mathbb{Z} , \mathbb{N} , $-\mathbb{N}$, or $[1, N] = \{1, 2, \dots, N\} \subset \mathbb{N}$ with $j+1$ denoting the follower of vehicle j and $j-1$ its preceder (Fig. 2.1(a)). We employ $J = \pm\mathbb{N}$ to be able to refer to the situation of infinitely many cars on an open road with a leader or a last car, respectively, without having to redefine the direction in which the vehicles are counted. Note that we have $J \neq \mathbb{Z}/N\mathbb{Z}$ because of uniqueness of the relation. Without loss of generality, we may therefore restrict our attention to these sets. We will write \mathbf{x} or $(x_j)_{j \in J}$ to denote the positions of all vehicles, regardless of the cardinality of J .

Assume that the positions are at least $n-1$ -times continuously differentiable with respect to time, $x_j(t) \in \mathcal{C}^{n-1}(\mathbb{R}^+)$. As for the position $x_j(t)$, the velocity $v_j = \dot{x}_j \in \mathbb{R}$ may be mapped to the tangent space $T_{\mathcal{R}(x_j)}\mathcal{X}$, if necessary. By

$$\mathbf{u}_j(t_0) := [x_j(t_0), \dot{x}_j(t_0), \ddot{x}_j(t_0), \dots]^\top = \left(\frac{d^k}{dt^k} x_j(t) \Big|_{t=t_0} \right)_{k \in [0, n-1]} \in \mathbb{R}^n$$

we denote the state of vehicle j at time $t_0 \geq 0$, $\mathbf{u} = (\mathbf{u}_j)_{j \in J}$ is the state of the whole system. The space of possible states at a fixed time $\mathcal{U}_J^n := (\mathbb{R}^n)^{|J|}$ is called the state space.

With a function $\mathbf{f} : \mathcal{U}_J \rightarrow \mathbb{R}^{|J|}$, we have the ordinary differential equation (ODE)

$$\dot{\mathbf{u}}(t) = \left[\frac{d\mathbf{x}}{dt}(t), \dots, \frac{d^{n-1}}{dt^{n-1}} \mathbf{x}(t), \mathbf{f}(\mathbf{u}(t)) \right]^\top. \quad (2.4)$$

In order to work with ODEs instead of delay differential equations (DDEs), we have to ignore reaction time:

Assumption 2.3 The drivers' reactions are instantaneous.

In a car-following model, we want the j -th component to depend on its own state \mathbf{u}_j , the states $\mathbf{u}_{j-1}, \dots, \mathbf{u}_{j-m_1}$ of its $m_1 \in \mathbb{N}$ preceding vehicles and possibly $\mathbf{u}_{j+1}, \dots, \mathbf{u}_{j-m_f}$, the states of its $|m_f|$ followers, where $m_f \in -\mathbb{N}_0$ (Fig. 2.2). For $J = \mathbb{Z}$, these exists for any j . For $J = \pm\mathbb{N}$ or $J = [1, N]$, we need to introduce boundary conditions to make up for missing vehicles at the beginning and/or end of the queue.

The sign conventions here are chosen such that we are counting upwards from a leading car, if there is one. Also, we have $[m_f, m_1] = [0, 1]$ in the simplest case where each vehicle only takes information from its direct predecessor and its own state into account.

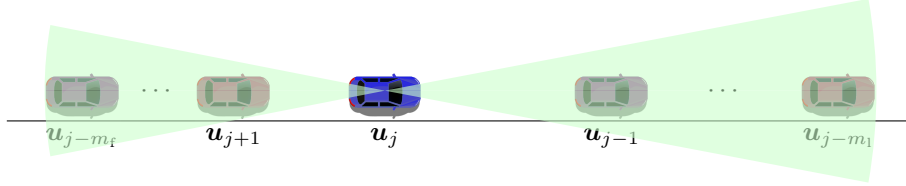


Figure 2.2: Zone of attention of vehicle j : The number of leaders and followers that are considered is denoted by m_1 and $-m_f$, respectively.

Definition 2.1 We call the function $\mathbf{bc} : \mathcal{U}_J^n \rightarrow \mathcal{U}_{\mathbb{Z}}^n$ a **microscopic boundary condition** if its projection to \mathcal{U}_J^n is the identity.

Periodic boundary conditions are given by the function

$$\mathbf{bc}_{\text{per}} : \mathcal{U}_{[1, N]}^n \rightarrow \mathcal{U}_{\mathbb{Z}}^n$$

$$(\mathbf{u}_j)_{j \in [1, N]} \mapsto \left(\begin{array}{l} \mathbf{u} : \mathbb{Z} \rightarrow \mathbb{R}^n \\ j \mapsto \mathbf{u}_{j \bmod N} - \left[\left[\frac{j}{N} \right] \cdot l, 0, \dots, 0 \right]^\top \end{array} \right) \quad (2.5)$$

i.e. after application of \mathbf{bc}_{per} we have $\mathbf{u}_{N+1} = [x_1 - l, v_1, \dots]^\top$, as usual (Fig. 2.1(b)).

In the context of traffic flow, periodic boundary conditions are often used synonymous to a circular road setting. However, we see that this is slightly misleading: so far, periodicity refers only to the relations between vehicles.

After completion with a boundary condition, we can safely assign a headway to all vehicles:

Definition 2.2 Given $(x_j)_{j \in J}$ and, for $J \neq \mathbb{Z}$, a boundary condition \mathbf{bc} , the **headway** is defined as

$$h_j := x_{j-1} - x_j, j \in J \quad (2.6)$$

To avoid confusion, we do not make use of the term “time headway” that is used in some publications; here, the headway is always a spatial quantity.

Definition 2.3 ODE (2.4), completed by a boundary condition if necessary, is called a **microscopic car-following model** (CFM) if \mathbf{f} can be written as $\mathbf{g} \circ \mathbf{bc}$ with $\mathbf{g} = (g_j)_{j \in J}$,

$$g_j(\mathbf{u}) = g_j(\mathbf{u}_{j-m_1}, \dots, \mathbf{u}_{j-1}, \mathbf{u}_j, \mathbf{u}_{j+1}, \dots, \mathbf{u}_{j-m_f}),$$

i.e.

$$\frac{\partial g_{j'}}{\partial \left(\frac{d^k}{dt^k} x_j \right)} = 0 \quad \forall k \in [0, n-1], j' - j \notin [m_f, m_1].$$

The ODE system can then be written shortly as

$$\frac{d^n x_j}{dt^n}(t) = g_j(\mathbf{u}_{j-m_1}(t), \dots, \mathbf{u}_{j-1}(t), \mathbf{u}_j(t), \mathbf{u}_{j+1}(t), \dots, \mathbf{u}_{j-m_f}(t)) \quad \forall j \in J \quad (2.7)$$

or alternatively as a first-order system

$$\dot{\mathbf{u}}_j(t) = \mathbf{g}_j(\mathbf{u}_{j-m_1}(t), \dots, \mathbf{u}_{j-1}(t), \mathbf{u}_j(t), \mathbf{u}_{j+1}(t), \dots, \mathbf{u}_{j-m_f}(t)) \quad \forall j \in J, \quad (2.8)$$

where $\mathbf{g}_j : \mathbb{R}^{n \cdot (m_1 - m_f + 1)} \rightarrow \mathbb{R}^n$ and \mathbf{u}_l is implicitly understood to be defined with the help of the respective boundary condition for $l \notin J$.

The components g_j are then called **car-following functions**. Often, we will consider models with $g_j \equiv g$; g will then be referred to as “the” car-following function of the model. In the case $n = 2$, we may also call g the **acceleration law**.

A CFM with an initial condition $\mathbf{u}(0) = \mathbf{u}^0$ forms a **microscopic initial value problem** (IVP).

This definition is illustrated in Ex. 2.1.

Definition 2.4 A function $\mathbf{x} : (t_{\text{start}}, t_{\text{end}}) \times J \rightarrow \mathbb{R}^{|J|}$ with $t_{\text{start}} \in \mathbb{R} \cup \{-\infty\}$, $t_{\text{end}} \in \mathbb{R} \cup \{+\infty\}$ is called a **solution** to a CFM if each component is n -times differentiable with respect to time and (2.8) is satisfied.

Using the same car-following function for all vehicles requires the assumption that the differences between drivers are of no importance for our model:

Assumption 2.4 All vehicle-driver units are created equal.

If not stated otherwise, we will also assume that the road is homogeneous:

Assumption 2.5 The car-following functions g_j depends on the headways $h_{j-m_f}, \dots, h_{j-(m_f-1)}$, but not explicitly on the position of any of the vehicles, i.e.

$$\sum_{k=m_f}^{m_1} \frac{\partial g_j}{\partial x_{j-k}} = 0. \quad (2.9)$$

As long as this is satisfied, any solution will be invariant to spatial translation and we may write the model in terms of the headways h_j , $j \in J$ instead of positions x_j without loss of information, since positions may be recovered from the headways by fixing an arbitrary index $j^* \in J$ and using

$$x_j(t) = \int_0^t v_{j^*}(\theta) d\theta + C + \sum_{k=\min(j^*, j)+1}^{\max(j^*, j)} h_k(t). \quad (2.10)$$

2.2 Special solutions

For many models, it can be shown that they admit one or more type(s) of special solutions. In some cases, models may even be “tailor-made” with the aim of showing a certain solution behaviour.

Once found, these special solutions may help us to deduce existence results for a region around them or be subjected to stability analysis. Unfortunately, except for very special cases, we will not be able to write down special solutions explicitly; rather, they have to be characterised by certain properties.

Definition 2.5 A solution $\mathbf{x}(t)$ to a CFM is called a **quasistationary** solution (QS) with **equilibrium velocity** v_e if

$$x_j(t) = x_j(0) + v_e t \quad \forall j \in J. \quad (2.11)$$

In headway coordinates, this is a **stationary** solution. A (quasi-)stationary solution is called **homogeneous** (hQS) if $h_j \equiv h_e$ for all $j \in J$ (Fig. 2.3). If this is not the case, it is called **inhomogeneous** (iQS).

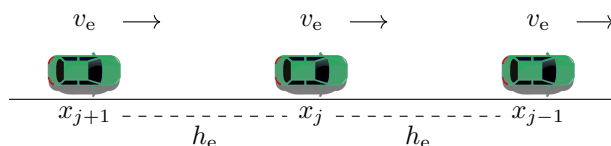


Figure 2.3: In a quasistationary solution, all vehicles are going at the same velocity. In the homogeneous case, the distances between vehicles are constant, too

For $J = \mathbb{N}$, a boundary condition with leading cars at an equilibrium velocity v_e and corresponding headway h_e may be introduced by setting

$$\mathbf{bc}_e : \mathcal{U}_{\mathbb{N}} \times \mathbb{R}^+ \rightarrow \mathcal{U}_{\mathbb{Z}}$$

$$(\mathbf{u}_j)_{j \in [1, N]} \mapsto \left(\begin{array}{l} \mathbf{u} : \mathbb{Z} \rightarrow \mathbb{R}^n \\ j \mapsto \begin{cases} \mathbf{u}_j & \text{for } j > 0 \\ v_e t - j h_e & \text{else} \end{cases} \end{array} \right).$$

The discrimination between homogeneous and inhomogeneous case could also be made in the following definitions. For simplicity, we refrain from doing so and focus on the homogeneous cases, motivated by Assumption 2.4.

We are also interested in solutions where the trajectories are shifted copies of each other, but not necessarily affine functions:

Definition 2.6 A solution $\mathbf{x}(t)$ to a CFM is called a (homogeneous) **travelling wave** (TW) or **shift-invariant** if

$$x_j(t) = x_{j+1}(t + \Delta t) + \Delta x \quad \forall j \in J. \quad (2.12)$$

Equivalently, $\mathbf{x}(t)$ is a TW if there is a function $W : \mathbb{R} \rightarrow \mathbb{R}$ such that

$$v_j(t) = W(\Delta t \cdot x_j(t) + t \cdot \Delta x) \quad (2.13)$$

and the intersections of the trajectories $x_j(t)$ with the line $\frac{\Delta x}{\Delta t}t + C$ are equidistant.

With circular road boundary conditions, TWs are periodic in the following sense:

Definition 2.7 Let $T \in \mathbb{R}^+$. A TW is called a **T -periodic** solution (PS) if W satisfies $W(\theta+T) = W(\theta)$ for all $\theta \in \mathbb{R}$.

In the case of fixed bottlenecks, when Assumption 2.5 is not satisfied, we may expect TWs that do not move in the road frame:

Definition 2.8 A TW is called **standing** or, in the case of a circular road, a **pony on a merry-go-round solution** (POM) if $\Delta x = 0$.

POMs may also be generalised:

Definition 2.9 A solution $\mathbf{x}(t)$ to a CFM is called a **quasi-POM** (qPOM) if there is a function $W : [0, L] \times [0, T] \rightarrow \mathbb{R}$ such that $v_j(t) = W(x_j \bmod L, t \bmod T)$.

Finally, TWs may also occur in the form of heteroclinic solutions:

Definition 2.10 A TW is called a **heteroclinic solution** (HS) if there are $v_{\pm} \in \mathbb{R}$ such that $\lim_{\theta \rightarrow \pm\infty} W(\theta) = v_{\pm}$.

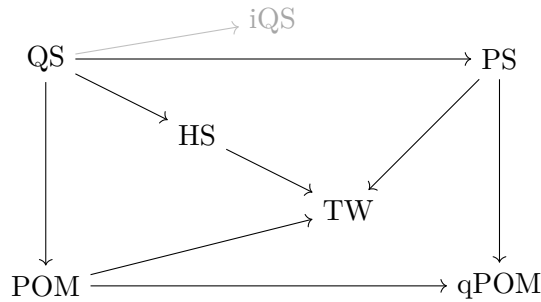


Figure 2.4: Relations between the special solutions introduced in Def. 2.6-2.10. Arrows indicate subsets, e.g. $QS \rightarrow HS$ means that any quasistationary solution is also a heteroclinic solution

2.2.1 Existence of nearby solutions

Assuming that a given car-following model admits a special solution $\bar{\mathbf{x}}(t)$ like the ones described above, a key task is to analyse the evolution of the model for initial conditions that are in some sense “close” to it.

For this question to be meaningful, we have to specify what we understand by closeness, and of course to ensure the existence of solutions close to the special solution.

Definition 2.11 (Banach space ℓ_J^n) For $n \in \mathbb{N}$ and an index set J subject to assumption 2.1, let $\|\cdot\|_2$ denote the Euklidean norm on \mathbb{R}^n and define the norm $\|\cdot\|_J$ on \mathcal{U}_J^n as

$$\begin{aligned} \|\cdot\|_J : \mathcal{U}_J^n &\rightarrow \mathbb{R}^+ \\ \mathbf{u} &\mapsto \sqrt{\sum_{j \in J} \|\mathbf{u}_j\|_2^2}, \end{aligned} \quad (2.14)$$

which induces the Banach spaces

$$\ell_J^n := \left\{ \mathbf{u} \in \mathcal{U}_J^n : \sum_{j \in J} \|\mathbf{u}_j\|_2^2 < \infty \right\}. \quad (2.15)$$

Theorem 1 (Cauchy's existence theorem) Let $\bar{\mathbf{x}} : J \times (0, t_{\text{end}})$ be a solution to a CFM with \mathbf{f} locally Lipschitz continuous in \mathcal{U}_J^n . For any $\mathbf{u}^0 \in \mathcal{U}_J^n$ such that $\mathbf{u}_0 - \bar{\mathbf{u}}(0) \in \ell_J^n$, there is a $t_{\text{max}} \in \mathbb{R}^+ \cup \{\infty\}$ such that there is in $(0, t_{\text{max}})$ exactly one solution to the CFM with $\mathbf{u}(0) = \mathbf{u}_0$.

Proof: Denote by $P_n : \mathbb{R}^n \rightarrow \mathbb{R}^{n-1}$ the projection of an n -dimensional vector to its second to last component. Let $\mathbf{y} := \mathbf{u} - \bar{\mathbf{u}}$ and apply the proof of Cauchy's existence theorem for ODEs on Banach spaces in DIEUDONNÉ (1960, p. 280) to the system of first-order ODEs

$$\dot{\mathbf{y}}_j(t) = \begin{bmatrix} P_n(\mathbf{y}_j(t) + \bar{\mathbf{u}}_j(t)) \\ g_j(\mathbf{y}(t) + \bar{\mathbf{u}}(t)) \end{bmatrix} - \dot{\bar{\mathbf{u}}}_j(t), \quad j \in J. \quad (2.16)$$

□

Theorem 2 (Comparison of solutions) Let $\bar{\mathbf{u}}$ be a solution to a CFM and let κ denote the Lipschitz constant of the car-following function \mathbf{f} .

For any initial data $\mathbf{u}^0, \mathbf{w}^0$ such that $\mathbf{u}^0 - \bar{\mathbf{u}}(0) \in \ell_J^n, \mathbf{w}^0 - \bar{\mathbf{u}}(0) \in \ell_J^n$ and corresponding solutions $\mathbf{u}(t), \mathbf{w}(t)$ we have

$$\|\mathbf{u}(t) - \mathbf{w}(t)\|_J \leq \|\mathbf{u}^0 - \mathbf{w}^0\|_J \exp(\kappa t)$$

Proof: See DIEUDONNÉ (1960, p. 282), with the same notation as before. □

2.2.2 Linearisation

By using the linearity of the projection P_n and the expansion

$$g_j(\mathbf{y}(t) + \bar{\mathbf{u}}(t)) = g_j(\bar{\mathbf{u}}(t)) + \nabla_{\mathbf{u}} g_j|_{\mathbf{u}=\bar{\mathbf{u}}(t)} \cdot \mathbf{y}(t) + \mathcal{O}(\|\mathbf{y}\|_J^2), \quad (2.17)$$

the formulation (2.16) relative to a special solution may be used in the standard way to obtain the local linearisation which may, away from the boundaries, be written as

$$\dot{\mathbf{y}}_j(t) = \sum_{k=m_f}^{m_l} A_{j,k}(t) \mathbf{y}_{j-k} \quad (2.18)$$

where

$$A_{j,k}(t) = \begin{bmatrix} 0 & \delta_{j,k} & 0 & \text{---} & 0 \\ | & \diagdown & \diagdown & \diagdown & | \\ 0 & & 0 & & 0 \\ \text{---} & & & & \delta_{j,k} \\ \nabla_{\mathbf{u}_k} g_j(\mathbf{u})|_{\mathbf{u}=\bar{\mathbf{u}}(t)} \end{bmatrix}, \quad \delta_{j,k} = \begin{cases} 1 & \text{for } j = k \\ 0 & \text{for } j \neq k. \end{cases} \quad (2.19)$$

We observe the following special cases:

- $\bar{\mathbf{y}}$ is QS $\Rightarrow A_{j,k}(t) \equiv A_{j,k}$
- identical vehicles $\Rightarrow A(j,k)(t) \equiv A_k(t)$
- $\bar{\mathbf{y}}$ is TW $\Rightarrow A_{j,k}(t) = A_k(t - j\Delta t)$.

If assumption 2.5 is satisfied, we may use the headway h_j instead of the position x_j ; the linearisation will then be constructed from blocks of the form

$$B_{j,k}(t) = \begin{bmatrix} 0 & \delta_{j-1,k} - \delta_{j,k} & 0 & \text{---} & 0 \\ | & \diagdown & \diagdown & \diagdown & | \\ 0 & & \delta_{j,k} & & 0 \\ \text{---} & & & & \delta_{j,k} \\ \frac{\partial g_j}{\partial x_{j-1}} - \frac{\partial g_j}{\partial x_j} & P_n \left(\nabla_{\mathbf{u}_k} g_j(\mathbf{u})|_{\mathbf{u}=\bar{\mathbf{u}}(t)} \right) \end{bmatrix}. \quad (2.20)$$

2.3 Examples

Example 2.1 (The Bando model and its extensions)

The Bando model

$$\ddot{x}_j = a (V(x_{j-1} - x_j) - \dot{x}_j), \quad (2.21)$$

sometimes referred to as *the* “optimal velocity model”, is introduced in BANDO et al. (1995a).

V was originally called “legal velocity”, in some publications it is referred to as “range policy function”. In most of the literature, the term “optimal velocity function” is used. Key properties of a reasonable optimal velocity function are:

Assumption 2.6 The optimal velocity function (OVF) V satisfies

$$\text{i) } V(0) = 0, \quad \text{ii) } \lim_{h \rightarrow \infty} V(h) = v_{\max} < \infty, \quad \text{iii) } V' > 0.$$

The parameter $a > 0$ can be interpreted as a sensitivity and is often written as $\frac{1}{\tau}$, where τ is seen as a reaction time.

In terms of Def. 2.3, we have $n = 2$ and $[m_f, m_l] = [0, 1]$, i.e. a second order in time model with dependency of the vehicle directly ahead, where the state of the j -th vehicle is given by $\mathbf{u}_j = [x_j, v_j]^\top$ and the acceleration function is $g_j(\mathbf{u}) = g(\mathbf{u}_{j-1}, \mathbf{u}_j) = a(V(x_{j-1} - x_j) - v_j)$.

The most characteristic phenomena are discussed in BANDO et al. (1994, 1995b). In the early articles, only the circular road is considered. For N vehicles on a ring road of length l the CFM is completed by the periodic boundary condition \mathbf{bc}_{per} (cf. Def. 2.1 and (2.5)), with the effect that

$$g_j \circ \mathbf{bc}_{\text{per}}(\mathbf{u}) = \begin{cases} g(\mathbf{u}_{j-1}, \mathbf{u}_j) & \text{for } 1 < j \leq N \\ g([x_N + l, v_N]^\top, [x_1, v_1]^\top) & \text{for } j = 1. \end{cases}$$

All the experiments that are presented study perturbations of a trivial quasistationary solution (Fig. 2.5(a))

$$x_j(t) = v_e t - j h_e + C, \quad V(h_e) = v_e. \quad (2.22)$$

Solutions on the circular road that are periodic in headway and velocity (Fig. 2.5(b)) are studied in detail in GASSER et al. (2004).

Experiments that simulate an infinite lane are performed in BERG and WOODS (2001). Here transitions between quasistationary solutions in the form of travelling waves are studied (Fig. 2.5(c)).

Over the years, various extensions have been proposed, partly to address the limitations of the model imposed by the strong assumptions:

- MASON and WOODS (1997) and YANG et al. (2014) consider variants with multiple species that use different optimal velocity functions V_j and/or sensitivities a_j (cf. Assumption 2.4), resulting in quasistationary solutions with varying headways (Fig. 2.5(f)).
- BANDO et al. (1998), BANDO et al. (2000) extended their model to account for reaction time delays. This topic was later also studied in more detail e.g. in OROSZ et al. (2004a,b, 2005) (cf. Assumption 2.3).
- LENZ et al. (1999) discuss a model where drivers pay attention to what is happening further ahead, i.e. they use $m_l > 1$.
- JIANG et al. (2001) introduce a relative velocity term. If this is chosen to be linear, the model can be written as

$$\ddot{x}_j = \frac{\alpha}{\tau} (V(x_{j-1} - x_j) - \dot{x}_j) + \frac{1 - \alpha}{\tau} (v_{j-1} - v_j), \quad \alpha \in [0, 1]. \quad (2.23)$$

This approach has been found to have the potential to improve the results substantially and has been widely adopted (see e.g. WILSON and WARD 2011; KISS et al. 2019; TOMOEDA et al. 2018). We will refer to this model as the “aggressive driver model”.

- HUIJBERTS (2002b) motivates the study of non-monotonous OVF with a bus route system where a large distance between buses causes more passengers to wait at bus stops and thus leads to a reduction in speed (cf. Assumption 2.6).

- BURIC and JANOVSKY (2008) interpret crossings of the trajectories as overtaking (cf. Assumption 2.2).
- GASSER and WERNER (2010) introduce bottlenecks along a circular road by multiplying the OVF with a weight function $W : \mathbb{R} \rightarrow (0, 1]$ that reduces the optimal velocity in a certain area (cf. Assumption 2.5):

$$\ddot{x}_j = a(W(x_j) \cdot V(x_{j-1} - x_j) - \dot{x}_j). \quad (2.24)$$

Instead of Qs and PSs, we now have POMs (Fig. 2.5(d)) and quasi-POMs (Fig. 2.5(e)).

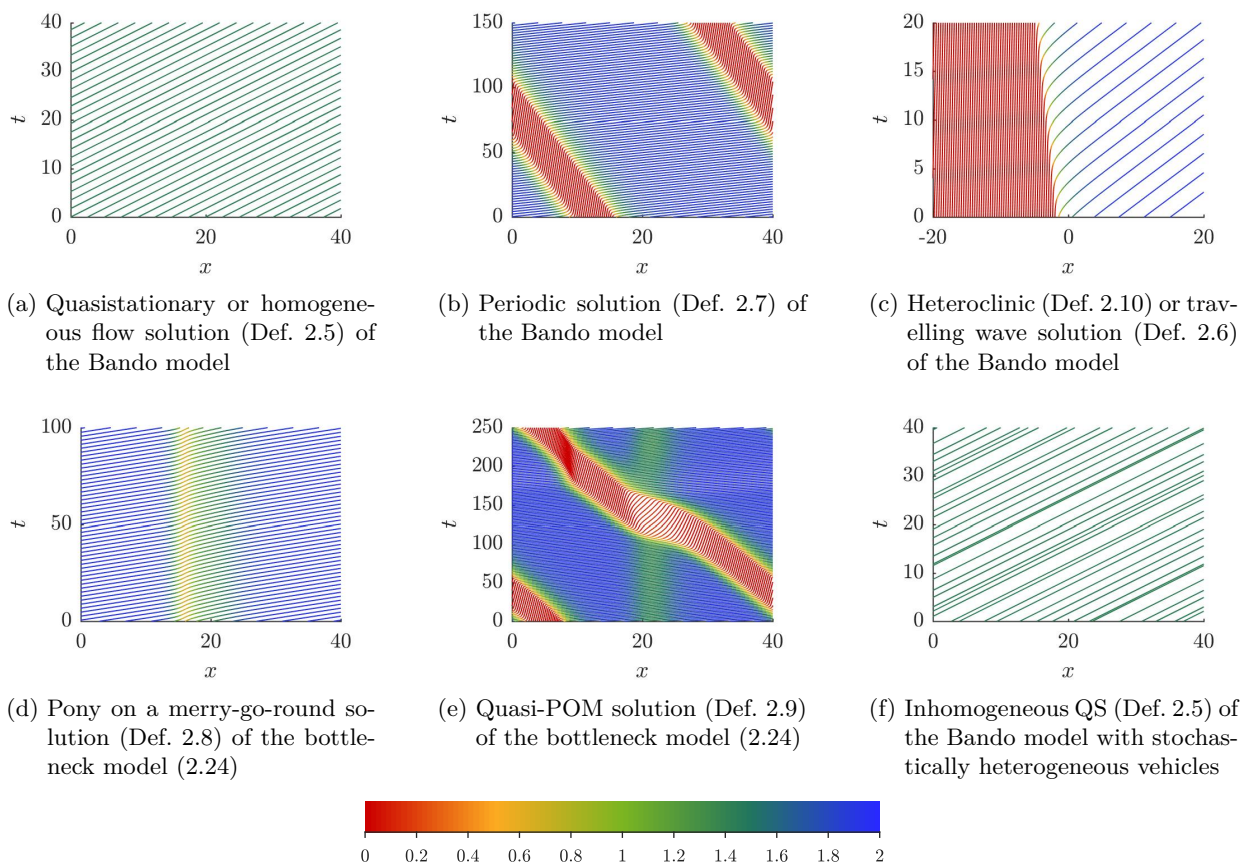


Figure 2.5: Realisations of the special solutions mentioned in the text, with color-coded velocities

Chapter 3

Micro-macro link

3.1 History

Let us briefly review some of the literature on the connection of microscopic and macroscopic traffic flow models.

In PAYNE (1971), Taylor expansions are applied to relate CFMs from GAZIS et al. (1961) of the form $\dot{x}_j(t + \tau) = V(x_{j-1}(t) - x_j(t) - h_e)$ to the PDE

$$\rho_t + (\rho v)_x = 0 \quad (3.1a)$$

$$v_t + vv_x = \frac{1}{\tau} (V_e(\rho) - v). \quad (3.1b)$$

The initial assumption on the headway-density relation here is $h = \frac{1}{\rho}$; later $h(x) = \frac{1}{\rho(x + \frac{1}{2\rho(x)})}$ is used as a heuristic correction, leading to the inclusion of a “pressure term” in (3.1).

HELBING (1998) introduces a coarse-graining procedure, inspired by fluid dynamics. In this way, the Bando model (2.21) is linked to Paynes’s macroscopic model

$$\rho_t + (\rho v)_x = 0 \quad (3.2a)$$

$$v_t + vv_x = \frac{1}{\tau} \left(V_e(\rho) - v + \frac{1}{2\rho} V_e'(\rho) \rho_x \right). \quad (3.2b)$$

Note that Payne’s model (3.2) may also be linked to the time-discrete Newell’s model

$$v(t + \tau) = \min \left(v_e, \frac{x_{j-1}(t) - x_j(t)}{\tau} \right) \quad (3.3)$$

as detailed in (TREIBER and KESTING 2013).

The assumption on the headway-density relation used here is

$$h(x) = \frac{1}{\rho(x + \frac{1}{2\rho(\dots)})}. \quad (3.4)$$

In BERG et al. (2000), the Bando model is considered and compared to the macroscopic Kerner-Konhäuser model (cf. KERNER and KONHÄUSER 1993)

$$\rho_t + (\rho v)_x = 0 \quad (3.5a)$$

$$v_t + vv_x = \frac{1}{\tau} (V_e(\rho) - v) - c \frac{\rho_x}{\rho} + \mu \frac{v_{xx}}{\rho}. \quad (3.5b)$$

The headway-density relation here is

$$\int_{x_j}^{x_{j-1}} \rho(x) dx = 1, \quad (3.6)$$

resulting in the macroscopic model

$$\rho_t + (\rho v)_x = 0 \quad (3.7a)$$

$$v_t + vv_x = \frac{1}{\tau} \left(V_e(\rho) - v + V_e'(\rho) \left(\frac{\rho_x}{2\rho} + \frac{\rho_{xx}}{6\rho^2} - \frac{\rho_x^2}{2\rho^3} \right) \right). \quad (3.7b)$$

In LEE et al. (2001), a coarse-graining approach is used to construct a micro-macro link for the Bando model. They present a systematic way to approximate $h(\rho)$ as

$$h \approx \rho^{-1} + \frac{1}{2\rho} \frac{\partial \rho^{-1}}{\partial x} + \frac{1}{6\rho^2} \frac{\partial^2 \rho^{-1}}{\partial x^2} + \frac{1}{6\rho} \left(\frac{\partial \rho^{-1}}{\partial x} \right)^2. \quad (3.8)$$

They note that this gives a different second order coefficient ($\frac{1}{6}$ instead of $\frac{1}{8}$) compared to an approach with Taylor expansions. Furthermore, they discuss the possibility of setting $h = \frac{1}{\rho}$ and dismiss it because it does not reflect the inherent anisotropy of traffic flow.

HELBING et al. (2002) interpolate the microscopic variables linearly to obtain macroscopic variables. In HELBING (2009), the microscopic variables are instead folded with smoothing functions. He obtains the macroscopic model

$$\rho_t + (\rho v)_x = 0 \quad (3.9a)$$

$$v_t + vv_t = \frac{1}{\tau} \left(\frac{1}{2} \left(V \left(\frac{1}{\rho(x)} \right) + V \left(\frac{1}{\rho(x + \frac{1}{\rho})} \right) \right) - v + \dots \right) \quad (3.9b)$$

that is explicitly non-local.

DI FRANCESCO and ROSINI (2015), DI FRANCESCO et al. (2017) are interested in the other direction: they prove that entropy solutions of scalar conservation laws may be found as many particle limits for corresponding “microscopic” equations under certain conditions.

3.2 Continuous microscopic car-following models

A central problem in the construction of a link between microscopic and macroscopic models is to map the microscopic variables that take arguments from the possibly infinite, but countable vehicle index set J to macroscopic quantities which are functions of the road position $x \in \mathbb{R}$. This typically involves some averaging procedure, as pointed out in the previous section and appears completely natural from the application’s point of view.

We would like to step back and take a different perspective here: What is a “good” equivalent to a macroscopic model? In macroscopic simulations, we will start at some initial condition, which is a function of x . If we want to run a microscopic simulation for comparison, these initial conditions

have to be sampled. There is some ambiguity in this process which is removed as soon as the position of an arbitrary vehicle is fixed. This means that in general there is a whole family of microscopic initial conditions corresponding to a single macroscopic one! Which one should we use?

Mathematically, we are in the lucky position to avoid choosing a single microscopic representative altogether. Instead, we extend our car-following model to continuous index sets J_{co} :

For $\mathcal{A}, \mathcal{B} \subset \mathbb{R}$ let $\mathcal{A} + \mathcal{B} := \{c \in \mathbb{R} : \exists a \in \mathcal{A}, b \in \mathcal{B} : a + b = c\}$.

Definition 3.1 Let $J_{\text{co}} \in \{\mathbb{R}, [0., N.], \mathbb{R}^\pm\}$.

$\mathcal{U}_{\text{co}} := \{f : J_{\text{co}} \rightarrow \mathbb{R}^n\}$, $[n, m_f, m_1] \in \mathbb{N}^3$, $f_{\text{co}} : J_{\text{co}} \times (\mathbb{R}^n)^{-m_f+1+m_1} \rightarrow \mathbb{R}$, and $\text{bc}_{\text{co}} : \mathcal{U}_{J_{\text{co}}} \rightarrow \mathcal{U}_{\mathbb{R}}$ form a **continuous microscopic car-following model** if the restrictions of J_{co} , \mathcal{U}_{co} and f_{co} to $J_{\text{co}} \cap (\mathbb{Z} + \xi)$ form a microscopic car-following model for each $\xi \in [0, 1)$. Note that we admit the car-following models to be connected by the boundary condition in special situations. For an initial datum $\mathbf{u}_{\text{co}}^0 : J_{\text{co}} \rightarrow \mathbb{R}^n$ with monotone first component \mathbf{x}_{co}^0 we analogously define a **continuous microscopic initial value problem** with **solution** $\mathbf{x} : J_{\text{co}} \times [t_0, t_1) \rightarrow \mathbb{R}$.

For appropriate boundary conditions, a continuous car-following model consists of a family of “classical” car following models that are independent of each other. Theorem 2 guarantees that the solutions to the initial problems stay close to each other (at least for finite time) if the initial condition is sufficiently smooth in j . In Ex. 3.3 we solve a continuous microscopic initial value problem numerically by solving the corresponding “classical” IVP for each ξ in a discretization of the interval $[0, 1)$ (cf. Fig. 3.6 a,b).

Since no averaging procedure is required, continuous car-following models are a natural candidate to construct a micro-macro-link from.

Assume that x_{co}^0 is smooth and $\frac{\partial x_{\text{co}}^0}{\partial j}$ is bounded away from zero. Then a corresponding solution $x_{\text{co}} : J_{\text{co}} \times [t_0, t_1)$ will have the same properties, at least on the restriction to some time interval $[t_0, t_2) \subset [t_0, t_1)$. We may then invert the function and instead consider $j : \mathbb{R} \times [t_0, t_2) \rightarrow J_{\text{co}}$.

For simplicity, we assume $[m_f, m_1] = [0, 1]$ and $n = 2$ for the moment, i.e.

$$\dot{x}_j(t) = v_j(t) \tag{3.10a}$$

$$\dot{v}_j(t) = f(x_j(t), h_j(t), v_j(t), v_{j-1}(t)). \tag{3.10b}$$

Using headway and velocity as macroscopic variables, it is now straightforward to obtain a system of PDEs from (3.10):

1. Transform the system to headway coordinates, depending on the position x rather than the index j :

$$\dot{h}(x, t) = v(x + h(x, t), t) - v(x, t)$$

$$\dot{v}(x, t) = f(x, h(x, t), v(x, t), v(x + h(x, t), t)).$$

2. Evaluate the total time derivative $\frac{d}{dt}$:

$$\begin{aligned} h_t(x, t) + v(x, t) \cdot h_x(x, t) &= v(x + h(x, t), t) - v(x, t) \\ v_t(x, t) + v(x, t) \cdot v_x(x, t) &= f(x, h(x, t), v(x, t), v(x + h(x, t), t)). \end{aligned}$$

3. Transform to scaled variables

$$\tilde{t} = \varepsilon t, \quad \tilde{x} = \varepsilon x, \quad \tilde{h}(\tilde{x}, \tilde{t}) = \varepsilon h(x, t), \quad \tilde{v}(\tilde{x}, \tilde{t}) = v(x, t)$$

with macroscopic dimensions (note that the external scaling factor cancels for \tilde{v}):

$$\begin{aligned} \tilde{h}_{\tilde{t}}(\tilde{x}, \tilde{t}) + \tilde{v}(\tilde{x}, \tilde{t}) \cdot \tilde{h}_{\tilde{x}}(\tilde{x}, \tilde{t}) &= \tilde{v}(\tilde{x} + \tilde{h}(\tilde{x}, \tilde{t}), \tilde{t}) - \tilde{v}(\tilde{x}, \tilde{t}) \\ \tilde{v}_{\tilde{t}}(\tilde{x}, \tilde{t}) + \tilde{v}(\tilde{x}, \tilde{t}) \cdot \tilde{v}_{\tilde{x}}(\tilde{x}, \tilde{t}) &= \varepsilon f\left(\frac{\tilde{x}}{\varepsilon}, \frac{\tilde{h}(\tilde{x}, \tilde{t})}{\varepsilon}, \tilde{v}(\tilde{x}, \tilde{t}), \tilde{v}(\tilde{x} + \tilde{h}(\tilde{x}, \tilde{t}), \tilde{t})\right). \end{aligned}$$

4. Replace the car-following function f with a function $\tilde{f}(\tilde{x}, \tilde{h}, \tilde{v}, \tilde{v}') := \varepsilon f\left(\frac{\tilde{x}}{\varepsilon}, \frac{\tilde{h}}{\varepsilon}, \tilde{v}, \tilde{v}'\right)$ that is more suitable for the new coordinates:

$$\tilde{h}_{\tilde{t}}(\tilde{x}, \tilde{t}) + \tilde{v}(\tilde{x}, \tilde{t}) \cdot \tilde{h}_{\tilde{x}}(\tilde{x}, \tilde{t}) = \tilde{v}(\tilde{x} + \tilde{h}(\tilde{x}, \tilde{t}), \tilde{t}) - \tilde{v}(\tilde{x}, \tilde{t}) \quad (3.14a)$$

$$\tilde{v}_{\tilde{t}}(\tilde{x}, \tilde{t}) + \tilde{v}(\tilde{x}, \tilde{t}) \cdot \tilde{v}_{\tilde{x}}(\tilde{x}, \tilde{t}) = \tilde{f}(\tilde{x}, \tilde{h}, \tilde{v}, \tilde{v}'). \quad (3.14b)$$

5. Optional: Approximate the nonlocality with Taylor expansions:

$$\tilde{f}(\tilde{\mathbf{u}}) = \tilde{f}(\tilde{\mathbf{u}}_e) + \partial_{\tilde{x}'} \tilde{f}(\tilde{\mathbf{u}}_e) \cdot \tilde{h} + \partial_{\tilde{v}'} \tilde{f}(\tilde{\mathbf{u}}_e) \cdot \tilde{h} \cdot \tilde{v}_{\tilde{x}} + \dots \quad (3.15)$$

For brevity of notation, we will omit the tilde in the following discussion.

3.3 Densities

What makes things complicated? In analogy to fluid dynamics, we do not want to use the headway, but a density ρ , in order to be able to rewrite (3.14a) in terms of mass conservation.

This will force us to perform a nonlinear coordinate change. Depending on its definition, $\rho(x)$ is possibly not even connected to $h(x)$ by means of a simple function, but depends on the values in a neighbourhood of x , too, by some integral transform.

We would like to link a microscopic CFM of the form (2.8) to a system of PDEs that is first order in time and consists of a mass conservation law, an equivalent to the car-following rule of the form

$$\frac{d}{dt} u_n(x, t) = f_{j(x)}(\mathbf{u}(x + h_{m_f}, t), \dots, \mathbf{u}(x + h_{m_1}, t)) \quad (3.16)$$

and, if applicable, $n - 2$ equations of the form $\frac{d}{dt} u_k = u_{k+1}$, $k \in [2, n - 1]$. To avoid nonlocalities, we may also wish to replace the right hand side of (3.16) by some Taylor approximation.

Our main tasks in the following are consequently to define the notion of a density, discuss how to obtain the distances from a vehicle at position x to its neighbours from the density profile, and to study the mass conservation law corresponding to the density definition.

3.3.1 Definitions

Motivated by the literature review, there are at least three possibilities of how to define a density $\rho : \mathbb{R} \rightarrow \mathbb{R}^+$ from a bijective function $x : J_{\text{co}} \rightarrow \mathbb{R}$:

- **Definition 3.2 (Inverse headway density $\tilde{\rho}$, IHD)**

$$\tilde{\rho}\left(\frac{x_j + x_{j-1}}{2}\right) := \frac{\varepsilon}{x_{j-1} - x_j} \quad (3.17a)$$

This approach emphasises the relation between density and headway and allocates the headway in the middle of the involved cars.

- **Definition 3.3 (Forward-looking density $\hat{\rho}$, FLD)**

$$\hat{\rho}(x_j) := \frac{\varepsilon}{x_{j-1} - x_j} \quad (3.17b)$$

This definition has a direct relation to the headway as well, but has a forward-looking, anisotropic character that will turn out helpful in order to incorporate a connection to the velocity field.

- **Definition 3.4 (Natural density $\check{\rho}$, ND)** Let $j : \mathbb{R} \rightarrow J_{\text{co}}$ be the “counting function” obtained as the inverse of the vehicles’ positions $x : J_{\text{co}} \rightarrow \mathbb{R}$.

$$\check{\rho} := -\varepsilon \frac{\partial j}{\partial x} \quad (3.17c)$$

From a physicist’s perspective, this may be the most “natural” choice due to its equivalence to the definition of a mass density. However, while definitions 3.2 and 3.3 will at least be applicable to a discrete set of positions for discrete J , differentiability requires continuity.

The main ideas behind the three definitions are illustrated in Fig. 3.3 of Ex. 3.1. Given the same $x : J_{\text{co}} \rightarrow \mathbb{R}$, the definitions will in general return different density profiles (Fig. 3.4).

Note that all definitions contain the scaling factor ε . When switching between formulations, it is reasonable to introduce a change in coordinates, too. Since vehicle behaviour is not supposed to change, we scale length and time by the same factor ε .

The choice of the letter ε might seem a bit unfortunate because we do not require ε to be particularly small: Unlike in fluid dynamics, we do not have $\mathcal{O}(10^{23})$ particles to perform limit operations

on. If we want to describe e.g. dynamics on a circular road, it is questionable whether any “many particle limit” is justified.

While $\varepsilon > 1$ makes little sense in practice, for direct comparison between continuous microscopic CFMs and macroscopic models, $\varepsilon = 1$ is a natural choice.

3.3.2 Headway-density relationships

Our next task is, given a vehicle at position x , to determine the distances to its neighbours $j(x) - k$, $k \in [m_f, m_1]$ from the density profile. We will write these distances as

$$h_k(x) := x_{j(x)-k} - x \quad \text{for } k \in [m_f, m_1] \quad (3.18)$$

i.e. $h(x) := h_{+1}(x)$ is the “standard” headway, h_{-1} the first backwards headway (which is, according to the definition, negative), etc. Note that this also includes the trivial distance to the own car $h_0 = 0$.

By induction, it holds that

$$h_{k\pm 1}(x) = h_k(x) + h_{\pm 1}(x + h_k). \quad (3.19)$$

Therefore, we may focus mainly on the standard headway.

3.3.2.1 Inverse headway density

For $\tilde{\rho}$, defined by (3.2), we have the conveniently symmetric expression

$$h_{\pm 1}(x) = \frac{\varepsilon}{\tilde{\rho} \left(x \pm \frac{\varepsilon}{2\tilde{\rho} \left(x \pm \frac{\varepsilon}{2\tilde{\rho}(\dots)} \right)} \right)}.$$

Let

$$T_k(y) := \sum_{j=1}^k \frac{d^j}{d\xi^j} \left(\frac{\varepsilon}{2\tilde{\rho}(\xi)} \right) \Big|_{\xi=x} \frac{y^j}{j!}.$$

i.e. (we omit the argument for brevity)

$$T_2(y) = \frac{\varepsilon}{2} \left(\frac{1}{\tilde{\rho}} - \frac{\tilde{\rho}_x}{\tilde{\rho}^2} \cdot y + \left(\frac{\tilde{\rho}_x^2}{\tilde{\rho}} - \frac{\tilde{\rho}_{xx}}{2\tilde{\rho}^2} \right) \cdot y^2 + \dots \right).$$

Then in $\mathcal{O}(\varepsilon^{n+1})$, we have

$$h(x) = 2T_n(T_{n-1}(\dots(T_1(T_0)))) \quad (3.20)$$

i.e.

$$h = \frac{\varepsilon}{\tilde{\rho}} - \frac{\varepsilon^2 \tilde{\rho}_x}{2\tilde{\rho}^3} + \frac{\varepsilon^3}{8\tilde{\rho}^5} \left(2(\tilde{\rho}_x)^2 - \tilde{\rho}_{xx} \right) + \mathcal{O}(\varepsilon^4). \quad (3.21)$$

An alternative approach to derive this is to introduce the centred headway $\tilde{h} = \frac{\varepsilon}{\tilde{\rho}}$.

The relation between centred headway \tilde{h} and forward headway h may then be written as

$$h(x) = \tilde{h} \left(x + \frac{1}{2} \tilde{h} \left(x + \frac{1}{2} \tilde{h}(\dots) \right) \right) \quad \text{or} \quad h(x) = \tilde{h} \left(x + \frac{h(x)}{2} \right). \quad (3.22)$$

To approximate this, let $T_k \tilde{h}(y)$ denote the n -th order Taylor approximation of \tilde{h} . With

$$T_n \tilde{h}(y) = \sum_{k=0}^n \frac{\partial^k}{\partial \xi^k} \tilde{h}(\xi, t) \Big|_{\xi=x} \frac{y^k}{k!} \quad (3.23)$$

we have

$$h(x) = T_n \tilde{h} \left(\frac{1}{2} T_{n-1} \tilde{h} \left(\dots \left(T_1 \tilde{h}(\tilde{h}) \right) \right) \right) + \mathcal{O}(\tilde{h}^{n+1}) \quad (3.24)$$

i.e.

$$h = \tilde{h} + \frac{1}{2} \tilde{h} \tilde{h}_x + \frac{1}{8} \left(2 \tilde{h}_x^2 + \tilde{h} \tilde{h}_{xx} \right) + \mathcal{O}(\tilde{h}^3), \quad (3.25)$$

which is equivalent to (3.21).

For $n = 2$, $m_l = 1$, $m_f = 0$ we have $f = f(x, x', v, v')$.

To first order in \tilde{h} , this gives

$$\begin{aligned} \tilde{h}_t + v \tilde{h}_x &= \tilde{h} v_x \\ v_t + v v_x &= f(x, x + \tilde{h}, v, v) + \partial_{v'} f(x, x + \tilde{h}, v, v) v_x \tilde{h}; \end{aligned} \quad (3.26)$$

to second order

$$\begin{aligned} \tilde{h}_t + v \tilde{h}_x &= \tilde{h} v_x \\ v_t + v v_x &= f(x, x + \tilde{h}, v, v) + \nabla_{[x', v']} f(x, x + \tilde{h}, v, v) \cdot \left[v_x \left(\tilde{h} + \frac{1}{2} \tilde{h} \tilde{h}_x \right) + \frac{v_{xx}}{2} \tilde{h}^2 \right] \\ &\quad + \frac{1}{2} \partial_{v' v'} f(x, x + \tilde{h}, v, v) v_x^2 \tilde{h}^2. \end{aligned} \quad (3.27)$$

3.3.2.2 Forward-looking density

For the forward-looking density $\hat{\rho}$, definition 3.3 directly gives

$$\hat{h}(x) = \hat{h}_{+1}(x) = \frac{\varepsilon}{\hat{\rho}}. \quad (3.28)$$

Note, however, that for the backwards headway we have to do a construction similar as before:

$$\hat{h}_{-1}(x) = - \frac{\varepsilon}{\hat{\rho} \left(x - \frac{\varepsilon}{\hat{\rho}(x - \frac{\varepsilon}{\hat{\rho}(\dots)})} \right)}. \quad (3.29)$$

3.3.2.3 Natural density

For $\check{\rho}$ defined by (3.4), we may write $\check{\rho}(x)$ as a Taylor series:

$$\check{\rho}(x + \delta) = \check{\rho} + \check{\rho}_x \delta + \frac{\check{\rho}_{xx}}{2} \delta^2 + \dots = \sum_{j=0}^{\infty} \frac{\delta^j}{j!} \frac{\partial^j \check{\rho}}{\partial x^j}.$$

By definition of $\check{\rho}$, we have

$$j(x+\delta) - j(x) = \frac{1}{\varepsilon} \int_x^{x+\delta} \check{\rho}(x+z) dz = \frac{1}{\varepsilon} \sum_{j=0}^{\infty} \frac{\delta^{j+1}}{(j+1)!} \frac{\partial^j \check{\rho}}{\partial x^j} = \sum_{j=1}^{\infty} \underbrace{\frac{1}{\varepsilon j!} \frac{\partial^{j-1} \check{\rho}}{\partial x^{j-1}}}_{=: a_j} \delta^j$$

with inverse function

$$\delta(n) = \sum_{j=1}^{\infty} b_j n^j.$$

For the coefficients A_j , we use the expression

$$\begin{aligned} b_1 &= a_1^{-1} = \frac{\varepsilon}{\check{\rho}} \\ b_2 &= -a_1^{-3} a_2 = -\frac{\varepsilon^2}{2} \frac{\check{\rho}_x}{\check{\rho}^3} \\ b_3 &= a_1^{-5} (2a_2^2 - a_1 a_3) = \frac{\varepsilon^3}{\check{\rho}^5} \left(\frac{\check{\rho}_x^2}{2} - \frac{\check{\rho} \check{\rho}_{xx}}{6} \right) \\ b_4 &= a_1^{-7} (a_1 a_2 a_3 - a_1^2 a_4 - 5a_2^3) \\ b_n &= \frac{1}{n a_1^n} \sum_{\left(\sum_{k=1}^n k b_k = n-1 \right)} (-1)^{\left(\sum_{k=1}^n b_k \right)} \frac{\left(n-1 + \sum_{k=1}^n b_k \right)!}{(n-1)! \prod_{k=1}^n b_k!} \prod_{k=2}^n \left(\frac{a_k}{a_1} \right)^{b_k} \end{aligned}$$

which can be found e.g. in MORSE and FESHBACH (1953). The headway to the k -th neighbour is then given by

$$\check{h}_{\pm k} = \sum_{j=1}^{\infty} b_j (\pm k)^j. \quad (3.30)$$

For the most important case $k=1$ we have

$$\check{h}(x) = \sum_{k=1}^{\infty} b_k = \frac{\varepsilon}{\check{\rho}} - \frac{\varepsilon^2}{2} \frac{\check{\rho}_x}{\check{\rho}^3} + \frac{\varepsilon^3}{\check{\rho}^5} \left(\frac{\check{\rho}_x^2}{2} - \frac{\check{\rho} \check{\rho}_{xx}}{6} \right) + \mathcal{O}(\varepsilon^4). \quad (3.31)$$

To this order, this corresponds to the approximation (3.8) from LEE et al. (2001).

The relations between the different headways and densities that have been introduced so far are summarised in Fig. 3.1.

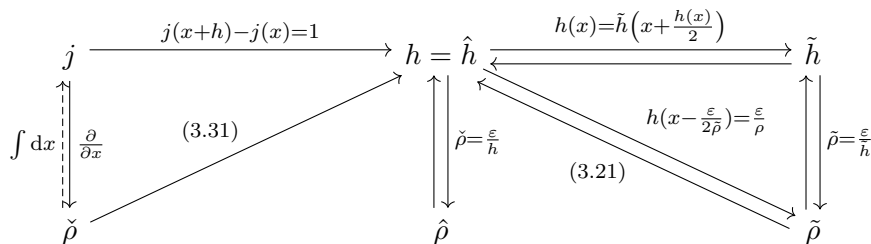


Figure 3.1: Overview of relations between the different density definitions introduced above and their corresponding headways

3.3.3 Continuity equations

We will now calculate mass conservation equations for the density definitions.

For the natural density $\check{\rho}$, the standard derivation from fluid dynamics is applicable, i.e. we have “pure” mass conservation

$$\check{\rho}_t + (\check{\rho}v)_x = 0. \quad (3.32a)$$

To obtain an equation for the inverse headway density $\tilde{\rho}$, we calculate the total derivative of (3.17a):

$$\begin{aligned} \frac{d}{dt}\tilde{\rho}(x, t) &= \tilde{\rho}_t + \frac{1}{2}\tilde{\rho}_x \left(v \left(x + \frac{\varepsilon}{2\tilde{\rho}} \right) + v \left(x - \frac{\varepsilon}{2\tilde{\rho}} \right) \right) = -\frac{\tilde{\rho}^2}{\varepsilon} \left(v \left(x + \frac{\varepsilon}{2\tilde{\rho}} \right) - v \left(x - \frac{\varepsilon}{2\tilde{\rho}} \right) \right) \\ &\Leftrightarrow \tilde{\rho}_t + \tilde{\rho}_x \left(\sum_{j=0}^{\infty} \frac{v^{(2j)}}{(2j)!} \left(\frac{\varepsilon}{2\tilde{\rho}} \right)^{(2j)} \right) = -\frac{2\tilde{\rho}^2}{\varepsilon} \left(\sum_{j=0}^{\infty} \frac{v^{(2j+1)}}{(2j+1)!} \left(\frac{\varepsilon}{2\tilde{\rho}} \right)^{(2j+1)} \right) \end{aligned} \quad (3.32b)$$

i.e.

$$\tilde{\rho}_t + \tilde{\rho}_x \left(v + \varepsilon^2 \frac{v_{xx}}{8\tilde{\rho}^2} \right) = -\tilde{\rho}v_x - \varepsilon^2 \frac{v_{xxx}}{24\tilde{\rho}} + \mathcal{O}(\varepsilon^4).$$

Alternatively, this may be obtained from the headway conservation equation

$$\tilde{h}_t + \tilde{h}_x \cdot \left(\frac{v \left(x + \frac{\tilde{h}}{2} \right) + v \left(x - \frac{\tilde{h}}{2} \right)}{2} \right) = v \left(x + \frac{\tilde{h}}{2} \right) - v \left(x - \frac{\tilde{h}}{2} \right)$$

which is approximated by

$$\tilde{h}_t + \tilde{h}_x \left(2 \sum_{j=0}^{\lfloor N/2 \rfloor} \frac{v^{(2j)}}{(2j)!} \left(\frac{\tilde{h}}{2} \right)^{2j} \right) = 2 \sum_{j=0}^{\lfloor N/2 \rfloor} \frac{v^{(2j+1)}}{(2j+1)!} \left(\frac{\tilde{h}}{2} \right)^{2j+1}.$$

For the forward-looking density, the same procedure applied to (3.17b) yields

$$\begin{aligned} \frac{d}{dt}\hat{\rho}(x, t) &= \hat{\rho}_t + \hat{\rho}_x v = -\frac{\hat{\rho}^2}{\varepsilon} \left(v \left(x + \frac{\varepsilon}{\hat{\rho}} \right) - v \right) \\ &= -\frac{\hat{\rho}^2}{\varepsilon} \sum_{j=1}^{\infty} \frac{v^j}{j!} \left(\frac{\varepsilon}{\hat{\rho}} \right)^j \\ &= -\hat{\rho}v_x - \varepsilon \frac{v_{xx}}{2} - \mathcal{O}(\varepsilon^2). \end{aligned} \quad (3.32c)$$

We see that the nonlocalities in definitions 3.2 and 3.3 have severe consequences for the continuity equation:

Each of the equations (3.32a) - (3.32c) has in first order the standard continuity equation $\rho_t + (\rho v)_x = 0$. As could be expected, the natural density recovers mass conservation exactly.

In contrast, for (3.32b) and (3.32c), we have correction terms including second and higher derivatives of v in space. No higher order derivatives in ρ appear.

For (3.32b), both $\rho_x v$ (“left hand side”) and ρv_x (“right hand side”) need to be corrected: The LHS correction is because definitions of ρ and v refer to different positions, i.e. x_j and $\frac{1}{2}(x_j + x_{j-1})$. On both sides, corrections come only with even powers of ε because of odd/even cancellation

effects. In (3.32c) we only have corrections on the RHS for the ρv_x -term.

The approximations (3.21), (3.28), (3.31) of the headway to the leading car all start with $\frac{\varepsilon}{\rho}$, higher order terms in ε are following.

Here, the FLD gives the “pure” case by construction. However, the ND is still attractive: while the formula for A_j is complicated, even for $[m_f, m_l] \neq [0, 1]$ all distances can directly be recovered from the series (3.30).

The choice of IHD seems to be disadvantageous in comparison, despite its “intuitive” definition. For the FLD $\hat{\rho}$, the PDE system can directly be calculated from system (3.14) by the transformation $h = \hat{h} = \frac{\varepsilon}{\hat{\rho}}$. It is therefore reasonable to do simulations in terms of the headways and transform to the corresponding densities in a post-processing step.

For the special case $n = 2$, $m_l = 1$, $m_f = 0$ we have

$$\hat{h}_t + v\hat{h}_x = v(x + \hat{h}) - v(x) \quad (3.33a)$$

$$v_t + vv_x = f(x, x + \hat{h}, v(x), v(x + \hat{h})), \quad (3.33b)$$

which can be approximated by

$$\hat{h}_t + v\hat{h}_x = \sum_{k=1}^N \frac{v^{(k)}}{k!} h^k \quad (3.34a)$$

$$v_t + vv_x = \sum_{k=0}^N \frac{1}{k!} \frac{\partial^k}{\partial v'^k} f(x, x + \hat{h}, v(x), v(x)) \left(\sum_{l=0}^{N-k} \frac{v^{(l)}}{l!} \hat{h}^l \right)^k. \quad (3.34b)$$

3.4 Numerics for macroscopic equations

3.4.1 Finite differences

We first introduce a finite difference discretisation for (3.34). To abbreviate the notation, we write the coefficients of the n -th order approximation of the m -th derivative as

$$\begin{aligned} c_i^{(m,n)}, \quad i \in \left[-\left\lfloor \frac{m+n}{2} \right\rfloor, \left\lfloor \frac{m+n}{2} \right\rfloor \right] & \quad \text{centered difference stencil} \\ \tilde{c}_i^{(m,n)}, \quad i \in [0, m+n-1] & \quad \text{forward (downstream) difference stencil} \\ \bar{c}_i^{(m,n)}, \quad i \in [1 - (m+n), 0] & \quad \text{backward (upstream) difference stencil.} \end{aligned}$$

Our approach is to discretise with finite difference approximation in space and integrate in time with a suitable ODE solver.

For the spatial derivatives on the left-hand side, information has to come from the upstream direction. Therefore, we use backwards differences (upwind scheme) in this part.

For $n = 2$, $m_f = 0$, $m_l = 1$, we have $f = f(x, x', v, v')$. On the right-hand side of (3.34a), information has to be taken from the downstream direction, since the headway is affected by the leading car. Consequently, forward differences are being used here.

The discretisation is then given by

$$\partial_t \hat{h}_i + \frac{v_i}{\Delta x} \sum_j \bar{c}_j^{(1,N)} \hat{h}_{i+j} = -v_i + \sum_{k=0}^N \frac{1}{k!} \frac{\hat{h}_i^k}{\Delta x^k} \sum_j \bar{c}_j^{(k,N)} v_{i+j} \quad (3.35a)$$

$$\partial_t v_i + \frac{v_i}{\Delta x} \sum_j \bar{c}_j^{(1,N)} v_{i+j} = \sum_{k=0}^N \frac{1}{k!} \frac{\partial^k}{\partial v^k} f(x_i, x_i + \hat{h}_i, v_i, v_i) \left(\sum_{l=0}^{N-k} \frac{1}{l!} \frac{\hat{h}_i^l}{\Delta x^l} \sum_j \bar{c}_j^{(l,N)} v_{i+j} \right)^k. \quad (3.35b)$$

At $\mathcal{O}(\hat{h})$, this gives

$$\partial_t \hat{h}_i = -\frac{v_i}{\Delta x} (-\hat{h}_{i-1} + \hat{h}_i) + \frac{\hat{h}_i}{\Delta x} (-v_i + v_{i+1}) \quad (3.36a)$$

$$\partial_t v = -\frac{v_i}{\Delta x} (-v_{i-1} + v_i) + f(x_i, x_i + \hat{h}_i, v_i, v_i) + \partial_v f(x_i, x_i + \hat{h}_i, v_i, v_i) \frac{\hat{h}_i}{\Delta x} (-v_i + v_{i+1}); \quad (3.36b)$$

at $\mathcal{O}(\hat{h}^2)$, we have

$$\partial_t \hat{h}_i = -\frac{v_i}{\Delta x} \left(\frac{1}{2} \hat{h}_{i-2} - 2\hat{h}_{i-1} + \frac{3}{2} \hat{h}_i \right) + \frac{\hat{h}_i}{\Delta x} \left(-\frac{3}{2} v_i + 2v_{i+1} - \frac{1}{2} v_{i+2} \right) + \frac{1}{2} \frac{\hat{h}_i^2}{\Delta x^2} (v_i - 2v_{i+1} + v_{i+1}) \quad (3.37a)$$

$$\begin{aligned} \partial_t v = & -\frac{v_i}{\Delta x} \left(\frac{1}{2} v_{i-2} - 2v_{i-1} + \frac{3}{2} v_i \right) + f(x_i, x_i + \hat{h}_i, v_i, v_i) \\ & + \partial_v f(x_i, x_i + \hat{h}_i, v_i, v_i) \left(\frac{\hat{h}_i}{\Delta x} \left(-\frac{3}{2} v_i + 2v_{i+1} - \frac{1}{2} v_{i+2} \right) + \frac{1}{2} \frac{\hat{h}_i^2}{\Delta x^2} (v_i - 2v_{i+1} + v_{i+1}) \right) \\ & + \frac{1}{2} \partial_{v^2} f(x_i, x_i + \hat{h}_i, v_i, v_i) \frac{\hat{h}_i^2}{\Delta x^2} \left(-\frac{3}{2} v_i + 2v_{i+1} - \frac{1}{2} v_{i+2} \right)^2, \end{aligned} \quad (3.37b)$$

etc.

Note that the term

$$\sum_{k=0}^N \frac{1}{k!} \frac{\hat{h}_i^k}{\Delta x^k} \sum_j \bar{c}_j^{(k,N)} v_{i+j}$$

in the RHS of (3.35a) can be interpreted as a polynomial approximation of the velocity $v(x)$ based on its values at sampling points x_i, \dots, x_{i+N} , evaluated at position $x_i + \hat{h}_i$. In this sense, the discretisation also directly approximates the underlying ODE (Fig. 3.2). From this observation we may conjecture that optimal results will be obtained if the grid size is on the order of magnitude of the mean inter-vehicle distance.

It is not surprising that this scale should be resolved in order to capture reasonably detailed traffic behaviour and obtain results that are directly comparable to the microscopic model. For an even finer resolution, the microscopic model would of course be preferable.

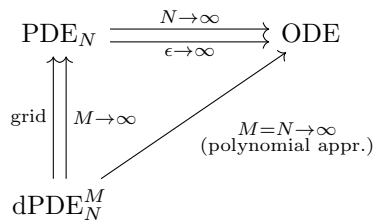


Figure 3.2: Connection between ODE (3.10), PDE (3.33), and spatial FD discretisation (3.35) for the “naive” formulation in headway and velocity

3.4.2 Finite volume

In order to respect the mass conservation in the natural density formulation, we employ finite volume methods. The source terms in the acceleration equation are integrated using a fractional step method.

The inverse headway density is also discretised in this way, with source terms also in the mass balance equation for higher-order approximations.

For the concrete implementation we use the software package `clawpack-5` (CLAWPACK DEVELOPMENT TEAM 2019); an introduction to the software can be found in LEVEQUE (2002).

Where not stated otherwise, the `sharpclaw` solver with high-order wave propagation schemes using WENO reconstruction and Runge-Kutta integration is chosen. Alternatively, the software allows to employ e.g. Godunov- or Lax-Wendroff-LeVeque-schemes.

3.5 Examples

Example 3.1 (Density definitions)

We consider a circular road with $N = 5$ vehicles on it and average headway $h_e = 1$, i.e. the circle length is $l = 5$. The initial vehicle distribution corresponding to a QS is then $x_j(0) = C - jh_e$, where C is an arbitrary constant. Regardless which one of the definitions 3.2-3.4 is chosen, this leads to a constant density $\rho_e \equiv 1$.

The differences between the density definitions become obvious if we add a N -periodic perturbation. Of course, we need to make sure any new vehicle distribution is still monotonically decreasing. In Fig. 3.3, the construction of the densities defined in the main text is illustrated for

$$x(j) = 5 - j - \sin^2\left(\frac{j}{5}\right). \quad (3.38)$$

When comparing the different density profiles, we observe that, while the results for IHD and ND are quite similar, the FLD is shifted to the left by ca. half an equilibrium headway, as could be expected from its definition.

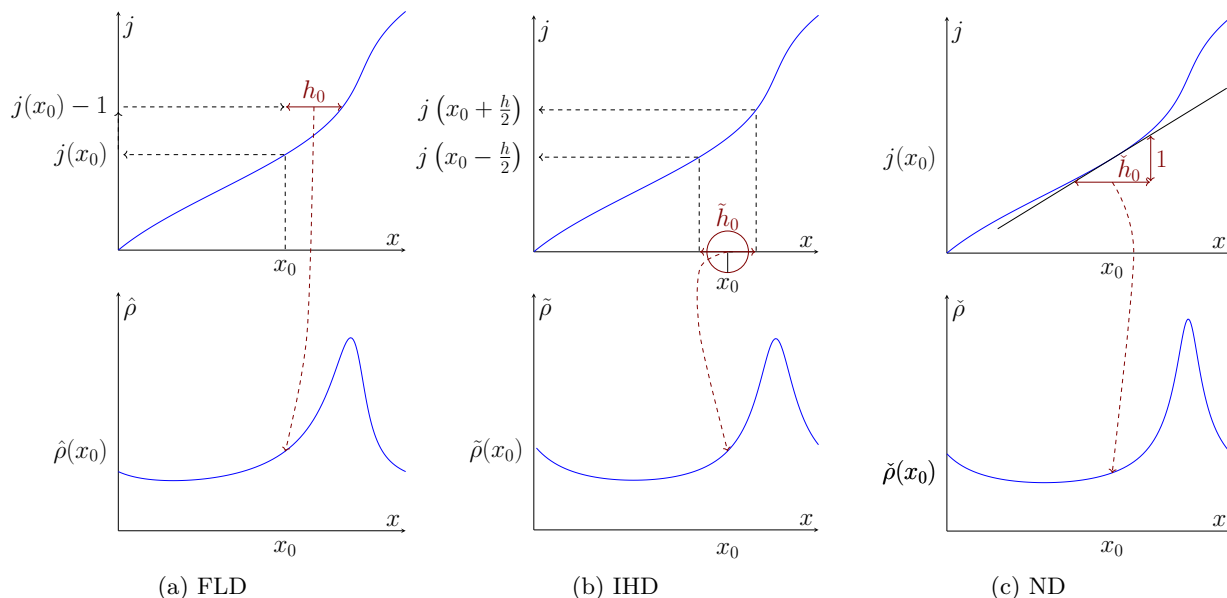


Figure 3.3: Construction of density from the graph of $j(x)$ for a ring with $J = [0, 5.]$ and continuous vehicle positions $x_j = 5 - \left(j + \sin^2 \frac{j\pi}{5}\right)$. Note that the values on the ordinate are decreasing in the upper row

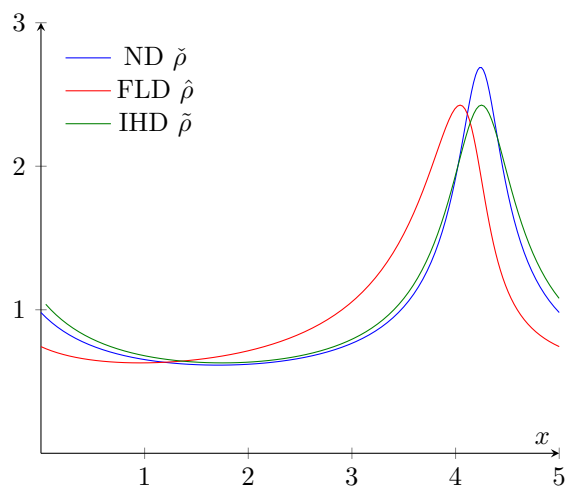


Figure 3.4: Direct comparison of the different density profiles obtained in Fig. 3.3. Due to the anisotropy in its definition, the profile for the forward-looking density is shifted slightly to the left compared to the “symmetric” densities

Example 3.2 (Comparison of micro-macro links for the Bando model)

From the literature mentioned in Sec. 3.1, LEE et al. (2001), HELBING (2009), and BERG et al. (2000) use the Bando model we discussed in Ex. 2.1 as an example.

Let us demonstrate which macroscopic models the different density definitions yield for the Bando model with aggressive drivers (2.23) with $n = 2$, $m_1 = 1$, $m_f = 0$ and the vehicle-independent

car-following function

$$f : \mathbb{R}^4 \rightarrow \mathbb{R}, \quad \left(\begin{bmatrix} x_j \\ v_j \end{bmatrix}, \begin{bmatrix} x_{j-1} \\ v_{j-1} \end{bmatrix} \right) \mapsto \frac{\alpha}{\tau} (V(x_{j-1} - x_j) - v_j) + \frac{1-\alpha}{\tau} (v_{j-1} - v_j).$$

As above, we set $\tilde{\mathbf{u}} = \left(\begin{bmatrix} x \\ v(x) \end{bmatrix}, \begin{bmatrix} x + \frac{\varepsilon}{\rho} \\ v(x) \end{bmatrix} \right)$.

The Taylor approximation in (3.15) becomes

$$\begin{aligned} \tilde{f}(\tilde{\mathbf{u}}) &= \frac{\alpha}{\tau} \left(\sum_{k=0}^{\infty} \frac{V^{(k)}\left(\frac{\varepsilon}{\rho}\right)}{k!} \left(h - \frac{\varepsilon}{\rho}\right)^k - v \right) + \frac{1-\alpha}{\tau} \left(\sum_{k=1}^{\infty} \frac{v^{(k)}}{k!} h^k \right) \\ &= \frac{\alpha}{\tau} \left(V\left(\frac{\varepsilon}{\rho}\right) - v + V'\left(\frac{\varepsilon}{\rho}\right) \left(h - \frac{\varepsilon}{\rho}\right) + \dots \right) \\ &\quad + \frac{1-\alpha}{\tau} \left(v_x h + \frac{v_{xx}}{2} h^2 + \dots \right). \end{aligned}$$

We refrain from the futile renaming of v . It is common to introduce an ‘‘equilibrium velocity function’’ $V_e(\rho) := V\left(\frac{\varepsilon}{\rho}\right)$. We are skipping this step in favour of the comparability with the microscopic formulation, but note that $V'\left(\frac{\varepsilon}{\rho}\right)$ is of order $\frac{1}{\varepsilon}$ due to the inner derivative, $V'_e(\rho) = -\frac{\varepsilon}{\rho^2} V'\left(\frac{\varepsilon}{\rho}\right)$.

After these considerations, we plug in the headway approximations (3.21), (3.28), and (3.31) and obtain the following macroscopic systems, where we omit the argument $\frac{\varepsilon}{\rho}$ of V, V' etc. for brevity. For the inverse-headway density, we have

$$\tilde{\rho}_t + \tilde{\rho}_x \left(v + \varepsilon^2 \frac{v_{xx}}{8\tilde{\rho}^2} \right) = -\tilde{\rho}v_x - \varepsilon^2 \frac{v_{xxx}}{24\tilde{\rho}} + \mathcal{O}(\varepsilon^4) \quad (3.39a)$$

$$\begin{aligned} v_t + vv_x &= \frac{\alpha}{\tau} \left[V - v + V' \cdot \left(-\frac{\varepsilon^2 \tilde{\rho}_x}{2\tilde{\rho}^3} + \frac{\varepsilon^3}{\tilde{\rho}^5} \left(\frac{\tilde{\rho}_x^2}{4} - \frac{\tilde{\rho}\tilde{\rho}_{xx}}{8} \right) + \dots \right) \right. \\ &\quad \left. + \frac{V''}{2} \cdot \left(-\frac{\varepsilon^2 \tilde{\rho}_x}{2\tilde{\rho}^3} + \dots \right)^2 + \dots \right] \\ &\quad + \frac{1-\alpha}{\tau} \left[v_x \left(\frac{\varepsilon}{\tilde{\rho}} - \frac{\varepsilon^2 \tilde{\rho}_x}{2\tilde{\rho}^3} + \frac{\varepsilon^3}{\tilde{\rho}^5} \left(\frac{\tilde{\rho}_x^2}{4} - \frac{\tilde{\rho}\tilde{\rho}_{xx}}{8} \right) + \dots \right) \right. \\ &\quad \left. + \frac{v_{xx}}{2} \left(\frac{\varepsilon}{\tilde{\rho}} - \frac{\varepsilon^2 \tilde{\rho}_x}{2\tilde{\rho}^3} + \dots \right)^2 + \dots \right] + \mathcal{O}(\varepsilon^3) \quad (3.39b) \end{aligned}$$

and for the forward-looking density we have

$$\begin{aligned} \hat{\rho}_t + \hat{\rho}_x v &= -\frac{\hat{\rho}^2}{\varepsilon} \sum_{j=1}^{\infty} \frac{v^j}{j!} \left(\frac{\varepsilon}{\hat{\rho}} \right)^j \\ v_t + vv_x &= \frac{\alpha}{\tau} (V - v) + \frac{1-\alpha}{\tau} \left(\sum_{k=1}^{\infty} \frac{v^{(k)}}{k!} \left(\frac{\varepsilon}{\hat{\rho}} \right)^k \right). \end{aligned}$$

Up to third order in ε , the latter yields

$$\hat{\rho}_t + \hat{\rho}_x v = - \left(\hat{\rho} v_x + \varepsilon \frac{v_{xx}}{2} + \varepsilon^2 \frac{v_{xxx}}{6\hat{\rho}} + \varepsilon^3 \frac{v_{xxxx}}{24\hat{\rho}^2} \right) + \mathcal{O}(\varepsilon^4) \quad (3.40a)$$

$$v_t + vv_x = \frac{\alpha}{\tau} (V - v) + \frac{1-\alpha}{\tau} \left(\varepsilon \frac{v_x}{\hat{\rho}} + \varepsilon^2 \frac{v_{xx}}{2\hat{\rho}^2} + \varepsilon^3 \frac{v_{xxx}}{6\hat{\rho}^3} \right) + \mathcal{O}(\varepsilon^4). \quad (3.40b)$$

For the natural density, we obtain

$$\check{\rho}_t + (\check{\rho}v)_x = 0 \quad (3.41a)$$

$$\begin{aligned} v_t + vv_x = & \frac{\alpha}{\tau} \left[V - v + V' \cdot \left(-\frac{\varepsilon^2 \check{\rho}_x}{2\check{\rho}^3} + \frac{\varepsilon^3}{\check{\rho}^5} \left(\frac{\check{\rho}_x^2}{2} - \frac{\check{\rho}\check{\rho}_{xx}}{6} \right) + \dots \right) \right. \\ & \left. + \frac{V''}{2} \cdot \left(-\frac{\varepsilon^2 \check{\rho}_x}{2\check{\rho}^3} + \dots \right)^2 + \dots \right] \\ & + \frac{1-\alpha}{\tau} \left[v_x \cdot \left(\frac{\varepsilon}{\check{\rho}} - \frac{\varepsilon^2 \check{\rho}_x}{2\check{\rho}^3} + \frac{\varepsilon^3}{\check{\rho}^5} \left(\frac{\check{\rho}_x^2}{2} - \frac{\check{\rho}\check{\rho}_{xx}}{6} \right) + \dots \right) \right. \\ & \left. + \frac{v_{xx}}{2} \cdot \left(\frac{\varepsilon}{\check{\rho}} - \frac{\varepsilon^2 \check{\rho}_x}{2\check{\rho}^3} + \dots \right)^2 + \dots \right] + \mathcal{O}(\varepsilon^3). \end{aligned} \quad (3.41b)$$

Example 3.3 (Numerical simulations)

For our numerical simulations, we consider the case $\alpha = 1$. At first order in ε , the systems in (3.39)-(3.41) reduce to

$$\rho_t + j_x = 0 \quad (3.42a)$$

$$j_t + \left(\frac{j^2}{\rho} + \frac{\varepsilon}{2\tau} V_e'(\rho) \right)_x = \frac{\rho}{\tau} \left(V_e(\rho) - \frac{j}{v} \right), \quad (3.42b)$$

independent of the underlying density definition. This changes at second order in ε . Here we have

$$\check{\rho}_t + j_x = 0 \quad (3.43a)$$

$$j_t + \left(\frac{j^2}{\check{\rho}} + \frac{\varepsilon}{2\tau} V_e'(\check{\rho}) \right)_x = \frac{\check{\rho}}{\tau} \left(V_e(\check{\rho}) - \frac{j}{v} + \frac{\varepsilon^2}{\check{\rho}^2} \left(V_e'(\check{\rho}) \left(\frac{\check{\rho}_{xx}}{6} - \frac{\check{\rho}_x^2}{4\check{\rho}} \right) + V_e''(\check{\rho}) \frac{\check{\rho}_x^2}{8} \right) \right) \quad (3.43b)$$

for the natural density (3.41),

$$\tilde{\rho}_t + j_x = -\varepsilon^2 \left(\frac{\tilde{\rho}_x v_{xx}}{8\tilde{\rho}^2} + \frac{v_{xxx}}{24\tilde{\rho}} \right) \quad (3.44a)$$

$$j_t + \left(\frac{j^2}{\tilde{\rho}} + \frac{\varepsilon}{2\tau} V_e'(\tilde{\rho}) \right)_x = \frac{\tilde{\rho}}{\tau} \left(V_e(\tilde{\rho}) - \frac{j}{v} + \frac{\varepsilon^2}{\tilde{\rho}^2} \left(V_e'(\tilde{\rho}) \left(\frac{\tilde{\rho}_{xx}}{8} - \frac{\tilde{\rho}_x^2}{4\tilde{\rho}} \right) + V_e''(\tilde{\rho}) \frac{\tilde{\rho}_x^2}{8} \right) \right) \quad (3.44b)$$

for the inverse headway density (3.39) and the headway PDE

$$h_t + vh_x = v_x h + \frac{v_{xx}}{2} h^2 \quad (3.45a)$$

$$v_t + vv_x = \frac{1}{\tau} (V(h) - v). \quad (3.45b)$$

instead of (3.40).

For the conservative part of the ND and IHD, we use a modified Riemann solver with Roe averaging for the isothermal Euler equations in density-flux formulation provided as an example with version 4.3 of `clawpack`. The solver was translated to `Fortran90` and is called by `pyclaw`.

The results for a test profile

$$\rho(x, 0) = \frac{1}{2} \left(1 + \exp \left(-0.05 (x + 50)^2 \right) + \chi_{[25,75]} \right), \quad v(x, 0) = V_e(\rho(x, 0)) \quad (3.46)$$

are displayed in Fig. 3.6 together with the corresponding microscopic simulation. Fig. 3.5 demonstrates the effects of the usage of different solvers and grid sizes on the quality of the results.

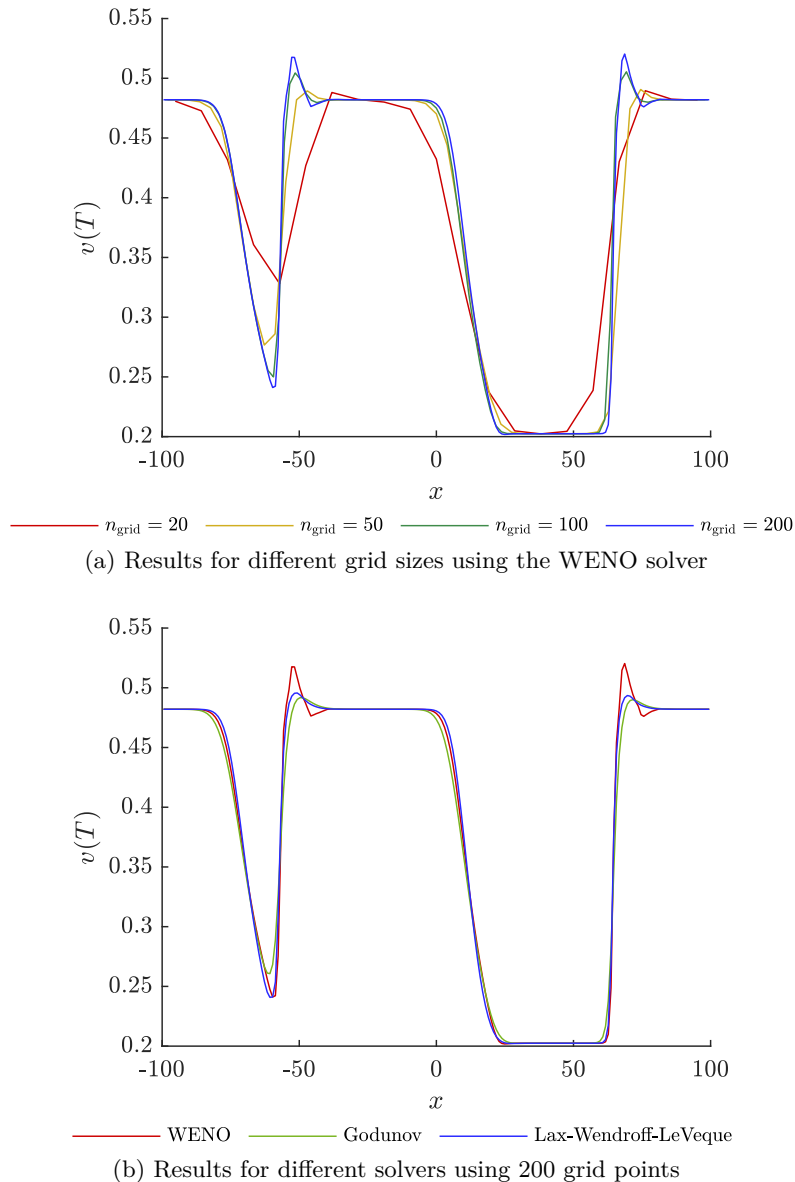


Figure 3.5: Comparison of different settings for the solution of the 2nd order natural density equations. The graphs show the velocity profiles at $T = 20$ for initial condition (3.46)

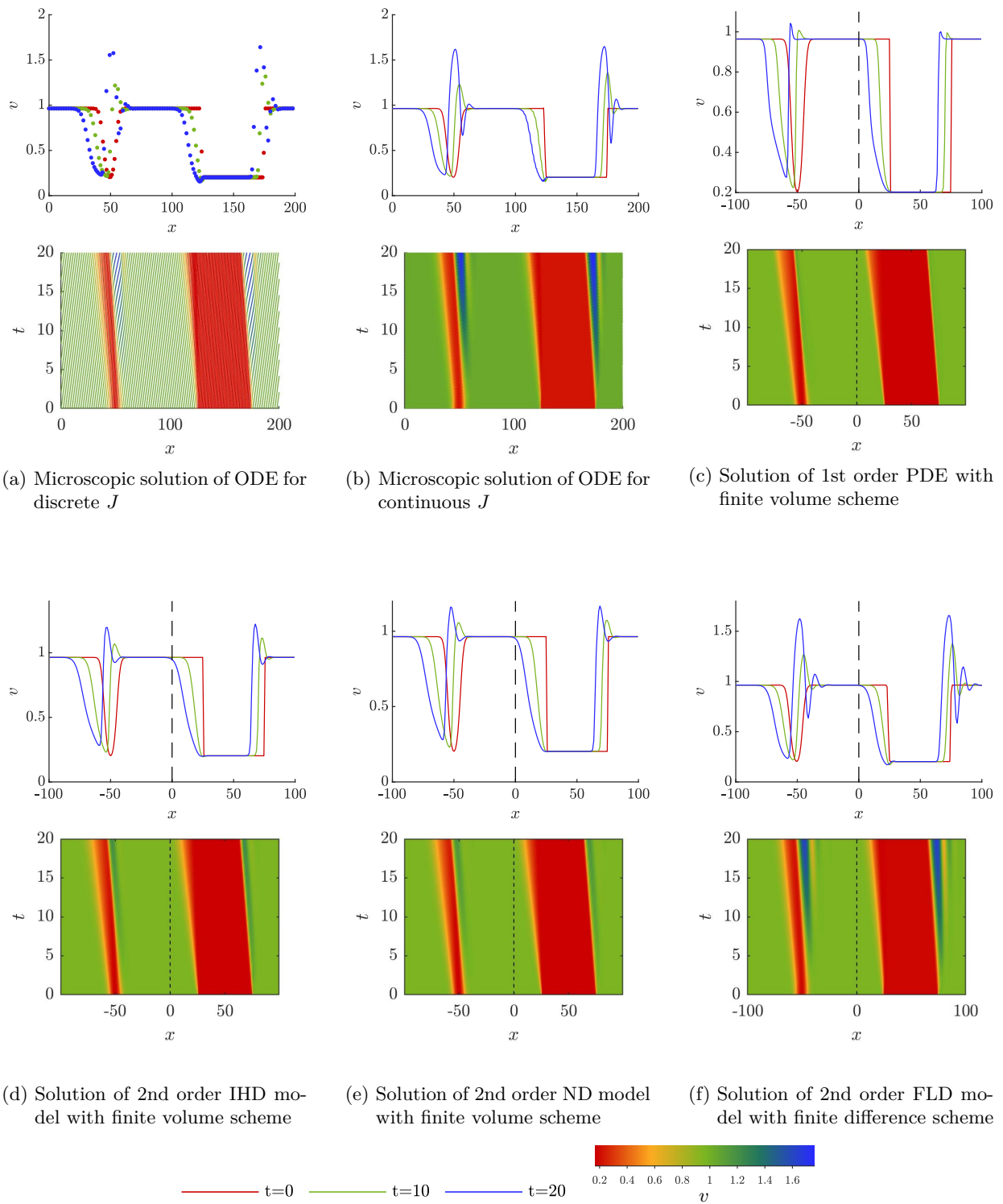


Figure 3.6: Comparison of discrete and continuous microscopic simulations (a,b) with the first order macroscopic model that is independent of the density definition (c), and the 2nd order results for the different density definitions (d-f) for initial condition (3.46). Colours in the upper and lower rows refer to different time snapshots and to velocity, respectively. The finite volume simulations are performed using a WENO solver and 200 grid points

II Quasistationary solutions

Chapter 4

Stability

In Sec. 4.1, we recall some of the well-known theory about linear stability, formulating it in terms of Toeplitz and Laurent operators, in order to emphasise the connections between the different road settings.

We will also briefly discuss the possibility of making statements about nonlinear stability with Lyapunov arguments.

Afterwards we demonstrate that the spectra of the sequences of macroscopic models derived in Sec. 3 not only have the same string stability properties due to their behaviour close to the origin, but also approximate the rest of the spectrum well.

4.1 Microscopic models

Discussion of stability of quasistationary solutions may be regarded as a main pillar of traffic flow theory and is addressed in a wide range of publications, see e.g. WILSON and WARD (2011) for a general approach and BANDO et al. (1994), HUIJBERTS (2002a) for a discussion of the Bando model. Largely unnoticed by much of the traffic flow community, related questions have also been discussed at length in the engineering community. In a recent survey, FENG et al. (2019) show that there is a wide range of definitions related to the stability of quasistationary solutions of a car-following model, which is thought of as a controller design for automated or assisted driving. The fact that they are apparently unaware of the seminal paper WILSON and WARD (2011) is another indication for a lack of communication between the two thematically closely related communities.

4.1.1 Linear stability in terms of Toeplitz and Laurent operators

Since not all of the settings we are interested in involve leading cars, we focus on stability with respect to perturbations of the initial conditions. We will work with the following definition:

Definition 4.1 (Linearised string stability) A quasistationary solution to a car-following model is called **linear string stable** if the linearisation of the CFM around the QS converges to zero as $t \rightarrow \infty$ for any initial condition $(\mathbf{u}_j^0)_{j \in J}$ in $\ell_n^2(J)$.

This notion of string stability is maybe closest related to what is referred to as the “original definition of string stability” in FENG et al. (2019):

A string of vehicle is stable if, for any set of bounded initial disturbances to all the vehicles, the position fluctuations of all the vehicles remain bounded and these fluctuations approach zeros as $t \rightarrow \infty$.

We consider the case of a car-following model satisfying assumptions 2.3-2.4 introduced in Sec. 2.1 with a quasistationary solution described by some equilibrium headway h_e and equilibrium velocity v_e . In this setting, the linearisation (2.18) simplifies to

$$\dot{\mathbf{u}}_j(t) = \sum_{k=m_f}^{m_1} A_k \mathbf{u}_{j-k}, \quad (4.1)$$

where

$$A_0 = \begin{bmatrix} 0 & 1 & 0 \\ \vdots & \ddots & \ddots \\ 0 & \cdots & 0 & 1 \\ \frac{\partial f_j}{\partial x_j} & \frac{\partial f_j}{\partial v_j} & \cdots \end{bmatrix} \quad \text{and} \quad A_k = \begin{bmatrix} 0 & \cdots & 0 \\ \vdots & & \vdots \\ 0 & \cdots & 0 \\ \frac{\partial f_j}{\partial x_{j-k}} & \frac{\partial f_j}{\partial v_{j-k}} & \cdots \end{bmatrix} \quad \text{for } k \neq 0 \quad (4.2)$$

i.e. the stability matrices $A_{j,k}(t)$ are constant with respect to time and index; the latter is of course not true as soon as assumption 2.4 is removed.

Globally, we may assemble the $n \times n$ -matrices A_k into an operator \mathcal{A} describing the instantaneous reaction of the system to a small perturbation.

$$(\dot{\mathbf{u}}_j)_{j \in J} = \mathcal{A} \cdot (\mathbf{u}_j)_{j \in J} \quad (4.3)$$

The type of \mathcal{A} now depends on the nature of the index set J and the boundary condition (Fig. 4.1).

In each case, A_{m_f}, \dots, A_{m_1} fill up the m_1 -th lower to $|m_f|$ -th upper block diagonal.

For finite vehicle numbers $N \in \mathbb{N}$, \mathcal{A} is a $n \cdot N \times n \cdot N$ -matrix. In the circular road setting with $N \in \mathbb{N}$ vehicles, the matrices A_k wrap around periodically such that there are exactly $m_1 - m_f + 1$ $n \times n$ -blocks in each row and column of the underlying $N \times N$ -grid (Fig. 4.1(a)). If we replace the periodic boundary condition by “phantom vehicles” at constant speed, thus considering a platoon of N vehicles on an open road, the wraparound vanishes and we obtain a block Toeplitz matrix (Fig. 4.1(b)).

Equivalently, for infinitely many vehicles, the block diagonals will either stretch incessantly to both sides if $J = \mathbb{Z}$, forming a block Laurent operator (Fig. 4.1(c)), or be cut on oneside if $J = \pm\mathbb{N}$, i.e. if there is a first or a last car, thus forming a block Toeplitz operator (Fig. 4.1(d)).

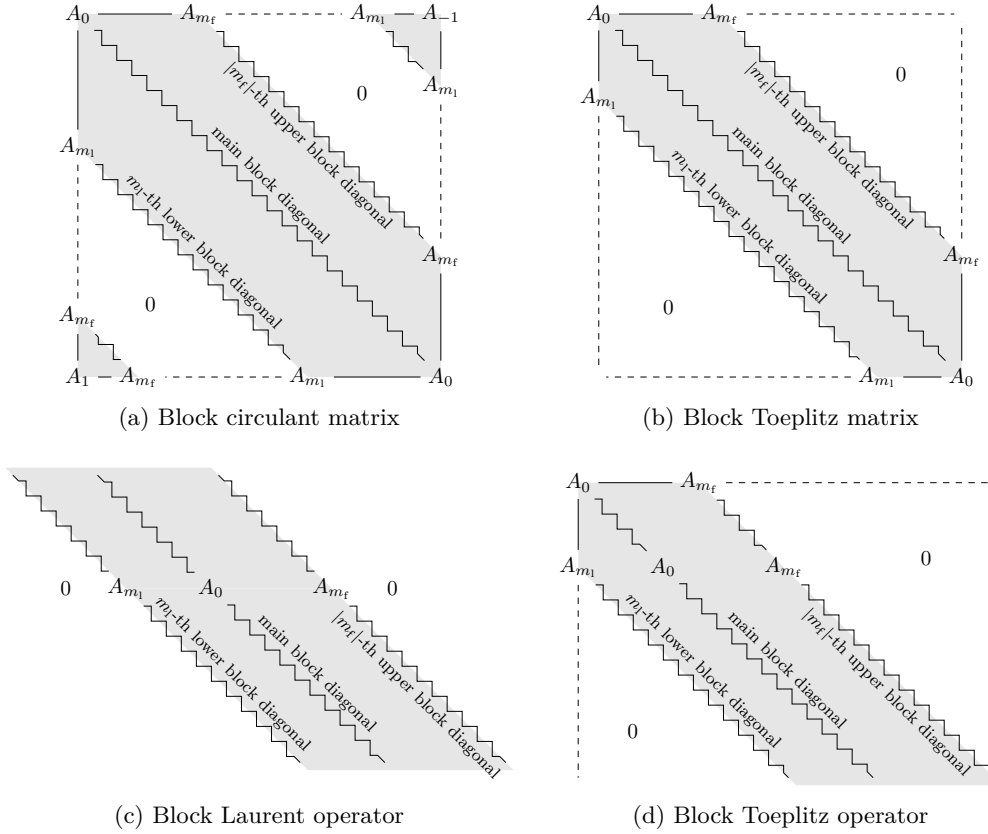


Figure 4.1: Structure of relevant matrices and operators

For Toeplitz matrices and -operators there is a well-developed theory, see e.g. BÖTTCHER and SILBERMANN (1999); TREFETHEN and EMBREE (2005). One of their main attractions is that the spectra for circulant matrices, Toeplitz and Laurent operators can be described in very simple terms.

The central notion in the area of matrices and operators of this kind is that of the *symbol*.

Definition 4.2 (symbol of \mathcal{A}) 1. Let \mathcal{A} be a circulant matrix or a Laurent- or Toeplitz operator with scalar entries $a_{m_f}, \dots, a_{m_1} \in \mathbb{R}$. The associated **symbol** is defined as the function

$$s : \mathbb{C} \rightarrow \mathbb{C}, \quad z \mapsto \sum_{k=m_f}^{m_1} z^k a_k. \quad (4.4)$$

2. If the entries are given by the matrices A_{m_f}, \dots, A_{m_1} , the associated symbol is the matrix-valued function

$$S : \mathbb{C} \rightarrow \mathbb{C}^{n \times n}, \quad z \mapsto \sum_{k=m_f}^{m_1} z^k A_k. \quad (4.5)$$

In the literature, Toeplitz operators are also known as discrete Wiener-Hopf operators, Laurent operators as multiplication operators, and frequently the appendix “with matrix-valued symbol” is used instead of the prefix “block” (cf. BÖTTCHER and SILBERMANN 2006).

Theorem 3 (Spectra of circulant matrices, Laurent- and Toeplitz operators)

Let \mathcal{A} be a circulant matrix or a Laurent- or Toeplitz operator with scalar entries $a_{m_f} \dots a_{m_l} \in \mathbb{R}$ and symbol $s : \mathbb{C} \rightarrow \mathbb{C}$.

1. $\lambda \in \mathbb{C}$ is in the spectrum $\sigma(\mathcal{A})$ iff there is a $\xi \in \begin{cases} \frac{2\pi}{N} \cdot [1, N] & \text{if } \mathcal{A} \text{ is a circulant matrix} \\ [0, 2\pi) & \text{if } \mathcal{A} \text{ is a Laurent operator} \end{cases}$ such that $\lambda = s(\exp(i\xi))$.

2. $\lambda \in \mathbb{C}$ is in the spectrum of a Toeplitz operator iff it is in the spectrum of the corresponding Laurent operator or enclosed by it with non-zero winding number.

Proof: See for example TREFETHEN and EMBREE (2005, p. 51) or BÖTTCHER and SILBERMANN (2006, p. 65). □

The reasoning in the proof of part 1 may be directly extended to the case of block circulant matrices and block Laurent operators:

Theorem 4 (Spectra of block circulant matrices and block Laurent operators)

Let \mathcal{A} be a block circulant matrix or Laurent operator constructed from real $n \times n$ -matrices A_{m_f}, \dots, A_{m_l} with symbol $S : \mathbb{C} \rightarrow \mathbb{C}^{n \times n}$. Then $\lambda \in \mathbb{C}$ is in its spectrum $\sigma(\mathcal{A})$ iff it is a root of the characteristic function χ ,

$$0 = \det(S(\exp(i\xi)) - \lambda \text{Id}) =: \chi(\lambda, \xi), \tag{4.6}$$

for some $\xi \in \begin{cases} \frac{2\pi}{N} [1, N] & \text{if } \mathcal{A} \text{ is a block circulant matrix} \\ [0, 2\pi) & \text{if } \mathcal{A} \text{ is a block Laurent operator.} \end{cases}$

Proof: See BÖTTCHER and SILBERMANN (2006, p. 101). □

In the case of block Toeplitz operators we need to be more careful because the operator \mathcal{A} may fail to be invertible even if its symbol $S(z) \in \mathbb{C}^{n \times n}$ is invertible for each z on the unit circle (BÖTTCHER and SILBERMANN 1999, p. 186).

Definition 4.3 (Fredholm operator) A bounded linear operator $\mathcal{A} : \ell_n^2(J) \rightarrow \ell_n^2(J)$ is called **Fredholm** if its kernel

$$\ker \mathcal{A} := \{ \mathbf{x} \in \ell_n^2(J) : \mathcal{A}\mathbf{x} = 0 \}$$

and cokernel

$$\text{coker } \mathcal{A} := \ell_n^2(J) / \text{im } \mathcal{A} = \ell_n^2(J) / \{ \mathbf{y} \in \ell_n^2(J) : \exists \mathbf{x} \in \ell_n^2(J) : \mathcal{A}\mathbf{x} = \mathbf{y} \}$$

are finite-dimensional. In this case, $\text{ind } \mathcal{A} := \dim \ker \mathcal{A} - \dim \text{coker } \mathcal{A}$ is called the **Fredholm index**.

Definition 4.4 (essential spectrum) For a bounded linear operator $\mathcal{A} : \ell_n^2(J) \rightarrow \ell_n^2(J)$, the **essential spectrum** is defined as the set

$$\sigma_{\text{ess}} := \{ \lambda \in \mathbb{C} : \mathcal{A} - \lambda \text{Id is not Fredholm} \}.$$

We observe that spectrum and essential spectrum coincide for $J = [1, N]$, and that the symbols of the occurring operators are continuous on the unit circle. With the notions introduced above we can formulate the following result by GOHBERG:

Theorem 5 (Spectra of block Toeplitz operators) *Let \mathcal{A} be a block Toeplitz operator constructed from real $n \times n$ -matrices A_{m_f}, \dots, A_{m_1} . Then $\lambda \in \mathbb{C}$ is in its essential spectrum $\sigma_{\text{ess}}(\mathcal{A})$ iff it is a root of the characteristic function χ from (4.6) for some $\xi \in [0, 2\pi)$. Moreover, the Fredholm index of $\mathcal{A} - \lambda \text{Id}$ is given by the negative of the winding number of the essential spectrum around this $\lambda \in \mathbb{C}$.*

Proof: See BÖTTCHER and SILBERMANN (1999, p. 188) and references therein. \square

The variable ξ introduced above can be viewed as an “index eigenvalue”, related to the spatial eigenvalues ν in PDE models that we will encounter in Sec. 4.2. For this reason we choose to refrain from the traditional notation as “ k ”, as e.g. in MITARAI and NAKANISHI (2000a); GASSER et al. (2004). Especially in physics literature, k is often associated with a wavenumber which has the dimension of an inverse length; we emphasise that this is not the case here. With this notation we are relatively close to SANDSTED and SCHEEL (2000). In physics literature we also often encounter $i\omega = \lambda$ for the temporal eigenvalues.

By induction, we may conclude from (2.19) and (2.18) that the characteristic polynomial χ in (4.6) is of the form

$$\chi(\lambda, \xi) = \lambda^n - [1, \lambda, \dots, \lambda^{n-1}] \cdot \sum_{k=m_f}^{m_1} e^{ik\xi} \nabla_{\mathbf{u}_k} f. \quad (4.7)$$

Thus, χ is a n -th order polynomial in λ , and $\chi \cdot z^{|m_f|}$ is a $|m_1 - m_f|$ -order polynomial in $z = e^{i\xi}$. Note that the image of the symbol for $z \in i\mathbb{R}$ is a closed curve that separates \mathbb{C} into connected components. For any given $\lambda \in \mathbb{C}$, there are $|m_1 - m_f|$ values of z solving $\deg(S(z) - \lambda \text{Id}) = 0$. It will turn out helpful to number them with values in $\mathbb{Z} + \frac{1}{2}$.

As λ moves within the inner part of the connected components, the number of values of z to the left and the right stays constant; sort them by real part, and let m^* denote the integer between the last one with negative and the first one with positive real part, i.e.

$$\begin{aligned} \text{Re}\left(z_{m_f+\frac{1}{2}}\right) &\leq \text{Re}\left(z_{m_f+\frac{3}{2}}\right) \leq \dots \leq \text{Re}\left(z_{m^*-\frac{1}{2}}\right) < 0 \\ &< \text{Re}\left(z_{m^*+\frac{1}{2}}\right) \leq \dots \leq \text{Re}\left(z_{m_1-\frac{3}{2}}\right) \leq \text{Re}\left(z_{m_1-\frac{1}{2}}\right). \end{aligned} \quad (4.8)$$

As we will see, $m^* \stackrel{!}{=} 0$ for $\text{Re}(\lambda) \gg 0$:

Consider (4.1) for $J = \pm\mathbb{N}_0$ together with initial conditions $\mathbf{u}_j(0) = \mathbf{u}_j^0$ and a boundary condition

$\mathbf{u}_j(t) = \mathbf{w}_j(t)$, $j \in \begin{cases} [-m_1, -1] & \text{for } J = \mathbb{N}_0 \\ [1, -m_f] & \text{for } J = -\mathbb{N}_0 \end{cases}$. In order to solve these, perform a Laplace transform:

$$\lambda \mathbf{u}_j - \mathbf{u}_j^0 = \sum_{k=m_f}^{m_1} A_k \mathbf{u}_{j-k} \quad (4.9)$$

We only need to consider the homogeneous case $u_j^0 \equiv 0$. The eigenvalue equation $\lambda \mathbf{v} = S(z)\mathbf{v}$ yields solutions to the homogeneous part of (4.9) for $j \notin [m_f, m_l]$.

These solutions make up two subspaces of dimensions $|m_{l,f} - m^*|$ of solutions that are in $l^2(\pm\mathbb{N}_0)$, respectively. For $J = \mathbb{N}_0$ and a given λ , we now need to find a unique linear combination of the solutions to $z_{m^*+\frac{1}{2}}, \dots, z_{m_l-\frac{1}{2}}$ that also satisfies the m_l boundary conditions; for $J = -\mathbb{N}_0$, a unique linear combination of the solutions to $z_{m_f+\frac{1}{2}}, \dots, z_{m^*-\frac{1}{2}}$ needs to satisfy m_f boundary conditions. Obviously, this will in general only be the case for $m^* = 0$.

Consequently, it is a reasonable assumption that $m^*(\lambda) = 0$ for $\text{Re}(\lambda) \gg 0$.

What happens for $m^*(\lambda) \neq 0$? Consider $m^* = 1$ which is of most interest in our setting. Now the solutions for $j \notin [m_f, m_l]$ split into a $|m_l| - 1$ -dimensional subspace of solutions for $J = \mathbb{N}_0$ and a $|m_f| + 1$ -dimensional subspace for $J = -\mathbb{N}_0$. This means that while the boundary condition cannot be satisfied for \mathbb{N}_0 any more, there now is a one-dimensional subspace that works for $-\mathbb{N}_0$, forming an eigenfunction of the system that is exponentially localised at the lower end of the motorcade, called a boundary mode (TREFETHEN and EMBREE 2005). In either case, invertibility of $\mathcal{A} - \lambda \text{Id}$ is lost, consequently λ is in the spectrum of \mathcal{A} . This motivates the following proposition, which can also be seen as a simple lemma of Theorem 5:

Proposition 4.1 Let \mathcal{A} be a block Toeplitz operator constructed from real $n \times n$ -matrices A_{m_1}, \dots, A_{m_f} . Then $\lambda \in \mathbb{C}$ is in its spectrum $\sigma(\mathcal{A})$ if it is in the essential spectrum of the corresponding Laurent operator or if $m^*(\lambda) \neq 0$, i.e. if λ is enclosed by the spectrum with nonzero winding number.

See Ex. 4.4 for an application of this theory to the Bando model.

For a finite platoon on the infinite lane, $J = [1, N]$, it has been noted that the eigenvalues do not give satisfactory information about the stability behaviour. In the case $m_f = 0$, it can be directly seen from the matrix \mathcal{A} that the eigenvalues are given by the so-called ‘‘platoon eigenvalues’’ with multiplicity N , i.e. $\sigma(\mathcal{A}) = \sigma(A_0)$ (WILSON and WARD 2011; WERNER 2013). Intuitively, we would expect these eigenvalues to approximate in some sense the spectra in the infinite-dimensional case.

As conjectured in WERNER (2013), key to this is the observation that the boundary modes to the Toeplitz operators for $\pm\mathbb{N}_0$ are ‘‘almost’’ eigenvectors for big N .

Definition 4.5 (ε -pseudospectrum) Let $\varepsilon > 0$, \mathcal{A} be in $\mathbb{R}^{N \times N}$. $\lambda \in \mathbb{C}$ is in the ε -**pseudospectrum** $\sigma_\varepsilon(\mathcal{A})$ of \mathcal{A} provided there is a vector $\mathbf{v} \in \mathbb{C}^N$ such that $\frac{\|(\mathcal{A}-\lambda)\mathbf{v}\|_2}{\|\mathbf{v}\|_2} \leq \varepsilon$.

Let $(\mathcal{A}_N)_{N \in \mathbb{N}}$ be the sequence of Toeplitz matrices for $N \in \mathbb{N}$ vehicles on an infinite lane.

For the scalar case $n = 1$, we have (TREFETHEN and EMBREE 2005, p. 61):

Theorem 6 (Convergence of ε -pseudospectra)

$\lim_{\varepsilon \rightarrow 0} \lim_{N \rightarrow \infty} \sigma_\varepsilon(\mathcal{A}_N) = \sigma(\mathcal{A}_\mathbb{N})$ in the Hausdorff metric.

Note that the generalisation of this theorem for block matrices and -operators ($n > 1$) shown in (BÖTTCHER and SILBERMANN 1999, p. 196) takes a far more complicated shape. However, for

$m_f = 0$, we can easily construct pseudoeigenvectors: Fix $\lambda \in \mathbb{C}$. Suppose there is $z \in \mathbb{C}$ with $|z| < 1$ and $\det(S(z) - \lambda \text{Id}) = 0$ so that we can find $\mathbf{w} \in \mathbb{C}^n$ such that $(S(z) - \lambda \text{Id})\mathbf{w} = 0$. Then $\mathbf{v}_{-\mathbb{N}} = (\mathbf{v}_j)_{j \in -\mathbb{N}} = (z^{-j}\mathbf{w})_{j \in -\mathbb{N}}$ is an exact eigenvector to $\mathcal{A}_{-\mathbb{N}}$.

From this we see that the vector $\mathbf{v}_{[1,N]} = (\mathbf{w}_j)_{j \in [1,N]} = (z^N \mathbf{w}, \dots, z^1 \mathbf{w})^\top$ gets asymptotically close to an eigenvector (Fig. 4.2):

$$\frac{\|(\mathcal{A}_N - \lambda) \mathbf{v}_{[1,N]}\|_2}{\|\mathbf{v}_{[1,N]}\|_2} = \frac{\sqrt{\sum_{l=1}^{m_1} \left\| \sum_{k=l}^{m_1} A_k \mathbf{w} z^{(N+k-l)} \right\|_2^2}}{\sqrt{\sum_{j=0}^{N-1} z^j} \|\mathbf{w}\|_2} \leq C |z|^N.$$

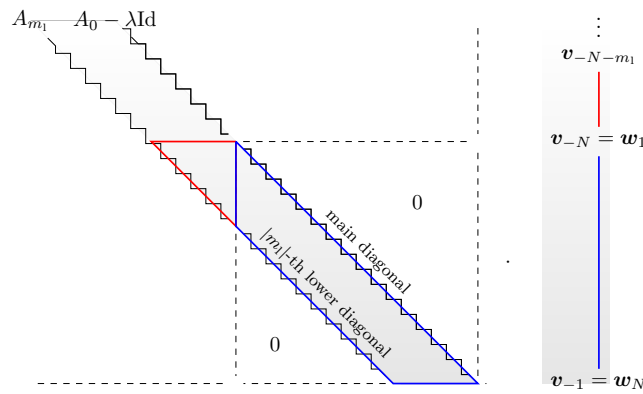


Figure 4.2: Construction of ε -pseudoeigenvectors for $m_f = 0$: For $|z| < 1$, the block Toeplitz operator for $J = -\mathbb{N}$ (left) has an eigenvector $\mathbf{v}_{-\mathbb{N}}$ (right). The first N entries of $\mathbf{v}_{-\mathbb{N}}$ are close to an eigenvector to the block Toeplitz matrix for N vehicles (blue), the error is given by the multiplication of the “overhanging” part of the Toeplitz operator (red triangle) with the vector $(\mathbf{v}_{1-N-m_1}, \dots, \mathbf{v}_{-N})^\top$. (red vertical line)

In this sense, the ε -pseudospectrum can give us insights for the nonscalar case $n > 1$ as well, e.g. for the transient behaviour of the Bando model for finite platoons (cf. Ex. 4.5).

On the open road without a leader, the construction above would lead to modes with unbounded amplitude and is therefore not reasonable.

We conclude that while the platoon eigenvalues do not yield much information for the behaviour of a motorcade with finite length, the pseudoeigenvalues and -vectors do. The unconditional stability of the platoon eigenvalues reflects the fact that each car will return to its position of rest eventually after an initial perturbation. By induction, this is also true for a finite motorcade. However, it may take a long time until all vehicles have reached their rest state again. The pseudoeigenvectors for $|z| < 1$ are exponentially localised at the upstream end of the motorcade. They indicate that it is only the lack of more vehicles that provides stability here.

4.1.2 Different frames of reference

In a microscopic traffic model, the natural independent variables are the vehicle index j and time t . We are thus taking the drivers’ perspective, which is a reasonable choice in many situations.

Sometimes, however, we may want to focus on the behaviour of the model in a certain spatial region (e.g. to conclude about emissions in a given area), or more generally on the behaviour observed while moving at a relative speed with respect to the heterogeneous solution. This distinction will become particularly important in Sec. 5, but also for the comparison of the stability properties with macroscopic models, which are usually formulated in a fixed reference frame.

In a continuous car-following model, this poses no major problem. We merely have to introduce an alternative, time-dependent vehicle index $\tilde{j} = j - ct$. In terms of \tilde{j} , the ODE (2.8) becomes

$$\begin{aligned} \dot{\mathbf{u}}_{\tilde{j}}(t) &= \frac{d}{dt} \mathbf{u}(\tilde{j}(t), t) = -c \cdot \frac{\partial}{\partial \tilde{j}} \mathbf{u}(\tilde{j}, t) + \frac{\partial}{\partial t} \mathbf{u}_{\tilde{j}}(t) \\ &= -c \cdot \frac{\partial}{\partial \tilde{j}} \mathbf{u}(\tilde{j}, t) + \mathbf{g}_{\tilde{j}}(\mathbf{u}_{\tilde{j}-m_1}(t), \dots, \mathbf{u}_{\tilde{j}-m_f}(t)) \quad \forall \tilde{j} \in J_{\text{co}}. \end{aligned} \quad (4.10)$$

Of course this also applies to the local linearisation (2.18), which now becomes

$$\frac{\partial}{\partial t} \mathbf{y}_{\tilde{j}}(t) + c \frac{\partial}{\partial \tilde{j}} \mathbf{y}_{\tilde{j}}(t) = \sum_{k=m_f}^{m_1} A_{\tilde{j},k}(t) \mathbf{y}_{\tilde{j}-k}. \quad (4.11)$$

We will then have to replace the characteristic polynomial $\chi(\lambda, \xi)$ in (4.6) by

$$0 = \det \left(S(\exp(i\xi)) - (\tilde{\lambda} + ic\xi) \text{Id} \right) =: \tilde{\chi}(\tilde{\lambda}, \xi). \quad (4.12)$$

For fixed $\xi \in \mathbb{C}$, the temporal eigenvalues in the different frames are simply related by $\lambda = \tilde{\lambda} + ic\xi$ (cf. MITARAI and NAKANISHI 2000a). Unfortunately there is no comparable formula for the relation between the roots of $\chi(\lambda, \cdot)$ and $\tilde{\chi}(\tilde{\lambda}, \cdot)$ for fixed $\lambda = \tilde{\lambda} \in \mathbb{C}$. While it may be possible to explicitly calculate the index eigenvalues for simple models (Ex. 4.2), in general they will have to be found numerically.

4.1.3 Acceleration models with a single leader

For $m_f = 0$, $m_1 = 1$, and $n = 2$ we have $f = f(x_j, x_{j-1}, v_j, v_{j-1})$. Then (2.18) becomes with $y_j = x_j - \bar{x}_j$, $w_j = v_j - v_e$

$$\begin{bmatrix} \dot{y}_j \\ \dot{w}_j \end{bmatrix} = \begin{bmatrix} 0 & 1 \\ \partial_{x_j} f & \partial_{v_j} f \end{bmatrix} \cdot \begin{bmatrix} y_j \\ w_j \end{bmatrix} + \begin{bmatrix} 0 & 0 \\ \partial_{x_{j-1}} f & \partial_{v_{j-1}} f \end{bmatrix} \cdot \begin{bmatrix} y_{j-1} \\ w_{j-1} \end{bmatrix}, \quad (4.13)$$

(4.6) becomes

$$\chi(\lambda, \xi) = \lambda \left(\lambda - \partial_{v_j} f - \partial_{v_{j-1}} f e^{i\xi} \right) - \underbrace{\left(\partial_{x_j} f + \partial_{x_{j-1}} f e^{i\xi} \right)}_{\stackrel{(2.9)}{=} \partial_{h_j} f(e^{i\xi} - 1)},$$

or, when writing the acceleration function as $g(h_j, v_j, \Delta v_j)$ with $\Delta v_j = v_{j-1} - v_j$ (cf. WILSON and WARD 2011):

$$\chi(\lambda, \xi) = \lambda \left(\lambda - \partial_{v_j} g - \partial_{\Delta v_j} g \left(e^{i\xi} - 1 \right) \right) - \partial_{h_j} g \left(e^{i\xi} - 1 \right).$$

Note that $\partial_{v_j} g = \partial_{v_j} f + \partial_{v_{j-1}} f$, $\partial_{\Delta v_j} g = \partial_{v_{j-1}} f$; the fact that i.g. $\partial_{v_j} f \neq \partial_{v_j} g$ might cause some

confusion at first glance.

For $n = 2$, the characteristic polynomial can be solved for λ :

$$\lambda_{\pm}(\xi) = \frac{\partial_{v_j} f + \partial_{v_{j-1}} f e^{i\xi}}{2} \pm \sqrt{\frac{(\partial_{v_j} f + \partial_{v_{j-1}} f e^{i\xi})^2}{4} + \partial_{h_j} f (e^{i\xi} - 1)}. \quad (4.14)$$

For a finite platoon on an open road, we only need to consider the eigenvalues of

$$A_0 = \begin{bmatrix} \mathbf{0} & \text{Id}_{n-1} \\ & \nabla_{\mathbf{u}_k} \end{bmatrix}$$

from the linearisation (2.18). In the context of the application, this corresponds to considering only the part of the linearisation that corresponds to own car: Can a driver correct his own small mistakes if everything else stays fix?

For $[m_f, m_l] = [0, 1]$, $n = 2$ this gives us the ‘‘platoon eigenvalues’’ (WILSON and WARD 2011)

$$\lambda_{\pm} = \frac{\partial_{v_j} f}{2} \pm \sqrt{\frac{(\partial_{v_j} f)^2}{4} - \partial_{h_j} f}. \quad (4.15)$$

In a reasonable model, the partial derivatives should satisfy $\partial_{v_j} f < 0$ and $\partial_{h_j} f > 0$, therefore the platoon eigenvalues lie in the open left complex half plane.

4.1.4 Lyapunov arguments

It is desirable to enhance the above stability results to the nonlinear case. In the finite-dimensional setting the principle of linearised stability allows local conclusions in this sense. The question whether this is also possible in the infinite-dimensional case, i.e. for $J = \mathbb{N}$ or $J = \mathbb{Z}$, has been raised in WERNER (2013).

4.1.4.1 Circular road

In order to motivate our approach to the infinite-dimensional problem, let us briefly discuss the situation on the circular road first.

If the system is formulated in terms of the vehicles’ positions, shift-invariance of the quasistationary solution corresponds to a singular eigenvalue with corresponding eigenvector

$$([x_j - \bar{x}_j, v_j - v_e]^\top)_{j \in J} = ([1, 0]^\top)_{j \in J}.$$

This ambiguity may of course be removed by transforming to headway coordinates, $h_j := x_{j-1} - x_j$. However, the singular eigenvalue remains, now with an eigenvector corresponding to a change in the circle length. We have incorporated the condition $x_{N-1} = x_1 + L$ into the system; since L does not explicitly appear, the boundary condition is not enforced. The most straightforward way of fixing this may be to reduce the number of ODEs to $2N - 1$ by substituting h_N with $L - \sum_{j=1}^{N-1} h_j$, as e.g. in GASSER et al. (2004). Unfortunately, there is no direct analogy to this in

the infinite-dimensional setting.

Our formulation in terms of Toeplitz- and Laurent operators in 4.1.1 suggests to use an approach based on Fourier techniques instead. Consequently, we apply a discrete Fourier transform, with $([y_k, z_k]^\top)_{k \in J}$ denoting the new coordinates:

$$F_N : \mathbb{R}^{2N} \rightarrow \mathbb{C}^{2N} \\ \left(\begin{bmatrix} h_j - h_e \\ v_j - v_e \end{bmatrix} \right)_{j=1, \dots, N} \mapsto \left(\sum_{j=1}^N \exp\left(\frac{2\pi i j k}{N}\right) \begin{bmatrix} h_j - h_e \\ v_j - v_e \end{bmatrix} \right)_{k=1, \dots, N} =: \left(\begin{bmatrix} y_k \\ z_k \end{bmatrix} \right)_{k=1, \dots, N}. \quad (4.16)$$

Now the condition $\sum_{j=1}^N h_j = L$ corresponds to $y_N \equiv 0$, so the ODE for y_N can be eliminated from the system.

In these coordinates, the linear part decouples and may be written as

$$\begin{bmatrix} \dot{y}_l \\ \dot{z}_l \end{bmatrix} = \underbrace{\begin{bmatrix} 0 & e_N^l - 1 \\ \sum_k e_N^{l \cdot k} \frac{\partial f_j}{\partial h_{j-k}} & \sum_k e_N^{l \cdot k} \frac{\partial f_j}{\partial v_{j-k}} \end{bmatrix}}_{=S'(e_N^l)} \cdot \begin{bmatrix} y_l \\ z_l \end{bmatrix} \quad l = 1, \dots, N-1,$$

where $e_N := \exp\left(\frac{2\pi i}{N}\right)$, where S' is closely related to the matrix-valued symbol introduced in (4.5): Using the identity $\sum_{k=m_f}^{m_l} \frac{\partial f_j}{\partial x_{j-k}} = 0$ from assumption 2.5, it may easily be checked that $S'(z)$ has the same eigenvalues $\lambda_\pm(z)$ as $S(z)$, but now $S' \cdot U = U \cdot \text{diag}(\lambda_\pm)$ is fulfilled by the transformation matrix

$$U^{-1}(z) = \begin{bmatrix} z-1 & z-1 \\ \lambda_+(z) & \lambda_-(z) \end{bmatrix}. \quad (4.17)$$

Let $U = \text{diag}(U(e_N^1), \dots, U(e_N^N))$ be the block diagonal operator composed from the elementary parts. We now define the function

$$L : \left\{ \left(\begin{bmatrix} h_j - h_e \\ v_j - v_e \end{bmatrix} \right)_{j \in J} \in \ell_2^2(J) : \sum_{j \in J} h_j - h_e = 0 \right\} \rightarrow \mathbb{R} \\ \mathbf{u} \mapsto \frac{1}{2} \|(UF_N)(\mathbf{u})\|_2^2. \quad (4.18)$$

By construction, L is a Lyapunov function for the linear part provided the nonzero eigenvalues have strictly negative real part:

$$\begin{aligned} \frac{d}{dt} L(\mathbf{u}) &= \nabla L(\mathbf{u}) \cdot f_{\text{lin}}(\mathbf{u}) = \left((UF_N)^\top (UF_N) \mathbf{u} \right) \cdot \left((UF_N)^{-1} D(UF_N) \mathbf{u} \right) \\ &\leq \max_{k=1, \dots, N-1} \text{Re} \left(\lambda_+ \left(e_N^k \right) \right) \|(UF_N) \mathbf{u}\|_2^2. \end{aligned}$$

We may thus find positive constants α_1 and α_3 (notation as in SWAROOP and HEDRICK (1996)) such that

$$\nabla L(\mathbf{u}) \cdot f_{\text{lin}}(\mathbf{u}) \leq -\alpha_1 \|\mathbf{u}\|_2^2 \quad \text{and} \quad \|\nabla L(\mathbf{u})\|_2 \leq \alpha_3 \|\mathbf{u}\|_2. \quad (4.19)$$

With this we can deduce that, at least in a small environment around the quasistationary solution $\mathbf{u} = 0$, L is also a Lyapunov function for the whole ODE:

$$\begin{aligned} \frac{d}{dt}L(\mathbf{u}) &= \nabla L(\mathbf{u}) \cdot (f_{\text{lin}}(\mathbf{u}) + f_{\text{nl}}(\mathbf{u})) \\ &\leq -\alpha_1 \|\mathbf{u}\|_2^2 + \|\nabla L(\mathbf{u})\|_2 \|f_{\text{nl}}(\mathbf{u})\|_2 \\ &\leq \left(\alpha_3 \frac{\|f_{\text{nl}}(\mathbf{u})\|}{\|\mathbf{u}\|} - \alpha_1 \right) \|\mathbf{u}\|_2^2 \end{aligned}$$

4.1.4.2 Infinite lane

Let us now check to what extent the considerations for the circular road can be generalised to the infinite lane without a leader, $J = \mathbb{Z}$.

Instead of the discrete Fourier transform (4.16), we apply the transformation

$$F : \quad l_2^2(\mathbb{Z}) \rightarrow \mathcal{C}^2([0, 2\pi])$$

$$\left(\begin{bmatrix} h_j - h_e \\ v_j - v_e \end{bmatrix} \right)_{j \in \mathbb{Z}} \mapsto \left(\sum_{j=-\infty}^{\infty} \exp(ij\theta) \begin{bmatrix} h_j - h_e \\ v_j - v_e \end{bmatrix} \right)_{\theta \in [0, 2\pi]} =: \left(\begin{bmatrix} y_\theta \\ z_\theta \end{bmatrix} \right)_{\theta \in [0, 2\pi]}. \quad (4.20)$$

U should now be regarded as a block diagonal operator on $\mathcal{C}^2([0, 2\pi])$. Unfortunately, since the eigenvalues are not isolated any more, we cannot take the biggest real part for α_1 . In order to have a non-zero constant to estimate the non-linear part against, we need an additional assumption on the sequence $\mathbf{u} = (u_j)_{j \in \mathbb{Z}}$. It appears reasonable to postulate that, in addition to $\bar{\mathbf{h}} = h_e$ and $\bar{\mathbf{v}} = v_e$, the sequence is of moderate decay, i.e. for all $n \in \mathbb{N}$, $(j^n \cdot u_j)_{j \in J}$ is in l_1^2 . From this we may see that we have finite upper bounds on the derivatives of its Fourier transform:

$$\left\| \frac{d^n}{d\theta^n} \begin{bmatrix} y_\theta \\ z_\theta \end{bmatrix} \right\|_\infty \leq \left\| j^n \begin{bmatrix} h_j - h_e \\ v_j - v_e \end{bmatrix} \right\|_1.$$

Since the Fourier transform F is an isometry, $\|\mathbf{y}\|_2 = \|\mathbf{h} - h_e\|_2$, $\|\mathbf{z}\|_2 = \|\mathbf{v} - v_e\|_2$. From the bounds on the derivatives we see that y and z cannot be concentrated arbitrarily close to the origin. If additional properties of the function $\text{Re}(\lambda_+(\theta))$ are known, it may consequently be possible to obtain a non-zero estimate.

4.1.4.3 Weak coupling theorem

Depending on the model, other ways of applying Lyapunov techniques may be possible. FENG et al. (2019) refers to SWAROOP and HEDRICK (1996), where the following ‘‘weak coupling theorem’’ is proven:

Proposition 4.2 (weak coupling theorem) Consider the CFM

$$\dot{\mathbf{u}}_j = f(\mathbf{u}_j, \mathbf{u}_{j-1}, \dots, \mathbf{u}_{j-m_1}) \quad (4.21)$$

where $j \in \mathbb{N}$, $\mathbf{u}_{j-i} \equiv 0 \forall i \geq j$, $x \in \mathbb{R}^n$, $f : \mathbb{R}^{n \cdot (m_1+1)} \rightarrow \mathbb{R}^n$, $f(0, \dots, 0) = 0$.

If f is globally Lipschitz in its arguments, i.e.

$$\|f(\mathbf{y}_1, \dots, \mathbf{y}_{m_1}) - f(\mathbf{z}_1, \dots, \mathbf{z}_{m_1})\| \leq \sum_{j=1}^{m_1} l_j \|\mathbf{y}_j - \mathbf{z}_j\| \quad (4.22)$$

and the origin of $\dot{x} = f(x, 0, \dots, 0)$ is globally exponentially stable, then for sufficiently small l_j , $j = 2, \dots, m_1$, the interconnected system is globally exponentially string stable.

The idea of the proof is to use the estimates stemming from the exponential stability of the single vehicle to show that a weighted summation of the individual Lyapunov functions is robust enough to deal with the inter-vehicle relations, provided these are sufficiently weak.

However, as shown in the examples, in practice this theorem is not very helpful since inter-vehicle relations are crucial. For the models we are concerned with, this may or may not work, as demonstrated in the examples.

4.2 Macroscopic models

4.2.1 Linearisation

Set $r := \rho - \rho_e$, $w := v - v_e$.

The linearisation of the continuity equation (3.32) depends on the underlying density definition:

- for the ND, linearisation of (3.32a) is simply

$$\check{r}_t + \check{r}_x v_e = -\rho_e w_x \quad (4.23a)$$

- for the IHD, (3.32b) becomes

$$\tilde{r}_t + v_e \tilde{r}_x = -\frac{2\rho_e^2}{\varepsilon} \left(\sum_{j=0}^{\infty} \frac{w^{(2j+1)}}{(2j+1)!} \left(\frac{\varepsilon}{2\rho_e} \right)^{(2j+1)} \right) \quad (4.23b)$$

- finally, for the FLD, from (3.32c) we have

$$\hat{r}_t + \hat{r}_x v_e = -\frac{\rho_e^2}{\varepsilon} \sum_{j=1}^{\infty} \frac{w^{(j)}}{j!} \left(\frac{\varepsilon}{\rho_e} \right)^j. \quad (4.23c)$$

We may also write this in the more general form

$$r_t + v_e r_x = \mathbf{q}_w \cdot \left[w_x, w_{xx}, \dots, w^{(n_w)} \right]^T, \quad (4.24)$$

where

$$\mathbf{q}_w = -\rho_e \begin{cases} \left[1, 0, 0, \dots \right]^\top & \text{for the ND} \\ \frac{2\rho_e}{\varepsilon} \left[\frac{\varepsilon}{2\rho_e}, 0, \frac{1}{3!} \left(\frac{\varepsilon}{2\rho_e} \right)^3, 0, \dots \right]^\top & \text{for the IHD} \\ \frac{\rho_e}{\varepsilon} \left[\frac{\varepsilon}{\rho_e}, \frac{1}{2} \left(\frac{\varepsilon}{\rho_e} \right)^2, \dots \right] & \text{for the FLD.} \end{cases} \quad (4.25)$$

For car-following functions of order $n > 2$, we may set $\mathbf{y} := \mathbf{u} - \mathbf{u}_e$, where $\mathbf{y} = \left[r, w, y_3, \dots, y_n \right]^\top$. The equations $\frac{d}{dt}u_k = u_{k+1}$ for $k = 2, \dots, n-1$ are already linear.

A Taylor expansion of $\frac{d}{dt}u_n = f_{j(x)}(\mathbf{u})$ yields

$$\begin{aligned} \frac{\partial}{\partial t}y_n + v_e \frac{\partial}{\partial x}y_n = f_{j(x)}(\mathbf{u}_e) + \sum_{k=m_f}^{m_1} \left(\frac{\partial}{\partial x_{j-k}} f_{j(x)}(\mathbf{u}_e) \cdot \left(h_k(\rho_e + r) - k \frac{\varepsilon}{\rho_e} \right) \right. \\ \left. + \sum_{l=2}^n \frac{\partial}{\partial u_{l,j-k}} f_{j(x)}(\mathbf{u}_e) \cdot y_l(h_k(\rho_e + r)) \right) + \dots \end{aligned} \quad (4.26)$$

In order to get a local equation, we need to replace the inner terms h_k and y_l with their Taylor expansions as well. Denoting the first-order terms of $h_k(\rho_e + r) - k \frac{\varepsilon}{\rho_e}$ by $h'_k(r)$, we get to the linearisation

$$\frac{\partial}{\partial t}y_n + v_e \frac{\partial}{\partial x}y_n = \sum_{k=m_f}^{m_1} \left(\frac{\partial}{\partial x_{j-k}} f_{j(x)}(\mathbf{u}_e) h'_k(r) + \sum_{l=2}^n \frac{\partial}{\partial u_{l,j-k}} f_{j(x)}(\mathbf{u}_e) \cdot \left(\sum_{s=0}^{\infty} \frac{1}{s!} \frac{\partial^s y_l}{\partial x^s} \left(\frac{k\varepsilon}{\rho_e} \right)^s \right) \right). \quad (4.27)$$

For $n = 2$, this simplifies to

$$w_t + v_e w_x = \sum_{k=m_f}^{m_1} \frac{\partial}{\partial x_{j-k}} f_{j(x)}(\mathbf{u}_e) h'_k(r) + \frac{\partial}{\partial v_{j-k}} f_{j(x)}(\mathbf{u}_e) \cdot \left(\sum_{s=0}^{\infty} \frac{1}{s!} \frac{\partial^s w}{\partial x^s} \left(\frac{k\varepsilon}{\rho_e} \right)^s \right). \quad (4.28)$$

Let us now discuss the linearisation of the density-headway relation $h(\rho)$. Again, we focus on the special but most important case $h'_{+1} = \left. \frac{\partial h_{+1}}{\partial \rho} \right|_{\rho=\rho_e}$.

– Inverse headway density: from (3.21), we find:

$$\tilde{h}'(r) = -\frac{\varepsilon r}{\rho_e^2} - \frac{\varepsilon}{\rho_e^2} \sum_{k=1}^{\infty} \frac{r^{(k)}}{k!} \left(\frac{\varepsilon}{2\rho_e} \right)^k = -\frac{\varepsilon}{\rho_e^2} \sum_{k=0}^{\infty} \frac{r^{(k)}}{k!} \left(\frac{\varepsilon}{2\rho_e} \right)^k. \quad (4.29a)$$

– Forward looking density: from (3.28), we directly have

$$\hat{h}'(r) = -\frac{\varepsilon}{\rho_e^2} r. \quad (4.29b)$$

– Natural density: from (3.31), we obtain

$$\check{h}'(r) = -\frac{\varepsilon r}{\rho_e^2} - \sum_{k=2}^{\infty} \frac{\varepsilon^k r^{(k-1)}}{k! \rho_e^{k+1}} = -\frac{\varepsilon}{\rho_e^2} \sum_{k=1}^{\infty} \frac{r^{(k-1)}}{k!} \left(\frac{\varepsilon}{\rho_e} \right)^{k-1}. \quad (4.29c)$$

Similar to (4.24), (4.28) may also be written in the form

$$w_t + v_e w_x = \mathbf{q}_r \cdot [r, r_x, r_{xx}, \dots, r^{(n_r)}]^\top + \mathbf{p} \cdot [w, w_x, w_{xx}, \dots, w^{(n_w)}]^\top. \quad (4.30)$$

For $[m_f, m_l] = [0, 1]$ we have

$$\mathbf{p} = \frac{\partial}{\partial v_j} f_{j(x)}(\mathbf{u}_e) [1, 0, 0, \dots] + \frac{\partial}{\partial v_{j-1}} f_{j(x)}(\mathbf{u}_e) \left[1, \frac{\varepsilon}{2\rho_e}, \frac{1}{3!} \left(\frac{\varepsilon}{\rho_e} \right)^2, \dots \right] \quad (4.31)$$

$$\mathbf{q}_r = -\frac{\varepsilon}{\rho_e^2} \frac{\partial f_j}{\partial x_{j-1}} \begin{cases} \left[1, \frac{\varepsilon}{4\rho_e}, \frac{1}{3!} \left(\frac{\varepsilon}{2\rho_e} \right)^2, \dots \right] & \text{for the IHD,} \\ \left[1, 0, 0, \dots \right] & \text{for the FLD} \\ \left[1, \frac{\varepsilon}{2\rho_e}, \frac{1}{3!} \left(\frac{\varepsilon}{\rho_e} \right)^2, \dots \right] & \text{for the ND.} \end{cases} \quad (4.32)$$

4.2.2 Characteristic polynomial and string stability

Proposition 4.3 The microscopic characteristic polynomial in the road frame (4.12) is recovered in the limit $n_{r,w} \rightarrow \infty$, independent of the choice of density definition.

Proof: Application of the exponential ansatz $\mathbf{y}(x, t) = [r_0, w_0, y_3(0), \dots, y_n(0)]^\top \exp(\lambda t + \nu x)$ to (4.24) yields

$$(\lambda + \nu v_e) r_0 = w_0 \mathbf{q}_w \cdot [1, \nu, \nu^2, \dots]^\top \xrightarrow{n_w \rightarrow \infty} -\frac{\rho_e^2}{\varepsilon} w_0 \begin{cases} 2 \sinh\left(\frac{\varepsilon \nu}{2\rho_e}\right) & \text{for the IHD} \\ \exp\left(\frac{\varepsilon \nu}{\rho_e}\right) - 1 & \text{for the FLD} \\ \frac{\varepsilon \nu}{\rho_e} & \text{for the ND} \end{cases}. \quad (4.33)$$

From $\frac{d}{dt} u_k = u_{k+1}$, we obtain

$$\frac{y_{k+1}(0)}{y_k(0)} = \lambda + v_e \nu, \quad k \in [2, n-1]; \quad (4.34)$$

by induction, we have

$$y_k(0) = w_0 (\lambda + v_e \nu)^{k-2}. \quad (4.35)$$

Applying (4.29) to $r(x) = r_0 \exp(\lambda t + \nu x)$, we obtain

$$h'_{+1}(r) \xrightarrow{n_r \rightarrow \infty} -\frac{\varepsilon r}{\rho_e^2} \begin{cases} \exp\left(\frac{\varepsilon \nu}{2\rho_e}\right) & \text{for the IHD} \\ 1 & \text{for the FLD} \\ \frac{\rho_e}{\varepsilon \nu} \left(\exp\left(\frac{\varepsilon \nu}{\rho_e}\right) - 1 \right) & \text{for the ND.} \end{cases} \quad (4.36)$$

From this we see by induction, with (3.19) and an evaluation of the geometric sum (or, in the case of ND, by direct linearisation of (3.30))

$$h'_k \xrightarrow{n_r \rightarrow \infty} -\frac{\varepsilon r}{\rho_e^2} \begin{cases} \frac{\exp\left(\frac{\varepsilon\nu k}{\rho_e}\right) - 1}{2 \sinh\left(\frac{\varepsilon\nu}{2\rho_e}\right)} & \text{for the IHD} \\ \frac{\exp\left(\frac{\varepsilon\nu k}{\rho_e}\right) - 1}{\exp\left(\frac{\varepsilon\nu}{\rho_e}\right) - 1} & \text{for the FLD} \\ \frac{\rho_e}{\varepsilon\nu} \left(\exp\left(\frac{\varepsilon\nu k}{\rho_e}\right) - 1 \right) & \text{for the ND.} \end{cases} \quad (4.37)$$

Now we may combine conservation law (4.33), headway approximation (4.37), and higher order additions (4.34) with the linearisation of the car-following function (4.27).

First we note that (4.37) can be plugged into (4.33) to obtain

$$\lambda + \nu v_e = w_0 \frac{\exp\left(\frac{\varepsilon\nu k}{\rho_e}\right) - 1}{h'_k}. \quad (4.38)$$

With (4.35), we have

$$h'_k = y_n(0) \frac{\exp\left(\frac{\varepsilon\nu k}{\rho_e}\right) - 1}{(\lambda + \nu v_e)^{n-1}}. \quad (4.39)$$

Now we plug the exponential ansatz into (4.27), giving

$$(\lambda + v_e \nu) y_n(0) = \sum_{k=m_f}^{m_1} h'_k \frac{\partial}{\partial x_{j-k}} f_{j(x)}(\mathbf{u}_e) + \sum_{l=2}^n \frac{\partial}{\partial u_{l,j-k}} f_{j(x)}(\mathbf{u}_e) \cdot w_l^0 \cdot \exp\left(\frac{\varepsilon\nu k}{\rho_e}\right), \quad (4.40)$$

which can be combined with (4.39) to

$$\begin{aligned} (\lambda + v_e \nu)^n &= \sum_{k=m_f}^{m_1} \left(\exp\left(\frac{\varepsilon\nu k}{\rho_e}\right) - 1 \right) \frac{\partial}{\partial x_{j-k}} f_{j(x)}(\mathbf{u}_e) \\ &\quad + \sum_{l=2}^n (\lambda + v_e \nu)^{l-1} \frac{\partial u_{l,j-k}}{\partial f_{j(x)}}(\mathbf{u}_e) \cdot \exp\left(\frac{\varepsilon\nu k}{\rho_e}\right) \\ &\stackrel{(2.9)}{=} \sum_{k=m_f}^{m_1} \sum_{l=1}^n (\lambda + v_e \nu)^{l-1} \frac{\partial}{\partial u_{l,j-k}} f_{j(x)}(\mathbf{u}_e) \cdot \exp\left(\frac{\varepsilon\nu k}{\rho_e}\right). \end{aligned} \quad (4.41)$$

A substitution of the spatial eigenvalues ν by $\frac{i\xi}{h_e}$ and comparison with the characteristic polynomial in the Eulerian reference frame (4.12) and the shape of matrices A_k in (4.2) proves the claim. \square

If we consider a given system for different density definitions up to a finite order of ε , we will have different characteristic polynomials in general.

The corrections to the density conservation for IHD and FLD turn out to be crucial since the characteristic polynomial can not be recovered otherwise.

It has been shown in BERG et al. (2000) for the Bando model that micro- and low order macroscopic model have the same string stability criterium. This is true for a much more general case under certain assumptions.

For $n = 2$, the characteristic function of a macroscopic model is given by a polynomial that is second order in λ and at least second order in ν . The coefficients up to second order in ν do not change when higher-order derivatives are included into the model.

Generically, string stability of the microscopic model on the infinite lane is determined by the

curvature of its spectrum in the origin. This property is already correctly represented in the lowest-order order macroscopic approximation and does not deteriorate for higher-order approximations. Note that, unlike the microscopic case, the polynomial in ν diverges for $\nu \rightarrow \pm i\infty$ and the essential spectrum will thus protrude arbitrarily wide into the right complex half plane in general. However, a realistic initial datum $[r_0, w_0]^\top(\nu)$ may be assumed to have bounded support, since wavelengths below the minimal distance of cars are not physically meaningful.

4.3 Examples

Example 4.1 (A first-order microscopic traffic model)

We consider the microscopic equivalent of the LWR model, which may be thought of as a first-order “cousin” of the Bando model:

Let $V : \mathbb{R} \rightarrow \mathbb{R}$ be an OVF, e.g. $V(h) = \tanh(h - 2) + \tanh(2)$. Fix $h_e \in \mathbb{R}^+$. Let $V^*(h) = V(h_e) + \beta(h - h_e)$, where $\beta := \left. \frac{\partial V}{\partial h} \right|_{h=h_e}$, $\beta > 0$.

Let $f : \mathbb{R} \times \mathbb{R} \rightarrow \mathbb{R}$, $f(x_j, x_{j-1}) = V(x_{j-1} - x_j + h_e)$; $f^* : \mathbb{R} \times \mathbb{R} \rightarrow \mathbb{R}$, $f^*(x_j, x_{j-1}) = V^*(x_{j-1} - x_j + h_e)$. Note that the coordinates are chosen such that the equilibrium is in $x_j \equiv 0$, i.e. x_j does not denote the actual position of vehicle j , but its deviation from the quasistationary solution. The actual positions may be recovered by $x_j + j \cdot h_e + C$.

Linearisation yields the operators depicted in Fig. 4.3 with common symbol $f(z) = \beta(z - 1)$; consequently, the spectra are given by

- The N -th roots of unity, multiplied and shifted to the left by β , for N vehicles on a circular road
- The eigenvalue $-\beta$ with multiplicity N for a platoon of N vehicles on an open road
- A circle of radius β with center $-\beta$ for infinitely many vehicles without a leader, $J = \mathbb{Z}$
- A closed disk of radius β with center $-\beta$ for infinitely many vehicles with a leader, $J = \mathbb{N}$

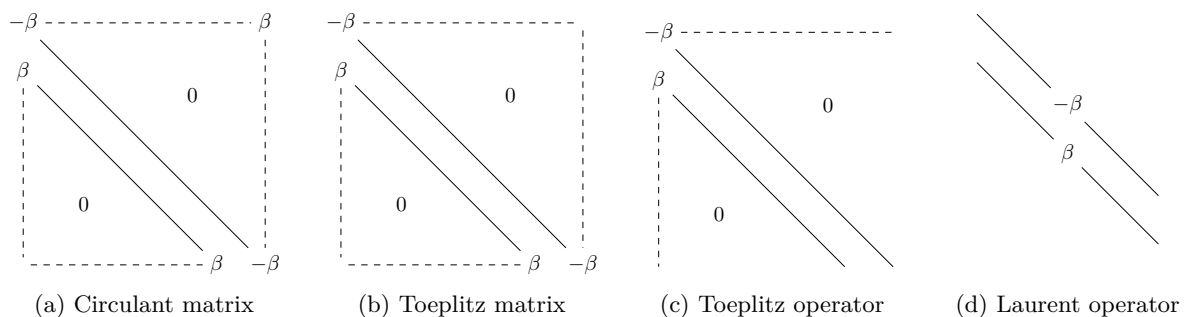


Figure 4.3: Structure of relevant matrices and operators in Ex. 4.1

Example 4.2 (Index eigenvalues for different reference frames)

We again consider the simplistic first order traffic model $v_j = V(x_{j-1} - x_j)$ with $n = 1$ and characteristic polynomial $\chi(\lambda, \xi) = \lambda + ic\xi - \beta(\exp(i\xi) - 1)$. For $c = 0$, we have

$$h_e\nu = i\xi = \ln\left(\frac{\lambda}{\beta} + 1\right) + 2\pi il, l \in \mathbb{Z}.$$

On the other hand, for $c \neq 0$ we have

$$h_e\nu = i\xi = -\frac{\lambda + \beta}{c} - W\left(-\frac{\beta}{c} \exp\left(-\frac{\lambda + \beta}{c}\right)\right) \quad (4.42)$$

where $W(z)$ denotes the multivariate Lambert W function of $z \in \mathbb{C}$, returning the roots of the expression $z - x \cdot \exp(x)$ (Fig. 4.4).

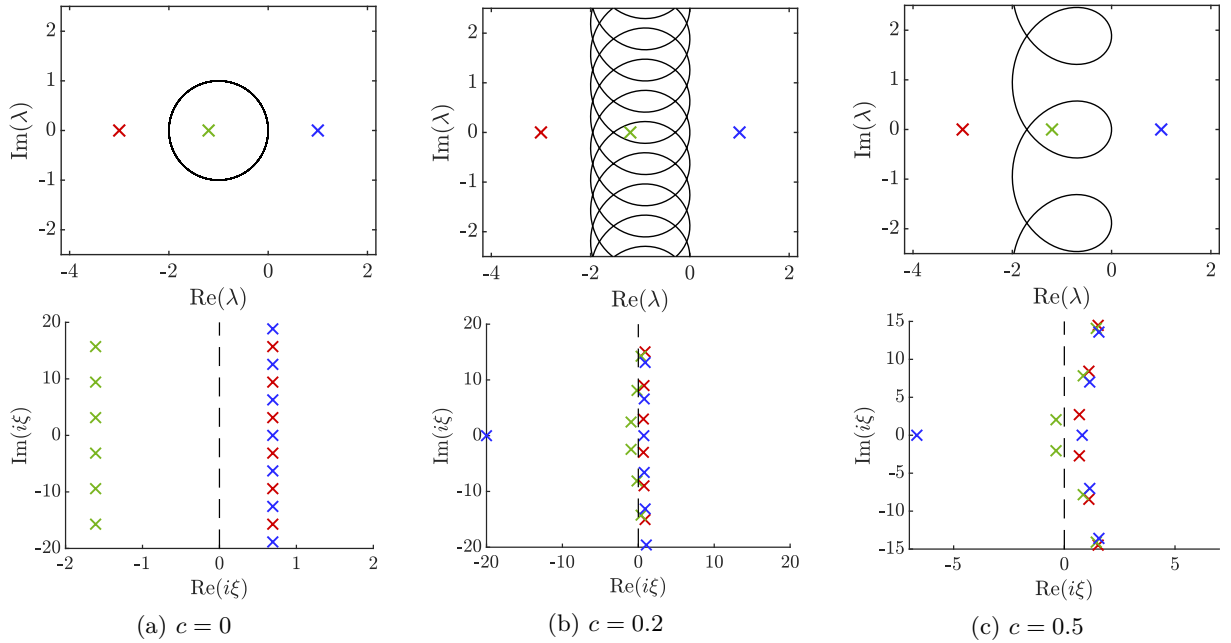


Figure 4.4: Spectra (top) and spatial eigenvalues for selected values of λ (bottom) for the characteristic function $\chi = \lambda + ic\xi - \beta(\exp(i\xi) - 1)$ of the first-order microscopic optimal velocity model. When changing to a co-moving coordinate system, the string stability properties stay the same but the roots ξ move

Example 4.3 (A Lyapunov function)

We demonstrate that the “weak coupling theorem” from SWAROOP and HEDRICK (1996) is not a big help for the model in Ex. 4.1, since it is barely applicable for the affine-linear f^* :

By the triangle inequality, f^* is globally Lipschitz with Lipschitz constants $l_{1,2} = \beta$.

The origin of $\dot{x} = f^*(x, 0)$ is trivially globally exponentially stable with Lyapunov function $W(x) = \frac{1}{2}x^2$, and the estimates

$$\alpha_l \|x\|^2 \leq W(x) \leq \alpha_h \|x\|^2 \quad (4.43a)$$

$$\frac{\partial W}{\partial x} f(x, 0) \leq -\alpha_1 \|x\|^2 \quad (4.43b)$$

$$\left\| \frac{\partial W}{\partial x} \right\| \leq \alpha_3 \|x\| \quad (4.43c)$$

are satisfied for $\alpha_l = \alpha_h = \frac{1}{2}$, $\alpha_1 = \beta$, $\alpha_3 = 1$.

As in the proof of the WCT in SWAROOP and HEDRICK (1996), we now pick $0 < d < 1$ and sum the local Lyapunov functions W to the global Lyapunov function candidate $\mathbf{W} : \mathbb{R}^N \rightarrow \mathbb{R}$, $\mathbf{W}((x_j)_{j \in \mathbb{N}}) = \sum_{j=1}^{\infty} d^j W(x_j)$. Global minimality of $\mathbf{W}(0)$ is thus fulfilled. Analogously to the proof, we estimate $\dot{\mathbf{W}}$:

$$\begin{aligned} \frac{d}{dt} \mathbf{W}((x_j)_{j \in J}) &= \sum_{j=1}^{\infty} d^j \left. \frac{\partial W}{\partial x} \right|_{x=x_j} f^*(x_j, x_{j-1}) \\ &\leq \sum_{j=1}^{\infty} d^j \left. \frac{\partial W}{\partial x} \right|_{x=x_j} (f^*(x_j, 0) + l_2 \|x_{j-1}\|) \\ &\leq \sum_{j=1}^{\infty} d^j (-\alpha_1 \|x_j\|^2 + l_2 \alpha_3 \|x_j\| \|x_{j-1}\|) \\ &\leq \sum_{j=1}^{\infty} d^j \left(\left(\frac{l_2 \alpha_3}{2} - \alpha_1 \right) \|x_j\|^2 + \frac{l_2 \alpha_3}{2} \|x_{j-1}\|^2 \right) \leq 0 \end{aligned}$$

Since $\frac{l_2 \alpha_3}{2} = \frac{1}{2} \alpha_1$ in this case, the last inequality is sharp, so it is not robust enough to make room for an additional nonlinearity.

The reason for this is obvious: since f^* is antisymmetric in x_j and x_{j-1} , the coupling cannot be considered weak.

However, we may also confirm that \mathbf{W} is a Lyapunov function by direct calculation (as pointed out by E. FELACO):

$$\begin{aligned} \frac{d}{dt} \mathbf{W}((x_j)_{j \in J}) &= \beta \sum_{j=1}^{\infty} x_j (x_{j-1} - x_j) = -\frac{\beta}{2} \left(x_1^2 + \sum_{j=1}^{\infty} (x_j^2 - 2x_j x_{j-1} + x_{j-1}^2) \right) \\ &= -\frac{\beta}{2} \left(x_1^2 + \sum_{j=1}^{\infty} (x_{j-1} - x_j)^2 \right) < 0 \end{aligned}$$

This approach has the advantage that it may be extended to (slightly) more realistic non-linear OVEs f : We first transfer the system to headway coordinates $h_j = x_{j-1} - x_j$ (note that, as before, this headway definition is shifted so that the QS corresponds to the origin), $\dot{h}_j = V(h_{j-1}) - V(h_j)$. Let $W(h) := \int_0^h V(y) dy$ and $\mathbf{W}((h_j)_{j \in \mathbb{N}}) := \sum_{j=1}^{\infty} W(h_j)$.

Then we have

$$\frac{d}{dt} \mathbf{W}((h_j)_{j \in J}) = \sum_{j=1}^{\infty} V(h_j) (V(h_{j-1}) - V(h_j)) = -\frac{1}{2} \sum_{j=1}^{\infty} (V(h_{j-1}) - V(h_j))^2.$$

Concavity of W , induced by strict monotonicity of V , is needed in order to show global minimality of $\mathbf{W}(0)$:

$$\mathbf{W}((h_j)_{j \in \mathbb{N}}) = \sum_{j=1}^{\infty} W(h_j) > \beta \sum_{j=1}^{\infty} h_j = 0$$

Example 4.4 (String stability of quasistationary solutions in the Bando model)

For the standard Bando model, the characteristic polynomial in the drivers' coordinate system

can be written as

$$0 = \det \left(\underbrace{\begin{bmatrix} 0 & 1 \\ -a\beta & -a \end{bmatrix}}_{A_0} - \lambda \text{Id} + \exp(i\xi) \underbrace{\begin{bmatrix} 0 & 0 \\ a\beta & 0 \end{bmatrix}}_{A_1} \right), \quad (4.44)$$

where $\beta = V'(h_e)$. Since $n = 2$, we are now dealing with block matrices and -operators (Fig. 4.5).

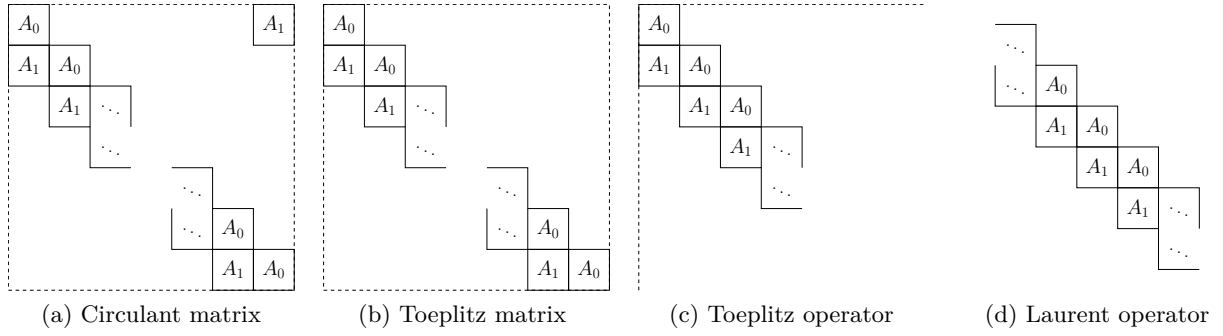


Figure 4.5: Structure of relevant matrices and operators for the Bando model

The spectra of the circulant matrix, Laurent- and Toeplitz operator are given by (Fig. 4.6)

$$\sigma = \left\{ \lambda \in \mathbb{C} : \lambda = -\frac{a}{2} \pm \sqrt{\frac{a^2}{4} + a\beta(z-1)}, \quad z \in \begin{cases} \{z \in \mathbb{C} : z^N = 1\} & \text{circulant matrix} \\ \{z \in \mathbb{C} : |z| = 1\} & \text{Laurent operator} \\ \{z \in \mathbb{C} : |z| \leq 1\} & \text{Toeplitz operator} \end{cases} \right\}. \quad (4.45)$$

The spectrum of the Toeplitz matrix does not depend on N and is given the eigenvalues of A_0 ,

$$\sigma_{TM} = \left\{ -\frac{a}{2} \pm \sqrt{\frac{a^2}{4} - a\beta} \right\}. \quad (4.46)$$

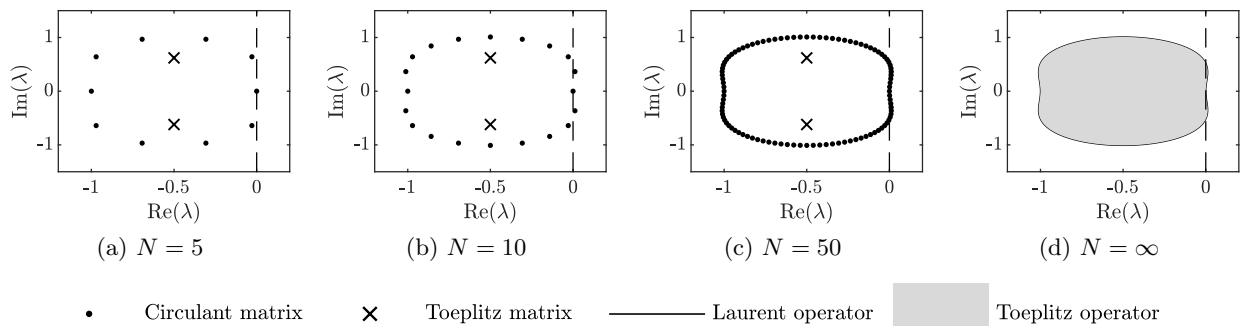


Figure 4.6: Spectra of the Bando model for parameters $a = 1$, $h_e = 1.3$. Note that the circular road model is stable for $N = 5$, but unstable for $N \geq 10$

Example 4.5 (Pseudospectra and -modes of the Bando model)

The pseudospectra

$$\sigma_\varepsilon(\mathcal{A}_N) = \{\lambda \in \mathbb{C} : |\det(\mathcal{A}_N - \lambda \text{Id})| \leq \varepsilon\} \quad (4.47)$$

for the Toeplitz matrices \mathcal{A}_N of the Bando model (Fig. 4.5(b)) can be calculated numerically with the package `EIGTOOL` for different values of ε and N (Fig. 4.7). We observe that for fixed $\varepsilon > 0$, the pseudospectra appear to converge towards the spectrum of the Toeplitz operator as $N \rightarrow \infty$.

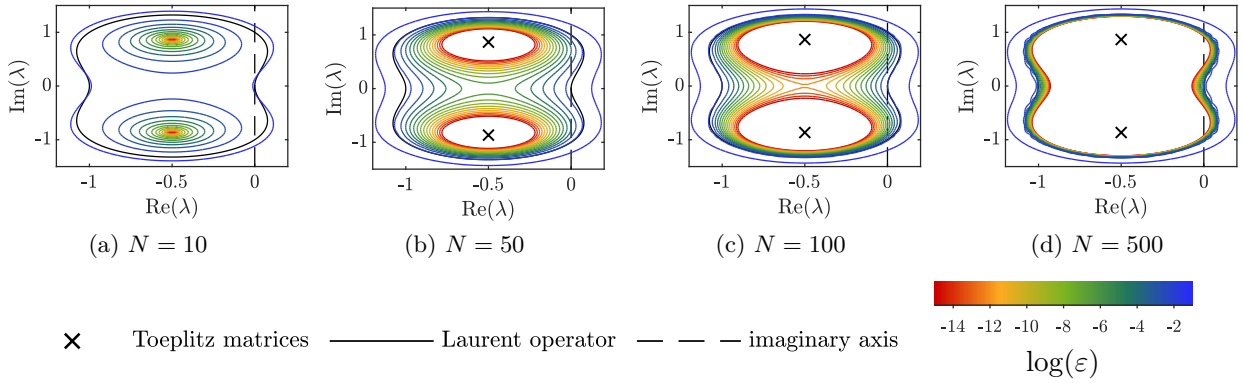


Figure 4.7: ε -pseudospectra of the Toeplitz matrices for the Bando model, calculated with `EIGTOOL`. As $N \rightarrow \infty$ and $\varepsilon \rightarrow 0$, the ε -pseudospectra approximate the (essential) spectrum of the Toeplitz operator (cf. Fig. 4.6(d))

Example 4.6 (The characteristic polynomial of macroscopic models)

We again consider the Bando model with aggressive drivers (2.23) from Ex. 2.1. For brevity, we set $a = \frac{\alpha}{\tau}$ and $\gamma = \frac{1-\alpha}{\tau}$.

Locally, the linearisation is given by

$$\ddot{y}_j = a(\beta(y_{j-1} - y_j) - \dot{y}_j) + \gamma(\dot{y}_{j-1} - \dot{y}_j). \quad (4.48)$$

In Eulerian coordinates, the microscopic characteristic polynomial is

$$(\lambda + ic\xi) \cdot (\lambda + ic\xi + a - \gamma \exp(i\xi)) - a\beta(\exp(i\xi) - 1). \quad (4.49)$$

Linearising the PDEs we derived in Ex. 3.2, we find the linearisation up to n th order in ε for the IHD model (3.39) is

$$\tilde{r}_t + v_e \tilde{r}_x = -\frac{2\rho_e^2}{\varepsilon} \sum_{j=0}^{\lfloor n/2 \rfloor} \frac{w^{(2j+1)}}{(2j+1)!} \left(\frac{\varepsilon}{2\rho_e}\right)^{2j+1} \quad (4.50a)$$

$$w_t + v_e w_x = a\beta \left(-\frac{\varepsilon}{\rho_e^2} \sum_{j=0}^{n-1} \frac{r^{(j)}}{j!} \left(\frac{\varepsilon}{2\rho_e}\right)^j \right) - aw + \gamma \left(\sum_{j=0}^n \frac{w^{(j)}}{j!} \left(\frac{\varepsilon}{\rho_e}\right)^j - w \right). \quad (4.50b)$$

The corresponding characteristic polynomial is

$$(\lambda - \nu v_e) \cdot \left(\lambda - \nu v_e + a - \gamma \sum_{j=0}^n \frac{1}{j!} \left(\frac{\varepsilon \nu}{\rho_e} \right)^j \right) - 2a\beta \left(\sum_{j=0}^{\lfloor n/2 \rfloor} \frac{1}{(2j+1)!} \left(\frac{\varepsilon \nu}{2\rho_e} \right)^{2j+1} \right) \cdot \left(\sum_{j=0}^{n-1} \frac{1}{j!} \left(\frac{\varepsilon \nu}{2\rho_e} \right)^j \right). \quad (4.51)$$

Linearisation of the forward-looking headway (3.40) yields

$$\hat{r}_t + \hat{r}_x v_e = -\frac{\rho_e^2}{\varepsilon} \sum_{j=1}^{n+1} \frac{w^{(j)}}{j!} \left(\frac{\varepsilon}{\rho_e} \right)^j \quad (4.52a)$$

$$w_t + v_e w_x = -a\beta r \frac{\varepsilon}{\rho_e^2} + aw + \gamma \left(\sum_{j=0}^n \frac{w^{(j)}}{j!} \left(\frac{\varepsilon}{\rho_e} \right)^j - w \right) \quad (4.52b)$$

with characteristic polynomial

$$(\lambda - \nu v_e) \cdot \left(\lambda - \nu v_e + a - \gamma \sum_{j=0}^n \frac{1}{j!} \left(\frac{\varepsilon \nu}{\rho_e} \right)^j \right) - a\beta \left(\sum_{j=1}^{n+1} \frac{1}{j!} \left(\frac{\varepsilon \nu}{\rho_e} \right)^j \right). \quad (4.53)$$

Finally, for the natural density in (3.41) we obtain

$$\check{r}_t + \check{r}_x v_e = -\rho_e w_x \quad (4.54a)$$

$$w_t + v_e w_x = a\beta \left(-\frac{\varepsilon}{\rho_e^2} \sum_{k=1}^n \frac{r^{(k-1)}}{k!} \left(\frac{\varepsilon}{\rho_e} \right)^{k-1} \right) - aw + \gamma \left(\sum_{j=0}^n \frac{w^{(j)}}{j!} \left(\frac{\varepsilon}{\rho_e} \right)^j - w \right). \quad (4.54b)$$

Interestingly, this yields the same characteristic polynomial (4.51) as PDE (4.50). As $n \rightarrow \infty$, both (4.51) and (4.53) converge towards the microscopic characteristic polynomial (4.49).

Chapter 5

Linear analysis of jam behaviour

In this chapter, we are investigating the question in which direction a small perturbation to an unstable quasistationary solution of a given car-following model moves while it is growing. In traffic flow, this corresponds to the question of where an emerging traffic jam moves. The answer will of course depend on the frame of reference we have in mind. Two points of view are especially important: The drivers' perspective (or rather that of a theoretical driver at equilibrium velocity v_e who is not affected by the perturbation) and the perspective from the side of the road. As in Sec. 4.1.2, we will refer to these as the index- and road frame or, as in fluid mechanics, as the Lagrangian and Eulerian point of view, respectively.

In a second step, it is of course interesting to obtain upper and lower bounds for the speed of information in order to determine the area in x, t -space to which the result of a localised perturbation is confined. Once we are able to detect whether a perturbation is moving up- or downstream in a given reference frame, this problem is solved, too: Finding the velocities of the fronts a traffic jam is equivalent to finding the coordinate systems in which these are at rest. Without loss of generality, we may therefore concentrate on the two aforementioned systems in the following.

5.1 Historical overview

Historically, the speed of a perturbation has often been associated with group velocities. Briefly, this can be explained as follows: For a linear PDE $u_t = f(u, u_x, \dots)$ with initial profile

$$u_0(x) = e^{-\varepsilon x^2} \cdot e^{ik_0 x}, \quad k_0 \in \mathbb{R}, \varepsilon > 0$$

a Fourier transform gives

$$u_0(k) \sim e^{-\frac{(k-k_0)^2}{4\varepsilon}}.$$

If an exponential ansatz $u = e^{\lambda t + ikx}$ yields the local approximation

$$\lambda(k) = \lambda_0 + i\sigma(k - k_0) \tag{5.1}$$

to the essential spectrum, we have

$$u(k, t) \sim e^{-\frac{(k-k_0)^2}{4\varepsilon}} e^{(\lambda_0 + i\sigma(k-k_0)) \cdot t}$$

where $\sigma = \left. \frac{\partial \lambda}{\partial ik} \right|_{k=k_0}$ denotes the group velocity.

After the inverse Fourier transform we obtain

$$u(x, t) \sim e^{\lambda_0 t} \cdot e^{-\varepsilon(x+\sigma t)^2} \cdot e^{ik_0 x}.$$

From this, one might argue naively that the instability is of convective nature if for all unstable wavenumbers k the corresponding group velocities σ are real and in a certain interval.

While this approximation may be applicable for $\sigma \in \mathbb{R}$, it breaks down for $\sigma \in \mathbb{C}$, i.e. in a dissipative medium. The problem here is not so much that the solution might explode if $(\operatorname{Re}(\sigma))^2 - (\operatorname{Im}(\sigma))^2 < 0$, but mainly the distortion of the pulse because of the $e^{2i\operatorname{Re}(\sigma)\operatorname{Im}(\sigma)tx}$ -term.

This issue was raised when after publication of special relativity in 1905, W. WIEN objected that, for a refractive index of light smaller than one (which occurs for absorptive media), phase and group velocity may well be higher than the speed of light. In a talk titled “Ein Einwand gegen die Relativtheorie der Elektrodynamik und seine Beseitigung” in 1907, A. SOMMERFELD discussed this issue and, on the basis of thought experiments, pointed out that neither the phase nor the group velocity are of relevance here but what he called the “signal velocity”, which can be calculated by means of complex integration. These ideas were further worked out in SOMMERFELD (1914), BRILLOUIN (1914) and later translated to English and republished in BRILLOUIN and SOMMERFELD (1960) (cf. PRYCE 1961). The focus of this work is on the “signal velocity”, the phrases “convective/absolute stability” are not yet used. The key idea in their approach is a sophisticated variation of curves along which complex integrals are evaluated.

Central ideas from this line of work were later applied to microscopic traffic flow models by WARD and WILSON.

BRIGGS worked, apparently unaware of Brillouin/Sommerfeld, on the interaction between electron-streams and plasmas. The key phrase here is the distinction between “temporal” and “spatial” instability. The work is based on early ideas from LIFSHITZ; vice versa, LIFSHITZ and PITAEVSKII (1981) refer closely to formalism in BRIGGS (1964). BREVDO (1988) can also be attributed to this line of thought, with interesting applications to periodic solutions later on in BREVDO and BRIDGES (1996, 1997) (to be discussed in Sec. 7.2).

SHERRATT et al. (2014) give an introduction and overview to the topic from a biological point of view, with special emphasis on the ideas of SANDSTED and SCHEEL who introduced the notions of transient and remnant instability which we will address in Sec. 5.3.

For traffic flow models, the topic was discussed by different authors:

- TREIBER and KESTING (2011) use an approximation by group velocities and find good agreement with simulations
- MITARAI and NAKANISHI (1999, 2000a,b) use the PDE formalism from LIFSHITZ and PITAEVSKII (1981) for the microscopic Bando model
- WARD and WILSON (WARD 2009; WARD and WILSON 2011; WILSON and WARD 2011) apply ideas from BRILLOUIN and SOMMERFELD (1960) explicitly to a microscopic system with leader on the infinite lane and compare these results to group velocity calculations.

In this section we are going to compare the different approaches for detecting convective and absolute instability in microscopic traffic flow models. We will also compare the results to those obtained for the corresponding macroscopic models. After that, we are going to adopt the notions of transient and remnant instability to microscopic traffic flow models and provide an example for a situation where this approach may be more helpful.

5.2 Convective and absolute instability

We start with an application of the general theory for convective and absolute instability as in LIFSHITZ and PITAEVSKII (1981), first to macroscopic and subsequently also to microscopic traffic flow models.

5.2.1 Macroscopic models

We have found that the linearisations in section 4.2 are of the form

$$\begin{bmatrix} r_t + v_e r_x \\ w_t + v_e w_x \end{bmatrix} = \begin{bmatrix} \mathbf{0} & \mathbf{q}_w \\ \mathbf{q}_r & \mathbf{p} \end{bmatrix} \begin{bmatrix} (r, r_x, r_{xx}, \dots, r^{(n_r)}) \\ (w, w_x, w_{xx}, \dots, w^{(n_w)}) \end{bmatrix} \quad (5.2)$$

where $\mathbf{q}_{w,r}$ and \mathbf{p} are defined in (4.25), (4.32), and (4.31), respectively.

Let us start by writing the solution of the linear PDE (5.2) in terms of Laplace- and Fourier transforms. For convenience, we do not rename the functions, but simply write out the independent variables explicitly. We have

$$[r, w]^\top(x, \lambda) = \int_0^\infty e^{-\lambda t} [r, w]^\top(x, t) dt \quad (5.3a)$$

$$[r, w]^\top(\nu, \lambda) = \int_{-\infty}^\infty e^{-\nu x} [r, w]^\top(x, \lambda) dx. \quad (5.3b)$$

Let $q_r(\nu) := \sum_{j=0}^{n_r} \nu^j \mathbf{q}_r^{j+1}$ and analogously for p_w and q_w .

Together with the initial condition $[r, w]^\top(x, 0) = [r_0, w_0]^\top(x)$, after transformation (5.2) becomes

$$\left((\lambda + v_e \nu) \text{Id} - \underbrace{\begin{bmatrix} 0 & q_w(\nu) \\ q_r(\nu) & p(\nu) \end{bmatrix}}_{=: A(\nu)} \right) \begin{bmatrix} r \\ w \end{bmatrix}(\nu, \lambda) = \begin{bmatrix} r_0 \\ v_0 \end{bmatrix}(\nu). \quad (5.4)$$

For given (λ, ν) , (5.4) can be solved for $[r, w]^\top$ provided (let $q(\nu) := q_r(\nu) \cdot q_w(\nu)$)

$$\chi(\lambda, \nu) := \det((\lambda + v_e \nu) \text{Id} - A(\nu)) = (\lambda + \nu v_e) (\lambda + \nu v_e - p(\nu)) + q(\nu) \neq 0. \quad (5.5)$$

Afterwards, we go back to x, t -space by the inverse transformations:

$$\begin{bmatrix} r \\ w \end{bmatrix} (x, \lambda) = \int_{-i\infty}^{+i\infty} e^{\nu x} \begin{bmatrix} r \\ w \end{bmatrix} (\nu, \lambda) d\nu \quad (5.6a)$$

$$\begin{bmatrix} r \\ w \end{bmatrix} (x, t) = \int_{\sigma-i\infty}^{\sigma+i\infty} e^{\lambda t} \begin{bmatrix} r \\ w \end{bmatrix} (x, \lambda) d\lambda. \quad (5.6b)$$

The Laplace-integral (5.6b) is carried out last. We assume that the integrand, determined by (5.6a), is analytic; then we can pull the integration contour down as far as possible and the integral will be dominated by the poles of the integrand, where the contour gets stuck.

Looking at the inner integral (5.6a), we see that it is finite (provided suitable decay of $[r_0, v_0](\nu)$) if (5.5) holds. This means that the poles in (5.6b) depend only on λ , not on x .

We may assume there is only a finite set of poles $\Lambda = \{\lambda_c(j), j = 1, 2, \dots, m\}$. In the long run, the evolution of $[r, w](x, t)$ will then be dominated by the surrounding of the pole(s) with the biggest real part.

In order to find out where the λ -contour gets stuck, we look at the inner Fourier integral (5.6a) again. It is easy to see that the integrand in (5.6a) has poles if $\chi(\nu, \lambda) = 0$.

Assumption 5.1 (wellposedness) The essential spectrum protrudes finitely wide into the right half-plane.

When we fix the imaginary part of λ and choose its real part to be large enough, consequently no spatial eigenvalue can be on the contour.

If we now deform the contour by decreasing the real part of λ , the associated spatial eigenvalues move and, as we touch the essential spectrum, at least one of them crosses the imaginary axis. However, we may deform the contour of the integration over ν as necessary and go on. As long as the contour can be deformed continuously without crossing the spatial eigenvalues, everything is fine. At some point, however, the ν -contour may be “pinched” by spatial eigenvalues. In general, this will happen only at certain distinct values of λ . In this case, the integration contour in ν cannot be deformed away from the spatial eigenvalues and the integrand in (5.6b) has a pole. It may be observed that a necessary condition for this to happen is

$$\chi(\nu_c, \lambda_c) = 0 \quad (5.7a)$$

$$\wedge \quad \frac{\partial \chi}{\partial \nu}(\nu_c, \lambda_c) = 0 \quad (5.7b)$$

for $(\lambda_c, \nu_c) \in \mathbb{C} \times \mathbb{C}$. We can write (5.7b) as $\lambda + v_e \nu = \frac{v_e p(\nu) - q'(\nu)}{2v_e - p'(\nu)}$ and plug this into (5.7a):

$$\left(\frac{v_e p(\nu) - q'(\nu)}{2v_e - p'(\nu)} \right) \left(\frac{v_e p(\nu) - q'(\nu)}{2v_e - p'(\nu)} - p(\nu) \right) + q(\nu) = 0$$

$$(v_e p(\nu) - q'(\nu)) (v_e p(\nu) - q'(\nu) - p(\nu) (2v_e - p'(\nu))) + q(\nu) (2v_e - p'(\nu))^2 = 0. \quad (5.8)$$

However, so far this only guarantees that two of the spatial eigenvalues merge, but not that they

fix the integration contour between them. For this, we need to ensure that the colliding eigenvalues were on different sides of the contour when the corresponding λ still had a bigger real part. This may be achieved in different ways.

If χ is of low order in ν , it may be feasible to perform a curve discussion to determine the asymptotic behaviour of the meeting spatial eigenvalues as $\lambda \rightarrow +\infty$; this approach is taken in LIFSHITZ and PITAEVSKII (1981).

We may set up a complex initial value problem:

$$\begin{aligned} \forall h > 0 : \quad 0 &= \chi(\lambda_c + h, \nu(h)) = 0 \\ \Rightarrow \frac{d\nu}{dh}(h) &= -\frac{\chi_\lambda(\lambda_c + h, \nu(h))}{\chi_\nu(\lambda_c + h, \nu(h))}, \quad \nu(0) = \nu_c. \end{aligned} \quad (5.9)$$

This is not a well-posed problem due to the root in the denominator at $h = 0$. However, note that we have the limit

$$\lim_{\nu \rightarrow \nu_c} \frac{\chi_\nu(\lambda_c, \nu)}{\nu - \nu_c} = \chi_{\nu\nu}(\lambda_c, \nu_c).$$

Furthermore, as long as the order of ν_c as a zero of $\chi(\lambda_c, \nu)$ is not higher than two (which is generically fulfilled), $\chi_{\nu\nu}(\lambda_c, \nu_c) \neq 0$. To utilise this, we make an ansatz

$$\begin{aligned} \forall h \in \mathbb{R} : \quad 0 &= \chi\left(\lambda_c + \frac{h^2}{2}, \nu(h)\right) = 0, \\ \Rightarrow \frac{d\nu}{dh}(h) &= \begin{cases} -\frac{\chi_\lambda(\lambda_c, \nu_c)}{\chi_{\nu\nu}(\lambda_c, \nu_c)} & \text{for } h = 0 \\ -\frac{h \cdot \chi_\lambda(\lambda_c + h, \nu(h))}{\chi_\nu(\lambda_c + h, \nu(h))} & \text{else} \end{cases}, \quad \nu(0) = \nu_c. \end{aligned} \quad (5.10)$$

Unless we do run into another branch point along the way, (5.10) is well defined. Even if, we may restart the continuation there, so this poses no serious problem.

Note that λ increases in real part for both signs of h . As we follow $\nu(h)$ from $h = 0$ towards $h \rightarrow \pm\infty$, we therefore recover the origins of the colliding spatial eigenvalues.

Now we may formulate a pinching condition as follows:

Definition 5.1 (general pinching condition) Let (λ_c, ν_c) be a branch point and $\nu(h)$, $h \in \mathbb{R}$ be the corresponding solution to (5.10). (λ_c, ν_c) satisfies the **pinching condition** if

$$\lim_{h \rightarrow \infty} \operatorname{Re}(\nu(+h)) \cdot \operatorname{Re}(\nu(-h)) < 0. \quad (5.11)$$

The approach chosen in SANDSTEDTE and SCHEEL (2000) is based on the distribution of the spatial eigenvalues for $\operatorname{Re}(\lambda) \gg 0$ and uses the notion of the Morse index:

Definition 5.2 (Morse index i_∞) Pick any $\lambda_\infty \in \mathbb{C}$ to the right of the essential spectrum. Solve $0 = \chi(\lambda_\infty, \nu)$ for ν and sort the roots by real part:

$$\operatorname{Re}(\nu_1) \leq \operatorname{Re}(\nu_2) \leq \dots \leq \operatorname{Re}(\nu_{i_\infty}) < 0 < \operatorname{Re}(\nu_{i_\infty+1}) \leq \dots \leq \operatorname{Re}(\nu_{m-1}) \leq \operatorname{Re}(\nu_m). \quad (5.12)$$

The **Morse index** i_∞ is given by the number of spatial eigenvalues with real part smaller zero.

Note that the distribution of spatial eigenvalues between the left and right half-plane by definition changes if and only if λ is in the essential spectrum. The requirement that the colliding spatial eigenvalues originated from different sides may then be formalised as follows:

Definition 5.3 (pinching condition) Let (λ_c, ν_c) satisfy (5.7). Let ν_1, \dots, ν_m be the solutions to $\chi(\nu, \lambda_c) = 0$, sorted by real part as in (5.12). (λ_c, ν_c) satisfies the **pinching condition** if

$$\nu_{i_\infty} = \nu_c = \nu_{i_\infty+1}, \quad (5.13)$$

where i_∞ is the Morse index introduced in Def. 5.2.

Proposition 5.1 For polynomial χ , pinching according to Def. 5.3 implies pinching according to Def. 5.1.

Proof: By definition of the Morse index i_∞ and Assumption 5.1, there is an $r \in \mathbb{R}$ such that for all $\text{Re}(\lambda) > r$ we have $\text{Re}(\nu_{i_\infty}) < 0$ and $\text{Re}(\nu_{i_\infty+1}) > 0$. \square

To conclude about the effect of the pole we encounter in a branch point satisfying the pinching condition, we employ a Taylor expansion around (λ_c, ν_c) . Locally, the solution of (5.4) is given by

$$\begin{bmatrix} r \\ w \end{bmatrix}(\nu, \lambda) \approx \frac{1}{\frac{\partial \chi}{\partial \lambda} \Big|_c (\lambda - \lambda_c) + \frac{1}{2} \frac{\partial^2 \chi}{\partial \nu^2} \Big|_c (\nu - \nu_c)^2} \begin{bmatrix} \lambda_c + v_e \nu_c - p(\nu_c) & -q_w(\nu_c) \\ -q_r(\nu_c) & \lambda_c + v_e \nu_c \end{bmatrix} \begin{bmatrix} r_0 \\ v_0 \end{bmatrix}(\nu_c). \quad (5.14)$$

As long as the matrix does not vanish in the branch point, it does not influence the asymptotic behaviour.

Implicit derivation shows us

$$\frac{\partial^2 \lambda}{\partial \nu^2} \Big|_c = \frac{\frac{\partial^2 \chi}{\partial \nu^2} \Big|_c \frac{\partial \chi}{\partial \lambda} \Big|_c^2 + \frac{\partial^2 \chi}{\partial \lambda^2} \Big|_c \frac{\partial \chi}{\partial \nu} \Big|_c^2 - 2 \frac{\partial^2 \chi}{\partial \nu \partial \lambda} \Big|_c \frac{\partial \chi}{\partial \lambda} \Big|_c \frac{\partial \chi}{\partial \nu} \Big|_c}{\frac{\partial \chi}{\partial \lambda} \Big|_c^3} = \frac{\frac{\partial^2 \chi}{\partial \nu^2} \Big|_c}{\frac{\partial \chi}{\partial \lambda} \Big|_c}. \quad (5.15)$$

By setting

$$f(\lambda) = \frac{1}{2 \sqrt{\frac{\partial^2 \chi}{\partial \nu^2} \Big|_c \frac{\partial \chi}{\partial \lambda} \Big|_c} (\lambda - \lambda_c)}, \quad d(\lambda) := \sqrt{\frac{1}{\frac{\partial^2 \chi}{\partial \nu^2} \Big|_c} (\lambda - \lambda_c)} = \sqrt{\frac{\frac{\partial \chi}{\partial \lambda} \Big|_c (\lambda - \lambda_c)}{\frac{\partial^2 \chi}{\partial \nu^2} \Big|_c}}, \quad (5.16)$$

$$\frac{1}{\frac{\partial \chi}{\partial \lambda} \Big|_c (\lambda - \lambda_c) + \frac{1}{2} \frac{\partial^2 \chi}{\partial \nu^2} \Big|_c (\nu - \nu_c)^2} = f(\lambda) \left(\frac{1}{\nu - \nu_c - d(\lambda)} - \frac{1}{\nu - \nu_c + d(\lambda)} \right) \quad (5.17)$$

we can write the ν, λ -dependent part of the integral in (5.6a) as

$$f(\lambda) \int_{-i\infty}^{+i\infty} e^{\nu x} \left(\frac{1}{\nu - \nu_c - d(\lambda)} - \frac{1}{\nu - \nu_c + d(\lambda)} \right) d\nu. \quad (5.18)$$

Note that a sometimes overlooked necessary condition for this analysis to work is

$$\left. \frac{\partial \chi}{\partial \lambda} \right|_c \neq 0. \quad (5.19)$$

We may now split (5.18) and use residual calculus for the evaluation of the parts. At this point, the meaning of the pinching condition becomes clear again: Unless the poles are situated on opposite sides of the integration contour, the integrals will cancel each other. Note that $d(\lambda)$ does not influence the value of the integral.

We conclude that, as $\lambda \rightarrow \lambda_c$, $[r, w](\lambda, x) \rightarrow \infty$ like $\frac{1}{\sqrt{\lambda - \lambda_c}}$.

Putting this knowledge in the outer integral we see that it asymptotically grows like $\frac{1}{\sqrt{t}} e^{\lambda_c t + \nu_c x}$. If $\text{Re}(\lambda_c) > 0$, this will grow in any point in space; otherwise, we only have exponential growth along rays $x = ct$ for c in a given interval.

This motivates the following definition:

Definition 5.4 (convective/absolute instability) An unstable quasistationary solution of a macroscopic model is called **convectively unstable** (cu) if all (λ_c, ν_c) satisfying the branch point condition (5.7), nondegeneracy condition (5.19) and the pinching condition (5.13) satisfy $\text{Re}(\lambda_c) < 0$.

If an unstable QSS is not convectively unstable, it is called **absolutely unstable** (au).

We are also interested in a more detailed classification of convective instability:

Definition 5.5 (convective upstream (downstream) instability) A convectively unstable quasistationary solution is **convectively upstream (downstream) unstable** (cuu/cdu) if it stays convectively unstable for any frame of reference where standing objects are moving upstream (downstream).

5.2.1.1 Low order

We now apply this technique to the low order approximations from Sec. 4.2, where the resulting polynomials can be solved exactly.

From Sec. 4.2.1, remember the linearisations of the first-order PDE for IHD and ND (4.50, 4.54):

$$r_t + v_e r_x = -\rho_e w_x \quad (5.20a)$$

$$w_t + v_e w_x = f_h \frac{\varepsilon}{\rho_e^2} \left(r + \varepsilon \frac{r_x}{2\rho_e} \right) + f_v w + f_{\Delta v} \frac{w_x}{\rho_e} \quad (5.20b)$$

and FLD (4.52)

$$r_t + v_e r_x = -\frac{\rho_e^2}{\varepsilon} \left(w_x \frac{\varepsilon}{\rho_e} + \frac{w_{xx}}{2} \left(\frac{\varepsilon}{\rho_e} \right)^2 \right) \quad (5.21a)$$

$$w_t + v_e w_x = f_h \frac{\varepsilon}{\rho_e^2} r + f_v w + f_{\Delta v} \frac{w_x}{\rho_e}. \quad (5.21b)$$

System (5.20) may be written in matrix form as

$$\begin{bmatrix} r_t \\ w_t \end{bmatrix} + \begin{bmatrix} v_e & \rho_e \\ f_h \frac{\varepsilon^2}{2\rho_e^3} & v_e - \frac{f_{\Delta w}}{\rho_e} \end{bmatrix} \begin{bmatrix} r_x \\ w_x \end{bmatrix} = \begin{bmatrix} 0 & 0 \\ f_h \frac{\varepsilon}{\rho_e^2} & f_v \end{bmatrix} \begin{bmatrix} r \\ w \end{bmatrix}; \quad (5.22)$$

with the initial condition $\begin{bmatrix} r, w \end{bmatrix}^\top(x, 0) = \begin{bmatrix} r_0, w_0 \end{bmatrix}^\top(x)$, after transformation (5.22) becomes

$$\left(\lambda \text{Id} + \nu \begin{bmatrix} v_e & \rho_e \\ f_h \frac{\varepsilon^2}{2\rho_e^3} & v_e - \frac{f_{\Delta w}}{\rho_e} \end{bmatrix} - \begin{bmatrix} 0 & 0 \\ f_h \frac{\varepsilon}{\rho_e^2} & f_v \end{bmatrix} \right) \begin{bmatrix} r \\ w \end{bmatrix}(\nu, \lambda) = \begin{bmatrix} r_0 \\ w_0 \end{bmatrix}(\nu). \quad (5.23)$$

We omit the equivalent formula for (5.21). In both cases, the characteristic polynomial reads (4.51, 4.53):

$$\chi(\lambda, \nu) = (\lambda - \nu v_e) \left(\lambda - \nu v_e + f_v + f_{\Delta v} \frac{\varepsilon \nu}{\rho_e} \right) - f_h \left(\frac{\varepsilon \nu}{\rho_e} + \frac{1}{2} \left(\frac{\varepsilon \nu}{\rho_e} \right)^2 \right). \quad (5.24)$$

In terms of (5.5), we have $p(\nu) := f_v + f_{\Delta v} \frac{\varepsilon \nu}{\rho_e}$, and $q(\nu) := -f_h \left(\frac{\varepsilon \nu}{\rho_e} + \frac{1}{2} \left(\frac{\varepsilon \nu}{\rho_e} \right)^2 \right)$.

For simplicity, we use $h_e = \frac{\varepsilon}{\rho_e}$, $c = \frac{v_e}{h_e}$ and set $z = \nu h_e$.

A simple curve discussion of $\lambda(ik)$, $k \in \mathbb{R}$, shows that the asymptotes for $k \rightarrow \pm\infty$ are parallel to the imaginary axis:

Solving $\chi(\lambda, \nu) = 0$ in (5.24) for λ yields

$$\lambda_{\pm}(\nu) = -\frac{f_v + f_{\Delta v} z}{2} \pm \sqrt{\frac{(f_v + f_{\Delta v} z)^2}{4} + f_h \left(z + \frac{z^2}{2} \right) + cz}. \quad (5.25)$$

With $a = \frac{(f_{\Delta v})^2}{4} + \frac{f_h}{2}$, $b = \frac{f_{\Delta v} f_v}{2} + f_h$ we have for $k \in \mathbb{R}$

$$\lim_{|k| \rightarrow \infty} \left| \lambda_{\pm}(ik) - \left(-\frac{f_v + f_{\Delta v} \frac{\varepsilon ik}{\rho_e}}{2} + ik v_e \pm \left(\sqrt{a} ik + \frac{b}{2\sqrt{a}} \right) \right) \right| \quad (5.26)$$

and obtain two vertical asymptotes at $-\frac{f_v}{2} \pm \frac{b}{2\sqrt{a}}$. This means in particular that Ass. 5.1 is satisfied and the essential spectrum protrudes only finitely wide into right-hand side.

From (5.24) we may directly see that

$$i_{\infty} = 1 \Leftrightarrow c^2 - cf_{\Delta v} - \frac{1}{2}f_h < 0. \quad (5.27)$$

If $i_{\infty} \neq 1$ there can be no relevant branch point so the QSS will be convectively unstable.

Solving (5.24) for z , we obtain

$$\begin{aligned} \chi(z, \lambda) &= \left(c^2 - cf_{\Delta v} - \frac{1}{2}f_h \right) z^2 + (-2\lambda c - cf_v + f_{\Delta v} \lambda - f_h) z + (\lambda^2 + \lambda f_v) \\ z_{\pm} &= -\frac{1}{2} \frac{-2\lambda c - cf_v + f_{\Delta v} \lambda - f_h}{c^2 - cf_{\Delta v} - \frac{1}{2}f_h} \pm \sqrt{\frac{1}{4} \left(\frac{-2\lambda c - cf_v + f_{\Delta v} \lambda - f_h}{c^2 - cf_{\Delta v} - \frac{1}{2}f_h} \right)^2 - \frac{\lambda^2 + \lambda f_v}{c^2 - cf_{\Delta v} - \frac{1}{2}f_h}}. \end{aligned} \quad (5.28)$$

Looking at the radicant, we note that the roots diverge for $c^2 - cf_{\Delta v} - \frac{1}{2}f_h$, which is not surprising after our prior observation. In this case, condition (5.7) is equivalent to the discriminant in (5.28) being zero, which is the case for

$$\frac{1}{4}(-2\lambda c - cf_v + f_{\Delta v}\lambda - f_h)^2 - (\lambda^2 + \lambda f_v) \left(c^2 - cf_{\Delta v} - \frac{1}{2}f_h \right) = 0. \quad (5.29)$$

We refrain from explicitly solving (5.29) for λ since the resulting complicated term gives no further insight for the general case.

In Ex. 5.4.2.2, we derive explicit formulas for the case of the Bando model.

We may also view the above results from the perspective of the criticism by DAGANZO (1995): If we ignore the source term, we have a hyperbolic conservation law. The characteristic polynomial of the first matrix is

$$(\lambda - v_e) \left(\lambda - v_e + \frac{f_{\Delta w}}{\rho_e} \right) + f_h \frac{\varepsilon^2}{2\rho_e^2} \quad (5.30)$$

with eigenvalues

$$\lambda_{\pm} = v_e - \frac{f_{\Delta w}}{2\rho_e} \pm \sqrt{\left(\frac{f_{\Delta w}}{2\rho_e} \right)^2 - f_h \frac{\varepsilon^2}{2\rho_e^2}}. \quad (5.31)$$

For the Bando model with $f_{\Delta w} = 0$, this seems to be a problem because the characteristic speed λ can be faster than the cars. This would be a contradiction to our conclusion that the system is convectively stable in the Lagrangian frame: In fact, symmetric eigenspeeds seem to be “prototypic” for absolute instability.

Compare AW and RASCLE (2000), in reply to DAGANZO (1995): Here this problem was noted as well for the Payne-Whitham model (PAYNE 1971; WHITHAM 1974)

$$\rho_t + (\rho v)_x = 0 \quad (5.32a)$$

$$v_t + vv_x + \frac{1}{\rho} (p(\rho))_x = \frac{1}{\tau} (V(\rho) - v) + \gamma v_{xx}. \quad (5.32b)$$

If we find q such that $(q(\rho))_x = \frac{1}{\rho} (p(\rho))_x$, we can write this as

$$\begin{bmatrix} \rho_t \\ v_t \end{bmatrix} + \underbrace{\begin{bmatrix} (\rho v)_x \\ \left(\frac{v^2}{2} + q(\rho) \right)_x \end{bmatrix}}_{(f(\rho, v))_x} = \begin{bmatrix} 0 \\ \frac{1}{\tau} (V(\rho) - v) + \gamma v_{xx} \end{bmatrix}. \quad (5.33)$$

From the Jacobian of f in (ρ_e, v_e) we find the characteristic speeds $v_e \pm \sqrt{p'(\rho_e)}$. The explanation by AW and RASCLE is that the problem is the derivative with respect to x . Their suggestion out is to use a “directional derivative” $\frac{\partial}{\partial t} + c \frac{\partial}{\partial x}$ instead of $\frac{\partial}{\partial x}$. This is not the place to discuss this approach; however, it may be argued that this avoids rather than solves the problem.

Since these were the only ones considered, the problem could be blamed on the spatial derivatives, too. However, we instead argue that the primary issue is the omitting of the source term in the analysis.

Here and in AW and RASCLE (2000), in the linearised model, the Jacobian of f is not the part where zeroth-order information about the distance to the car in front enters. In this sense, con-

sidering characteristic speeds calculated from the Jacobian cannot contain the right information. Note also that the source term has factor $\frac{1}{\tau}$, where τ is of the same order of magnitude as ε . This is the dominant term in the system so ignoring it cannot be a good idea.

5.2.1.2 Higher order

For higher order PDE approximations of a CFM, combination of (5.7a) and (5.7b) in general yields a polynomial of order greater four, whose roots need to be found numerically.

The main problem is that the essential spectra will have bad asymptotics as $k \rightarrow \pm\infty$; in general, Ass. 5.1 will not be satisfied. However, as discussed in Sec. 4.2.2, we may assume that the initial datum $[r_0, w_0]^\top(\nu)$ has bounded support.

This means that, since the position of the spectrum outside of the support of $[r_0, w_0]^\top(\nu)$ is not important for the integration, we may change it arbitrarily. Thus, we may adapt χ such that the essential spectrum has vertical asymptotes in λ -plane and branch points appear only for ν_c in the support of $[r_0, w_0]^\top(\nu)$. Then i_∞ from Def. 5.2 is well-defined and we may proceed as before.

5.2.2 Microscopic models

In MITARAI and NAKANISHI (1999) the ‘‘convective stability limit’’ (corresponding to the cuu-au instability boundary) was calculated for the Bando model, based on LIFSHITZ and PITAEVSKII (1981).

The necessary condition (5.7) is checked in terms of an equivalent formulation in ω and k , but no comments are made on the applicability of the theory or the necessity to check the pinching condition..

Therefore, let us go through the steps performed in section 5.2.1 and discuss at which points changes need to be introduced.

Since the correct frame of reference is crucial, we need to work with a linear CFM in the form (4.11), for simplicity we restrict ourselves to

$$\begin{bmatrix} \dot{y}_{\tilde{j}} \\ \dot{w}_{\tilde{j}} \end{bmatrix} = \underbrace{\begin{bmatrix} 0 & 1 \\ -f_h & f_v - f_{\Delta v} \end{bmatrix}}_{=:A} \begin{bmatrix} y_{\tilde{j}} \\ w_{\tilde{j}} \end{bmatrix} + \underbrace{\begin{bmatrix} 0 & 0 \\ f_h & f_{\Delta v} \end{bmatrix}}_{=:B} \begin{bmatrix} y_{\tilde{j}-1} \\ w_{\tilde{j}-1} \end{bmatrix}. \quad (5.34)$$

The independent variables are now $(\tilde{j}, t) \in \mathbb{Z} \times \mathbb{R}^+$ instead of $(x, t) \in \mathbb{R} \times \mathbb{R}^+$. In the transformations (5.3), we can keep the Laplace transform (5.3a) but have to replace the continuous Fourier transform (5.3b) by a discrete-time Fourier transform over the indices:

$$[y, w]^\top(\tilde{j}, \lambda) = \int_0^\infty e^{-\lambda t} [y, w]^\top(\tilde{j}, t) dt \quad (5.35a)$$

$$[y, w]^\top(\xi, \lambda) = \sum_{\tilde{j}=-\infty}^\infty e^{-i\xi\tilde{j}} [y, w]^\top(\tilde{j}, \lambda) dx. \quad (5.35b)$$

After both transformations, (5.34) with initial data $[y, w]^\top(\tilde{j}, 0) = [y_0, w_0]^\top(\tilde{j})$ becomes

$$\left((\lambda + ic\xi)\text{Id} - \underbrace{\begin{bmatrix} 0 & 1 \\ f_h(e^{i\xi} - 1) & f_v + f_{\Delta v}(e^{i\xi} - 1) \end{bmatrix}}_{=A+e^{i\xi}B} \right) \begin{bmatrix} y \\ w \end{bmatrix}(\xi, \lambda) = \begin{bmatrix} y_0 \\ w_0 \end{bmatrix}(\xi). \quad (5.36)$$

Solvability of (5.36) is again determined by the characteristic function

$$\chi(\lambda, \xi) = \det \left((\lambda + ic\xi)\text{Id} - (A + e^{i\xi}B) \right) = (\lambda + ic\xi) \underbrace{(\lambda + ic\xi - f_v - f_{\Delta v}(e^{i\xi} - 1))}_{\tilde{p}(\xi)} - \underbrace{f_h(e^{i\xi} - 1)}_{\tilde{q}(\xi)}. \quad (5.37)$$

Note that for any given λ_0 , there is a countably infinite set of roots $\{\xi_0 \in \mathbb{C} : \chi(\lambda_0, \xi_0) = 0\}$

The back-transformation is given by

$$[y, w]^\top(\tilde{j}, \lambda) = \int_{-\pi}^{\pi} e^{i\xi\tilde{j}} [y, w]^\top(\xi, \lambda) d\xi \quad (5.38a)$$

$$[y, w]^\top(\tilde{j}, t) = \int_{\sigma-i\infty}^{\sigma+i\infty} e^{\lambda t} [y, w]^\top(\tilde{j}, \lambda) d\lambda. \quad (5.38b)$$

Although the index set is discrete, the back-transformation includes integration over two continuous sets, one of which is bounded.

By the same arguments as before, we now have to search for branch points $(\xi_c, \lambda_c) \in \mathbb{C}^2$ such that

$$\chi(\xi_c, \lambda_c) = 0 \quad (5.39a)$$

$$\wedge \frac{\partial \chi}{\partial \xi}(\xi_c, \lambda_c) = 0. \quad (5.39b)$$

Again, equivalently to our treatment of (5.7), we may solve $\frac{\partial \chi}{\partial \xi} = 0$ for $\lambda + \xi c$ and plug the result into $\chi = 0$:

$$\begin{aligned} 0 &= \frac{cp(\xi) - q'(\xi)}{p'(\xi) - 2c} \cdot \left(\frac{cp(\xi) - q'(\xi)}{p'(\xi) - 2c} + p(\nu) \right) + q(\xi) \\ \Leftrightarrow 0 &= (cp(\xi) - q'(\xi))^2 + p(\xi)(cp(\xi) - q'(\xi))(p'(\xi) - 2c) + q(\xi)(p'(\xi) - 2c)^2. \end{aligned} \quad (5.40)$$

We may substitute $z = e^{i\xi}$. Note that (5.40) is a third order polynomial in z .

Solving and resubstitution gives three sequences of branch points.

As a sufficient condition, we may apply definition 5.1.

Definition 5.6 (Convective/absolute instability for microscopic models)

An unstable quasistationary solution (h_e, v_e) of a microscopic model is called **convectively unstable** if all (λ_c, ν_c) satisfying the necessary condition (5.39) and the sufficient condition as described above satisfy $\text{Re}(\lambda_c) < 0$.

If an unstable CFM is not convectively unstable, it is called **absolutely unstable**.

5.2.2.1 Comparison with the approach by Ward and Wilson

Let us now consider the approach presented in WARD and WILSON (2011) which is loosely based on BRILLOUIN and SOMMERFELD (1960), which in turn is a republication of SOMMERFELD (1914) and BRILLOUIN (1914).

Their basic assumption is that perturbations are caused by the leading car, and the initial conditions for all other cars are zero. The underlying index set is $J = \mathbb{N}$.

After (5.35a), we have the system

$$\tilde{\lambda} [y, w]^\top(j, \tilde{\lambda}) = \begin{cases} [y_0, w_0]^\top(j) + A [y, w]^\top(j, \tilde{\lambda}) & j = 0 \\ A [y, w]^\top(j, \tilde{\lambda}) + B [y, w]^\top(j-1, \tilde{\lambda}) & j > 0. \end{cases} \quad (5.41)$$

Here, we write $\tilde{\lambda}$ instead of $\tilde{\lambda}$, since for now we are still in the vehicles' coordinate frame.

Since $J \neq \mathbb{Z}$, we cannot apply (5.35b).

The solution to (5.41) can be written recursively as

$$[y, w]^\top(j, \tilde{\lambda}) = \left[(\tilde{\lambda} \text{Id} - A)^{-1} B \right]^j (\tilde{\lambda} \text{Id} - A)^{-1} [y, w]^\top(\tilde{\lambda}, j=0). \quad (5.42)$$

Without loss of information, this can be written in y only as in WARD and WILSON (2011), since $w(\lambda, j=0)$ depends only on $y(\lambda, j=0)$ and the initial value $w(j=0, t=0)$. We stick with the matrix formulation for ease of comparison with our former calculations.

Let z_\pm be the eigenvalues of $(\tilde{\lambda} \text{Id} - A)^{-1} B$, i.e.

$$(\tilde{\lambda} \text{Id} - A)^{-1} B = U^{-1} \text{diag} [z_\pm] U. \quad (5.43)$$

Note that z_\pm and U implicitly depend on $\tilde{\lambda}$.

The retransformation by means of (5.38b) can be written as

$$[y, w]^\top(j, t) = \int_{\sigma-i\infty}^{\sigma+i\infty} U^{-1} \text{diag} [\exp(\tilde{\lambda}t + j \ln z_\pm)] U (\tilde{\lambda} \text{Id} - A)^{-1} [y_0, w_0]^\top(\tilde{\lambda}) d\tilde{\lambda}. \quad (5.44)$$

For fixed j , this expression converges to 0 as $t \rightarrow \infty$, provided we have platoon stability: Pull σ to the left. Again the contour “sticks” to the poles of the integrand. These occur for $\det(\tilde{\lambda} \text{Id} - A) = 0$, corresponding to the platoon eigenvalues, whose real part is smaller than zero by assumption. Now we consider the evolution along a ray $j = ct$ and apply the method of steepest descent to

$$\exp\left(t\left(\tilde{\lambda} + c \ln z_+\right)\right)$$

by finding the saddle point of $\tilde{\lambda} + c \ln z_+$ with biggest real part, implying the necessary condition

$$\frac{\partial}{\partial \tilde{\lambda}} \left(\tilde{\lambda} + c \ln z_+(\tilde{\lambda}) \right) = 0. \quad (5.45)$$

Proposition 5.2 Condition (5.45) is equivalent to the necessary condition (5.39).

Proof: z_+ is defined in (5.43). It is easy to see that this is equivalent to it being a solution of

$$\tilde{\chi}(\tilde{\lambda}, z_+) := \det \left(A + \frac{1}{z_+} B - \tilde{\lambda} \text{Id} \right) = 0. \quad (5.46)$$

(5.46) obviously corresponds to (5.39a); comparison with (5.37) shows we may set $\tilde{\lambda} = \lambda + ic\xi$, $\zeta = e^{i\xi}$.

Now we may simplify the LHS of (5.45) as

$$\frac{\partial}{\partial \tilde{\lambda}} \left(\tilde{\lambda} + c \ln z_+ \right) = 1 + c \frac{\partial \xi}{\partial \tilde{\lambda}} = 1 - c \frac{\partial \tilde{\chi}}{\partial \tilde{\lambda}} / \frac{\partial \tilde{\chi}}{\partial \xi} = 1 - c \frac{\frac{\partial \chi}{\partial \tilde{\lambda}}}{\frac{\partial \chi}{\partial \xi} - c \frac{\partial \chi}{\partial \lambda}},$$

making the equivalence of (5.45) to (5.39b) obvious. \square

This can also be shown by direct comparison of the third-order polynomials for the branch point condition. However, the variant presented here gives more insight into the structural relation between the two approaches and provides a better interpretation of the variables occurring in the different settings.

The sufficient conditions formulated by WARD and WILSON (2011) are

1. $\tilde{\lambda}_c$ is the global maximum of $\text{Re} \left(\tilde{\lambda} + c \ln z_+(\tilde{\lambda}) \right)$ along the contour.
2. The λ -contour must not cross the platoon eigenvalues.

With

$$\tilde{\lambda} + c \ln z_+(\tilde{\lambda}) = \lambda, \quad (5.47)$$

it is easy to see that maximality of $\text{Re} \left(\tilde{\lambda} + c \ln z_+(\tilde{\lambda}) \right)$ in $\tilde{\lambda}_c$ corresponds to λ_c being the rightmost point on the integration contour in the other setting.

The necessity of the latter condition can be directly seen from (5.44).

5.2.3 Drawbacks

The meaning of the branch point condition (5.7) or its equivalent (5.45) are far from intuitive. The visualisations are all done in the ν - and λ -plane, with no obvious interpretation in the application context.

This critique applies maybe even more to the approach presented in WARD and WILSON (2011), which may be one of the reasons it has seen little application in practice.

As described in SANDSTED and SCHEEL (2000), using the concepts of convective and absolute instability may give unexpected results for PDEs on finite domains with separated boundary

conditions: Under certain circumstances, perturbations may not be convected out of a system of finite length, but instead be “reflected” at the boundary.

A similar phenomenon may occur in microscopic traffic flow models for two lanes if information is exchanged between lanes locally.

Assume both one-way models are in a convectively unstable parameter regime, but perturbations are convected to the right on one lane and to the left on the other. The overall system will then be convectively unstable as well. Without interaction, the amplitude of the perturbation will eventually decay at each fixed location. This changes if an interaction between the lanes is introduced at certain points: upon leaving an interval between such points on one lane, part of the perturbation will “reenter” on the other lane and travel back. This will be repeated at the other end of the interval in reverse order (Ex. 5.4).

The distinction between convective and absolute instability introduced in Def. 5.5 does not account for this. This means that we can construct models that are convectively unstable, but neither convectively upstream nor downstream unstable.

5.3 Transient and remnant instability

5.3.1 Macroscopic models

Consider a linear PDE $u_t = f(u, u_x, \dots)$. As we know, its solution consists of a weighted integral over modes of the form $\exp(\lambda t + \nu(\lambda)x)$, where each pair $\lambda, \nu(\lambda)$ solves the characteristic equation $\chi(\lambda, \nu(\lambda)) = 0$. If there are pairs with $\text{Re}(\nu(\lambda)) = 0, \text{Re}(\lambda) > 0$, we have instability. Conversely, we have stability if for all λ in the right complex half plane the imaginary axis is free of spatial eigenvalues.

Since the spatial eigenvalues move continuously with λ and for given λ there are always $m \in \mathbb{N}$ spatial eigenvalues, by definition of the Morse index in (5.12) this means that for all λ in the right complex half plane there are i_∞ spatial eigenvalues in the left and $m - i_\infty$ in the right complex half plane .

We would now like to have some sort of “filter” that helps us to qualitatively classify the contribution from the neighbourhood of an arbitrary but fixed $\lambda \in \mathbb{C}$.

To this end, we multiply the solution with an exponential weight $e^{\eta(\lambda)x}$. By doing so, we are effectively studying a variant of the PDE, in which $\nu(\lambda)$ is replaced by $\nu(\lambda) + \eta(\lambda)$ (Fig. 5.1). This means that in general, we will be able to “fix” the distribution of spatial eigenvalues towards the desired state (5.12). However, a problem arises whenever $\text{Re}(\nu_{i_\infty}(\lambda)) = \text{Re}(\nu_{i_\infty+1}(\lambda))$: In this case, these two spatial eigenvalues will always be crossing the imaginary axis together, and the desired distribution cannot be achieved. This is the case if, but not only if, $\nu_{i_\infty} = \nu_{i_\infty+1}$, i.e. in a branch point of $\chi(\lambda, \nu)$.

$$\begin{array}{ccc}
 \mathbf{u}(x, t) & \xrightarrow{\text{PDE}} & \mathbf{u}(x, t + s) & H^1 \\
 \downarrow \cdot e^{\eta x} & & \downarrow \cdot e^{\eta x} & \downarrow \\
 \tilde{\mathbf{u}}(x, t) & \xrightarrow{\text{PDE}_\eta} & \tilde{\mathbf{u}}(x, t + s) & H_\eta^1
 \end{array}$$

Figure 5.1: Application of exponential weights to the solution of a PDE

This motivates the main definition of this section, adapted from SANDSTEDE and SCHEEL (2000):

Definition 5.7 (transient and remnant instability) An unstable linear PDE is called **transiently unstable** (tu) if for each λ in the right half plane there is an $\eta(\lambda) \in \mathbb{R}$ such that

$$\text{Re}(\nu_1) \leq \text{Re}(\nu_2) \leq \dots \leq \text{Re}(\nu_{i_\infty}) < \eta(\lambda) < \text{Re}(\nu_{i_\infty+1}) \leq \dots \leq \text{Re}(\nu_{m-1}) \leq \text{Re}(\nu_m). \quad (5.48)$$

A transiently unstable linear PDE is called **transiently upstream (downstream) unstable** (tuu/tdu) if all such η may be chosen from \mathbb{R}^+ (\mathbb{R}^-).

An unstable linear PDE is called **remnantly unstable** (ru) if it is not transiently unstable.

In this context, the concept of the absolute spectrum will be helpful:

Definition 5.8 The **absolute spectrum** is given by the $\lambda \in \mathbb{C}$ for which

$$\text{Re}(\nu_{i_\infty}(\lambda)) = \text{Re}(\nu_{i_\infty+1}(\lambda)).$$

Proposition 5.3 An unstable QS is transiently unstable if and only if its absolute spectrum lies in the left half plane.

Proof: For $\lambda \in \mathbb{C}$ arbitrary but fixed, it is clear that (5.48) is true if and only if $\text{Re}(\nu_{i_\infty}(\lambda)) \neq \text{Re}(\nu_{i_\infty+1}(\lambda))$. \square

5.3.2 Microscopic models

In order to emphasise the connection to the macroscopic setting, in the following we will work with $i\xi$, rotating the index eigenvalues ξ by $\frac{pi}{2}$. After division by h_e , we may also refer to them as “microscopic spatial eigenvalues” $\nu = \frac{i\xi}{h_e}$.

In the index frame, the spectrum is given by a closed curve, for each fixed $\lambda \in \mathbb{C}$ there are countably infinitely many roots that are spaced equidistantly on a vertical line. If λ is in the inner area of the closed curve, all the microscopic spatial eigenvalues are in the left half-space, if λ lies outside of closed curve, all spatial eigenvalues are in the right half-space. We may also assign an orientation to the spectrum so that we can regard the inner as to the left and the outer as to the right of it.

In the road frame, the spectrum is “stretched” in the direction of the imaginary axis. For fixed ξ , we have n solutions $\lambda_1(\xi), \dots, \lambda_n(\xi)$. The solutions are continuously differentiable in ξ , so we obtain n smooth curves for $i\xi \in \mathbb{R}$.

In this sense, for $c = 0$, the branches of the spectrum can be regarded as completely “coiled”, and a non-zero c has the effect of spreading them out in the direction of the imaginary axis.

By definition, whenever λ crosses the spectrum, a spatial eigenvalue crosses the imaginary axis. When crossing the “coiled” spectrum of the index frame, infinitely many spatial eigenvalues move to the left or right simultaneously. This is different in the case $c \neq 0$. In general, up to points where the branches cross themselves or each other, the distribution of spatial eigenvalues changes by 1 when crossing a branch of the essential spectrum (cf. Ex. 4.2).

In order to determine the distribution of eigenvalues for a particular $\lambda \in \mathbb{C}$ with $c \neq 0$, it is helpful to remember the classification of the connected components by the orientation of the spectrum that we introduced before. Since the spectrum is no longer given by a closed curve, there is no component that directly corresponds to the inner area. Instead, we have two large connected areas to the left and the right of the spectrum and a periodic pattern formed by the n branches. From this we may see that the spatial distribution is changed by n when λ moves from the very right to the very left (same orientation of branches assumed). For λ with real part big enough, we have n spatial eigenvalues with negative real part, for λ with real part small enough all spatial eigenvalues are in the right complex half plane. As $c \searrow 0$, the real parts of the n spatial eigenvalues to the left approach $-\infty$ for $\text{Re}(\lambda) \gg 0$; in the center, regions with multiple spatial eigenvalues on the left are created by intersections of the essential spectrum with itself.

Equivalently to the macroscopic case, we may therefore sort the spatial eigenvalues for fixed λ by ascending real part,

$$\text{Re}(\nu_1(\lambda)) \leq \text{Re}(\nu_2(\lambda)) \leq \dots, \quad (5.49)$$

or, in terms of the “index eigenvalues” ξ , by decreasing imaginary part

$$\text{Im}(\xi_1(\lambda)) \geq \text{Im}(\xi_2(\lambda)) \geq \dots \quad (5.50)$$

As pointed out in SHERRATT et al. (2014), in the macroscopic case the distribution of the spatial eigenvalues for temporal eigenvalues with big real part corresponds to the number of separated boundary conditions that need to be prescribed at the end points when the PDE is considered on a domain of finite length $x_d - x_u$. We may compare this to the situation we have for microscopic models: In the cases we study in the examples, all but n spatial eigenvalues are located in the right side of the complex plane if $\text{Re}(\lambda)$ is big enough. Due to the anisotropic nature of these models, the major part of the necessary information has to be provided at the downstream end, where the behaviour of the “missing” leading vehicle has to be explained. In fact, since we are trying to reconstruct the profiles over the length $h(x_d)$ from the spatial derivatives at x_d , we do need infinitely many terms to obtain the full Taylor series. At the upstream end, far less information is needed: As long as $m_f = 0$, no knowledge about vehicles beyond x_u is required. All we need to know is at which rate and at what speed vehicles are arriving in x_u . In the first order model, even the latter is unnecessary since speed and headway are directly connected by means of the OVF. For the pinching condition to be satisfied, the right branch points to look out for are consequently those arising as collisions of the spatial eigenvalues ν_n and ν_{n+1} . The same holds true for the

absolute spectrum, where we need to look for λ with $\operatorname{Re}(\nu_n(\lambda)) = \operatorname{Re}(\nu_{n+1}(\lambda))$. In order to find the absolute spectrum, we may start from the branch points that satisfy the pinching condition and perform a numerical continuation of the roots of the function

$$g : \mathbb{C} \times \mathbb{C} \times \mathbb{R} \rightarrow \mathbb{C}^2$$

$$(\lambda, \xi, d) \mapsto \begin{bmatrix} \chi(\lambda, \xi) \\ \chi(\lambda, \xi + d) \end{bmatrix},$$

similar to what is proposed in SHERRATT et al. (2014).

In order to ensure that we stay on the right branch, we need to monitor the number of spatial eigenvalues to the left of the pair $\nu, \nu + id$. We may do so by calculating the integral

$$\frac{1}{2\pi i} \int_C \frac{\frac{\partial \chi}{\partial \xi}(\lambda, \xi)}{\chi(\lambda, \xi)} d\xi, \quad (5.51)$$

where C is a path enclosing the relevant area, e.g. a rectangle given by the points $R + i(\operatorname{Im}(\xi) + \varepsilon)$, $R(1 + i) + i(\operatorname{Im}(\xi) + \varepsilon)$, $R(i - 1) + i(\operatorname{Im}(\xi) + \varepsilon)$, and $-R + i(\operatorname{Im}(\xi) + \varepsilon)$ with $R \gg 1$. When a third spatial eigenvalue crosses the line through ξ_{i_∞} and $\xi_{i_\infty+1}$, a triple point occurs and the continuation needs to be restarted (cf. Ex. 5.3).

Again, the absolute spectrum may be interpreted in terms of exponential weights. Consider a CFM $\dot{\mathbf{u}}_j = f(\mathbf{u}_{m_{j+1}}, \dots, \mathbf{u}_{j+m_f})$, where $\mathbf{u}(t) = (\mathbf{u}_j(t))_{j \in J} \in \ell_J^n$ denotes the deviation from a quasistationary solution. Instead, we may as well consider a weighted state

$$\tilde{\mathbf{u}}_j(t) := \exp(\eta \cdot (ct - j)) \cdot \mathbf{u}_j(t) \quad (5.52)$$

where the weight applied to vehicle j depends on time t and index j (Fig. 5.2).

$$\begin{array}{ccc} \mathbf{u}_j(t) & \xrightarrow{\text{ODE}} & \mathbf{u}_j(t+s) & \ell^2 \\ \downarrow \cdot e^{\eta(ct-j)} & & \downarrow \cdot e^{\eta(c(t+s)-j)} & \downarrow \\ \tilde{\mathbf{u}}_j(t) & \xrightarrow{\text{ODE}_{\tilde{\eta}}} & \tilde{\mathbf{u}}_j(t+s) & \ell_\eta^2 \end{array}$$

Figure 5.2: Application of exponential weights to a microscopic model

For a quasistationary solution, with $c = \frac{v_e}{h_e}$ we have weights that are proportional to the position $x_j(t)$; for $c = 0$, the weights are fixed on the vehicles themselves.

By elementary calculations, we find that the evolution of $\tilde{\mathbf{u}}$ is governed by the ODE

$$\begin{aligned} \dot{\tilde{\mathbf{u}}}_j &= \lim_{s \rightarrow 0} \frac{\tilde{\mathbf{u}}_j(t+s) - \tilde{\mathbf{u}}_j(t)}{s} \\ &= \lim_{s \rightarrow 0} \frac{\exp(\eta \cdot (c(t+s) - j)) \cdot \mathbf{u}_j(t+s) - \exp(\eta \cdot (ct - j)) \cdot \mathbf{u}_j(t)}{s} \\ &= \exp(\eta \cdot (ct - j)) \cdot \dot{\mathbf{u}}_j(t) + \lim_{s \rightarrow 0} \frac{(\exp(\eta \cdot (c(t+s) - j)) - \exp(\eta \cdot (ct - j))) \cdot \mathbf{u}_j(t+s)}{s} \\ &= \exp(\eta \cdot (ct - j)) \cdot (\dot{\mathbf{u}}_j(t) + \eta c \cdot \mathbf{u}_j(t)) \end{aligned}$$

$$\begin{aligned}
 &= \exp(\eta \cdot (ct - j)) \cdot f\left(\exp(\eta \cdot (j + m_1 - ct)) \tilde{\mathbf{u}}_{m_{j+1}}(t), \dots, \exp(\eta \cdot (j + m_f - ct)) \tilde{\mathbf{u}}_{j+m_f}(t)\right) \\
 &\quad + \eta c \cdot \tilde{\mathbf{u}}_j(t)
 \end{aligned} \tag{5.53}$$

In the linearisation, we have

$$\dot{\tilde{\mathbf{u}}}_j = \left(\sum_{l=m_1}^{m_f} \exp(\eta l) \cdot A_l \cdot \tilde{\mathbf{u}}_{j+l} \right) + \eta c \cdot \tilde{\mathbf{u}}_j \tag{5.54}$$

and the characteristic polynomial $\chi(\lambda, i\xi)$ is replaced by $\chi(\tilde{\lambda}, \eta c + i\tilde{\xi})$. For fixed λ , the spatial eigenvalues are simply shifted by η .

We may also fix $\xi \in \mathbb{R}$ and study the deformation of the essential spectrum. However, since the weight η in the definition of transient and absolute instability is allowed to depend on λ , we may *not* directly conclude that the system is absolutely unstable if the spectrum can not be “pulled” into the left half-plane completely by a single weight η .

An interesting observation can be made in the case $c = 0$, i.e. in the index frame, for $m_f = 0$. For $\eta \rightarrow -\infty$, (5.54) is reduced to

$$\dot{\mathbf{u}}_j = A_0 \cdot \mathbf{u}_{j+l} \tag{5.55}$$

and the essential spectrum is asymptotically pulled back to the platoon eigenvalues. Since these are assumed to have negative real part (WILSON and WARD 2011), we can conclude that a reasonable CFM model of this form is always at most transiently upstream unstable in the index frame. This was of course to be expected, since $m_f = 0$ prohibits any information from flowing downstream relative to the vehicles.

5.4 Examples

5.4.1 Reaction-diffusion equations

Example 5.1

Consider the reaction-diffusion-advection equation (RDA)

$$u_t = u_{xx} + au_x + bu \tag{5.56}$$

with parameters $(a, b) \in \mathbb{R}^2$ and initial data

$$u(x, 0) = u_0(x) = e^{-\sigma x^2}. \tag{5.57}$$

Then it is easily checked that

$$u(x, t) = \frac{\exp(bt)}{\sqrt{1 + 4\sigma t}} \exp\left(-\frac{\sigma(x + at)^2}{1 + 4\sigma t}\right) \tag{5.58}$$

solves the PDE, e.g. by comparison of the partial derivatives

$$\begin{aligned} u_t &= bu - \frac{2\sigma}{1+4\sigma t}u - \left(\frac{2a\sigma(x+at)}{1+4\sigma t} - \frac{4\sigma^2(x+at)^2}{(1+4\sigma t)^2} \right) u \\ u_x &= -\frac{2\sigma(x+at)}{1+4\sigma t}u, \quad u_{xx} = \left(\frac{2\sigma(x+at)}{1+4\sigma t} \right)^2 u - \frac{2\sigma}{1+4\sigma t}u. \end{aligned}$$

The characteristic polynomial is

$$\chi(\lambda, \nu) = \nu^2 + a\nu + b - \lambda, \tag{5.59}$$

the essential spectrum is therefore given by

$$\sigma_{\text{ess}}(a, b) = \left\{ \lambda \in \mathbb{C} : \exists k \in \mathbb{R} : \lambda = (b - k^2) + aki \right\}$$

and we have stability if and only if $b < 0$.

Convective/absolute instability The classification of the unstable region $b > 0$ into convectively and absolutely unstable regimes is worked out in BREVDO and BRIDGES (1996).

Looking for branch points (λ_c, ν_c) , we observe that $\frac{\partial \chi}{\partial \nu} = 0 \Leftrightarrow \nu_c = -\frac{a}{2}$; plugging this into (5.59) yields $\lambda_c = b - \frac{a^2}{4}$.

Solving $\chi(\lambda_c + h, \nu_c + \delta) = 0$ for ν yields $\delta(h) = \pm\sqrt{h}$. For this branch point, the pinching condition is fulfilled since the spatial roots diverge to $\pm\infty$ as $h \rightarrow \infty$, fixing the contour between them as $h \searrow 0$.

We see that the PDE is absolutely unstable for $\frac{a^2}{4} < b$.

In order to classify the convectively unstable regions $\frac{a^2}{4} > b > 0$, $a \leq 0$, note that transferring PDE (5.56) to a coordinate system $\tilde{x} = x + ct$ moving at speed c (i.e., upstream for $c > 0$ and vice versa) only results in replacing a by $a + c$. Therefore, it is easy to see that a convectively unstable parameter pair with $a < 0$ stays convectively unstable for any $c \geq 0$ and vice versa. From definition 5.5 we see that we have convective upstream and downstream instability for $a > 0$ and $a < 0$, respectively.

E.g. by plugging the ansatz $x = ct$ into the analytic solution (5.58), we see that asymptotically for $t \rightarrow \infty$, the solution grows only in the cone where $b - \frac{(c+a)^2}{4} > 0$, bounded by $c = -a \pm 2\sqrt{b}$ (Figs. 5.3, 5.4).

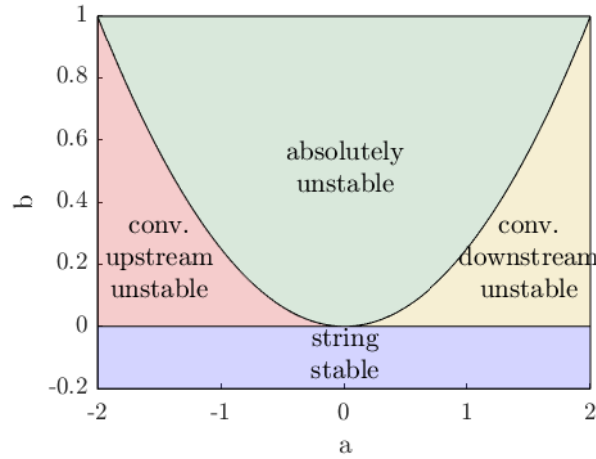


Figure 5.3: Stability classification in parameter space for reaction diffusion equation (5.56)

Transient/remnant instability Instead, we may apply exponential weights in order to classify the PDE as transiently or remnantly unstable. The procedure is very similar to Example 1 in SANDSTEDT and SCHEEL (2000).

Interpreting the real part of ν as an exponential weight, we may write the the characteristic polynomial (5.59) as

$$\chi(\lambda, \eta, k) = -\lambda - k^2 + ik(2\eta + a) + \eta(\eta + a) + b \tag{5.60}$$

i.e. the essential spectrum is given by a parabola opened to the left with vertex at $\lambda = \eta(\eta + a) + b$. The optimal weight, giving the minimal value for the real part of the vertex is $\eta^* = -\frac{a}{2}$. At this value, the weighted spectrum degrades to the ray $(-\infty, b - \frac{a^2}{4}]$. For all λ in $\mathbb{C} \setminus (-\infty, b - \frac{a^2}{4}]$, including the complete right half plane, $\mathcal{T}^{\eta^*}(\lambda)$ is invertible with one spatial root on each side of the imaginary axis. From this we may conclude that for the scalar PDE, transient and remnant instability are the same as convective and absolute.

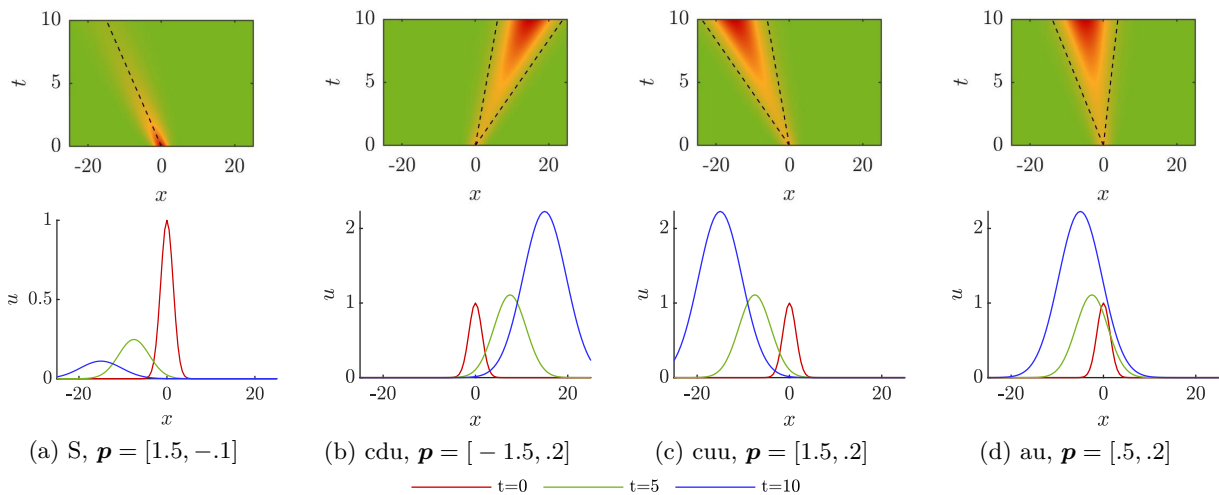


Figure 5.4: Examples for (in)stability classes for reaction-diffusion equation

Example 5.2 (A two-component RDA)

Similar to Ex. 2 in SANDSTED and SCHEEL (2000), we now combine two equations of the type discussed above to study the differences between the concepts of convective and transient instability.

We consider two “species” u_1, u_2 , both subject to PDE (5.56) but with possibly different parameters $a_{1,2}, b_{1,2}$. In a traffic context, we may think of the dynamics on two adjacent but unrelated lanes.

If the species do not interact, we could of course solve each equation independently. However, if we choose to solve them together, the characteristic polynomial becomes

$$\begin{aligned}\chi(\lambda, \nu) &= (\nu^2 + a_1\nu + b_1 - \lambda)(\nu^2 + a_2\nu + b_2 - \lambda) \\ &= (\nu^2 + \bar{a}\nu + \bar{b} - \lambda)^2 - (\hat{a}\nu + \hat{b})^2,\end{aligned}\tag{5.61}$$

where $\bar{a} = \frac{a_1+a_2}{2}$, $\hat{a} = \frac{a_2-a_1}{2}$, $\bar{b} = \frac{b_1+b_2}{2}$, $\hat{b} = \frac{b_2-b_1}{2}$.

Consequently, we have

$$\sigma_{\text{ess}}(\mathbf{a}, \mathbf{b}) = \sigma_{\text{ess}}(a_1, b_1) \cup \sigma_{\text{ess}}(a_2, b_2).\tag{5.62}$$

Convective/absolute instability Naïvely looking for branch points, we find that

$$\frac{\partial \chi}{\partial \nu} = 2(2\nu + \bar{a})(\nu^2 + \bar{a}\nu + \bar{b} - \lambda) - 2\hat{a}(\hat{a}\nu + \hat{b}) = 0\tag{5.63}$$

plugged into (5.61) yields

$$\left(\frac{\hat{a}(\hat{a}\nu + \hat{b})}{2\nu + \bar{a}}\right)^2 - (\hat{a}\nu + \hat{b})^2 = 0 \Leftrightarrow (\hat{a}^2 - (2\nu + \bar{a})^2)(\hat{a}\nu + \hat{b}) = 0.$$

We see that this is the case for $\nu_c \in \{-\frac{\hat{b}}{\hat{a}}, -\frac{\bar{a}\hat{a}}{2}\}$ where $\nu_c^* = -\frac{\hat{b}}{\hat{a}}$ has multiplicity 2. Consequently, the branch point condition $\chi(\nu_c, \lambda_c) = 0$, $\chi_\nu(\nu_c, \lambda_c) = 0$ is fulfilled for

$$(\nu_c, \lambda_c) \in \left\{ \left(-\frac{a_1}{2}, b_1 - \frac{a_1^2}{4}\right), \left(-\frac{a_2}{2}, b_2 - \frac{a_2^2}{4}\right), \left(-\frac{\hat{b}}{\hat{a}}, \bar{b} + \frac{\hat{b}^2}{\hat{a}^2} - \frac{\bar{a}\hat{b}}{\hat{a}}\right) \right\}.\tag{5.64}$$

The first two points were of course to be expected, since these are the branch points from the individual RDAs. We may already conclude that the system is absolutely unstable if one of the components is, as could have been expected.

Let us study the additional branch point $(\nu_c^*, \lambda_c^*) = \left(-\frac{\hat{b}}{\hat{a}}, \bar{b} + \frac{\hat{b}^2}{\hat{a}^2} - \frac{\bar{a}\hat{b}}{\hat{a}}\right)$ in some more detail. This spatial double root corresponds to a collision of an eigenvalue for u_1 with one from u_2 . Intuitively, this should have no effect, since the subsystems are independent of each other. In order to see this, we need to recall our analysis of the asymptotic behaviour of (5.14): Formally, the solution is given by

$$\mathbf{u}(\nu, \lambda) = \left(\frac{1}{\chi(\nu, \lambda)} \begin{bmatrix} \chi_2(\nu, \lambda) & 0 \\ 0 & \chi_1(\nu, \lambda) \end{bmatrix} \right) \mathbf{u}_0(\nu).\tag{5.65}$$

Since $\chi_1(\nu_c^*, \lambda_c^*) = \chi_2(\nu_c^*, \lambda_c^*) = 0$, the matrix *does* vanish in (ν_c^*, λ_c^*) and in its vicinity we have with $\delta_\lambda := (\lambda - \lambda_c^*)$, $\delta_\nu := (\nu - \nu_c^*)$:

$$\mathbf{u}(\nu, \lambda) = \left(\frac{1}{\frac{1}{2}\chi_{\lambda\lambda}\delta_\lambda^2 + \chi_{\lambda\nu}\delta_\lambda\delta_\nu + \frac{1}{2}\chi_{\nu\nu}\delta_\nu^2} \left(\begin{bmatrix} \chi_2 & 0 \\ 0 & \chi_1 \end{bmatrix}_\lambda \delta_\lambda + \begin{bmatrix} \chi_2 & 0 \\ 0 & \chi_1 \end{bmatrix}_\nu \delta_\nu \right) \right) \mathbf{u}_0(\nu) \quad (5.66)$$

where all partial derivatives are evaluated in (ν_c^*, λ_c^*) . Note that $\chi_\lambda = 0$. Expansion into partial fractions shows that δ_λ appears with a power of 1, not $\frac{1}{2}$ like in the factor f in (5.16). Therefore, this “artificial” branch point does not dominate the long-time behaviour even if it is to the right of the other two.

We may get an intuition for this if we compare its Taylor expansion to that of a “proper” branch point: In the “degenerate” case, the spatial eigenvalues leave the collision without having interacted. When they are numbered by real part, the two eigenvalues merely change their indices and thus only temporarily pinch the integration contour. On the other hand, in the “proper” case, the spatial eigenvalues are leaving orthogonally to their arrival, thereby destroying the contour.

Since we were able to rule out the additional branch point, the system is convectively unstable if one RDA is convectively unstable and the other one is stable or convectively unstable (Fig. 5.7, Fig. 5.6). As discussed in Sec. 5.2.3, this classification may not be desired since it does not take into account the direction of the convection.

Transient/absolute instability If we consider the two-component system, both spectra have to be optimised with the same weight $\eta(\lambda)$. Equivalently to what we saw for absolute instability, the system is obviously remnantly unstable if at least one RDA is.

As discussed in Ex. 5.1, application of an exponential weight η moves the real part of the essential spectrum by $\eta(\eta + a)$, so only weights between $-a$ and 0 pull the spectrum back, as desired. From this it directly follows that the system will be *remnantly* (but not absolutely!) unstable if $a_1 \cdot a_2 < 0$, i.e. if the convective terms are directed in opposing directions.

Conversely, if $a_1 \cdot a_2 > 0$ and b_1, b_2 are sufficiently small, it is possible to pull both spectra to the left of the imaginary axis with the same weight.

However it is possible that the system is remnantly unstable even if both systems are transiently unstable and the convective terms are directed in the same direction: For $b_{1,2} = \frac{a_{1,2}^2}{4} - \varepsilon$, we would need a weight that is arbitrarily close to $-\frac{a_{1,2}}{2}$ (Fig. 5.5).

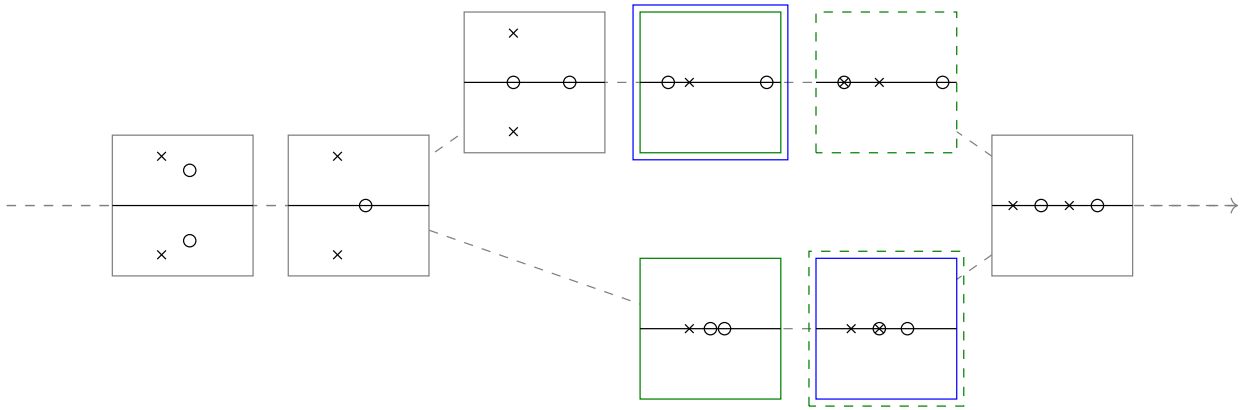


Figure 5.5: Distribution of spatial roots in the two-component system for $\lambda \in \mathbb{R}$. Depending on the parameters, two cases can be considered. Green: the branch point $\max_{i=1,2} (a_i^2/4 - b_i)$ is decisive for convective/absolute instability. The collision between spatial roots of the subsystems (dashed outline) is not relevant here. Blue: for transient/remnant instability, we need to look for the rightmost point with $\text{Re}(\nu_2) = \text{Re}(\nu_3)$

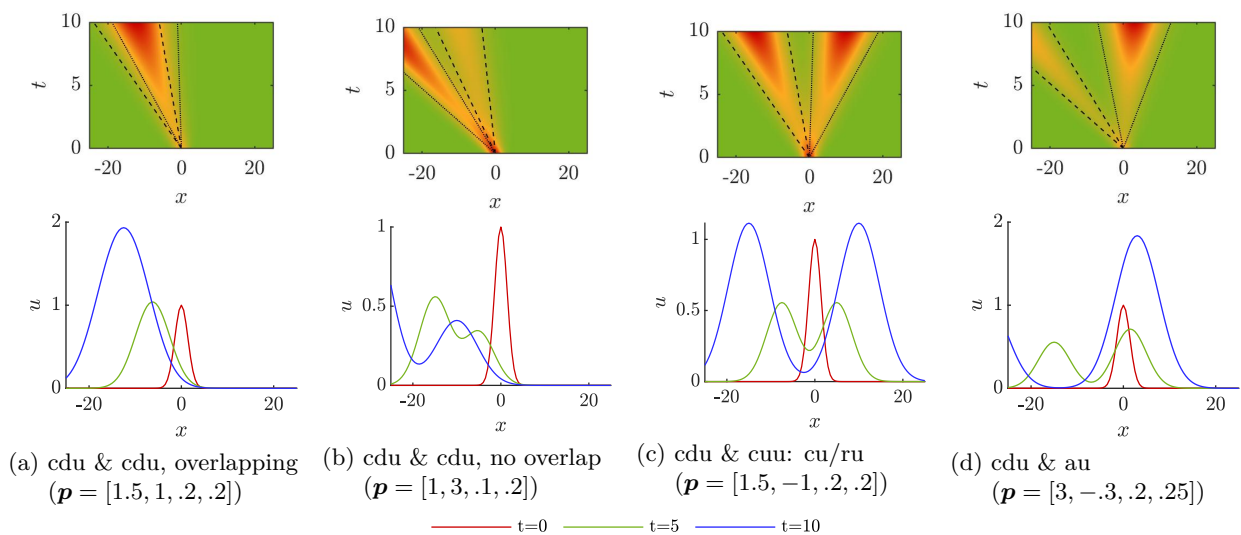


Figure 5.6: Examples from instability classes for two-component reaction-diffusion-advection system with two species and parameter vector $\mathbf{p} = [a_1, a_2, b_1, b_2]$. Displayed is the mean $u = \frac{1}{2}(u_1 + u_2)$ of the components.

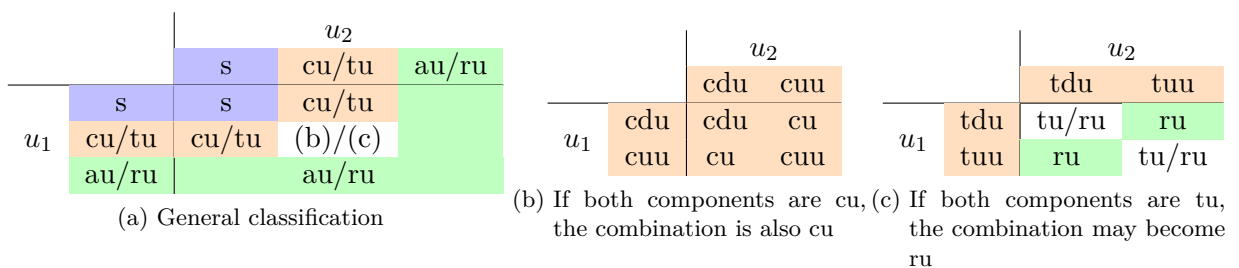


Figure 5.7: Instability classification for two-component system

5.4.2 Traffic flow models

5.4.2.1 Microscopic models

Example 5.3 (Instability classification for the Bando model)

The classification of the parameter space for the Bando model can be performed by numerical continuation of the relevant branch points (Fig. 5.8). The cuu-au-boundary is identical to the one obtained in MITARAI and NAKANISHI (2000a), whereas the lower au-cdu-boundary was not found there. The shape of the diagram is qualitatively very similar to the example presented in WARD and WILSON (2011) for the Bando model with aggressive drivers. Tests with parameter values from the different regions illustrate the meaning of the classification (Fig. 5.10). Calculation of the absolute spectra for these parameters verifies that the rightmost points of the absolute spectra are given by the pinching branch points (5.9). Classification into transiently and remnantly unstable parameter regions yields the same results in this case.

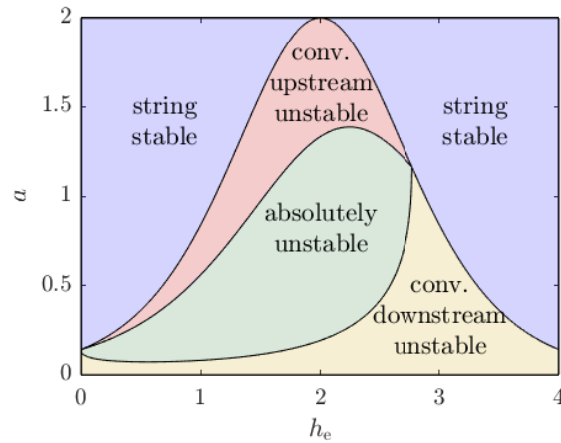


Figure 5.8: Instability classification in parameter space for the microscopic Bando model

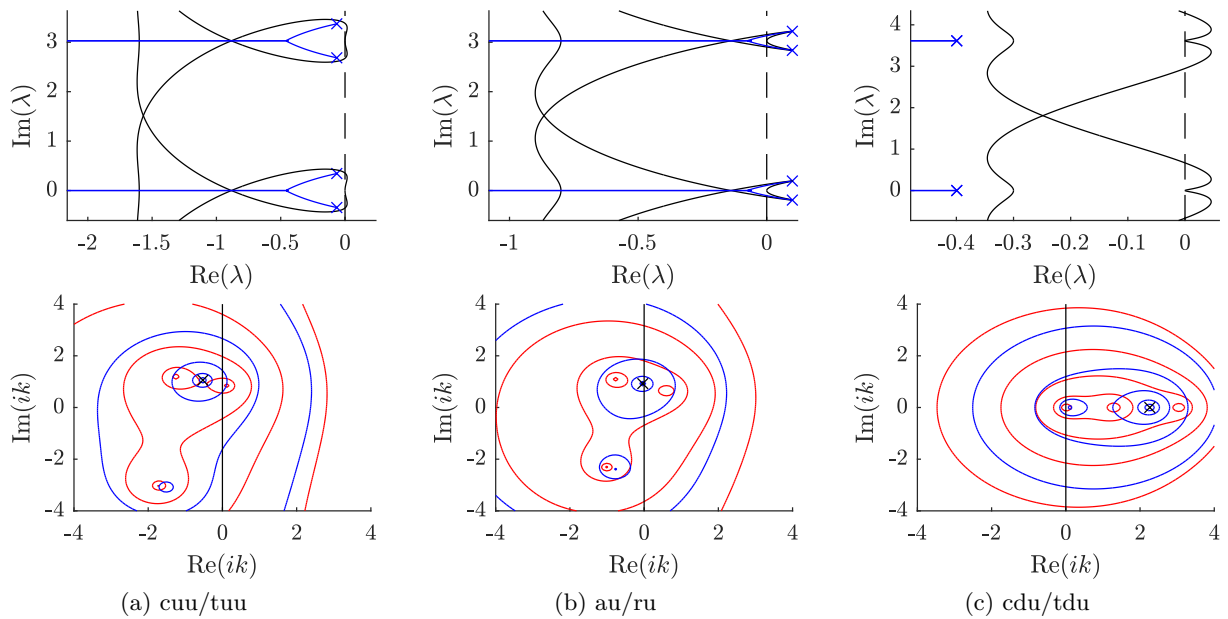


Figure 5.9: Top row: spectra (black), branch points λ_c satisfying the pinching condition (crosses) and absolute spectra (blue) for the microscopic Bando model. Bottom row: Double spatial eigenvalues ξ_c (crosses) and contour lines of $\log|\chi(\lambda_c, \xi)|$ (blue) and $\log|\chi(\lambda_c + \varepsilon, \xi)|$ (red), demonstrating that the pinching condition is satisfied. Note the triple points in $\lambda \approx -0.4$ in (a) and $\lambda \approx -0.1$ in (b). In (c), choosing a higher value of ε would move the two leftmost spatial eigenvalues to the left of the imaginary axis but obscure the fact that the second and third eigenvalue are meeting in ξ_c for $\lambda = \lambda_c$.

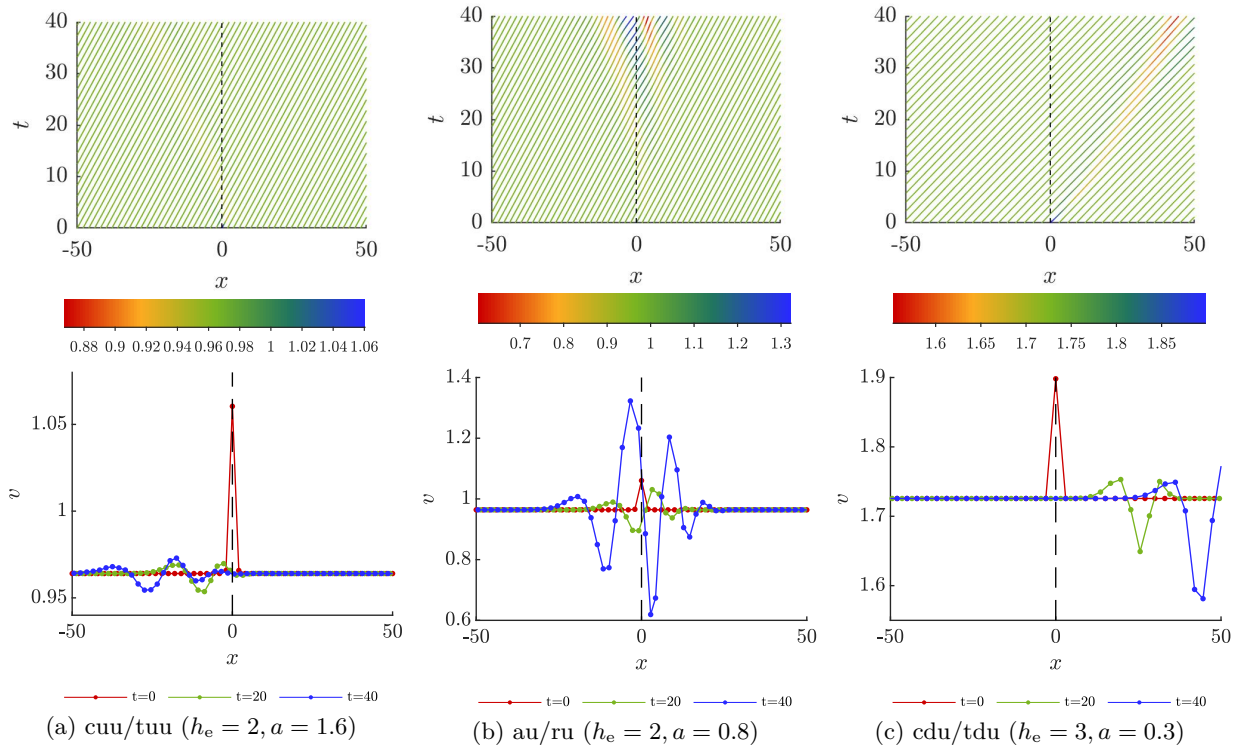


Figure 5.10: Examples from instability classes (see Fig. 5.8) for the microscopic Bando model: In the Eulerian frame, a small initial perturbation localised in $x = 0$ at initial time evolves as predicted by the classification

Example 5.4 (A model with two lanes)

We demonstrate that in a traffic flow context, we may encounter situations where the distinction between transient and convective instability becomes relevant, similar to the RDA example in Ex. 5.2.

Consider a situation where two different kinds of vehicles use adjacent lanes. On each lane, we impose Assumptions 2.1 and 2.2 regarding the indices, i.e. there is no overtaking or changing of lanes. However, there may still be interactions when the vehicles come close or pass each other. Such an interaction depends of course on the context and may be modelled in different ways. Maybe the simplest form is to assume that, due to the narrowness of the road, a high density of one class slows down the other and vice versa. This may be the case everywhere or only on some sections of the road.

Within this example, we denote the different species by subscripts 1, 2 and write the vehicle index as an argument: $x_i(j, t)$ is the position at time t of vehicle j from species i , which in turn has the index set J_i .

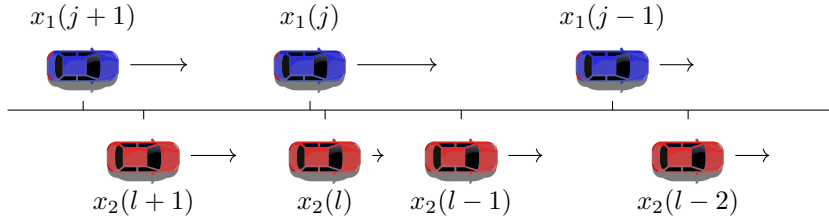


Figure 5.11: Setup for two-lane model. In the depicted situation, the headway $h_{1 \rightarrow 2}$ that vehicle j observes on the adjacent lane is calculated as a weighted average between the distances $x_2(l-1) - x_2(l)$ and $x_2(l) - x_2(l+1)$, ensuring continuity when $x_1(j)$ overtakes $x_2(l)$ or is itself overtaken by $x_2(l+1)$

For fixed t and $J_{1,2} = \mathbb{Z}$, the function

$$l_{1 \rightarrow 2} : J_1 \rightarrow J_2$$

$$j \mapsto \min_{l \in J_2} \{l \in J_2 : x_2(l, t) \geq x_1(j, t)\}$$

is well-defined and returns the index l of the vehicle on lane 2 that is next to or directly ahead of vehicle j on lane 1; on the circular road, we may define an analogous function in a straightforward fashion. The function $l_{2 \rightarrow 1} : J_2 \rightarrow J_1$ is defined symmetrically.

The vehicle at position x_j cuts the headway $h_2(l_{1 \rightarrow 2}(j))$ by a certain ratio $\alpha_{1 \rightarrow 2}(j)$

$$\alpha_{1 \rightarrow 2}(j) := \frac{x_2(l_{1 \rightarrow 2}(j)) - x_1(j)}{x_2(l_{1 \rightarrow 2}(j)) - x_2(l_{1 \rightarrow 2}(j) + 1)} \quad (5.67)$$

which we may use for a weighted average between $h_2(l_{1 \rightarrow 2}(j))$ and $h_2(l_{1 \rightarrow 2}(j) - 1)$:

$$h_{1 \rightarrow 2}(j) := \alpha_{1 \rightarrow 2}(j) \cdot h_2(l_{1 \rightarrow 2}(j)) + (1 - \alpha_{1 \rightarrow 2}(j)) \cdot h_2(l_{1 \rightarrow 2}(j) - 1). \quad (5.68)$$

For this example, we prefer this approach over alternative ways along the lines discussed in Sec. 3.3.1 because it is relatively easy to implement and continuous when the vehicles move relative to each other. However, the exact definition is not crucial here.

We may now set

$$\dot{v}_1(j) = a_1 [W_1(h_1(j), h_{1 \rightarrow 2}(j), x_1(j)) - v_1(j)] \quad (5.69a)$$

$$\dot{v}_2(j) = a_2 [W_2(h_2(j), h_{2 \rightarrow 1}(j), x_2(j)) - v_2(j)] \quad (5.69b)$$

where $W_{1,2}$ are modified optimal velocity functions with

$$W_1(h_1, h_2, x_1) = V(h_1) \cdot (1 - \varepsilon \cdot f(h_2) \cdot g(x_1)); \quad (5.70)$$

here, $f(h)$ describes how the optimal speed is reduced by the headway on the adjacent lane and $g(x)$ describes the heterogeneity of the narrowness along the road. With $f \equiv 1$, this reduces to two independent versions of the bottleneck model from GASSER and WERNER (2010).

Assume now that the interaction takes only place in a certain region, i.e. $g(x)$ has compact

support. Away from the narrow regions, the lanes behave independently and perturbations behave like discussed in Ex. 5.3.

Most interesting is the coupling of two lanes that are convectively up- and downstream unstable when considered separately at several points. In combination, their behaviour will be remnantly unstable, as in Ex. 5.2: The slightest coupling will cause a perturbation that is convected downstream on one lane to reappear on the other lane, where it will travel upstream and “re-ignite” a perturbation on the downstream lane at the next coupling. This means that part of the perturbation is trapped and amplifies between the couplings, similar to the situation in a laser (Fig. 5.12).

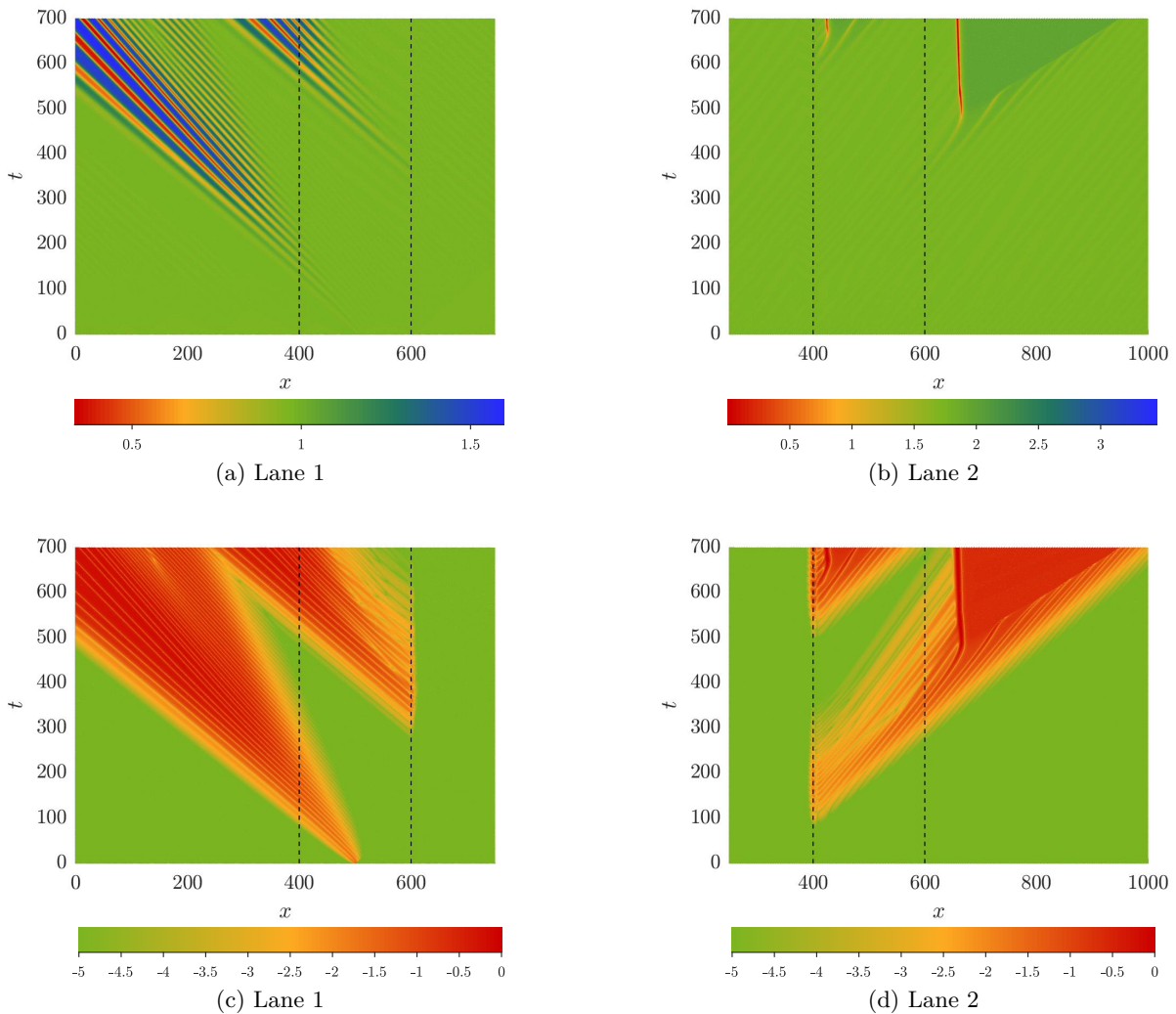


Figure 5.12: Results of a two-lane simulation on a circular road with $L = 100$ and couplings at $x = \frac{L}{2} \pm \frac{L}{10}$. Subfigures (a,b) and (c,d) show velocity v and $\log|v - v_e|$, respectively.

A situation of special interest is that of two lanes with opposing directions. If the individual lanes are convectively upstream unstable in this scenario, the system will be remnantly unstable provided there are couplings between the lanes, which can hardly be avoided in practice.

5.4.2.2 Macroscopic models

Example 5.5 (Instability classification for the models linked to the Bando model)

For the low-order macroscopic equivalents to the Bando model we can find the boundaries between convectively and absolutely unstable parameter regions analytically:

With $f_h = aV'(h_e) =: a\beta$, $f_v = a$, and $f_{\Delta v} = 0$ for the Bando model, (5.24) becomes

$$(\lambda - cz)(\lambda - cz + a) - a\beta \left(z + \frac{z^2}{2} \right). \quad (5.71)$$

Then setting $\frac{\partial \chi}{\partial z} = 0$ yields

$$\lambda - cz = -\frac{a}{2} + d(1 + z), \quad \text{where } d := -\frac{a\beta}{2c}. \quad (5.72)$$

We plug (5.72) into (5.71); the result

$$d^2(1 + z)^2 - \frac{a^2}{4} - a\beta \left(z + \frac{z^2}{2} \right) = 0 \quad (5.73)$$

is then solved for z :

$$z = -1 \pm \sqrt{1 - \frac{d^2 - \frac{a^2}{4}}{d^2 - \frac{a\beta}{2}}}. \quad (5.74)$$

Using $\lambda = (d + c)z - \frac{a}{2} + d$, we easily see that a pair of purely imaginary branch points crosses the imaginary axis for $a = 2c$ (au-cdu). However, one of these eigenvalues returns if the line $d^2 = \frac{a\beta}{2}$ is crossed. This corresponds to $a = \frac{c^2}{\beta}$ (au-cuu). The resulting classification is displayed in Fig. 5.13(a).

For the Lagrangian frame we have to set $c = 0$. Starting again from (5.71), we have $\frac{\partial \chi}{\partial z} = 0$ for $z = -1$ and $\lambda^2 + a\lambda + \frac{a\beta}{2} = 0$, leading to branch points $\lambda_{\pm} = -\frac{a}{2} \pm \sqrt{\frac{a^2}{4} - \frac{a\beta}{2}}$. Note that when the radicant is multiplied by $\frac{4}{a}$, we recover the string instability criterion, meaning that the radicant is negative for all relevant parameter values. So all of these are convectively unstable in a frame that is moving with the vehicles.

For the higher-order models the classification can be done by numerical continuation of the branch points satisfying the pinching condition. Since they have the same characteristic polynomial (cf. Ex. 4.6), the classification for ND and FLD yields the same results (Fig. 5.13); however, the classification for the IHD is only marginally different (Fig. 5.17). Simulations at the representative parameter values lead to very similar results for ND (Fig. 5.15), FLD (Fig. 5.16), and IHD (Fig. 5.18).

Overall we may conclude that, while the absolutely unstable parameter region starts out notably smaller in the first-order macroscopic models (Fig. 5.13 (a), Fig. 5.17 (a)) than in the microscopic model (Fig. 5.8), already at third order (Fig. 5.13 (c), Fig. 5.17 (c)) the classifications are visually indistinguishable from each other.

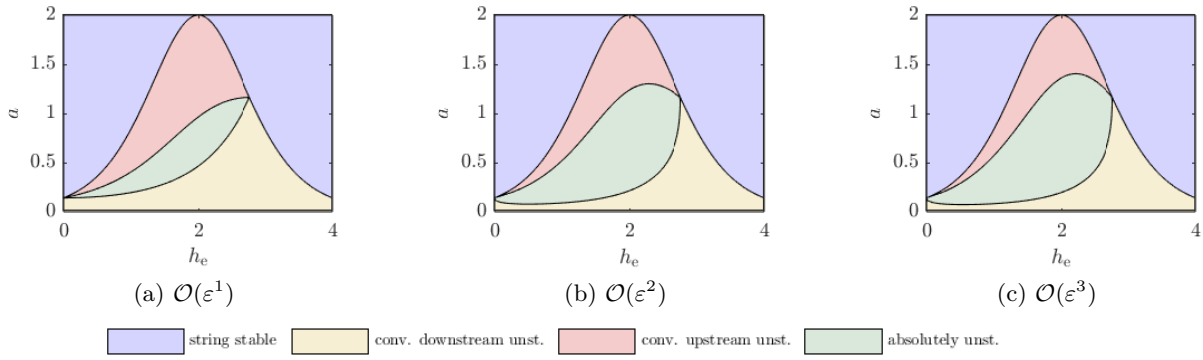


Figure 5.13: Stability classification in parameter space for ND/FLD Bando model equivalents up to third orders in ε . The classification in (a) was obtained analytically, (b) and (c) were classified by numerical continuation of branch points

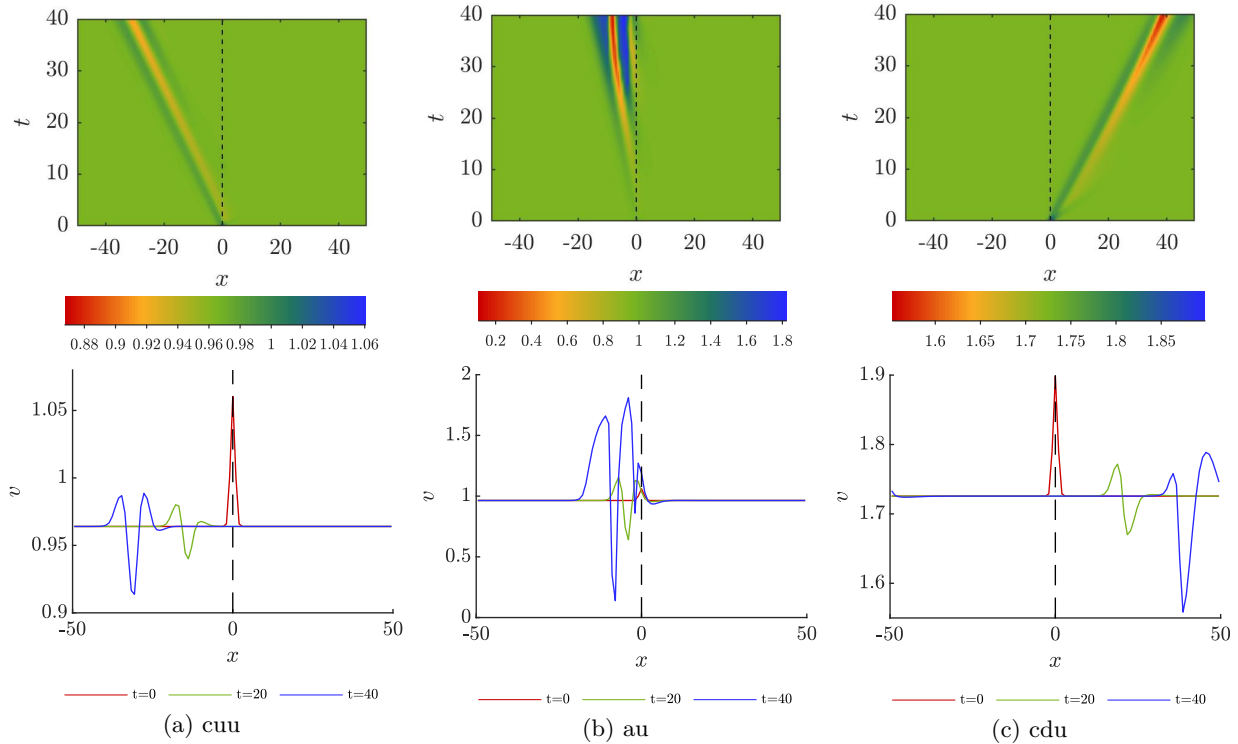


Figure 5.14: Examples from instability classes for $\mathcal{O}(\varepsilon^1)$ -ND/IHD Bando model equivalent; same parameter values as in Fig 5.10 (cf. Appendix A, Fig. 1 for density plots)

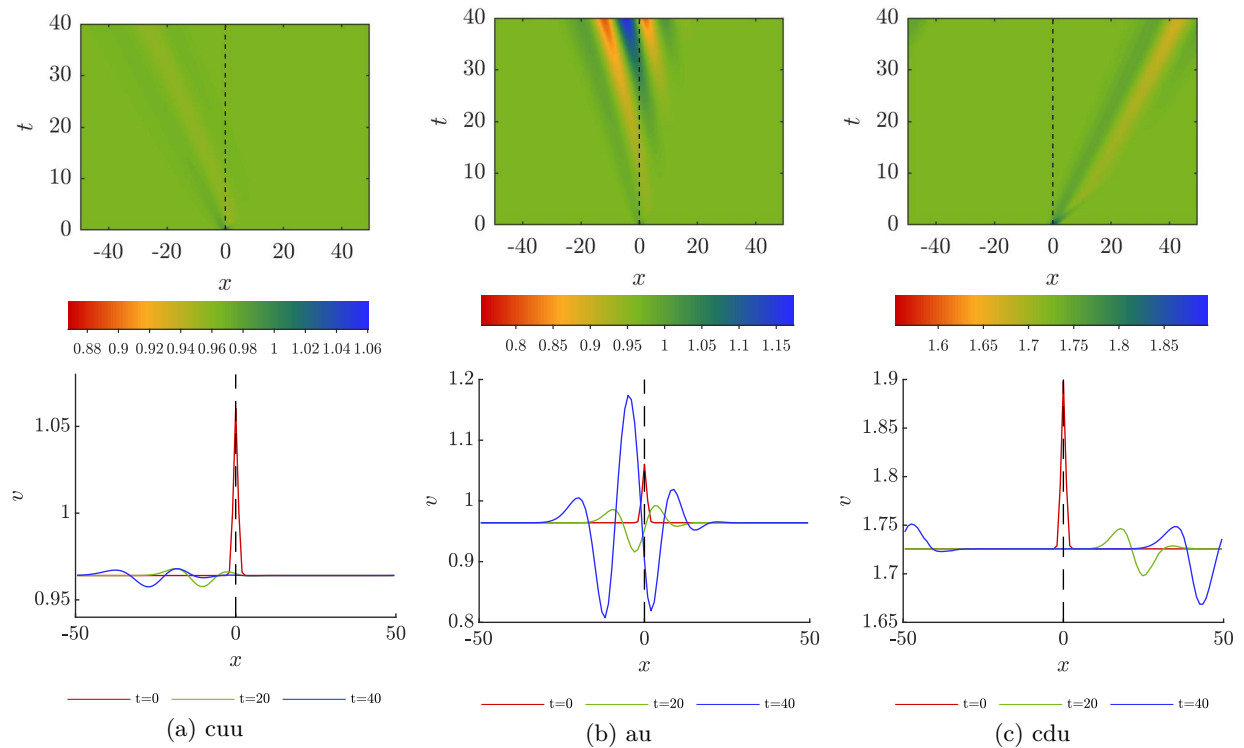


Figure 5.15: Examples from instability classes for $\mathcal{O}(\varepsilon^2)$ -ND Bando model equivalent, (cf. Appendix A, Fig. 2 for density plots)

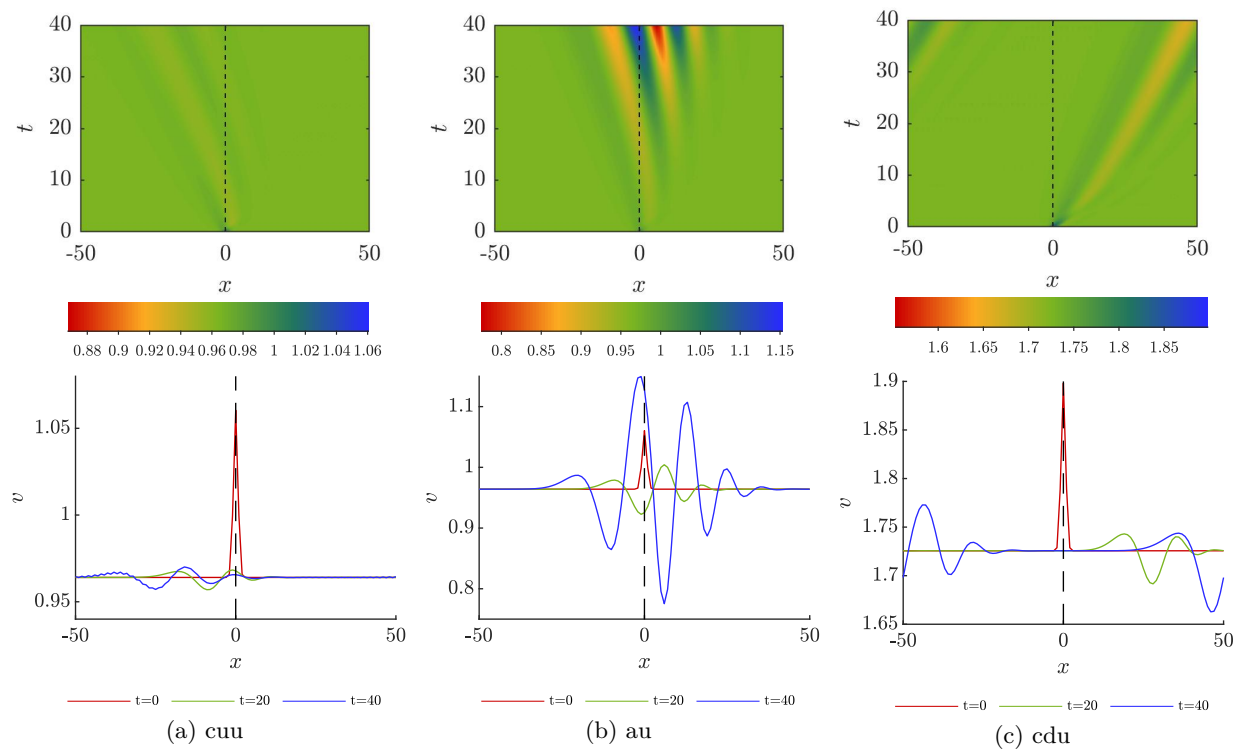


Figure 5.16: Examples from instability classes for $\mathcal{O}(\varepsilon^2)$ FLD Bando model equivalent; same parameter values as in Fig 5.10 (cf. Appendix A, Fig. 3 for density plots)

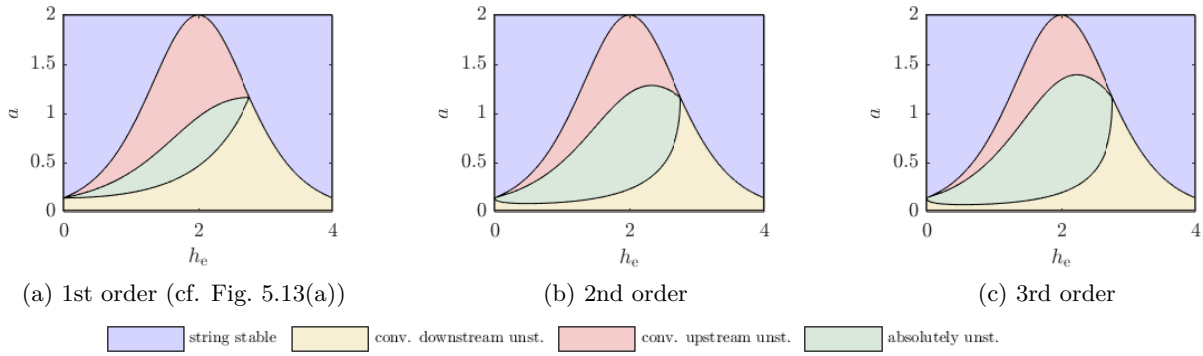


Figure 5.17: Stability classification in parameter space for IHD Bando model equivalents for different orders in ε

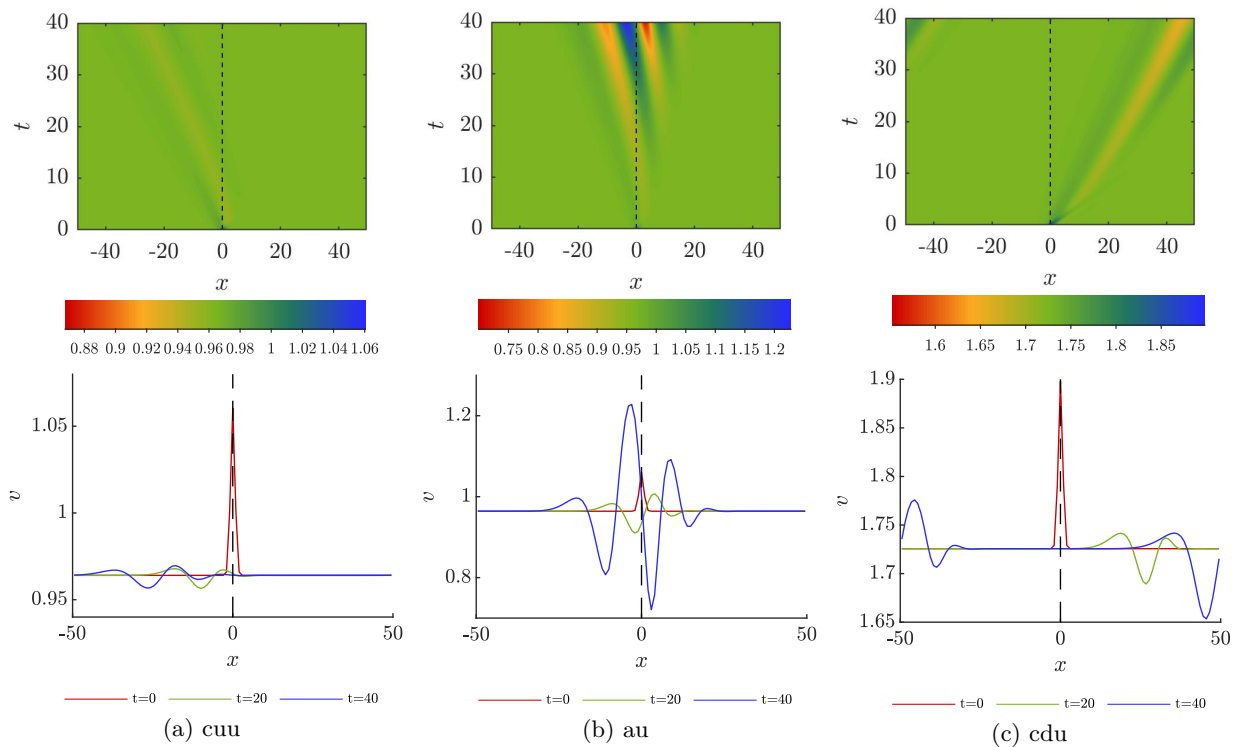


Figure 5.18: Examples from instability classes for $\mathcal{O}(\varepsilon^2)$ -IHD Bando model equivalent; same parameter values as in Fig 5.10 (cf. Appendix A, Fig. 4)

III Shift-invariant solutions

Chapter 6

Finding solutions

In this chapter, we are studying a special kind of travelling wave solutions in which the vehicle trajectories are shifted copies of each other with a constant translation vector between them.

Such solutions are typical for periodic solutions on the circular road. In Sec. 6.1 we are going to recall some of the existing theory on periodic solutions on the circular road and try to generalise it to the infinite lane with $J = \mathbb{Z}$. This will also help us to find heteroclinic solutions, a topic we are going to discuss in Sec. 6.2.

Much of the material presented in this chapter is currently under review in similar form in VON ALLWÖRDEN and GASSER (submitted 2018).

6.1 Periodic solutions

6.1.1 Circular road

The existence and continuation of periodic solutions on the circular road has been discussed for the Bando model and variants thereof in GASSER et al. (2004), GASSER et al. (2007), and TOMOEDA et al. (2018). The effects of reaction-time delay in this context have been studied in detail in OROSZ and STÉPÁN (2004, 2006); OROSZ et al. (2004b, 2005, 2009), and KISS et al. (2019).

We emphasise that the solutions of interest will be periodic in h and v . In our setup $x_j \in \mathbb{R}$ should be monotonically growing and the circular road is modelled via the boundary condition, so periodic x would not be meaningful. Besides, due to assumption 2.5 on the homogeneity of the road, the individual vehicles have no information about the circle length.

On the circular road, linear stability of the quasistationary solutions is lost through a complex conjugated pair of eigenvalues crossing the imaginary axis. However, before the Hopf theorem can be applied, the system needs to be reformulated in order to avoid the singular eigenvalue that is due to the translational invariance along the road. This can be done by transforming it into a variant of h, v -coordinates. The most intuitive way to do this may be to use the identity

$h_N = l - \sum_{j=1}^{N-1} h_j$ to eliminate the ODE for the N -th vehicle. Alternatively, we might also perform a discrete Fourier transform on h and drop the trivial ODE for the evolution of the average, as discussed in Sec. 4.1.4.1.

The Hopf theorem guarantees a family of periodic solutions in the neighbourhood of the bifurcation point. While there is little hope of writing the periodic solutions down analytically in general, they take a very simple form in the linear model: For an eigenvalue $i\omega$ with $\omega \in \mathbb{R}$ of $S\left(\exp\left(\frac{2\pi ik}{N}\right)\right)$ from (4.5) with eigenvector \mathbf{w} , the family of periodic solution is given by

$$[h, v]^\top(j, t) = [h_e, v_e]^\top + A \cos\left(\omega t - \frac{2\pi k}{N} j\right) \operatorname{Re}(\mathbf{w}), \quad A \in \mathbb{R}^+. \quad (6.1)$$

We observe that each car does the same as its preceder, only Δt time units later and at a position shifted by Δx units. Formally, we may write

$$[h, v]^\top(j, t) = [h, v]^\top(j + 1, t + \Delta t), \quad x(j, t) = x(j + 1, t + \Delta t) + \Delta x. \quad (6.2)$$

Comparing this with the circular road condition

$$x(N + 1) = x(1) + Nh_e, \quad (6.3)$$

we directly obtain the necessary condition

$$kT = \Delta t \cdot N, \quad k \in \mathbb{N}. \quad (6.4)$$

For a periodic solution with $x(j, t) = x(j, t + T)$ and $L := \int_0^T v(j, t) dt$ we can deduce

$$\Delta x + \frac{L}{T} \Delta t = h_e \quad (6.5)$$

without using the circular road condition (6.3).

Let us briefly review the basic idea behind the continuation of periodic solutions. In practice, this should be done in terms of the reduced $2N - 1$ -dimensional system, but for now the additional terminology would only draw the attention from the main points.

The periodic solutions can be characterised by their initial values $[h, v]^\top(j, 0) \in \mathbb{R}^{2N}$, a parameter vector $\mathbf{p} \in \mathbb{R}^m$, and the time period $T \in \mathbb{R}^+$. To have uniqueness, we need to impose a phase condition, e.g. $h(1, 0) = h_e$, which can be written in standard form as $g([h, v]) \stackrel{!}{=} 0$ for some function $g : \mathbb{R}^{2N} \rightarrow \mathbb{R}$. Let

$$\Phi^t : \mathbb{R}^{2N+m} \times \mathbb{R}^+ \rightarrow \mathbb{R}^{2N+m} \quad (6.6)$$

be the evolution operator for the traffic model ODE system enhanced by the trivial ODE $\dot{\mathbf{p}} = 0$ for the parameter. We are then looking for roots of a function $F([h, v], \mathbf{p}, T) = 0$ defined as

$$F : \mathbb{R}^{2N} \times \mathbb{R}^m \times \mathbb{R}^+ \rightarrow \mathbb{R}^{2N+m}, \quad ([h, v], \mathbf{p}, T) \mapsto \begin{bmatrix} \Phi^T([h, v, \mathbf{p}]) - [h, v, \mathbf{p}]^\top \\ g([h, v]) \end{bmatrix} \quad (6.7)$$

Table 6.1: Popular continuation software packages

Name	Language	Developers	since	current version
AUTO	Fortran / C	DOEDEL et al.	1976	AUTO-07p
MATCONT	Matlab	DHOOGHE et al.	2003	7.1
DDE-BIFTOOL	Matlab	ENGELBORGHES et al. and J. SIEBER	2001	3.1.1
COCO	Matlab	DANKOWICZ and SCHILDER	2013	2017

To extend a given branch of periodic solutions, we can now calculate the Jacobian DF of F in its last point, and go into the direction(s) of its null space.

As a starting point, we may use the stationary solution $h_j \equiv h_e, v_j \equiv v_e$ in the bifurcation point with trivial amplitude 0 and time period $T = \frac{2\pi k}{\omega}$.

For numerical continuation, $D\Phi^T$ in DF can be calculated by integrating the Jacobian of the acceleration function f along the trajectory. We can then use the extrapolation in the direction of the null space as an initial guess for $F = 0$, which is solved together with a step-length constraint like

$$\|\mathbf{p}_{\text{new}} - \mathbf{p}_{\text{old}}\| - \varepsilon = 0$$

by standard algorithms.

In praxis, this is taken care of by dedicated continuation software (Tab. 6.1). In a traffic context, AUTO2000 has been used e.g. in GASSER et al. (2004), MATCONT in BURIC and JANOVSKY (2008), and DDE-BIFTOOL by OROSZ et al..

Proposition 6.1 If the initial condition has property (6.2), the above procedure yields a curve of periodic solutions that do so, too.

Proof: If $([h, v], \mathbf{p}, T)$ satisfies (6.2), it is a root of F by construction, but also of

$$\begin{aligned} \tilde{F} : \mathbb{R}^{2N} \times \mathbb{R}^m \times \mathbb{R}^+ &\rightarrow \mathbb{R}^{2N+m} \\ ([h, v], \mathbf{p}, T) &\mapsto \begin{bmatrix} \Phi^{T/N}([h, v, \mathbf{p}]) - [\text{Sh} \cdot [h, v], \mathbf{p}]^\top \\ g([h, v]) \end{bmatrix} \end{aligned} \quad (6.8)$$

We need to show that the null spaces of the Jacobians of F and \tilde{F} are the same.

Since g is unchanged, this reduces to comparing how $\Phi^{T/N}$ and Φ^T deform their tangential spaces. For the operator $\Phi^{T/N}$, a small initial perturbation $[\delta h, \delta v, \delta \mathbf{p}]$ of the arguments will be mapped to a deformation $J\Phi^{T/N} \cdot [\delta h, \delta v, \delta \mathbf{p}]$ in the output. An additional deformation δT in the period T will add $\delta T \cdot \frac{\partial}{\partial T} \Phi^{T/N} = \delta T \cdot \frac{1}{N} f([h, v, \mathbf{p}](T/N))$. The idea is now to look for a subspace such that the effect of the error is neutralised by the (linear) shift operator Sh.

(For brevity, write $f(T/N)$, $J\Phi^{T/N}(t)$, ... instead of $f([h, v, \mathbf{p}](T/N))$, $J\Phi^{T/N}([h, v\mathbf{p}](0))$, ...)

$$[\text{Sh}[\delta h, \delta v], \delta \mathbf{p}] = J\Phi^{T/N}(0) \cdot [\delta h, \delta v, \delta \mathbf{p}] + \delta T \cdot \frac{1}{N} f(T/N). \quad (6.9)$$

If we evolve further, the effect of the initial perturbation will grow and we need to compare with

the effect of the two-shift:

$$\begin{aligned} [\text{Sh}^2[\delta h, \delta v], \delta \mathbf{p}] &= J\Phi^{T/N}(T/N) \cdot \left(J\Phi^{T/N}(0) \cdot [\delta h, \delta v, \delta \mathbf{p}] + \delta T \cdot \frac{1}{N} f(T/N) \right) + \delta T \cdot \frac{1}{N} f(2T/N) \\ &= J\Phi^{2T/N}(0) \cdot [\delta h, \delta v, \delta \mathbf{p}] + \delta T \cdot \frac{2}{N} f(2T/N) \end{aligned} \quad (6.10)$$

where in the last equality we used that $J\Phi^{T/N} \cdot f(t) = f(t + T/N)$.

Iterating this, we see that

$$[\text{Sh}^N[\delta h, \delta v], \delta \mathbf{p}] = J\Phi^T(0) \cdot [\delta h, \delta v, \delta \mathbf{p}] + \delta T \cdot f(T). \quad (6.11)$$

It is also clear that this procedure may be performed backwards. \square

More branches of periodic solutions emerge as more pairs of eigenvalues cross the imaginary axis. With the notation introduced above, we may define the family of shift-invariant periodic solutions on the circular road for fixed $N \in \mathbb{N}$ as

$$\mathcal{P}_{\text{circ}}(N) := \left\{ (\mathbf{p}, [h_0, v_0], T) \in \mathbb{R}^m \times \mathbb{R}^{2N} \times \mathbb{R}^+ : \tilde{F}([h_0, v_0], \mathbf{p}, T) = 0 \right\}. \quad (6.12)$$

6.1.2 Infinite lane

Now let $\mathcal{P}_{\text{line}}$ denote the set of periodic solutions for $J = \mathbb{Z}$. We can show that $\mathcal{P}_{\text{line}} \neq \emptyset$ by mapping the periodic solutions from the circle into it by an appropriate function

$$\psi : \bigcup_{N \in \mathbb{N}} \mathcal{P}_{\text{circ}}(N) \rightarrow \mathcal{P}_{\text{line}}.$$

It is easy to see that the projection of the image of ψ to the coordinates $(\mathbf{p}, \Delta t)$ is dense near the curve of bifurcation points.

The obvious question now is whether we can complete the family of curves of periodic solutions to a hypersurface in the extended parameter space in the sense of the completion of \mathbb{Q} to \mathbb{R} . The fact that condition (6.4) for commensurability of Δt and T is not necessary on the infinite lane suggests that this may be possible. The new solutions with $\frac{\Delta t}{T} \notin \mathbb{Q}$ would then be unique to the infinite lane. This is related to the question whether closeness in the parameters $(\mathbf{p}, \Delta t, T)$ also implies closeness in the velocity profiles. If we construct a sequence of periodic solutions on the circular road in order to approximate a value $\frac{\Delta t}{T} \notin \mathbb{Q}$, the profiles should be converging in some sense if the completion is to make sense. In order to calculate general solutions with $\frac{\Delta t}{T} \in \mathbb{R}$, we take a step back and remember that, regardless of the system considered, a periodic solution of type (6.2) contains all relevant information within a single trajectory (Fig. 6.1).

So instead of systems with N or even infinitely many vehicles, a natural ansatz is to consider the delay differential equation

$$\dot{h}(t) = v(t + \Delta t) - v(t) \quad (6.13a)$$

$$\dot{v}(t) = f(h(t), v(t), v(t + \Delta t)). \quad (6.13b)$$

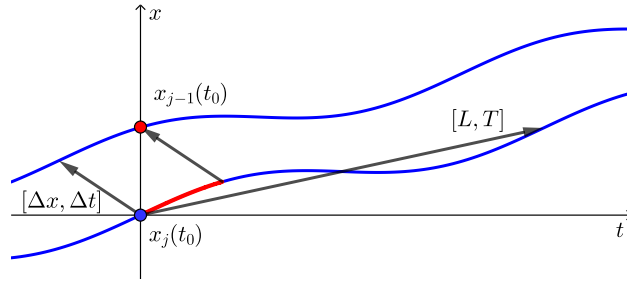


Figure 6.1: Structure of shift-invariant solutions

Similar approaches have been proposed in (STUMPF 2016b) and in (SHEN and SHIKH-KHALIL 2018). While the former does not include a spatial shift, the latter work is studying the first-order in time model $\dot{x}_j = V(x_{j-1} - x_j)$ (cf. Ex. 4.1), and is concerned with heteroclinic solutions (cf. discussion of Ex. 6.5).

The forward delay $\Delta t > 0$ introduces technical difficulties. For practical calculations, it is therefore reasonable to consider a scaled version of (6.13) with inverted time.

The dimensionality is not really lost, but can be considered “hidden” in the initial condition. We stress that the delay we introduce here does not correspond to reaction time, but is used to extract the preceding car’s velocity.

It is easily checked that $h(t) \equiv h_e$, $v(t) \equiv v_e$ is a stationary solution of (6.13) and that the linearisation around it yields the characteristic equation

$$\chi(\lambda) = \lambda (\exp(\lambda \Delta t) f_{v_1} + f_v - \lambda) + f_h (\exp(\lambda \Delta t) - 1) = 0. \quad (6.14)$$

As might be expected from our previous experience, (6.14) has a singular eigenvalue.

In the (h, v) -coordinates on the circular road, we could argue that the singular eigenvalue was due to the fact that the condition $\sum_{j=1}^N h_j \equiv L$ had not been exploited yet. Plugging this into the system, thereby reducing its dimension by one, solved the problem. However, there is no immediate analogy to this procedure possible here.

Since we are exploiting the shift-invariant structure (6.2) in (6.13), the more natural choice in this case is to replace $h(t)$ in (6.13b) by

$$h(t) = x(t + \Delta t) + \Delta x - x(t) = \Delta x + \int_0^{\Delta t} v(\theta + \Delta t) d\theta \quad (6.15)$$

and drop the obsolete (6.13a), obtaining

$$\dot{v}(t) = f \left(\int_0^{\Delta t} v(t + \theta) d\theta + \Delta x, v(t), v(t + \Delta t) \right). \quad (6.16)$$

In some sense, this can of course be seen as an analogy to the procedure applied on the circular

road. For a periodic solution with $v(t) = \phi(\frac{t}{T})$, the relation (6.19) between Δx and h_e becomes

$$\Delta x = h_e - v_e \Delta t, \quad (6.17)$$

where $v_e = \int_0^T v(\theta) d\theta$.

The periodic solutions on the infinite lane satisfying (6.2) can then be characterised as roots of

$$G : \mathbb{R}^m \times \mathbb{R}^+ \times \mathbb{R}^+ \times \mathcal{C}_{\text{per}}([0, 1]) \rightarrow \mathcal{C}([0, 1]) \times \mathbb{R}$$

$$(\mathbf{p}, T, \Delta t, \phi) \mapsto \left[\begin{array}{c} \frac{d}{dt} \phi(t/T) - f \left(\Delta x + \int_0^{\Delta t} \phi\left(\frac{t+\theta}{T}\right) d\theta, \phi\left(\frac{t}{T}\right), \phi\left(\frac{t+\Delta t}{T}\right) \right) \\ g(\phi(0)) \end{array} \right], \quad (6.18)$$

where

$$\Delta x = h_e - \Delta t \int_0^1 \phi(\theta) d\theta \quad (6.19)$$

(compare (6.5)) and g is a phase condition. To avoid problems, it is of course reasonable to choose a condition that is related to its counterpart on the circular road in (6.7).

Now we can properly define $\mathcal{P}_{\text{line}}$ in terms of roots of G as

$$\mathcal{P}_{\text{line}} := \left\{ (\mathbf{p}, \Delta t, T, \phi) \in \mathbb{R}^m \times \mathbb{R}^+ \times \mathbb{R}^+ \times \mathcal{C}_{\text{per}}([0, 1]) : G(\mathbf{p}, T, \Delta t, \phi) = 0 \right\}. \quad (6.20)$$

The canonical way to map the periodic solutions on the circle onto $\mathcal{P}_{\text{line}}$ is then

$$\psi : \bigcup_{N \in \mathbb{N}} \mathcal{P}_{\text{circ}}(N) \rightarrow \mathcal{P}_{\text{line}}$$

$$(N, \mathbf{p}, [h_0, v_0], T) \mapsto (\mathbf{p}, \Delta t, T, v_1(t/T + \theta)) \quad (6.21)$$

where $\theta = \theta(N, \mathbf{p}, [h_0, v_0], T) \in \mathbb{R}$ is necessary to map between the phase conditions.

The definition of Δx inherits the frame-dependency from v . The ratio $c = \frac{\Delta x}{\Delta t}$ describes the velocity of the periodic solutions. In particular, for this choice of Δx , the travelling waves are moving downstream for $\Delta x < 0$ and upstream for $\Delta x > 0$ in the road frame. We may compare this distinction with the classification of convective and transient up- and downstream instability we discussed in Sec. 5.2 and 5.3, respectively. While the discussion there was purely linear, the value of Δx captures the nonlinear behaviour of the travelling waves. On the other hand, while the periodic solutions assumed here have a very special structure, the linear discussion applies to small perturbations of the quasistationary state.

In (6.16), we are now considering an integro-delay equation. Its characteristic equation is

$$\chi(\lambda) = \lambda - \begin{cases} \frac{f_h}{\lambda} (\exp(\lambda \Delta t) - 1) + f_v + f_{v_1} \exp(\lambda \Delta t) & \text{for } \lambda \neq 0 \\ f_h \Delta t + f_v + f_{v_1} & \text{for } \lambda = 0 \end{cases}. \quad (6.22)$$

It is easy to check that all purely imaginary eigenvalues $\pm i\omega$ of $S\left(\exp\left(\frac{2\pi ik}{N}\right)\right)$ found on the circular road satisfies (6.22) for $\Delta t = \frac{2\pi k}{N\omega}$.

For a given model and fixed Δt we may check that the eigenvalues $\pm i\omega$ are isolated and that the nondegeneracy condition is fulfilled, which is generically the case so that the Hopf theorem in a form suitable for delay differential equations like e.g. in (FARIA and MAGALHAES 1995) may be applied.

By this procedure we obtain a curve of Hopf points in $(h_e, \Delta t)$ -space in which the Hopf points we know from the circular road are embedded.

To follow the periodic solutions that emerge from the curve of Hopf points through parameter space, we have to use numerical continuation software again. In order to numerically implement this, we invert and rescale time and approximate the integral in (6.16) with a quadrature rule using n different delays.

Let us briefly mention that there are different possibilities to interpret the obtained periodic solutions. If T and Δt are commensurable, the solution is of course feasible for $N = T/\Delta t$ cars on the circular road. This idea can be extended to the rational case where $T/\Delta t = m/n$ with natural numbers m, n : The solution is then feasible for a circular road of appropriate length with m cars, the circle being covered at any given time by n full spatial oscillations.

It can also be shown that a solution that lies close to one of the branches obtained from the circular road with $N := \left\lfloor \frac{T}{\Delta t} \right\rfloor$ yields a solution to the delay differential equation

$$\ddot{x}_\alpha(t) = f((x_{\alpha+1}(t - \tau) - x_\alpha(t)), \dot{x}_\alpha(t), \dot{x}_{\alpha+1}(t + \tau)) \quad (6.23)$$

if the delay is chosen as $\tau := \frac{T}{N} - \Delta t$. Here, τ can be interpreted as a reaction time. The different possibilities to interpret a periodic solution to (6.16) are summarised in Table 6.2.

Table 6.2: Different interpretations to a periodic solution of (6.16) s.t. $x(t + T) = x(t) + l$

		Circular road $x_{N+1} = x_1 + Nh_e$	Infinite lane $\bar{h} = h_e$
ODE (6.13)	solution	$x_j(t) = x(t + j\Delta t) + j\Delta x$	
	condition	$N\Delta t = nT$ $N(h_e - \Delta x) = nl, \quad n \in \mathbb{N}$	$\frac{l\Delta t}{T} + \Delta x = h_e$
DDE (6.23)	solution	$x_j(t) = x(t + j(\Delta t + \tau)) + j\Delta x$	
	condition	$N(\Delta t + \tau) = nT$ $N(h_e - \Delta x) = nl, \quad n \in \mathbb{N}$	$\frac{l(\Delta t + \tau)}{T} + \Delta x = h_e$

6.2 Heteroclinic solutions

Similar to macroscopic models, travelling waves can be expected to occur in microscopic models when a group of faster vehicles approach a slower group from behind. When we think of a queue forming at a red traffic light or the situation at the end of a traffic jam, this behaviour is desirable. For the Bando model, sharp local transitions are characteristic and were already observed in the initial paper BANDO et al. (1995a). On the infinite lane, they dominate the long-term behaviour

for string unstable parameter values (cf. WERNER (2013), see Fig. 1.4(b)). The admissible jumps have been studied in detail in BERG and WOODS (2001).

In the examples for the previous section we observe that periodic solutions on the circle tend to have a special structure as $N \rightarrow \infty$ and “collapse” in a single point of the $\Delta x, \Delta t$ parameter space. The ansatz (6.13) can be seen as a microscopic analogy to a travelling wave ansatz for the macroscopic equations, which is typically made to determine admissible jump solution to the Riemann problem.

In an infinite-dimensional setting, a heteroclinic solution connecting an upstream state u_- with a downstream state u_+ should satisfy (cf. Def. 2.6)

$$u_j(t + \Delta t) = u_{j-1}(t) \tag{6.24a}$$

$$\lim_{t-j\Delta t \rightarrow \pm\infty} u_j(t) = u_{\pm}. \tag{6.24b}$$

Let the limiting states u_{\pm} be characterised by up- and downstream headway h_{\pm} and -velocity v_{\pm} . It is easy to see from a geometrical argument that the shift vector $(\Delta x, \Delta t)$ is given by

$$\Delta t = \frac{h_+ - h_-}{v_+ - v_-} \tag{6.25a}$$

$$\Delta x = \frac{h_+ v_- - h_- v_+}{v_+ - v_-}. \tag{6.25b}$$

We may now compute the speed of the travelling wave as $\frac{\Delta x}{\Delta t} =: c$ and easily see that this is equivalent to the well-known macroscopic jump-condition

$$c = \frac{\rho_+ v_+ - \rho_- v_-}{\rho_+ - \rho_-}. \tag{6.26}$$

In order to find heteroclinic solutions numerically, different approaches are possible:

“Experimentally”, to get a first impression or find an initial guess for an iterative scheme, we may simply simulate a large number of cars with a leader on an infinite lane with initial condition $u_j(0) \equiv u_-$, $j > 0$ and boundary condition $u_0(t) = (h_+, v_+)$. Heteroclinic transitions can then be isolated in the solution by some heuristic. This approach is apparently applied in BERG and WOODS (2001).

Alternatively, we may formulate an approximation to (6.24) for a finite number of cars as a root-finding problem, e.g. in the form

$$F : \mathbb{R}^{2 \cdot (N+1)} \times \mathbb{R}^2 \times \mathbb{R} \rightarrow \mathbb{R}^{2N} \times \mathbb{R}^2 \times \mathbb{R} \times \mathbb{R}^2$$

$$(u_0, \dots, u_N, h_{\pm}, \Delta t) \mapsto \left[\begin{array}{c} \Phi_{u_0 \equiv \text{const}}^{\Delta t} \begin{bmatrix} u_1 \\ \vdots \\ u_N \end{bmatrix} - \begin{bmatrix} u_0 \\ \vdots \\ u_N - 1 \end{bmatrix} \\ h_0 - h_+ \\ h_N - h_- \\ \Delta t - \frac{h_+ - h_-}{v_+ - v_-} \\ g_1(u_0, \dots, u_N) \\ g_2(h_{\pm}, \Delta t) \end{array} \right], \quad (6.27)$$

where g_1 is a phase condition ensuring uniqueness, e.g. $v_{N/2}(0) = \frac{v_+ + v_-}{2}$, and g_2 is a function specifying a “target”, e.g. fixing h_+ to a particular value. Once a first heteroclinic solution has been found, g_2 can be used for continuation.

This approach may be considered “naïve” in the sense that $h_0 = h_+$, $h_N = h_-$ are not good tests if the convergence properties (6.24b) are fulfilled; more sophisticated conditions should be incorporated at this point. However, for N large enough, this approach already gives very satisfactory results in the cases that we studied (Ex. 6.5).

The approach that seems most natural from what we found in Sec. 6.1.2 is to equip the integro-delay ansatz (6.16) with a condition $\lim_{t \rightarrow \pm\infty} v(t) = v_{\pm}$. Conveniently, DDE-BIFTOOL also supports numerical continuation of branches of heteroclinic solutions, where a similar yet more sophisticated approach as in (6.27) is applied (cf. SIEBER et al. 2017).

6.3 Examples

Example 6.1 (Bifurcations on the circular road for fixed N)

We consider the standard Bando model on a circular road with OVF $V(h) = \tanh(h-2) + \tanh(2)$ as before. In this context, models similar to (6.23) have been studied as a reasonable generalisation with reaction time in OROSZ and STÉPÁN (2006) and BANDO et al. (2000). A detailed bifurcation analysis of this system is carried out in GASSER et al. (2004). A different approach for the continuation of periodic solutions using equation-free modeling has been presented in CARTER et al. (2017).

Bifurcations occur for

$$V'(h_e) = \frac{a}{1 + \cos\left(\frac{2\pi k}{N}\right)} \quad (6.28)$$

with $\omega = V'(h_e) \sin\left(\frac{2\pi k}{N}\right)$.

In GASSER et al. (2004), bifurcation diagrams are drawn with the norm of solution over the circle length. Here, we choose the average headway $h_e = \frac{L}{N}$ as a bifurcation parameter for easier comparability across vehicle numbers and use the velocity amplitude as a measure of the periodic solutions (as e.g. in OROSZ et al. (2004b)) to emphasise the symmetry due to the point-symmetry of the OVF around $h_e = 2$, $v_e = \tanh(2)$.

First, we fix the number of cars at $N = 20$ and the sensitivity at $a = 1$ (Fig. 6.2, 6.3). As h_e is varied from 0 to 2, one after another the eigenvalue pairs for $k = 1, \dots, 4$ cross the imaginary axis

from left to right; upon variation from 2 to 4, the eigenvalues pairs return in the opposite order. From each of these bifurcations, a curve of periodic solutions emanates and may be continued numerically (Fig. 6.2(a)). Continuation is done with DDE-BIFTOOL, introducing a trivial delay $\tau = 0$.

To get an idea of the behaviour of the periodic solutions, we consider the solutions from the different branches at a fixed headway $h_e = 1.75$, corresponding to a circle length $l = 35$. In the phase space portrait of the first car (Fig. 6.2(b)) we already see the typical pointed “hysteresis curve” for $k = 1$, while the curves are getting smoother for higher k . Similarly, in the velocity profiles (Fig. 6.2(c)) for the first car we see that the solution for $k = 4$ is still very close to a sinusoidal shape, whereas the $k = 1$ -solution remains close to a lower and a higher state for most of the time and switches rapidly in between. The full trajectory plots for these solutions (Fig. 6.3) show k regions of denser traffic moving in upstream direction; the speed of these “jams” appears to vary only slightly with k .

Example 6.2 (Bifurcations on the circular road for varying N)

Next, we consider the branches emanating from the first bifurcation ($k = 1$) for different numbers of vehicles (Fig. 6.4, 6.5). In the chosen representation, the overall picture appears to be very similar to that in the previous experiment.

The trajectory plots (Fig. 6.5) show a single region of denser traffic moving upstream, where transitions become more pronounced for higher N , as can also be seen from the phase space portrait (Fig. 6.4(b)).

Example 6.3 (Bringing the periodic solutions together)

In order to understand the connection between the branches of periodic solutions for different values of N and k for fixed sensitivity $a = 1$, it is helpful to compare their bifurcation points in terms of their critical headway and the time shift Δt between trajectories, given as $\frac{2\pi k}{N\omega}$, where ω is the imaginary part of the critical eigenvalue pair (Fig. 6.6). We see that the points lie on a curve that may be parametrised by $\kappa = \frac{N}{k}$, $\kappa \in [4, \infty)$; note that the Bando model with $a = 1$ is unconditionally stable for $N \leq 4$.

This curve can also be described as a function from h_e to Δt as follows: As long as $V'(h_e) > \frac{a}{2}$, we can find $\kappa = \kappa(h_e) = \arccos\left(\frac{a}{V'(h_e)} - 1\right)$ satisfying $a = V'(h_e)(1 + c_\kappa)$.

From this we can determine $\omega(h_e) = V'(h_e) \sin(\kappa) = V'(h_e) \sqrt{1 - \left(\frac{V'(h_e)}{a} - 1\right)^2}$ and finally obtain the Hopf curve $\Delta t_c(h_e) = \frac{\kappa(h_e)}{\omega(h_e)}$ in $(h_e, \Delta t)$ -space.

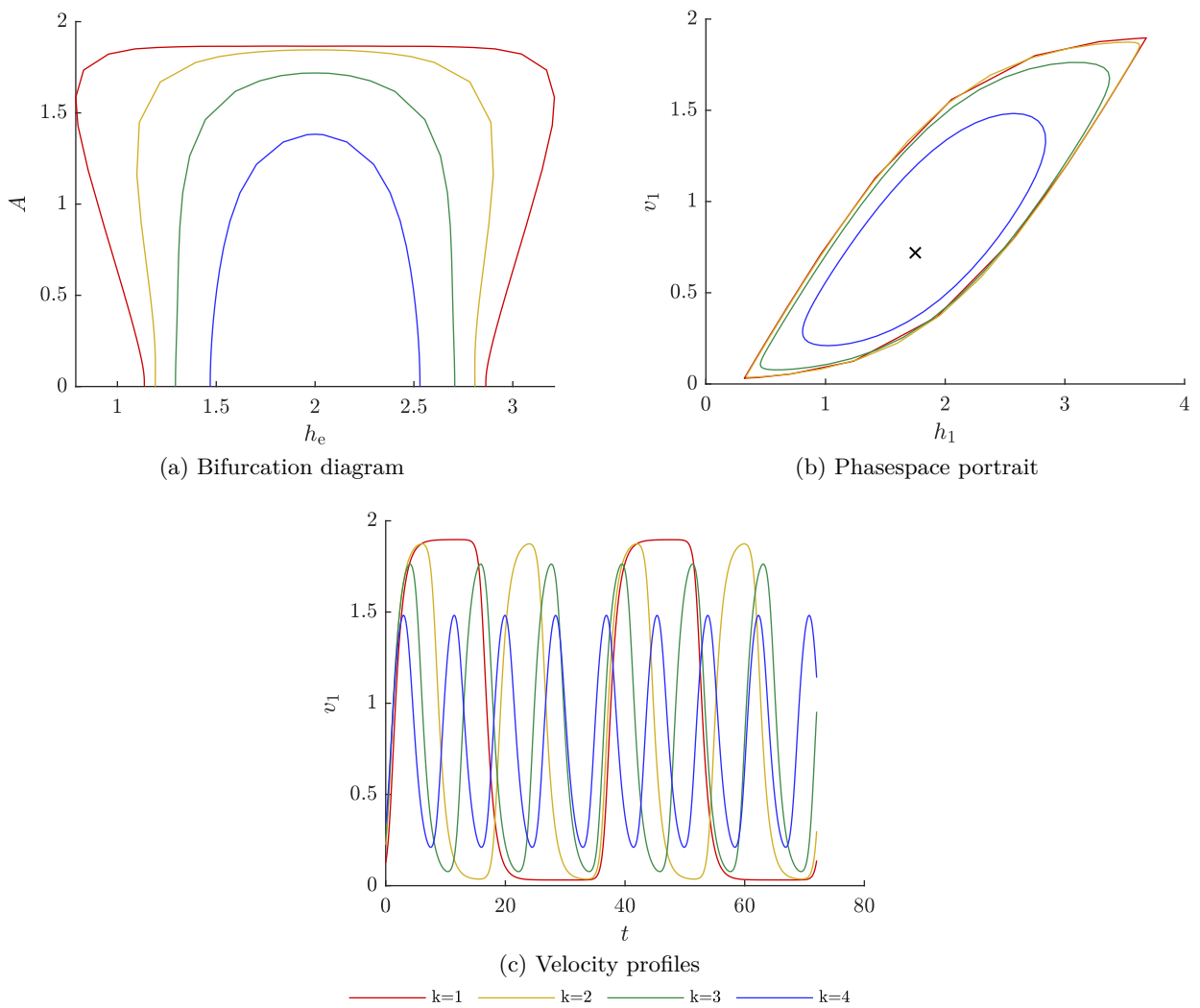


Figure 6.2: Bifurcation diagram for $N = 20$ vehicles on the circular road with branches $k = 1, \dots, 4$ corresponding to four pairs of eigenvalues crossing and re-crossing the imaginary axis as parameter h_e is varied, and behaviour of vehicle $j = 1$ within the solutions for $h_e = 1.75$

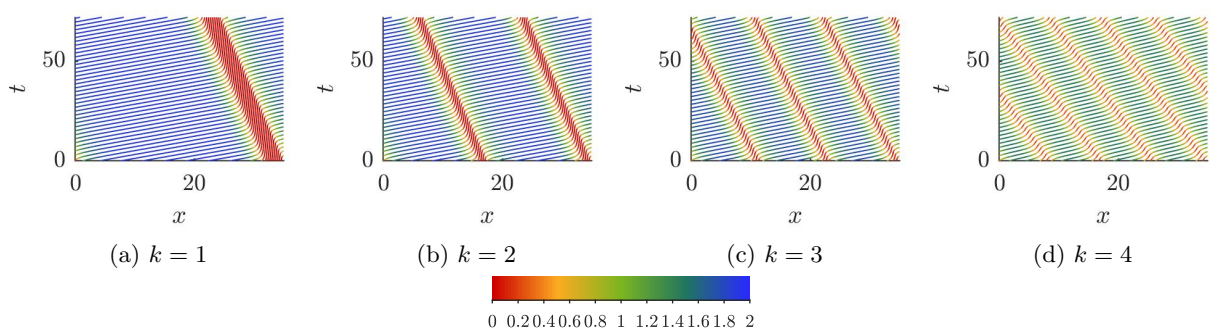


Figure 6.3: Trajectories of all 20 vehicles in the selected solutions with $h_e = 1.75$ from Fig. 6.2

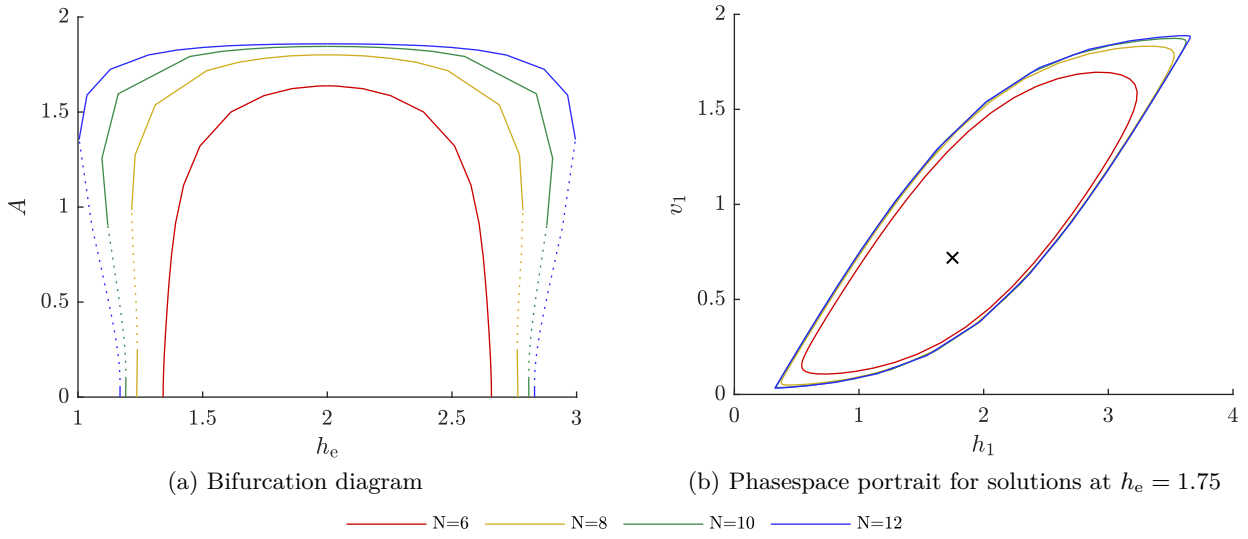


Figure 6.4: Comparison of periodic solutions for different numbers of vehicles on the circular road: Bifurcation diagram, demonstration of local supercriticality and behaviour of vehicle $j = 1$ in selected solutions

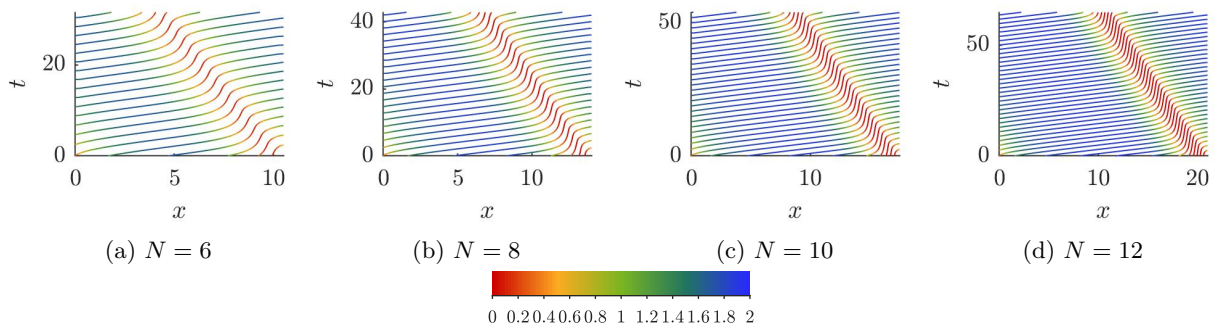


Figure 6.5: Trajectories of the selected solutions with $h_e = 1.75$ from Fig. 6.4

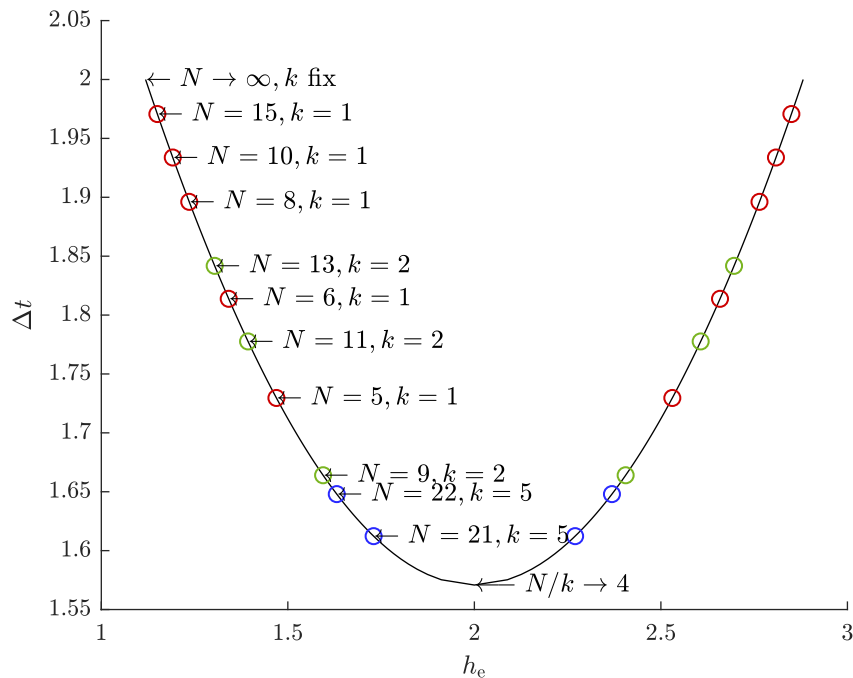


Figure 6.6: Bifurcation points and time shifts for fixed sensitivity $a = 1$. The bifurcation points for all possible vehicle numbers lie densely on a curve in $h_e, \Delta t$ -space

We may now introduce a “virtual” number of cars $\tilde{N} = 2\pi/\kappa$; for $\tilde{N} \in \mathbb{Q}$ and $\tilde{N} > 4$, we are in a Hopf point of the circular road. Starting from the Hopf curve, we can then use numerical continuation software to parametrise the adjacent surface of periodic solutions. Since continuation on the circular road becomes more costly with growing N , the most reasonable way to achieve such a parametrisation for a given interval $I \subset (4, \infty)$ while avoiding unnecessary recalculation of branches is to first calculate the branches for $N \in I \cap \mathbb{N}$, $k = 1$, then for $N \in \{N : \frac{N}{2} \in I, \frac{N}{2} \notin \mathbb{N}\}$, $k = 2$ etc.

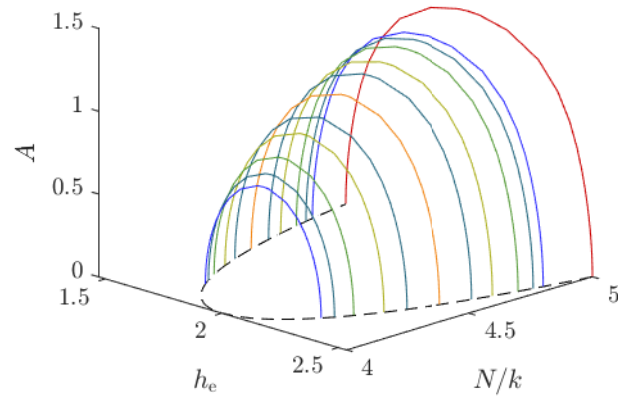
For \tilde{N} in the interval $(4, 5]$ (Fig. 6.7), this scheme yields the “canonical” sequence

$$(N(j), k(j))_{j \in \mathbb{N}} = (5, 1), (9, 2), (13, 3), (14, 3), (17, 4), (19, 4), \dots \quad (6.29)$$

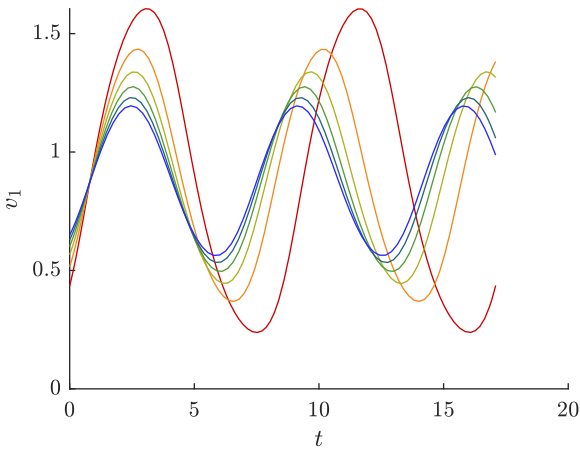
By calculating more branches, this may be continued to an arbitrary precision; however, we get a good overall impression of the emerging surface already if we stop at $k = 6$ (Fig.6.7(a)), although a higher resolution of the area close to $\tilde{N} = 4$ would be desirable. However, this requires calculation of the branches along the subsequence

$$(N(j), k(j))_{j \in \mathbb{N}} = (4j + 1, j) = (5, 1), (9, 1), (13, 3), (17, 4), (21, 5), (25, 6), \dots \quad (6.30)$$

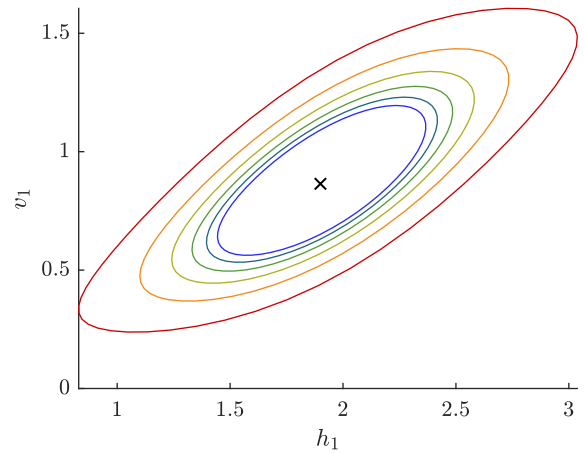
and quickly becomes very costly. Comparing the velocity profiles (Fig. 6.7(b)) and phase space portraits (Fig. 6.7(c)) along the periodic solutions with $h_e = 1.9$ on the six first branches along this subsequence makes this approach seem unjustified since the solutions appear very similar to each other.



(a) Branches of periodic solutions for the sequence in (6.29) up to $(N, k) = (29, 6)$



(b) Velocity profiles for the periodic solutions with $h_e = 1.9$ on the first six branches of the sequence in (6.30)



(c) Phasespace portrait for the periodic solutions with $h_e = 1.9$ on the first six branches of the sequence in (6.30)

— $k=1$ — $k=2$ — $k=3$ — $k=4$ — $k=5$ — $k=6$

Figure 6.7: Combination of branches of periodic solutions for different numbers of vehicles with “virtual vehicle number” $\tilde{N} \in (4, 5]$ to approximate part of the conjectured solution manifold on the infinite lane

Example 6.4 (Finding periodic solutions with the delay approach)

A better way to parametrise the space of periodic solutions is to use the delay approach discussed in Sec. 6.1.2. We discretise the integral in (6.16) by using a quadrature over $n = 20$ discrete delays. For better stability, time is inverted in the branch computations to have standard backward delays. For each T -periodic solution $v(t)$ with shift vector $(\Delta t, \Delta x)$, we get another solution $\tilde{v}(t) = 2 \tanh(2) - v(t)$ from the point symmetry of the chosen OVF around $(2, \tanh(2))$. For the time shift we have $\Delta t = \tilde{\Delta}t$, for the spatial shift we may calculate from (6.15) the relation

$$\tilde{\Delta}x = \tilde{h}(t) - \int_0^{\tilde{\Delta}t} \tilde{v}(t) dt = 4 - h(t) - \int_0^{\Delta t} 2 \tanh(2) - v(t) dt = 4 - 2 \tanh(2)\Delta t - \Delta x. \quad (6.31)$$

We see that in $(\Delta t, \Delta x)$ -space, the periodic solutions will be symmetric to the line $\Delta t = \frac{2 - \Delta x}{\tanh(2)}$. To exploit this, we exchange the parameter Δx by

$$\Delta y := \Delta x - 2 - \tanh(2)\Delta t \quad (6.32)$$

in our simulations.

We may now take any point on the Hopf curve we determined before (Fig. 6.6), calculate the corresponding spatial shift Δy from (6.17) and (6.32) and use it as a starting point for a branch of periodic solutions, where either Δy or Δt is held fixed (Fig. 6.8(d)). Afterwards, Δx and h_e can be recomputed for each periodic solution in the obtained branch. Only the part to the left of the symmetry axis is calculated by continuation, the other half can be concluded on. Although the same number of steps is used in each continuation in Δt , the length of the resulting branches in parameter space is very different; the branches seem to stop in a boundary curve with a cusp on the symmetry axis. If we try to continue the branches beyond this curve by force, continuation fails. The boundary can be recovered asymptotically if branches for circular road systems with growing \tilde{N} are projected into the picture ($N = 5, 10, 20, k = 1$ are displayed, where 10 and 20 are already very close to each other)

When we consider the velocity amplitudes as a function of h_e and Δt (Fig. 6.8), we recognise the overall shape we saw in our previous results (cf. Figs. 6.2(a), 6.4(a) 6.7(a)). The direct comparison with selected branches obtained from the circular road shows very good agreement between the results obtained from both approaches. The side and top view give more insight into the delicate structure of the surface (Figs. 6.8(b), 6.8(c)).

Note the highly nonlinear mapping between Δx and h_e : while the kind of periodic solutions with near rectangular profile that is so typical for the Bando model takes a lot of room on the “top shield” in the $h_e, \Delta t$ -measure, this area is actually very coarsely represented by the chosen equidistant parametrisation in $\Delta t, \Delta y$. If the velocity amplitude is viewed as a function of Δx and Δt , however (Fig. 6.8(e)), these solutions are concentrated in a very small region around the cusp on the symmetry axis. This representation may be considered to reflect the nature of these solutions more closely: even if they span a wide range of average headways, their main difference is in the ratio of time the solution dwells in the upper and lower state.

Only a small part of the obtained solutions has values of Δx smaller than zero. This corresponds to our intuition and empirical results TREIBER and KESTING (2011, cf.) that typically, jams travel upstream in an Eulerian frame.

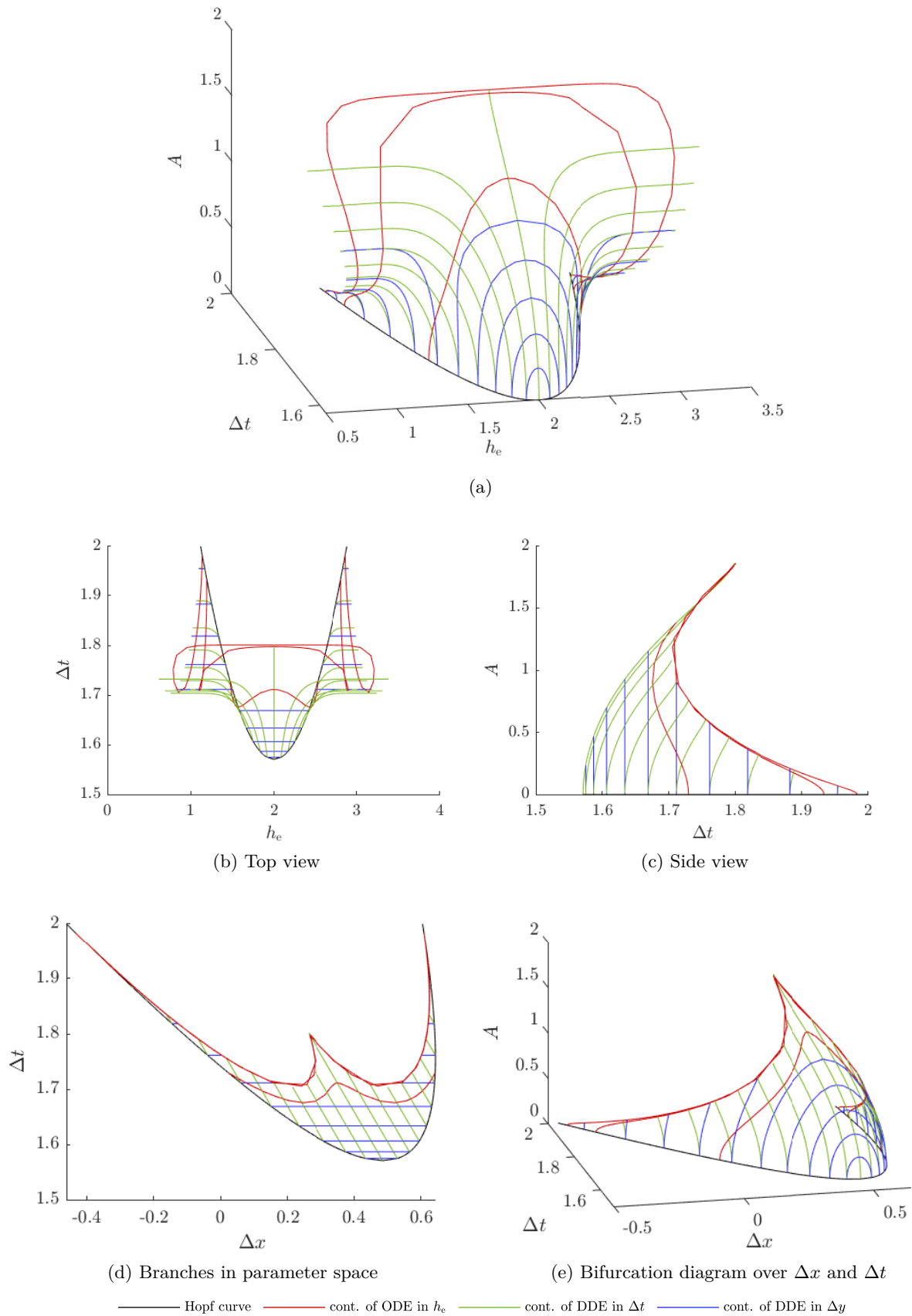


Figure 6.8: Periodic solutions on the infinite lane obtained from the integro-delay approach (6.16), compared with results of “traditional” ODE continuation, in different projections. Note the collapse of the “shield” of high-amplitude solutions in (a,b) to a “cusp” in $\Delta x, \Delta t$ -space (d,e)

Example 6.5 (Transitions between quasistationary solutions in the Bando model)

We extract a periodic solution close to the “hysteresis curve” from the previous example. In good approximation it can be viewed as a combination of two heteroclinic solutions from a lower to a higher equilibrium headway and back. We split the solution and use it as an initial guess for a continuation of heteroclinic solutions in `DDE-BIFTOOL`. For comparison, we also perform a “naïve” continuation with the approach from (6.27). The results match very well (Fig. 6.10), reproducing and extending the transitions found experimentally in BERG and WOODS (2001). Especially interesting are the newly found solutions beyond the intersection with the line $h_d = h_u$, which are travelling downstream in the road frame (Fig. 6.9 (e),(f)).

Note that only the parts of the transition branches below the main diagonal in Fig. 6.10(c) satisfy the entropy solution formulated in ANSORGE (1990) that a jump should only occur when vehicles are going from the less dense into the denser region. However, although the situations depicted in Fig. 6.9 (a-d) are thus not to be expected in real life, they are valid solutions of the Bando model. It is also interesting to compare these results to the heteroclinic solutions obtained in (SHEN and SHIKH-KHALIL 2018). Since they studied a model that is first order in time, it was found that generically, for fixed Δx there is a whole family of transitions connecting up- and downstream headways, subject to (6.25). For appropriate values of Δx and Δt , any two headways can be connected. This is not true for the Bando model, which is second order in time: Transitions are only possible for special combinations of h_+ and h_- (cf. Fig. 6.10(c)), and we need to allow both Δx and Δt to vary in order to find them. This can be seen as an analogy to the situation for scalar conservation laws and systems of them, where the Rankine-Hugoniot jump condition has to be satisfied component-wise.

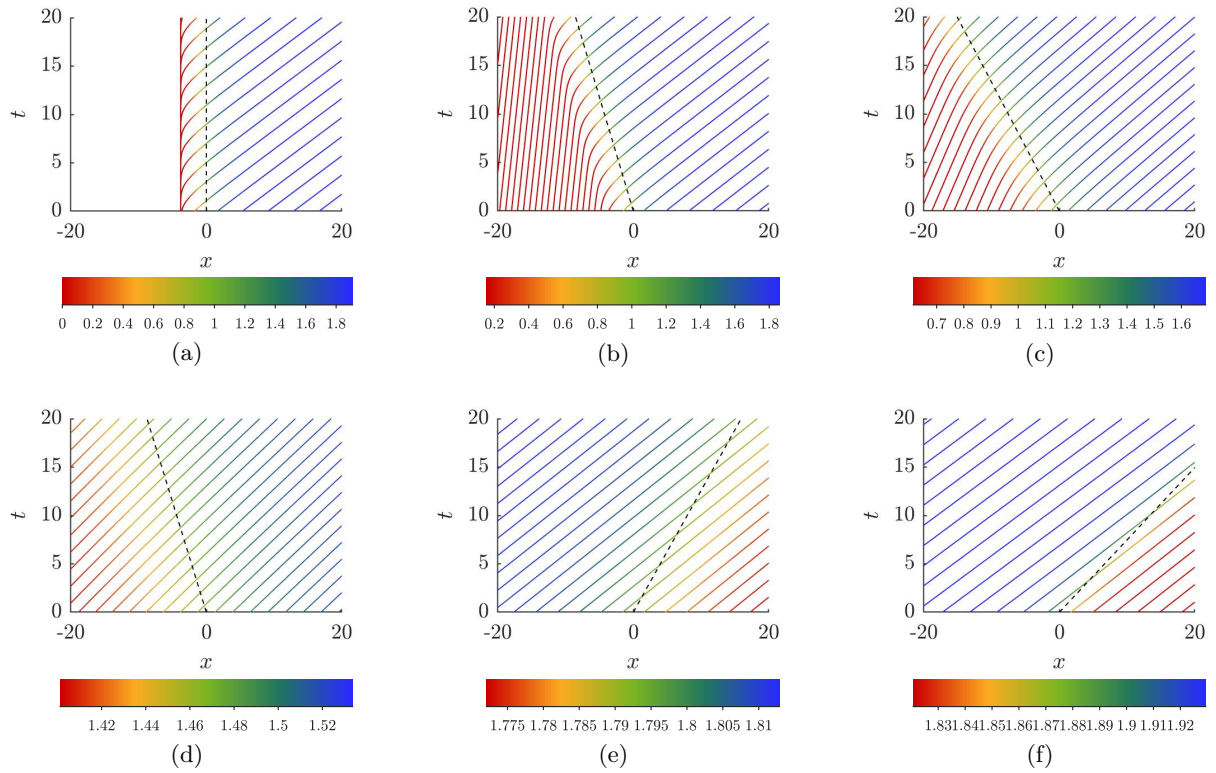


Figure 6.9: Trajectory plots for heteroclinic solutions of the Bando model (Examples taken from the continuation in Fig. 6.10). Note that the solutions in (a-d) are unentropic in the sense of ANSORGE (1990)

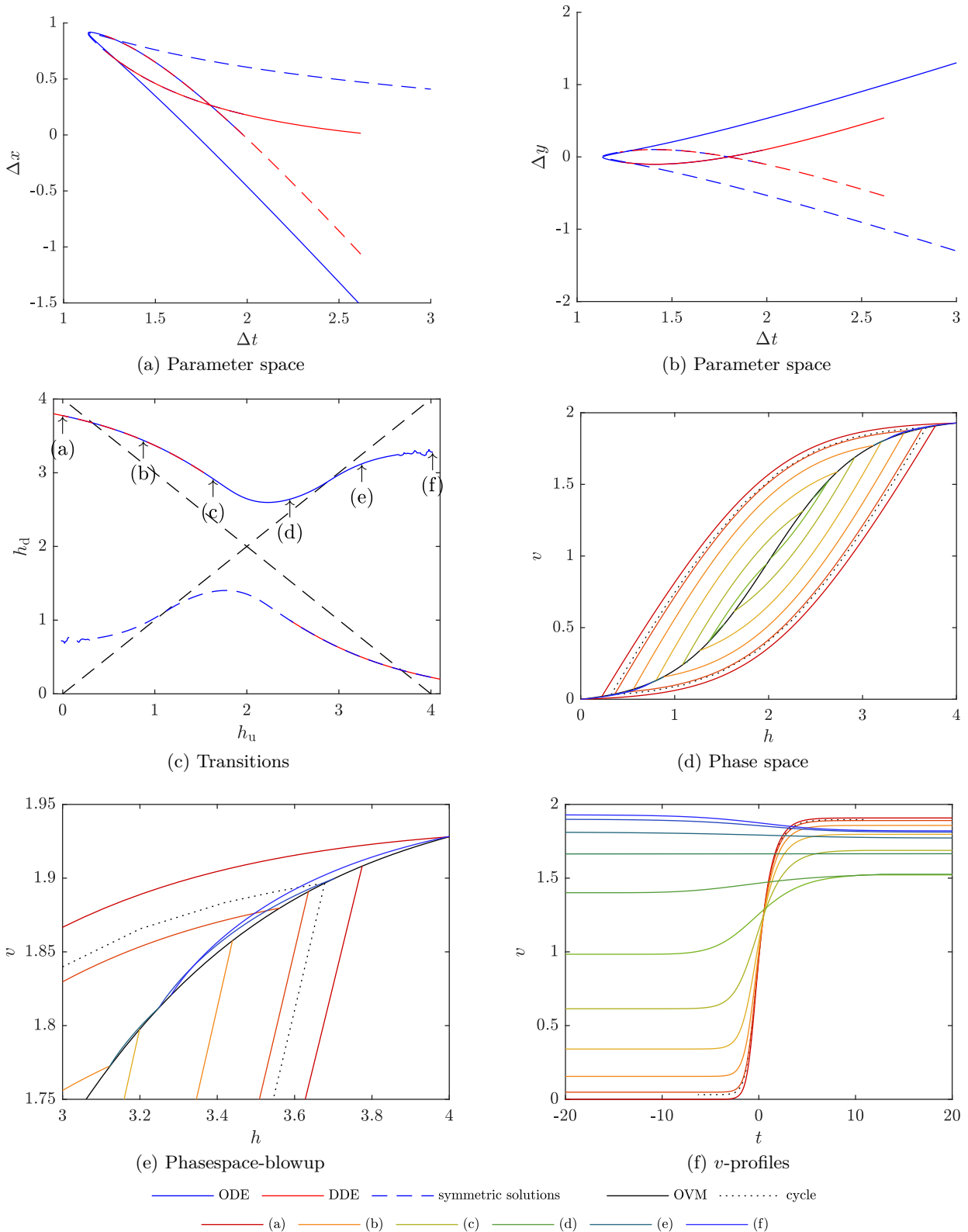


Figure 6.10: Heteroclinic solutions found by cutting the asymptotic periodic solutions in the “cusp” in Figs. 6.8(c)-(e) and numerical continuation (red in (a-c)) and a continuation using the ODE ansatz (6.27) with $N = 100$ vehicles (blue). In each case, the symmetry of the used OVF yields another branch (dashed). The classical “hysteresis curve”-periodic solution is dotted in (d) and corresponds to the intersections of the branches with the line $4 - h$ in (c)

Chapter 7

Stability and jam behaviour

On the circular road, the first Lyapunov coefficient can be calculated to conclude about stability of the periodic solutions close to the bifurcation point. Although it is possible to calculate the first Lyapunov coefficient for the integro-delay differential equation (6.16) as well (see Appendix B.2), unfortunately its positivity would not imply local stability of the corresponding periodic solutions on the infinite lane. We considered (6.13) because we were looking for a solution where all trajectories are just shifted copies of each other. This is not true any more if a perturbation appears on the infinite lane, unless this is periodic in nature as well, which is not realistic. The space of possible perturbations of the periodic solution in the shift setting is too small, therefore we need to find a way to consider more general perturbations. However, the Lyapunov coefficient can still tell us about the local geometry of the solution surface.

7.1 Floquet multipliers and exponents

7.1.1 Circular road

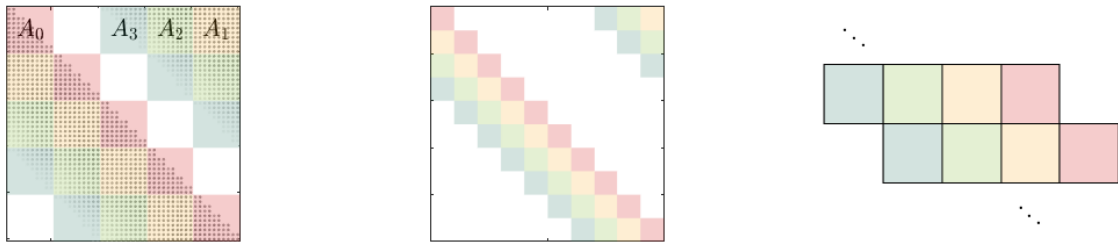
The Hopf theorem can be used to check for local (in-) stability of periodic solutions close to the critical parameter value. As we move away from it, their stability properties may change. To determine the stability of an arbitrary periodic solution, we need to calculate its Floquet multipliers (cf. e.g. TESCHL 2012). To this end, we integrate the matrix-valued ODE

$$\dot{J}(t) = \mathcal{A}(\vec{y}(t), \vec{z}(t)) \cdot J(t) \tag{7.1}$$

with initial condition $J(0) = \text{Id}$ along with the time integration of the periodic solution over one time period T and calculate the eigenvalues of $J(T)$ afterwards. If these lie inside of the unit circle (except for a multiplier 1 that is always present for periodic solutions), we have stability. Numerically, this can be implemented relatively easy with a standard ODE solver. Stability calculation of periodic solutions is also a standard feature of numerical continuation software.

In the $J(T)$, the $n \times n$ -block at position $(j, j - m)$ describes the influence of the initial perturbation of the driver m vehicles ahead to the state of vehicle j after one time period T . While in instantaneous stability matrix \mathcal{A} only the block diagonals in the range $[m_l, m_f]$ around the main diagonal are non-zero, this does not hold for the integral: An initial perturbation $m > m_l$ vehicles ahead may not have an immediate effect, but eventually it will. However, we may expect that this influence will decay quickly with growing m . Consequently, the entries in the off-diagonal blocks should decay quickly.

What happens if we place a periodic solution on a circle twice as big, with twice as many cars?



(a) Jacobian of a periodic solution on the circular lane that has been “copied” five times (b) Jacobian for ten copies on the circular road (c) Block Laurent operator for the infinite lane

Figure 7.1: By symmetry, the matrices $J(T)$ have a block circulant structure for $k > 1$. When the circle is big enough that information does not flow back within one time period, this can be used to construct an associate block Laurent operator for periodic solutions on the infinite lane

Similar to what we found for the homogeneous solutions, we cannot expect the stability properties to be the same for both situations. Locally, close to the bifurcation curve, we can see that typically the periodic solution will be unstable on the bigger circle. Recall that generically eigenvalues with smaller k cross the imaginary axis first. So if the bifurcation on the smaller circle is caused by the pair of eigenvalues $\lambda_+(1), \bar{\lambda}_+(1)$, this corresponds to the pair $\lambda_+(2), \bar{\lambda}_+(2)$ on the bigger circle. Consequently, on the bigger circle we generically already have $\text{Re}(\lambda_+(1)) > 0$. From this we see that periodic solutions in a neighbourhood will have a Floquet multiplier close to $\exp(\lambda_+(1) \cdot T)$, i.e. outside of the unit circle. This also explains why the Lyapunov coefficients for these systems give us no information about stability on the infinite lane. Similarly, in GASSER et al. (2004) all the calculated branches of higher order ($k \geq 2$) periodic solutions are unstable, even globally. In OROSZ et al. (2004a), the same effect is found in a system with reaction-time delay.

7.1.2 Infinite lane

As we already noted at the beginning of this chapter, even if we may use (6.16) to find solutions on the infinite lane, its stability properties as a solution of (6.16) are not equivalent to the properties on the infinite lane.

If $T/\Delta t \in \mathbb{Q}$, we can directly apply the methods from the previous section. Find $N, k \in \mathbb{N}$ such that $\frac{N}{k} = \frac{T}{\Delta t}$ and consider a sequence of circular roads with $n \cdot N$ vehicles, $n \in \mathbb{N}$. Analogously to the case for the homogeneous solution, the Floquet multipliers will approximate the spectrum. Note that the Jacobians have a block circulant structure by symmetry, with blocks of size $2nN$. As soon as the circle is wide enough that information cannot flow back in the course of one time period there will only be a finite number of distinct $2nN$ -blocks that stay the same for circles with an arbitrarily high number of vehicles. For the standard case where $m_f = 0$, this will be indicated by a “gap” opening up to the right of the main block diagonal (Figs. 7.1(a), (b)).

We can therefore use these blocks to construct the corresponding block Laurent operator for the infinite lane and easily calculate its spectrum from its symbol, in analogy to the calculation of the

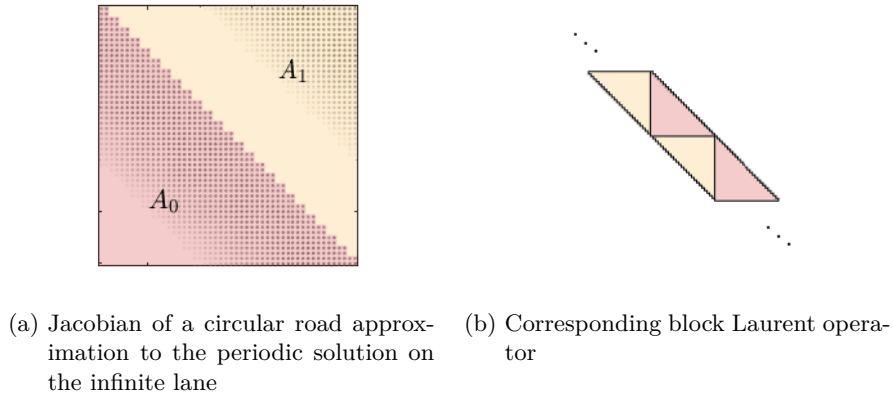


Figure 7.2: Constructing the stability operator on the infinite lane from a circular road approximation: As soon as $J(T)$ takes a banded form with zeros along the first upper $n \times n$ block diagonal, we can separate it into two distinct block triangular matrices A_0 , A_1 and use these to approximate the corresponding block Laurent operator

eigenvalues and the spectrum of the linearisation around the stationary solution of the circular road and the infinite lane, respectively (Fig. 7.1(c)). In order to find a given number M of points in the spectrum, we may then solve $\frac{M}{2Nn}$ eigenvalue problems of dimension $2Nn$, instead of a single M -dimensional one.

For a periodic solution with $T/\Delta t \notin \mathbb{Q}$, we may try to construct a sequence of periodic solutions on the circular road that approximate it. To this end, consider the sequence $(N(k))_{k \in \mathbb{N}}$, where

$$N(k) = \left\lfloor \frac{Tk}{\Delta t} \right\rfloor. \quad (7.2)$$

Then we have $\lim_{k \rightarrow \infty} \frac{N(k)}{k} = \frac{T}{\Delta t}$ and $\frac{N(k)}{k} < \frac{T}{\Delta t}$ for all $k \in \mathbb{N}$. We are consequently only interested in increasing subsequences of $(N(k))_{k \in \mathbb{N}}$. For each pair $(k, N(k))$, we may now view the periodic solution on the infinite lane as an approximation of a k -periodic solution on the circular road with N cars, where the length is given by (6.5). This approximation may then be used as an initial guess for a root of (6.7) and can be corrected to the desired precision by a Newton scheme, holding the other parameters fixed. Since the Newton algorithm guarantees convergence only locally, this procedure might fail for low k .

In order to approximate the spectrum of the infinite lane from this, we may again exploit the banded structure of the Jacobian when k is large enough. The corresponding operator can be constructed by “glueing” the separated parts in the Jacobians together in a straightforward way (Fig. 7.2).

Alternatively, we may directly look for Floquet exponents, i.e. $\mu \in \mathbb{C}$ such that $\exp(\mu T) = \Lambda$, where Λ is a Floquet multiplier and T the time period.

To this end, consider a periodic solution $u(t, j) = u(t - j\Delta t)$ to the parameter-dependent ODE

$$\dot{\mathbf{u}}(t, j) = f(\mathbf{u}(t, j), \mathbf{u}(t, j - 1), \mathbf{p}) \quad (7.3)$$

with linearisation

$$\dot{\mathbf{w}}(t, j) = A(\mathbf{u}(t - j\Delta t), \mathbf{p}) \mathbf{w}(t, j) + B(\mathbf{u}(t - j\Delta t), \mathbf{p}) \mathbf{w}(t, j - 1). \quad (7.4)$$

Since A, B are not constant, simply plugging in $\mathbf{v} \exp(\lambda t - ijk)$ as in the quasistationary case will not do. However, we may vary this approach slightly by exchanging the eigenvalue λ by the Floquet exponent μ and making an ansatz $\varphi(t - j\Delta t) \cdot \exp(\mu t - ijk)$ instead.

While the quasistationary case led to the eigenvalue problem

$$\lambda \cdot \mathbf{v} = (A + \exp(ik) B) \mathbf{v} \quad (7.5)$$

with constant eigenvector \mathbf{v} , we now have the T -periodic eigenfunction $\varphi(t) = \varphi(t + T)$ and the eigenvalue problem

$$\dot{\varphi}(t) + \mu\varphi(t) = A(\mathbf{u}(t))\varphi(t) + \exp(ik) B(\mathbf{u}(t))\varphi(t + \Delta t). \quad (7.6)$$

By linearity, the eigenfunction φ has two degrees of freedom: therefore, we may set up two functionals $f_{1,2} : \mathcal{C}(0, T) \rightarrow \mathbb{R}$ and demand $f_{1,2}(\varphi) \stackrel{!}{=} 0$, e.g. a condition on its norm and a phase condition.

The formally correct way to obtain (7.6), equivalent to what is done in BREVDO and BRIDGES (1997) (cf. also BREVDO and BRIDGES 1996), is to first perform a coordinate transform $\tilde{t} = t + j\Delta t$ to a system with a constant base state that is periodic in time. We then have to deal with the DDE system

$$\dot{\tilde{\mathbf{u}}}(\tilde{t}, j) = f(\tilde{\mathbf{u}}(\tilde{t}, j), \tilde{\mathbf{u}}(\tilde{t} + \Delta t, j - 1)) \quad (7.7)$$

which we can linearise. Afterwards, we may apply a Fourier transform in j and consider the matrix initial-value problem

$$\dot{\Phi}(\tilde{t}, k) = A(t)\Phi(\tilde{t}, k) + \exp(ik) B(t)\Phi(\tilde{t} + \Delta t, k), \quad \Phi(0, k) = \text{Id}. \quad (7.8)$$

According to Floquet theory, $\Phi(\tilde{t}, k)$ may be written as

$$\Phi(\tilde{t}, k) = C(\tilde{t}, k) \cdot \exp(D(k) \cdot \tilde{t}) \quad (7.9)$$

Putting this into (7.8), we observe the identity

$$\dot{C}(t) + C(t) \cdot D = A(t) \cdot C(t) + \exp(ik) B(t) \cdot C(t + \Delta t). \quad (7.10)$$

Thus, plugging in $C(t) \cdot \mathbf{v}(t)$ yields

$$\dot{\mathbf{v}}(k, t) = D(k)\mathbf{v}(k, t) \quad (7.11)$$

which may be Laplace transformed, giving

$$(\mu \text{Id} - D(k)) \mathbf{v}(k, \mu) = \mathbf{v}_0(k) \quad (7.12)$$

We may now combine (7.3) and (7.6) into an extended system, regarding μ and k as two additional complex-valued parameters. If the extra conditions on φ are incorporated as well, it is possible to do continuation in k while keeping the solution \mathbf{u} and the “original” parameters \mathbf{p} constant in order to obtain the spectrum.

Another promising direction to study stability of periodic solutions of this kind is to use the theory on so-called twisted Toeplitz- or Berezin-Toeplitz operators (TREFETHEN and EMBREE 2005; TREFETHEN and CHAPMAN 2004; BORTHWICK and URIBE 2003).

7.2 Convective/absolute instability

We are of course also interested in characterising the unstable periodic solutions as convective or absolute: In which direction will a small perturbation to a periodic solution move from the perspective of an observer at the side of the road?

To study this, we may apply the analysis on the back transformation of (7.12) performed in Sec. 5.2.2. Consequently, we are looking for branch points (μ_c, k_c) satisfying

$$\chi(\mu_c, k_c) = 0 \quad (7.13a)$$

$$\frac{\partial \chi}{\partial k}(\mu_c, k_c) = 0 \quad (7.13b)$$

$$\text{Re}(\mu_c) = 0 \quad (7.13c)$$

and a pinching condition, where $\chi(\mu, k) = \det \left(D(k) - \text{Id} \left(\mu + ik \frac{v_e}{h_e} \right) \right)$.

An equivalent approach that appears better suitable for numerical continuation is to transform (7.6) to road coordinates,

$$\dot{\varphi}(t) + \left(\mu + ik \frac{v_e}{h_e} \right) \varphi(t) = A(\mathbf{u}(t)) \varphi(t) + \exp(ik) B(\mathbf{u}(t)) \varphi(t + \Delta t) \quad (7.14)$$

and calculate its derivative with respect to k ($\psi := \frac{\partial \varphi}{\partial k}$),

$$\dot{\psi}(t) + \left(\frac{\partial \mu}{\partial k} + i \frac{v_e}{h_e} \right) \varphi(t) + \left(\mu + ik \frac{v_e}{h_e} \right) \psi(t) = A(\mathbf{u}(t)) \psi(t) + \exp(ik) B(\mathbf{u}(t)) (i\varphi + \psi)(t + \Delta t). \quad (7.15)$$

The derivative only adds a heterogeneity to (7.14). Therefore, ψ is not unique; addition of a solution to (7.14) gives a new ψ . Consequently, we need to include another condition. Since ψ is the derivative of the eigenfunction φ with respect to k , the most straightforward idea would be to demand that the value of the functionals $f_{1,2}$ do not change in the direction ψ , i.e. $\psi \cdot \nabla f_{1,2}(\varphi) \stackrel{!}{=} 0$; however, other conditions may be chosen just as well.

We may now set up an extended system with (7.3), (7.14), and (7.15) for the combined state $[\mathbf{u}, \varphi, \psi]^\top \in \mathbb{R}^2 \times \mathbb{C}^2 \times \mathbb{C}^2$ with the enlarged parameter vector $[p, k, \mu, \frac{\partial \mu}{\partial k}]$, together with the phase

condition on \mathbf{u} and four conditions ensuring uniqueness of φ and ψ .

To find the borders between regions of absolute and convective instability, we then have to fix $\text{Re}(\mu) = 0$, $\frac{\partial \mu}{\partial k} = 0$ and do a branch continuation. The cu-au borders for the quasistationary solutions can be chosen as a Hopf curve to start from.

7.3 Examples

Example 7.1

As shown in GASSER et al. (2004), for the OVF $V(h) = \tanh(h - 2) + \tanh(2)$, bifurcations are supercritical, but possibly very locally so. This result can be confirmed in the experiment: While the curvature at the bottom of the global bifurcation diagram seems to imply a subcritical bifurcation for $N \geq 8$ (Fig. 6.4(a)), a strong amplification around the bifurcation point (Fig. 6.4(b)) shows that all four branches are indeed supercritical and are asymptotically very similar to each other.

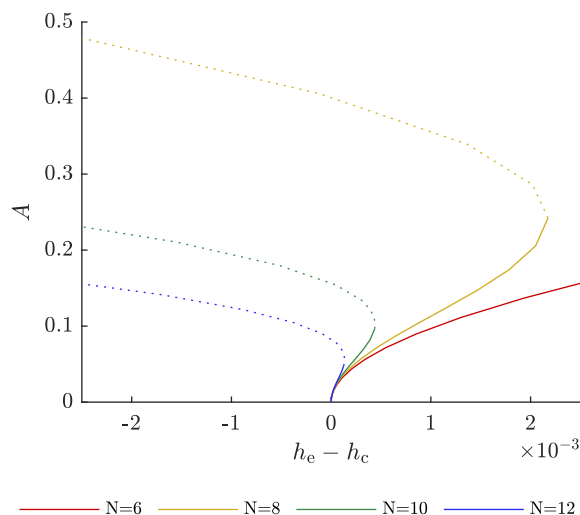


Figure 7.3: Local behaviour of bifurcation curves for $N = 6, \dots, 12$ close to the smaller critical headway h_c (cf. Fig. 6.4). As predicted by nonlinear analysis (cf. GASSER et al. 2004), all periodic solutions are *locally* stable close to the bifurcation point

Example 7.2 (Stability of the same velocity profile for different N)

Next, we demonstrate that a stable periodic solution on the circular road may lose stability if it is placed on a circle with an integer multiple of the original length and vehicle number (Fig. 7.4), as discussed in Sec. 7.1.1. We consider an arbitrary periodic solution with $N = 5$ cars and an average headway $h_e \approx 1.2$ (Fig. 7.4(a)). As expected, its Jacobian is dense, i.e. all vehicles “communicate” with each other during one time period. The Floquet multipliers, given by the eigenvalues of the Jacobian, lie within the unit circle, except for the trivial multiplier 1. When the circle length is doubled (Fig. 7.4(a)), additional multipliers appear, two of which lie outside of the unit circle. We may conclude that the periodic solution is unstable in this setting. If even more copies are considered (Figs. 7.4(c), (d)), the instability persists. We also note that already for ten vehicles, the magnitude of the entries in the first upper block diagonal, describing the influence of its follower on each vehicle, drops considerably. For the bigger circles, it is numerically zero,

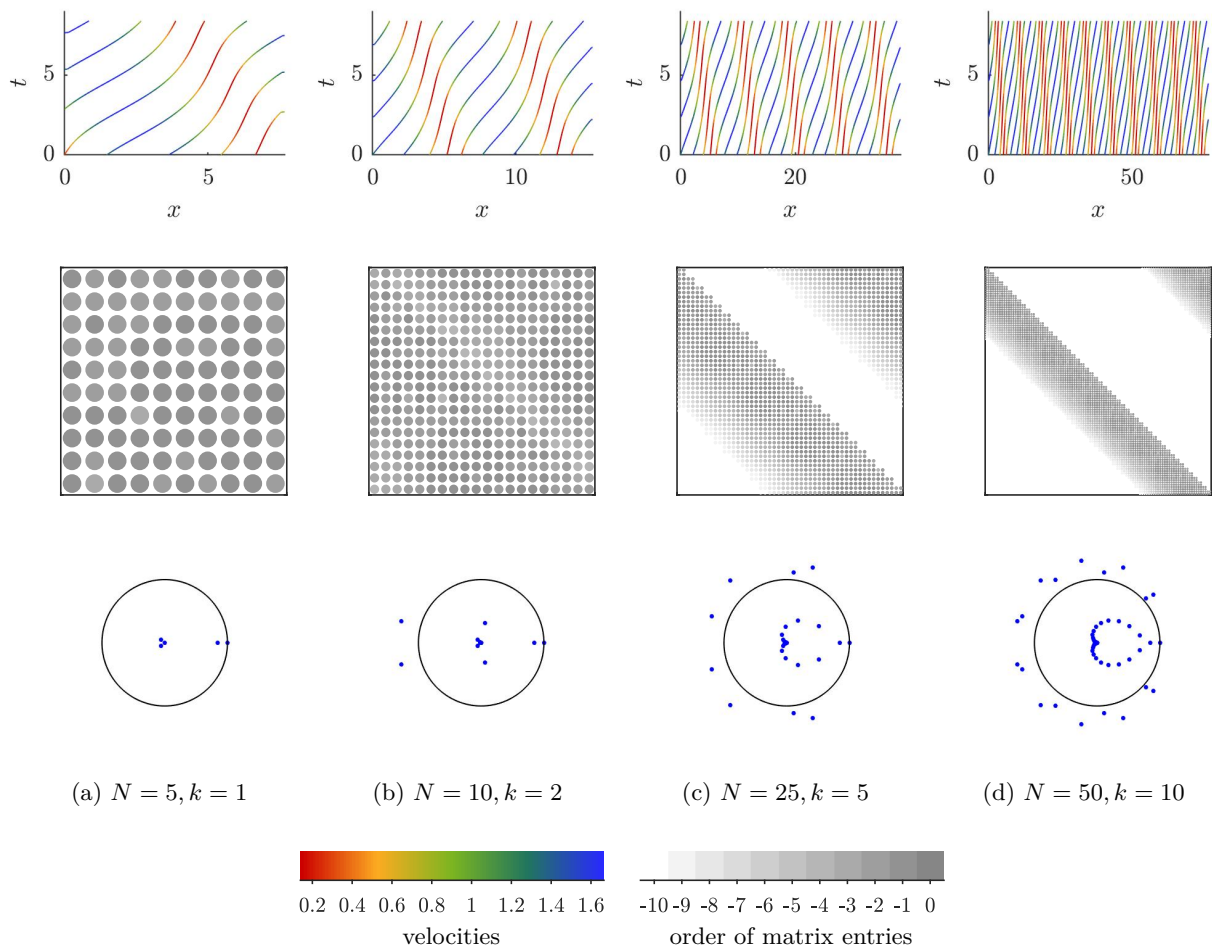


Figure 7.4: Periodic solutions may lose stability when placed on a bigger circle: The solutions in the top row of (b-d) are obtained by glueing together multiple copies of the solution in (a). While the corresponding matrices $J(T)$ get bigger in size, vehicles interact only with a limited range of neighbours within one time period (middle row). The Floquet multipliers (bottom) indicate that while the original solution is stable, the solutions on the bigger circles are not. Each set of Floquet multipliers is a subset of the one for the next bigger system.

and we observe that the order of the entries drops in magnitude as we move left from the main block diagonal. Also, in the Jacobian for $k = 10$ the block circulant structure becomes visible in the repeating pattern of entries with higher and lower magnitude in the nonzero entries (cf. Figs. 7.4(c), (d) to Figs. 7.1(a), (b)).

Example 7.3 (Approximation of periodic solutions on the infinite lane)

Our next example shows the approximation of a generic periodic solution on the infinite lane by circular road solutions as discussed in Sec. 7.1.2 (Fig. 7.5). We arbitrarily choose the solution with $\Delta x = 0.339$, $\Delta t = 1.7403$, $h_e = 1.797$, $T = 9.766$, corresponding to a virtual number of $\tilde{N} = 5.6115$ vehicles, and reconstruct the headway profile by integration. We calculate $N(k)$ according to (7.2) for $k \in [1, 50]$ and choose the subsequence that promises increasing accuracy (Fig. 7.5(a), Tab. 7.1). For each approximation, an initial guess is constructed by evaluation of the velocity- and headway profiles at equidistant points and subsequent correction, where h_e is

held fixed (the correction stays feasible even for high vehicle numbers since we can provide a good initial guess). Already for $(N, k) = (28, 5)$, the resulting solution cannot be distinguished from the target in the phase space profile. Calculation of the Jacobians and Floquet multipliers (Fig. 7.6) shows that the influence of the following car also becomes negligible for this value, allowing us to split the Jacobian into its upper and lower part and calculate an approximation of the spectrum on the infinite lane from this; this approximation changes very little when the next-better solution is considered (Figs. 7.6(c), (d)).

Table 7.1: Parameters for subsequence in Fig. 7.5, 7.6

	k	$N = \lfloor \tilde{N} \cdot k \rfloor$	N/k	$\frac{\tilde{N} - \frac{N}{k}}{\tilde{N}}$
1	1	5	5	0.109
2	2	11	5.5	0.0199
3	5	28	5.6	0.0020
4	18	101	5.611	0.0001

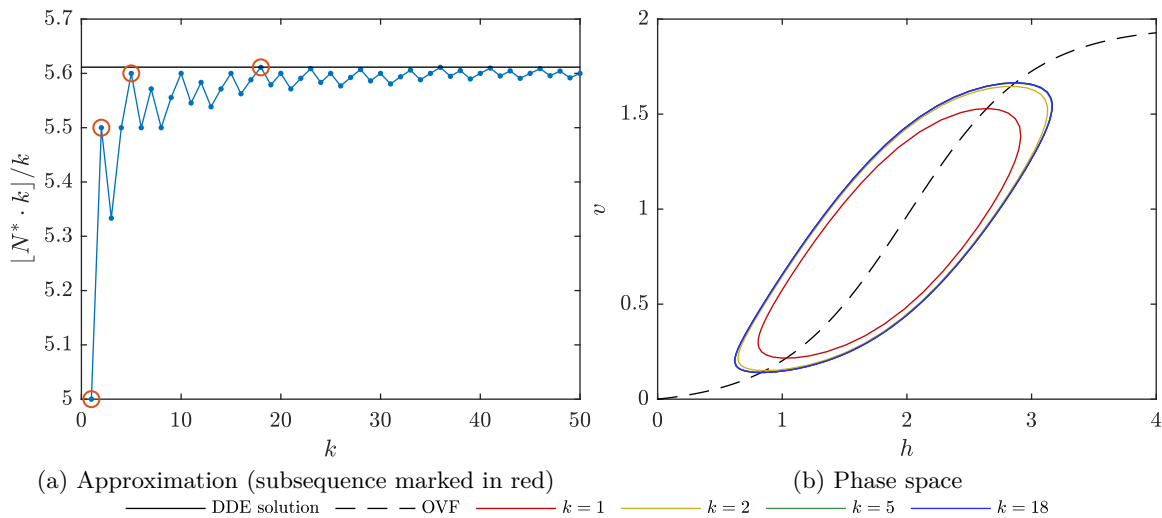


Figure 7.5: Approximation of a generic periodic solution on the infinite lane by periodic solutions on the circular road: A solution chosen randomly from the manifold depicted in Fig. 6.8 is evaluated at equidistant time intervals and taken as an initial guess for a sequence of circular road systems

Finally, we may apply the technique demonstrated above to compare the spectra for different periodic solutions in the infinite lane setting. In order to do so, we start at the Hopf point for the central headway $h_e = 2$ and continue in Δt , keeping Δy fixed (Fig. 7.7(a), cf. the symmetry axis in Fig. 6.8). From this branch, we pick four solutions and construct the best circular road approximation (7.2) that can be obtained with $N \leq 100$; the results are visually undistinguishable from the original solutions (Fig. 7.7(b)). We now use these approximations to calculate the infinite road spectra (Fig. 7.8). As may be expected, all the considered solutions are unstable when considered on the infinite lane. However, the maximal absolute value of the Floquet multipliers, and thus also the maximal real part in the associated spectra, shrinks towards the top and the

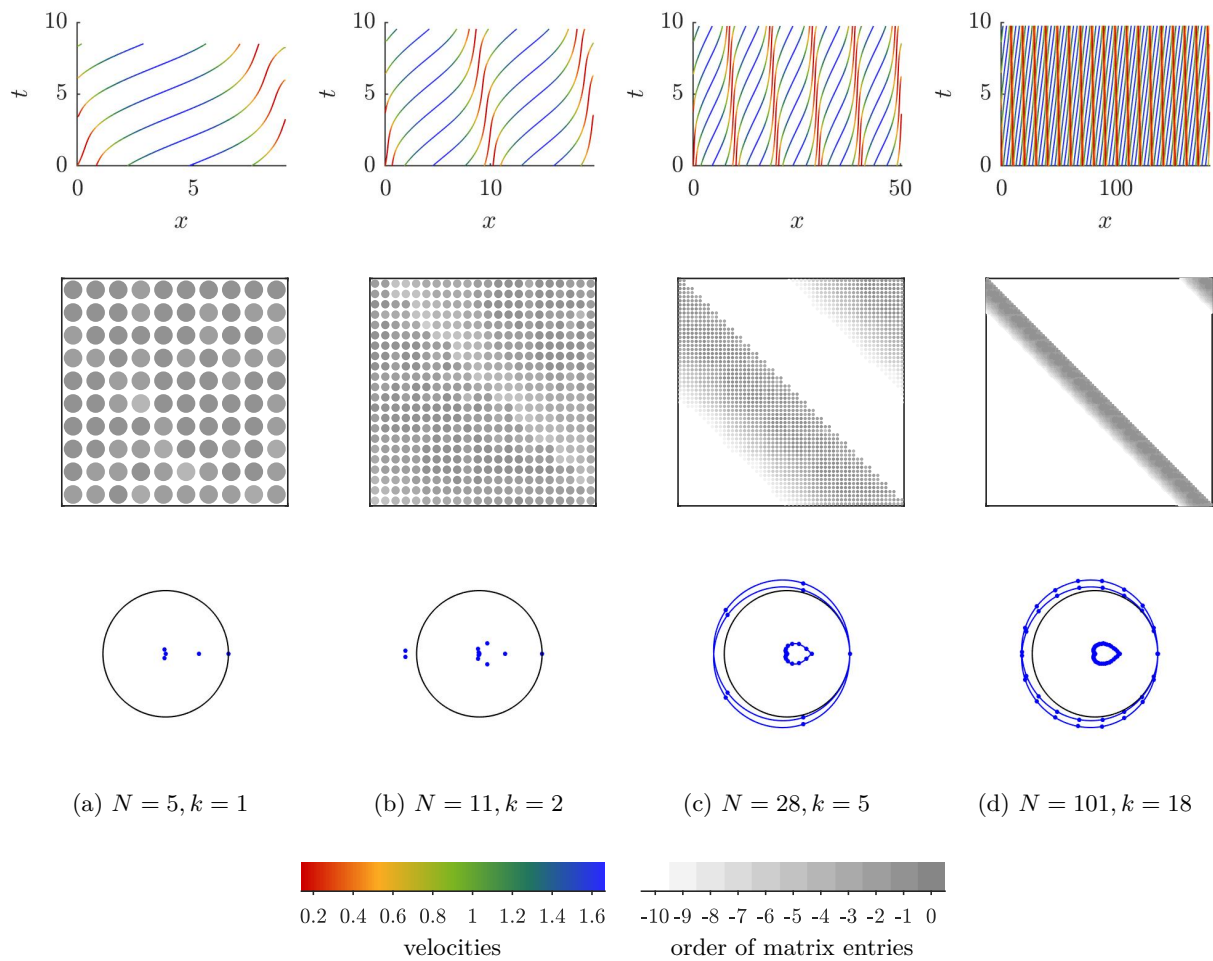


Figure 7.6: Comparison of the trajectories (top), shape of $J(T)$ (middle) and Floquet multipliers (bottom, blue dots) of the circular road approximations in Fig. 7.5. The matrices in (c,d) are cut and rearranged in a block Laurent operator as indicated in Fig. 7.2. Then the eigenvalues of the symbol are calculated on the unit circle to approximate its spectrum on the infinite lane (bottom, blue lines)

solution at the end of the branch (Fig. 7.8(d)) is only marginally unstable.

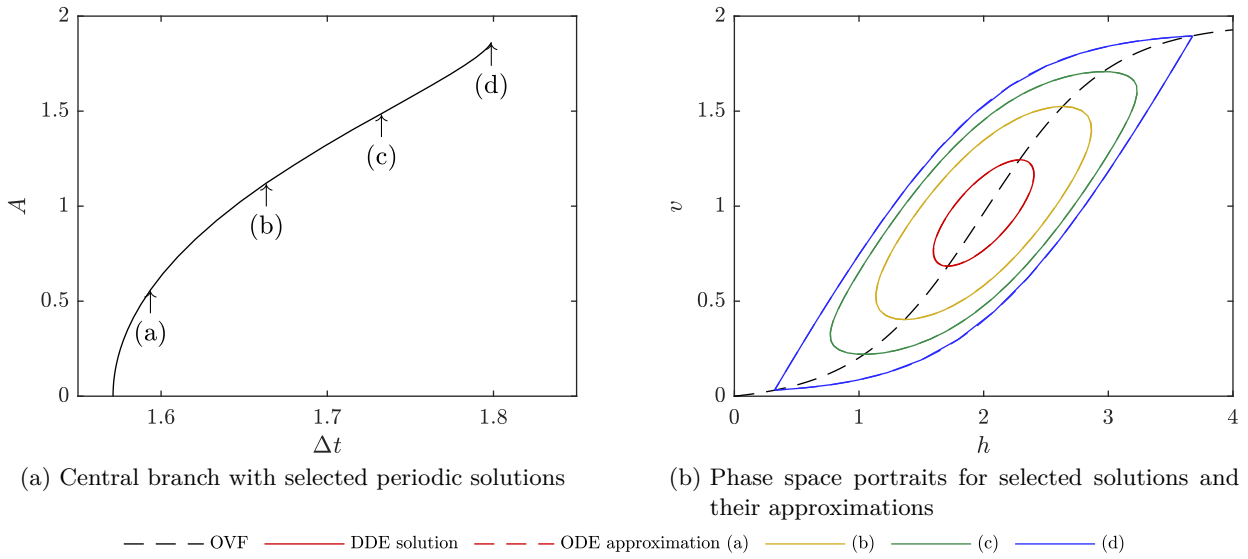


Figure 7.7: With increasing amplitude, the periodic solutions are getting less unstable: The procedure shown in Fig. 7.6 is performed for four solutions along the central branch ($h_e = 2, \Delta y = 0$) of the solution manifold in Fig. 6.8. Note that the DDE solutions and their ODE approximations (dashed) are visually indistinguishable

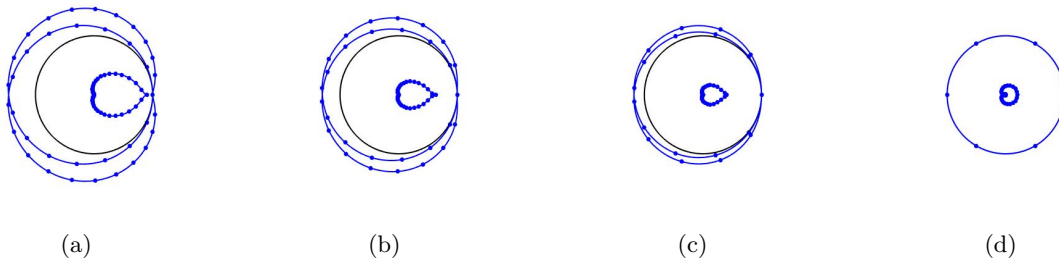


Figure 7.8: As the amplitude of the periodic solutions depicted in Fig. 7.7 increases, the maximal real parts in their spectra and thus also the maximal absolute values of their Floquet multipliers decrease

Example 7.4 (Convective and absolute instability of periodic solutions)

We expand the system we used for continuation of periodic solutions on the infinite lane by (7.14) and (7.15) in order to be able to simultaneously follow an eigenfunction and its derivative with respect to complex-valued k . In this formulation, k and the Floquet exponent μ become parameters. The branch point conditions (7.13) are included as additional parameter constraints. As starting points, the intersections of the cdu - au and au - cuu boundaries from Ex. 5.3 with the line $a = 1$ are used. The obtained branches of periodic solutions separate the surface we obtained in Ex. 6.4 into three regions (Fig. 7.9), with perturbations moving in upstream-, downstream-, or in both directions (Fig. 7.10). While the results look promising, the pinching condition is not yet verified and further testing and improvement of the code is necessary.

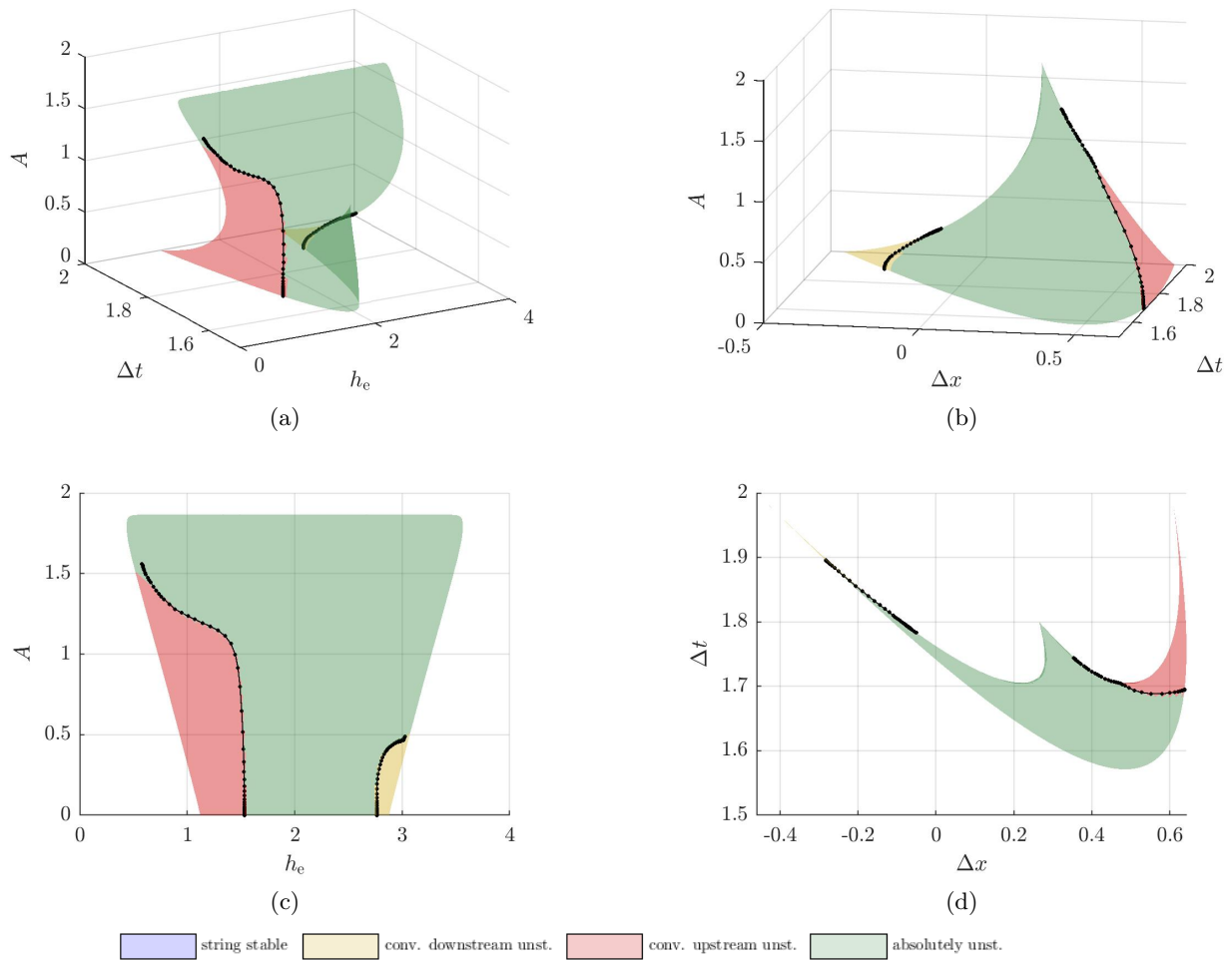


Figure 7.9: Convectively and absolutely unstable periodic solutions on the infinite lane: The solution manifold from Fig. 6.8 is classified by continuation of the borders found for the homogeneous flow case; the curve for $A = 0$ corresponds to a cut at $a = 1$ through the parameter space diagram in Fig. 5.8

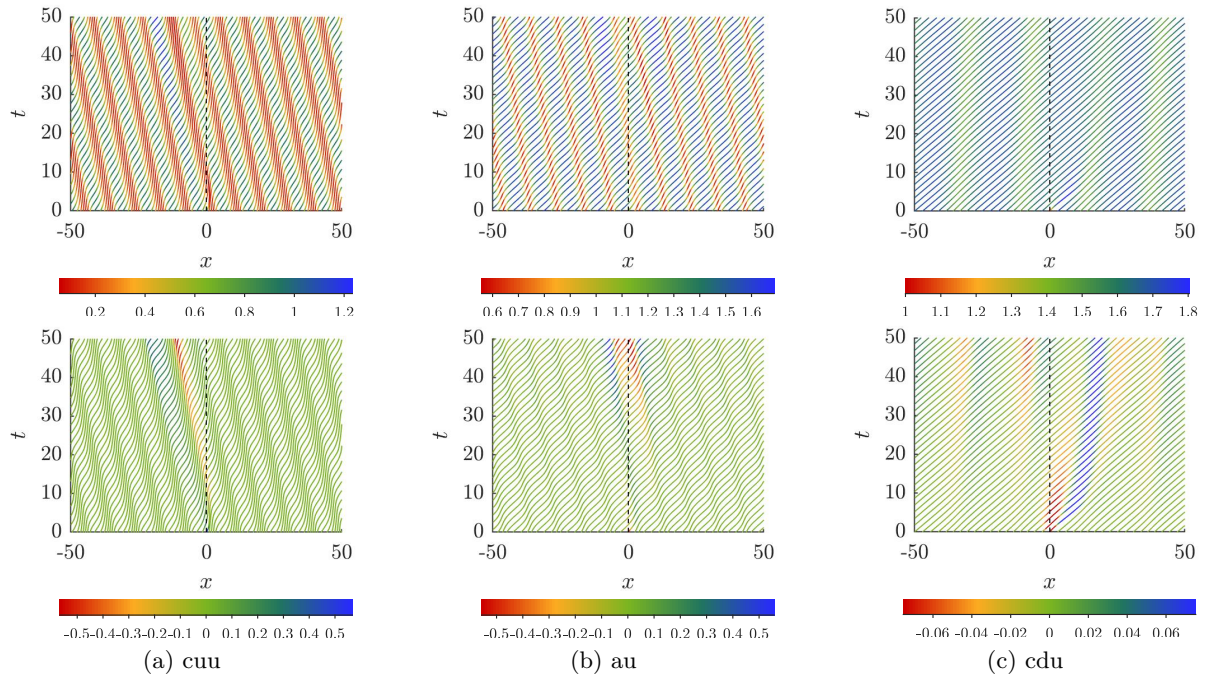


Figure 7.10: Examples of periodic solutions from the separated regions in Fig. 7.9. The colours in the top and bottom row show the actual velocities and their deviation from the expected velocities, respectively.

Chapter 8

Discussion and Outlook

8.1 Discussion

Let us briefly summarise the presented material and discuss the achievements that could be made. In Chapter 2, we set up a general framework for microscopic car-following models similar to the one in WILSON (2008) for different road topologies and index sets in which many of the existing CFMs can be studied. Restrictions and inherent assumptions were carefully pointed out. By an application of Cauchy’s existence theorem for ODEs on Banach spaces, we concluded about the existence of solutions close to certain special solutions such as Qs, Ps or TWs.

Based on different density definitions, we then systematically derived families of associated macroscopic models in Chapter 3. For the different density definitions to be meaningful, it turned out useful to introduce the notion of continuous index sets for microscopic car following models. This approach was motivated mainly by mathematical reasoning and has no obvious resemblance in real-life car following; its aim is to provide a simple mean for the construction of a PDE that resembles first and foremost the underlying ODE system rather than the modelled reality. In the literature, other approaches such as coarse-graining or mean field techniques and asymptotic arguments have been proposed. The latter, which is often motivated by similar problems in fluid dynamics, is problematic in this context because the ratio ε between micro- and macroscopic length- and time scales does barely justify asymptotic arguments. We observed that when the density is not defined via the derivative of the index with respect to the position, the mass conservation cannot be taken for granted in the form $\rho_t + (\rho v)_x = 0$. For the IHD and FLD, correction terms have to be applied to the local mass conservation already at second order in ε . This may seem surprising at first sight, since these definitions are in fact rather natural and have also been used in the literature before. However, we emphasise that this is merely an effect of the nonlocal character of the underlying density definitions and does *not* imply that the number of vehicles is not conserved in a closed system.

After this very general setup, we focused on different aspects of stability analysis of homogeneous flow solutions in the following two chapters.

Well-known results about string stability of linear models for the different road topologies under consideration could be recovered in Chapter 4. As pointed out in FENG et al. (2019), especially in the control theoretic field of traffic flow theory, multiple definitions of string stability have been proposed over the years. Since our main goal in this work was the comparison of different road topologies, we chose to focus on string stability in the sense of stability of linear systems with respect to initial perturbations. We emphasise that we did not show a principle of linearised stability, as discussed in WERNER (2013), for J with non-finite cardinality.

The setup we introduced in Chapter 2 suggested to perform the linear stability analysis in the framework of Laurent- and Toeplitz operators. In terms of this beautiful theory, the connections between the different settings became clearly visible.

The fact that the spectrum on the infinite lane with $J = \mathbb{Z}$ vehicles is approximated by the spectra of circular roads with the same average density as the number of vehicles N approaches infinity was hardly surprising. After all, this can be seen as a justification of the great effort put into the conduction of real-life circular-road experiments worldwide.

For finite groups of vehicles on an open road, the situation is different. For models that neglect following cars in the acceleration law, the eigenvalues of such a system are given by the “platoon eigenvalues” (WILSON 2008) of A_0 , each with multiplicity N , with no obvious relation to the infinite lane. Even worse, by definition A_0 only carries information from the partial derivatives of the driving rule with respect to the own vehicle’s state. This is due to the fact that in a finite platoon, by induction each vehicle will eventually return to equilibrium conditions after an initial perturbation, provided it does not amplify its own deviations. In the general setting with $m_f \neq 0$ the situation is more complicated, but the fact that the spectra of block Toeplitz matrices do not approximate those of block Laurent or Toeplitz operators still holds true. This is of course far from satisfying, especially because this might be considered the most (if not the only) realistic of the road topologies under consideration. However, this apparent problem could be resolved in the light of the general theory by an application of the concept of ε -pseudospectra, as anticipated in WERNER (2013). As $N \rightarrow \infty$, the ε -pseudospectra of the platoons do approach the spectrum on the infinite lane for $n = 1$. For $n > 1$ and $m_f = 0$, we could use similar arguments to construct ε -pseudomodes from the roots of the determinant of the symbol and the corresponding null spaces. The ε -pseudomodes, as equivalent of eigenvectors, provide an explanation of what is going on in the application: While the system is prohibited from oscillating at the downstream end by the boundary condition on the leading vehicle, oscillations may grow along the platoon. If the platoon is large enough, this growth may be very slow. Since the local properties of the systems are the same, the modes we found for $J = \mathbb{Z}$ and $\xi \in \mathbb{R}$ are then very close to being solutions for the platoon as well, if a small imaginary part is added to ξ so that the amplitude decays towards the leading vehicle. This also allowed interesting insights into the situation for $J = \pm\mathbb{N}$, i.e. semi-infinite motorcades on an open road. While typically this situation is studied with the boundary condition at the downstream end ($J = \mathbb{N}$), considering a final instead of a leading vehicle is sometimes more instructive in order to understand boundary modes in the context of traffic flow. The approximative solutions with exponential decay towards the leading car we found for the finite platoons are exact in this setting but, unlike for $J = \mathbb{Z}$, the corresponding modes are now bounded and measurable. For $n = 1$, the underlying fact from the general theory is that the spectrum of the Toeplitz operator is given by that of the Laurent operator together with those $\lambda \in \mathbb{C}$ enclosed with non-zero winding number. For matrix-valued symbols, a weaker statement holds.

After this, we briefly discussed the construction of Lyapunov functions. While this is possible for selected models, few things could be said for the general case. The applicability of the “weak

coupling theorem” from SWAROOP and HEDRICK (1996) can be questioned since for many relevant models the dependence of the surrounding vehicles’ behaviour can hardly be classified as “weak” in the necessary sense. The results for linear models suggested to argue with a possibly weak nonlinearity instead; however, additional assumptions would be necessary for this approach to succeed.

To be able to compare the microscopic stability results to the macroscopic case, the families of their macroscopic companions found in Chapter 3 were linearised. We found that the resulting linear PDEs are in general ill-posed in the sense that their essential spectra protrude arbitrarily wide into the right complex half-plane. Instead of completely dismissing these models, we argued that the asymptotic behaviour for large wave numbers is not relevant here since wave lengths below a certain length scale are physically meaningless in the context of traffic flow. When the correction terms to the continuity equation are taken into account, the characteristic polynomials for the macroscopic models based on the different density definitions can be seen as approximative sequences to the microscopic characteristic function. Interestingly, ND and FLD - exact in the continuity equation and the acceleration law, respectively - yield the same sequence of characteristic polynomials.

It is pointed out in TREIBER and KESTING (2011) that the stability of a second-order in time macroscopic traffic model is determined by the curvature of its essential spectrum at the origin, which correctly resembles its microscopic counterpart already at first order in ε .

We took a closer look at the string unstable quasistationary solutions in Chapter 5 and compared the existing approaches for the classification of microscopic models as convectively and absolutely unstable in WARD and WILSON (2011) and MITARAI and NAKANISHI (2000a). Although there appeared to be little connection at first, we found that the central necessary condition is the same in both approaches.

Since the underlying methodology was originally developed for PDEs, an application to the linked macroscopic models suggested itself. We analytically derived the cu/au boundaries at first order in ε and showed in a series of numerical experiments how the boundaries approach those of the microscopic model at higher order in ε .

Since the necessary conditions to identify the correct branch points which are derived in WARD and WILSON (2011) are not very intuitive, we employed the method of exponential weights from SANDSTEDTE and SCHEEL (2000) instead. This also allowed us to apply the notions of transient and remnant instability, which can be determined by calculation of the absolute spectrum. Special attention had to be paid to the definition of an equivalent to the Morse index because the microscopic characteristic function has infinitely many “spatial” roots. While in many cases the rightmost point of the absolute spectrum is a branch point satisfying the necessary “pinching condition” and transient and convective instability coincide, we gave an example of a microscopic traffic flow model where this is not the case. Here, the distinction between transient and remnant instability gives more information about the system than that between convective and absolute instability. The same idea is applicable to macroscopic models.

In Chapters 6 and 7 we left the quasistationary solutions in favour of the more general class of travelling waves, specifically periodic and heteroclinic solutions. In this part, we restricted our

attention to microscopic models.

We started by discussing how periodic solutions on the circular road of a certain shift-invariant type, discussed in detail e.g. in GASSER et al. (2004), can be transferred to the infinite lane in Chapter 6. This left us with the restriction that the quotient of time period T and time headway Δt has to be rational. Besides, similar solutions have to be taken from different circular road systems and numerical calculation of such solutions quickly becomes costly with rising N . We solved this issue by an integro-delay approach similar to the one in STUMPF (2016a) where we exploited the underlying symmetry.

This was simplified to a standard DDE by quadrature and implemented in numerical continuation software to parametrise the manifold of possible periodic solutions of the Bando model on the infinite lane. As could be expected, the famous “hysteresis curve” was recovered as a limiting case. Taking this as a starting point, we were also able to perform a continuation of heteroclinic solutions, recovering the diagram of allowed transitions found in BERG et al. (2000).

The stability of a periodic solution on the infinite lane was studied in Chapter 7 both as a limit to a sequence approximating it as solutions on circular roads, and by continuation of eigenfunctions. Although it is possible to calculate the first Lyapunov coefficient of the integro-delay equation (Appendix B.2), this has no implications to the solutions on the infinite lane beyond the local geometry of the solution manifold.

Finally, we took up the thread of Chapter 5 and discussed convective and absolute instability of periodic solutions. Since the pinching condition has not yet been checked, the numerical continuation of the convective/absolute boundaries has to be considered a preliminary result.

However, these results may serve the understanding of structure formation in the breakup of quasistationary solution. The convective instability of the involved periodic solutions has been suggested in MITARAI and NAKANISHI (2000a) and explains the transition from mild oscillations to jump solutions.

Throughout the text, most examples were based on the Bando model and variants thereof. Despite its known issues such as an over-simplification of driving behaviour and unbounded acceleration, this model was chosen due to its simplicity and historical importance for the development of traffic flow theory.

8.2 Outcome and applicability

Our application of results from operator theory to car-following models in a general framework allowed us to recover well known results from linear stability analysis and obtain a clear view on the influence of the road topologies. In particular, it helped us to understand in which sense the finite-dimensional systems converge to the infinite-dimensional case. The recognition of the importance of boundary pseudomodes for the transient behaviour of finitely many cars on an open road may also help in a unification of the interpretations of platoon and ring road experiments. Different PDEs have been proposed as macroscopic companions for the Bando model in the literature. By pointing out the relevance of the underlying density definition, we were able to explain e.g. the issue of the deviating coefficients in the second order discussed in LEE et al. (2001). We saw that, when worked out correctly, all three considered density definitions lead to sequences of macroscopic models with linearisations that are “good” in the sense that they have the same linear stability properties as the microscopic model with $J = \mathbb{Z}$ and even recover its characteristic polynomial in the limit. The choice of the density definition can thus depend on the context: For an emphasis on the equivalences to fluid dynamics, the natural density with its local mass conservation is reasonable. Where the focus is on comparison or connection of macroscopic and microscopic models, the inverse headway density may seem more attractive.

Our explanation of the common basis of the notions of convective and absolute instability in MITARAI and NAKANISHI (2000a) and WARD and WILSON (2011) in form of the underlying branch point condition and the simplified and more accessible necessary condition we presented may hopefully lead to more frequent application of this underestimated theory in the traffic flow community. The involved change of the reference frame is also important in a metaphorical way. In most studies of microscopic traffic flow, the vehicles and their drivers are the main interests. More attention should be paid to the impact they have on their surrounding in terms of locally raised levels of emissions etc.

We have seen that when roads are embedded in a network, the notions of transient and remnant instability are more instructive than convective and absolute instability. A better understanding of the nature of the instability on the links of a road network may help to establish control mechanisms that help to contain emerging congestions to a limited area and maintain overall flow.

The presented approach to shift-invariant periodic solutions establishes a connection between periodic solutions of different orders and on circles of different length. For large numbers of vehicles, numerical continuation of periodic solutions on the circular road becomes unfeasible; the proposed exploitation of the inherent symmetry makes this unproblematic. With this, it is also possible to directly compare related solutions without having to perform multiple continuations of systems with different vehicle numbers. The formulation in Δt and Δx also admits some insight into the nonlinear velocity of congestions in the road frame, with the line $\Delta x = 0$ separating between downstream- and upstream moving jams. The study of convective and absolute instability of periodic solutions may help to provide a better understanding of structure formation at the onset of congestion.

8.3 Open questions

The results we have obtained open up a multitude of interesting follow-up questions.

As usual, the most straightforward way to proceed is to re-examine the assumptions made at the beginning in Chapter 2. Although the restrictions made are common in the traffic flow literature, their relaxation would greatly promote the applicability of our research. From our everyday experience, amongst the most restrictive assumptions we formulated are that of instantaneous reactions, homogeneous drivers and a fixed order of vehicles.

There is a lot of existing literature on car-following models with reaction time. In a project with G. OROSZ, we have made first steps to generalise the concept of convective and absolute instability for microscopic models in this direction. Formally, the generalisation of the branch point condition is straightforward, and preliminary numerical results are promising. As may be expected, they indicate that with increasing reaction time the *cdu* region of parameter space grows while the *cuu* region shrinks. During the time the drivers need to process the information, the perturbation moves downstream with the column of vehicles. However, the theoretical background becomes more involved for delay differential equations. For example, difficulties arise already in the discrimination between string stable and -unstable parameter regions since it cannot be guaranteed any more that the spectrum starts to cross the imaginary axis at the origin.

The assumption of a time-invariant vehicle order can also be criticised. Models including mechanisms for overtaking typically employ rule-based behaviour which quickly make a detailed analysis unfeasible. We may argue that the linear analysis employed here is only applicable close to the special situations anyway. In many of these, such as homogeneous flow, heteroclinic transitions between different regimes, or POMs at bottlenecks, overtaking manoeuvres may typically not be desirable for reasonable drivers. It can also be shown that the introduced framework is flexible enough to include effects such as the merging or splitting of lanes as long as the ordering before and afterwards is predefined.

A generalisation with respect to the assumption of homogeneous drivers would be interesting from different perspectives. Separating J into two or more subsets with different driving laws can describe classes of vehicles, e.g. a road shared by cars and trucks, while randomly distributed variation of the acceleration laws could model different vehicle characteristics and driving styles. For the case $[m_f, m_l] = [0, 1]$ with $f_{v_1} = 0$, MASON and WOODS (1997) showed that the characteristic polynomial is insensitive to a permutation of the vehicles; it can be shown that the theory for convective and absolute instability can easily be extended, too. In general, the order of the vehicles is relevant and must be made subject to new assumptions. Systems with $m_1 > 1$ for one of the classes are of special interest with respect to connected and automated vehicles. For a repeating pattern, the linear theory developed here can be applied to the resulting system of identical platoons. Stability of multiclass models may also be studied in terms of so-called “twisted Toeplitz matrices” (TREFETHEN and EMBREE 2005). Approaches using transfer functions have also been made in this context (FENG et al. 2019). If the acceleration law is not constant we cannot expect periodic solutions of the shift-invariant type. If the individual driving rules are similar to each other, they may however serve as initial guesses for a numerical search.

Another possible direction for further research is to pursue the comparison of the different road topologies. So far, we have studied periodic solutions on the infinite lane and the circular road. We have also seen that platoons on the open road have boundary pseudomodes for each λ that is enclosed by the spectrum of the Laurent operator. This leads us to conjecture the existence of a family of periodic solutions for $J = -\mathbb{N}$ whose amplitude grows with increasing vehicle index, with corresponding “exponentially good periodic solutions” in an appropriate sense for platoons of finite length. Compared to the periodic solutions for $J = \mathbb{Z}$, this family can be expected to have yet another degree of freedom.

It would also be interesting to apply the concept of convective and absolute instabilities to other special solutions, in particular to the bottleneck case. To extend the results on periodic solutions to qPOMs, it would first be necessary to implement a numerical continuation of the bi-periodic density- and velocity profiles on $[0, L] \times [0, T]$, as outlined in GASSER and WERNER (2010).

The heteroclinic solutions in Chapter 6 strongly suggest to investigate the connection with jump solutions of the Riemann problems for corresponding macroscopic models. In BERG and WOODS (2001), the existence of “dispersive” solutions of the Bando model reminiscent of rarefaction waves is shown.

Finally, it would of course be exciting to establish cooperations with practitioners and to put the results to a test under real-life conditions. As indicated above, relevant areas include the local prediction of emission levels and the prediction of the dispersal of congestion on a network of roads.

Bibliography

- K. Aghabayk, M. Sarvi, and W. Young. A state-of-the-art review of car-following models with particular considerations of heavy vehicles. *Transport Reviews*, 35(1):82–105, 2015.
- R. Ansorge. What does the entropy condition mean in traffic flow theory? *Transportation Research Part B: Methodological*, 24(2):133 – 143, 1990.
- A. Aw and M. Rascle. Resurrection of “second order” models of traffic flow. *SIAM Journal on Applied Mathematics*, 60(3):916–938, 2000.
- M. Bando, K. Hasebe, A. Nakayama, A. Shibata, and Y. Sugiyama. Structure stability of congestion in traffic dynamics. *Japan Journal of Industrial and Applied Mathematics*, 11(2):203–223, 1994.
- M. Bando, K. Hasebe, A. Nakayama, A. Shibata, and Y. Sugiyama. Dynamical model of traffic congestion and numerical simulation. *Physical Review E*, 51(2):1035–1042, 1995a.
- M. Bando, K. Hasebe, K. Nakanishi, A. Nakayama, A. Shibata, and Y. Sugiyama. Phenomenological study of dynamical model of traffic flow. *J. Phys. I France*, 5(11):1389–1399, 1995b.
- M. Bando, K. Hasebe, K. Nakanishi, and A. Nakayama. Analysis of optimal velocity model with explicit delay. *Physical Review E*, 58(5):5429–5435, 1998.
- M. Bando, K. Hasebe, K. Nakanishi, and A. Nakayama. Delay of vehicle motion in traffic dynamics. *Japan Journal of Industrial and Applied Mathematics*, 17(2):275, Jun 2000.
- N. Bellomo and C. Dogbe. On the modeling of traffic and crowds: A survey of models, speculations, and perspectives. *SIAM Review*, 53(3):409–463, 2011.
- P. Berg and A. Woods. Traveling waves in an optimal velocity model of freeway traffic. *Physical review. E*, 63(3 Pt 2):036107, 2001.
- P. Berg, A. Mason, and A. Woods. Continuum approach to car-following models. *Physical Review E*, 61(2):1056–1066, 2000.
- D. Borthwick and A. Uribe. On the pseudospectra of Berezin-Toeplitz operators. *Methods and Applications of Analysis*, 10(1):031–066, 2003.
- A. Böttcher and B. Silbermann. *Analysis of Toeplitz Operators*. Springer Monographs in Mathematics. Springer Berlin Heidelberg, 2006. DOI: 10.1007/3-540-32436-4.
- A. Böttcher and B. Silbermann. *Introduction to Large Truncated Toeplitz Matrices*. Universitext. Springer New York, 1999.

- M. Brackstone and M. McDonald. Car-following: a historical review. *Transportation Research Part F: Traffic Psychology and Behaviour*, 2(4):181–196, 1999.
- L. Brevdo and T. J. Bridges. Absolute and convective instabilities of temporally oscillating flows. *Zeitschrift für angewandte Mathematik und Physik ZAMP*, 48(2):290–309, Mar 1997.
- L. Brevdo. A study of absolute and convective instabilities with an application to the Eady model. *Geophysical & Astrophysical Fluid Dynamics*, 40(1):1–92, 1988.
- L. Brevdo and T. J. Bridges. Absolute and convective instabilities of spatially periodic flows. *Philosophical Transactions: Mathematical, Physical and Engineering Sciences*, 354(1710):1027–1064, 1996.
- R. J. Briggs. *Electron-stream interaction with plasmas*. Cambridge, Mass, MIT-Press, 1964.
- L. Brillouin. Über die Fortpflanzung des Lichtes in dispergierenden Medien. *Annalen der Physik*, 349(10):203–240, 1914.
- L. Brillouin and A. Sommerfeld. *Wave Propagation and Group Velocity*. New York:Academic Press, 1960.
- L. Buric and V. Janovsky. On pattern formation in a class of traffic models. *Physica D: Nonlinear Phenomena*, 237(1):28 – 49, 2008.
- P. Carter, T. Chin, J. Ruth, B. Sandstede, and R. Santorella. Diffusion maps in equation-free modeling. (*preprint*), 2017.
- R. E. Chandler, R. Herman, and E. W. Montroll. Traffic dynamics: Studies in car following. *Operations Research*, 6(2):165–184, 1958.
- Clawpack Development Team. Clawpack software, 2019. URL <http://www.clawpack.org>. Version 5.6.0.
- C. F. Daganzo. Requiem for second-order fluid approximations of traffic flow. *Transportation Research Part B*, 29(4):277–286, 1995.
- H. Dankowicz and F. Schilder. *Recipes for continuation*. Soc. for Industrial and Applied Mathematics, Philadelphia PA, 2013.
- A. Dhooge, B. Sautois, W. Govaerts, and Y. Kuznetsov. MatCont: Matlab software for bifurcation study of dynamical systems. *ACM Transactions on Mathematical Software*, 29(2):p.141, 2003.
- M. Di Francesco and M. Rosini. Rigorous derivation of nonlinear scalar conservation laws from follow-the-leader type models via many particle limit. *Archive for Rational Mechanics and Analysis*, 217(3):831–871, 2015.
- M. Di Francesco, S. Fagioli, and M. D. Rosini. Deterministic particle approximation of scalar conservation laws. *Bollettino dell’Unione Matematica Italiana*, 10(3):487–501, Sep 2017.

-
- J. A. Dieudonné. *Foundations of modern analysis*. Pure and applied mathematics. Acad. Press, New York u.a., 1960.
- E. J. Doedel, R. C. Paffenroth, A. R. Champneys, T. F. Fairgrieve, Y. A. Kuznetsov, B. E. Oldeman, B. Sandstede, and X. Wang. AUTO97: Continuation and bifurcation software for ordinary differential equations (with HomCont). Technical Report , Concordia University, 1997.
- L. Elefteriadou. *An introduction to traffic flow theory*. Springer optimization and its application 84. Springer New York, New York, NY [u.a.], Springer, 2013.
- K. Engelborghs, T. Luzyanina, and G. Samaey. DDE-BIFTOOL v. 2.00: a Matlab package for bifurcation analysis of delay differential equations. Technical report, K.U. Leuven, Leuven, Belgium, 2001.
- T. Faria and L. Magalhaes. Normal forms for retarded functional differential equations with parameters and applications to hopf bifurcation. *Journal of Differential Equations*, 122(2):181 – 200, 1995.
- S. Feng, Y. Zhang, S. E. Li, Z. Cao, H. X. Liu, and L. Li. String stability for vehicular platoon control: Definitions and analysis methods. *Annual Reviews in Control*, 2019.
- I. Gasser and B. Werner. Dynamical phenomena induced by bottleneck. *Philosophical Transactions of the Royal Society A*, 368(1928):4543–4562, 2010.
- I. Gasser, G. Siritto, and B. Werner. Bifurcation analysis of a class of ‘car following’ traffic models. *Physica D: Nonlinear Phenomena*, 197(3):222–241, 2004.
- I. Gasser, T. Seidel, G. Siritto, and B. Werner. Bifurcation analysis of a class of car following traffic models II: Variable reaction times and aggressive drivers. *Bulleting of the Insititute of Mathematics, Academia Sinica*, 2(2):587–607, 2007.
- A. Gavriilidou, M. J. Wierbos, W. Daamen, Y. Yuan, V. L. Knoop, and S. P. Hoogendoorn. Large-scale bicycle flow experiment: Setup and implementation. *Transportation Research Record*, 2673 (5):709–719, 2019.
- D. C. Gazis, R. Herman, and R. W. Rothery. Nonlinear follow-the-leader models of traffic flow. *Operations Research*, 9(4):545–567, 1961.
- H. Greenberg. An analysis of traffic flow. *Operations Research*, 7(1):79–85, 1959.
- B. Greenshields. A study of traffic capacity. *Proceedings of the Highway Research Board, Washington D.C.*, 14:448–477, 1935.
- D. Helbing. Derivation of non-local macroscopic traffic equations and consistent traffic pressures from microscopic car-following models. *The European Physical Journal B*, 69(4):539–548, Jun 2009.

- D. Helbing, A. Hennecke, V. Shvetsov, and M. Treiber. Micro- and macro-simulation of freeway traffic. *Mathematical and Computer Modelling*, 35(5):517–547, 2002.
- D. Helbing. From microscopic to macroscopic traffic models. In J. Parisi, S. C. Müller, and W. Zimmermann, editors, *A Perspective Look at Nonlinear Media*, volume 503, pages 122–139. Springer Berlin Heidelberg, 1998.
- R. Herman, E. W. Montroll, R. B. Potts, and R. W. Rothery. Traffic dynamics: Analysis of stability in car following. *Operations Research*, 7(1):86–106, 1959.
- C. Hönicke, P. Bliss, and R. Moritz. Effect of density on traffic and velocity on trunk trails of formica pratensis. *The Science of Nature*, 102(3):1–9, 2015.
- H. J. C. Huijberts. Improved stability bound for steady-state flow in a car-following model of road traffic on a circular route. *Physical review. E Statistical, nonlinear, and soft matter physics*, 65:1–3, 2002a.
- H. Huijberts. Analysis of a continuous car-following model for a bus route: existence, stability and bifurcations of synchronous motions. *Physica A: Statistical Mechanics and its Applications*, 308(1):489 – 517, 2002b.
- R. Jiang, Q. Wu, and Z. Zhu. Full velocity difference model for a car-following theory. *Physical review. E Statistical, nonlinear, and soft matter physics*, 64(1):017101, 2001.
- B. S. Kerner and P. Konhäuser. Cluster effect in initially homogeneous traffic flow. *Phys. Rev. E*, 48:R2335–R2338, Oct 1993.
- B. S. Kerner. *The Physics of Traffic*. Understanding Complex Systems. Springer Berlin Heidelberg, Berlin, Springer, 2004. DOI: 10.1007/978-3-540-40986-1.
- F. Kessels. *Traffic flow modelling : Introduction to traffic flow theory through a genealogy of models*. EURO Advanced tutorials on operational research. Springer Cham, 2019.
- A. K. Kiss, S. S. Avedisov, D. Bachrathy, and G. Orosz. On the global dynamics of connected vehicle systems. *Nonlinear Dynamics*, 96(3):1865–1877, 2019.
- A. Klar, R. D. Kühne, and R. Wegener. Mathematical models for vehicular traffic. *Surv. Math. Ind.*, 6:215–239, 1996.
- Y. A. Kuznecov. *Elements of applied bifurcation theory*. Springer, New York NY [u.a.], 1995.
- H. Lazar, K. Rhouлами, and D. Rahmani. A review analysis of optimal velocity models. *Periodica Polytechnica. Transportation Engineering*, 44(2):123–131, 2016.
- H. K. Lee, H.-W. Lee, and D. Kim. Macroscopic traffic models from microscopic car-following models. *Physical Review E*, 64(5):056126, 2001.
- H. Lenz, C. Wagner, and R. Sollacher. Multi-anticipative car-following model. *The European Physical Journal B - Condensed Matter and Complex Systems*, 7(2):331–335, Jan 1999.

-
- R. J. LeVeque. *Finite Volume Methods for Hyperbolic Problems*. Cambridge Texts in Applied Mathematics. Cambridge University Press, 2002.
- M. Lewis. *Dispersal, individual movement and spatial ecology : a mathematical perspective*. Lecture notes in mathematics (2071). Berlin: Springer, 2013.
- E. M. Lifshitz and L. Pitaevskii. *Physical kinetics*. Pergamon Press, Oxford, 1981.
- M. J. Lighthill and G. B. Whitham. On kinematic waves. II. a theory of traffic flow on long crowded roads. *Proceedings of the Royal Society A: Mathematical Physical and Engineering Sciences*, 229(1178):317–345, 1955.
- A. D. Mason and A. W. Woods. Car-following model of multispecies systems of road traffic. *Physical Review E*, 55(3):2203–2214, 1997.
- N. Mitarai and H. Nakanishi. Stability analysis of optimal velocity model for traffic and granular flow under open boundary condition. *J. Phys. Soc. Jpn.*, 68(8):2475–2478, 1999.
- N. Mitarai and H. Nakanishi. Spatiotemporal structure of traffic flow in a system with an open boundary. *Physical review letters*, 85(8):1766–1769, 2000a.
- N. Mitarai and H. Nakanishi. Convective instability and structure formation in traffic flow. *Journal of the Physical Society of Japan*, 69(11):3752–3761, 2000b.
- R. Miucic, editor. *Connected Vehicles : Intelligent Transportation Systems*. Cham, Springer International Publishing, 2019.
- P. M. Morse and H. Feshbach. *Methods of theoretical physics : Pt. 1 Chapters 1 to 8*. New York, NY [u.a.], McGraw-Hill, 1953.
- K. Nagel, P. Wagner, and R. Woesler. Still flowing: Approaches to traffic flow and traffic jam modeling. *Operations Research*, 51(5):681–710, 2003.
- G. Orosz and G. Stépán. Hopf bifurcation calculations in delayed systems with translational symmetry. *Journal of Nonlinear Science*, 14(6):505–528, 2004.
- G. Orosz and G. Stépán. Subcritical hopf bifurcations in a car-following model with reaction-time delay. *Proceedings: Mathematical, Physical and Engineering Sciences*, 462(2073):2643–2670, 2006.
- G. Orosz, R. E. Wilson, and B. Krauskopf. Bifurcations in a car-following model with delay. In *Proceedings of the 5th IFAC Workshop on Time Delay Systems*, 2004a.
- G. Orosz, R. E. Wilson, and B. Krauskopf. Global bifurcation investigation of an optimal velocity traffic model with driver reaction time. *Physical Review E*, 70(2), 2004b.
- G. Orosz, B. Krauskopf, and R. Wilson. Bifurcations and multiple traffic jams in a car-following model with reaction-time delay. *Physica D: Nonlinear Phenomena*, 211(3):277 – 293, 2005.
-

- G. Orosz, R. E. Wilson, R. Szalai, and G. Stépán. Exciting traffic jams: Nonlinear phenomena behind traffic jam formation on highways. *Physical Review E - Statistical Nonlinear, and Soft Matter Physics*, 80(4):046205, 2009.
- H. J. Payne. Models of freeway traffic and control. In G. A. Bekey, editor, *Mathematical Models of Public Systems*, volume 1 of *Simulation Councils proceedings series*, pages 51 – 61, La Jolla, 1971. Society for Computer Simulation.
- L. A. Pipes. An operational analysis of traffic dynamics. *Journal of Applied Physics*, 24(3):274–281, 1953.
- M. H. L. Pryce. Wave propagation and group velocity. *Nature*, 191(4784):104, 1961.
- P. I. Richards. Shock waves on the highway. *Operations Research*, 4(1):42–51, 1956.
- B. Sandstede and A. Scheel. Absolute and convective instabilities of waves on unbounded and large bounded domains. *Physica D: Nonlinear Phenomena*, 145(3):233–277, 2000.
- W. Shen and K. Shikh-Khalil. Traveling waves for a microscopic model of traffic flow. *Discrete and Continuous Dynamical Systems*, 38(5):2571–2589, 2018.
- J. A. Sherratt, A. S. Dagbovie, and F. M. Hilker. A mathematical biologist’s guide to absolute and convective instability. *Bulletin of Mathematical Biology*, 76(1):1–26, 2014.
- J. Sieber, K. Engelborghs, T. Luzyanina, G. Samaey, and D. Roose. *DDE-BIFTOOL v. 3.1.1 Manual*, 2017.
- A. Sommerfeld. Über die Fortpflanzung des Lichtes in dispergierenden Medien. *Annalen der Physik*, 349(10):177–202, 1914.
- D. Sperling, editor. *Three Revolutions: Steering Automated, Shared, and Electric Vehicles to a Better Future*. Washington, DC, Island Press/Center for Resource Economics, 2018.
- R. E. Stern, S. Cui, M. L. D. Monache, R. Bhadani, M. Bunting, M. Churchill, N. Hamilton, R. Haulcy, H. Pohlmann, F. Wu, B. Piccoli, B. Seibold, J. Sprinkle, and D. B. Work. Dissipation of stop-and-go waves via control of autonomous vehicles: Field experiments. *Transportation Research Part C: Emerging Technologies*, 89:205 – 221, 2018.
- E. Stumpf. Local stability analysis of differential equations with state-dependent delay. *Hamburger Beiträge zur Angewandten Mathematik*, 2016a.
- E. Stumpf. On a delay differential equation arising from a car-following model: Wavefront solutions with constant-speed and their stability. *Hamburger Beiträge zur Angewandten Mathematik*, 2016b.
- Y. Sugiyama, M. Fukui, M. Kikuchi, K. Hasebe, A. Nakayama, K. Nishinari, S.-i. Tadaki, and S. Yukawa. Traffic jams without bottlenecks—experimental evidence for the physical mechanism of the formation of a jam. *New Journal of Physics*, 10(3):033001, 2008.

-
- D. Swaroop and J. K. Hedrick. String stability of interconnected systems. *IEEE Transactions on Automatic Control*, 41(3):349–357, March 1996.
- G. Teschl. *Ordinary differential equations and dynamical systems*. American Mathematical Society, Providence, RI, 2012.
- A. Tomoeda, T. Miyaji, and K. Ikeda. Bifurcation structure of a car-following model with nonlinear dependence on the relative velocity. *Transportmetrica A: Transport Science*, 14(5-6):503–519, 2018.
- L. N. Trefethen and S. J. Chapman. Wave packet pseudomodes of twisted Toeplitz matrices. *Communications on Pure and Applied Mathematics*, 57:1233–1264, 2004.
- L. N. Trefethen and M. Embree. *Spectra and pseudospectra : the behavior of nonnormal matrices and operators*. Princeton Univ. Press, Princeton, 2005.
- M. Treiber and A. Kesting. Evidence of convective instability in congested traffic flow: A systematic empirical and theoretical investigation. *Procedia - Social and Behavioral Sciences*, 17: 683–701, 2011.
- M. Treiber and A. Kesting. *Traffic Flow Dynamics*. Springer Berlin Heidelberg, 2013.
- H. von Allwörden and I. Gasser. On a general class of solutions for an optimal velocity model on an infinite lane. under review by *Transportmetrica A: Transport Science*, submitted 2018.
- F. v. Wageningen-Kessels, H. v. Lint, K. Vuik, and S. Hoogendoorn. Genealogy of traffic flow models. *EURO Journal on Transportation and Logistics*, 4(4):445–473, 2015.
- J. A. Ward. *Heterogeneity, Lane-Changing and Instability in Traffic: A Mathematical Approach*. PhD thesis, University of Bristol, 2009.
- J. A. Ward and R. E. Wilson. Criteria for convective versus absolute string instability in car-following models. *Proceedings of the Royal Society A*, 467(2132):2185–2208, 2011.
- B. Werner. *Microscopic traffic model on the infinite line: Quasi-stationary solutions, their stability and jam waves*. Hamburger Beiträge zur Angewandten Mathematik, 2013.
- G. B. Whitham. *Linear and nonlinear waves*. Wiley, New York, 1974.
- R. E. Wilson. Mechanisms for spatio-temporal pattern formation in highway traffic models. *Philosophical Transactions: Mathematical Physical and Engineering Sciences*, 366(1872):2017–2032, 2008.
- R. E. Wilson and J. A. Ward. Car-following models: fifty years of linear stability analysis – a mathematical perspective. *Transportation Planning and Technology*, 34(1):3–18, 2011.
- D. Yang, P. J. Jin, Y. Pu, and B. Ran. Stability analysis of the mixed traffic flow of cars and trucks using heterogeneous optimal velocity car-following model. *Physica A: Statistical Mechanics and its Applications*, 395:371 – 383, 2014.
-

Nomenclature

Abbreviations

au	absolutely unstable	67
CAV	connected and automated vehicle	1
cd _u	convectively downstream unstable	67
CFM	car-following model	12
cu	convectively unstable	67
cu _u	convectively upstream unstable	67
DDE	delay differential equation	11
FLD	forward-looking density	25
hQS	homogeneous quasistationary solution	14
HS	heteroclinic solution	15
IHD	inverse headway density $\tilde{\rho}$	25
iQS	inhomogeneous quasistationary solution	14
IVP	initial value problem	14
LHS	left hand side	29
ND	natural density	25
ODE	ordinary differential equation	11
OVF	optimal velocity function	17
PDE	partial differential equation	5
POM	pony on a merry-go-round solution	15
PS	periodic solution	15
qPOM	quasi-POM	15
QS	quasistationary solution	14
RDA	reaction-diffusion-advection equation	78
RHS	right hand side	29
ru	remnantly unstable	75
t _{du}	transiently downstream unstable	75
tu	transiently unstable	75
t _{uu}	transiently upstream unstable	75
TW	travelling waves	15

Greek letters

β	derivative of optimal velocity function at equilibrium headway	54
Δt	temporal shift	15
Δv	relative velocity	46
Δx	spatial shift	15

ε	scaling factor between micro- and macroscopic variables	25
Λ	Floquet multiplier	113
λ	temporal eigenvalue	42
μ	Floquet exponent	113
ν	spatial eigenvalue	43
ξ	index eigenvalue	42
$\check{\rho}$	natural density	25
$\hat{\rho}$	forward-looking density	25
$\tilde{\rho}$	inverse headway density	25
ρ	density (general)	24
σ	spectrum	42
σ_{ess}	essential spectrum	43
τ	reaction time	17
χ	characteristic function	42
ω	circular frequency	43

Indices

c	critical	66
co	continuous	23
e	equilibrium	14
ess	essential	43
f	following	12
l	leading	12
per	periodic	12

Latin letters

\mathcal{A}	operator of linearisation	40
A_k	stability matrix with respect to k -th vehicle ahead	17
bc	microscopic boundary condition	12
$C^n(M)$	space of n -times continuously differentiable functions on the set M	11
h	headway	12
Id	identity operator	42
i_∞	Morse index	65
\tilde{j}	time-dependent vehicle index of Eulerian framework	46
J	vehicle set	10
j	vehicle index	10
k	order of periodic solution	94
ℓ_J^n	Banach space for index set J	16
L	spatial period	15
l	circle length	12

m_f	(negative) number of following cars considered in a CFM.....	12
m_l	number of leading cars considered in a CFM.....	12
n	order of underlying differential equation in time	11
N	number of vehicles	11
\mathbb{N}	set of natural numbers excluding zero	11
\mathbb{N}_0	set of natural numbers including zero.....	11
$-\mathbb{N}$	set of negative integers excluding zero	11
\tilde{N}	virtual number of vehicles.....	104
\mathbb{Q}	set of rational numbers	96
\mathbb{R}	set of real numbers	10
S	matrix-valued symbol	41
s	scalar-valued symbol	41
Sh	shift operator	95
T	time period	15
t	time	10
\mathbf{u}	microscopic state.....	11
\mathcal{U}_J	state space.....	11
V	optimal velocity function.....	17
v_j	velocity of vehicle j	10
x_j	position of vehicle j	10
\mathbb{Z}	set of integers	11

Appendices

A Additional figures

The figures below show the density profiles for the numerical examples in Sec. 5.4.2.2. In the main text, for brevity only the velocity profiles were depicted.

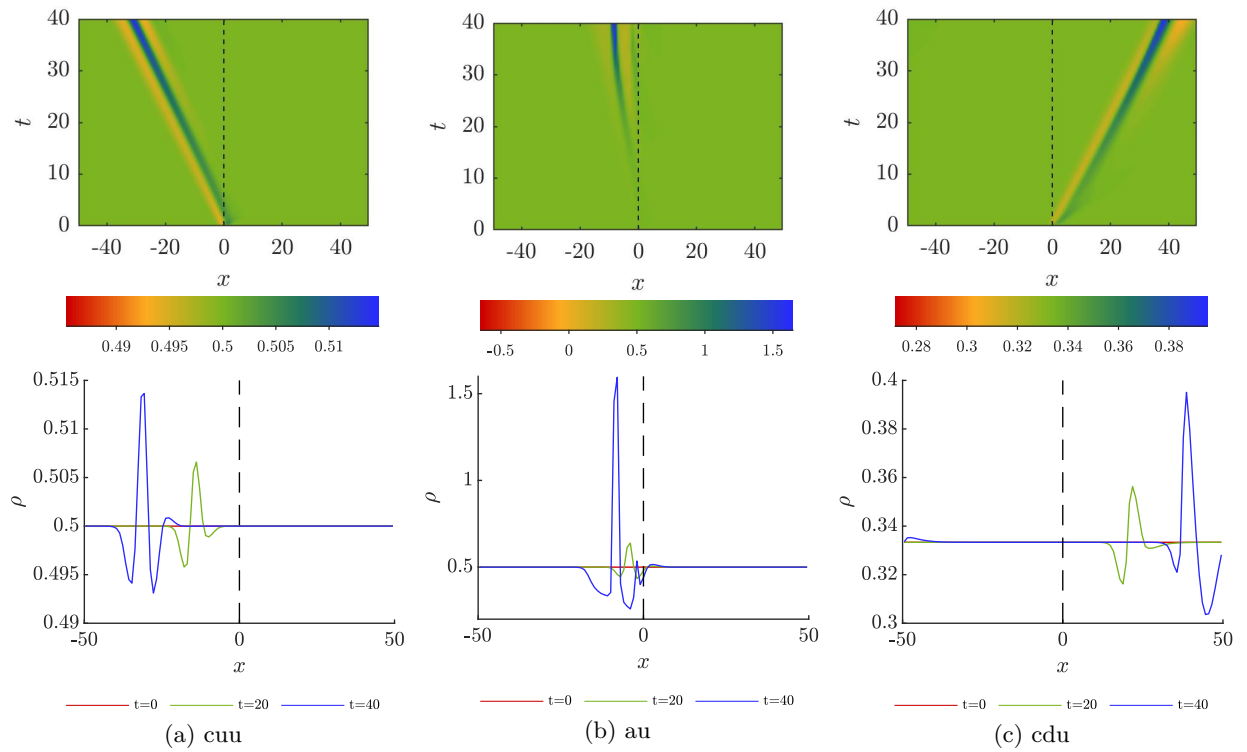


Figure 1: ND/IHD, 1st order: densities (cf. Fig. 5.14)

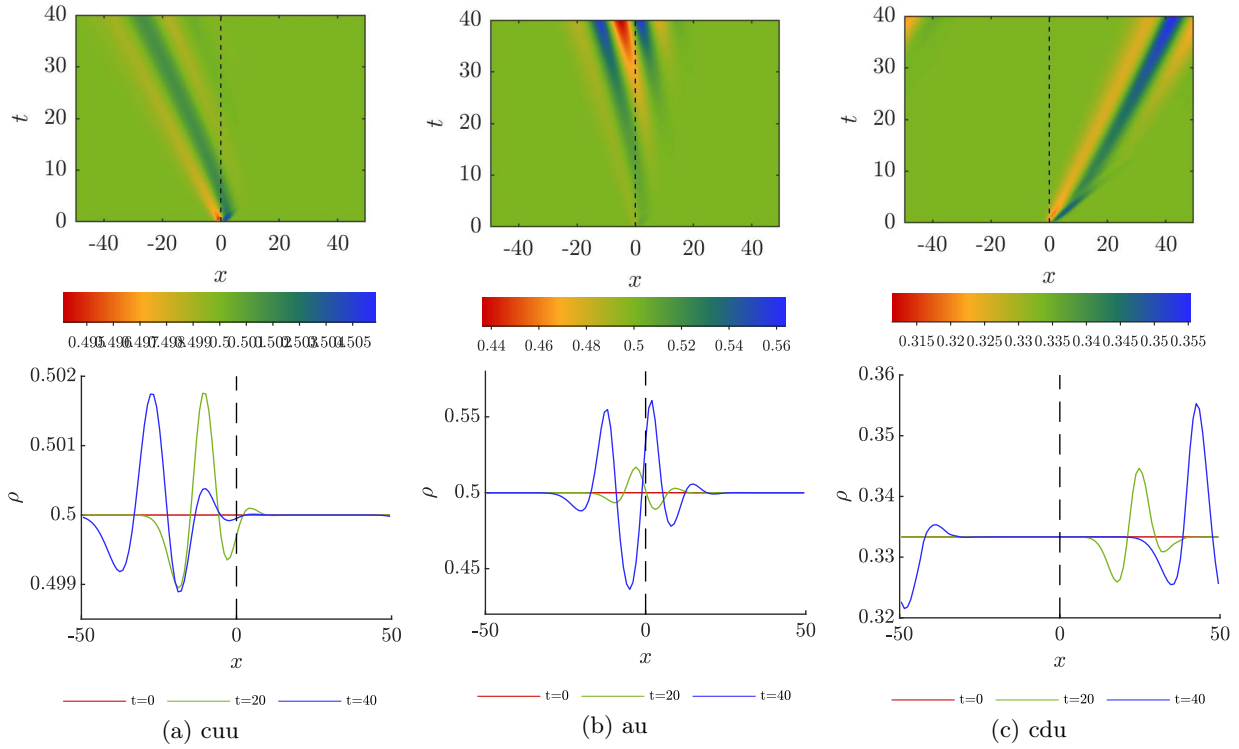


Figure 2: ND, 2nd order (cf. Fig 5.15)

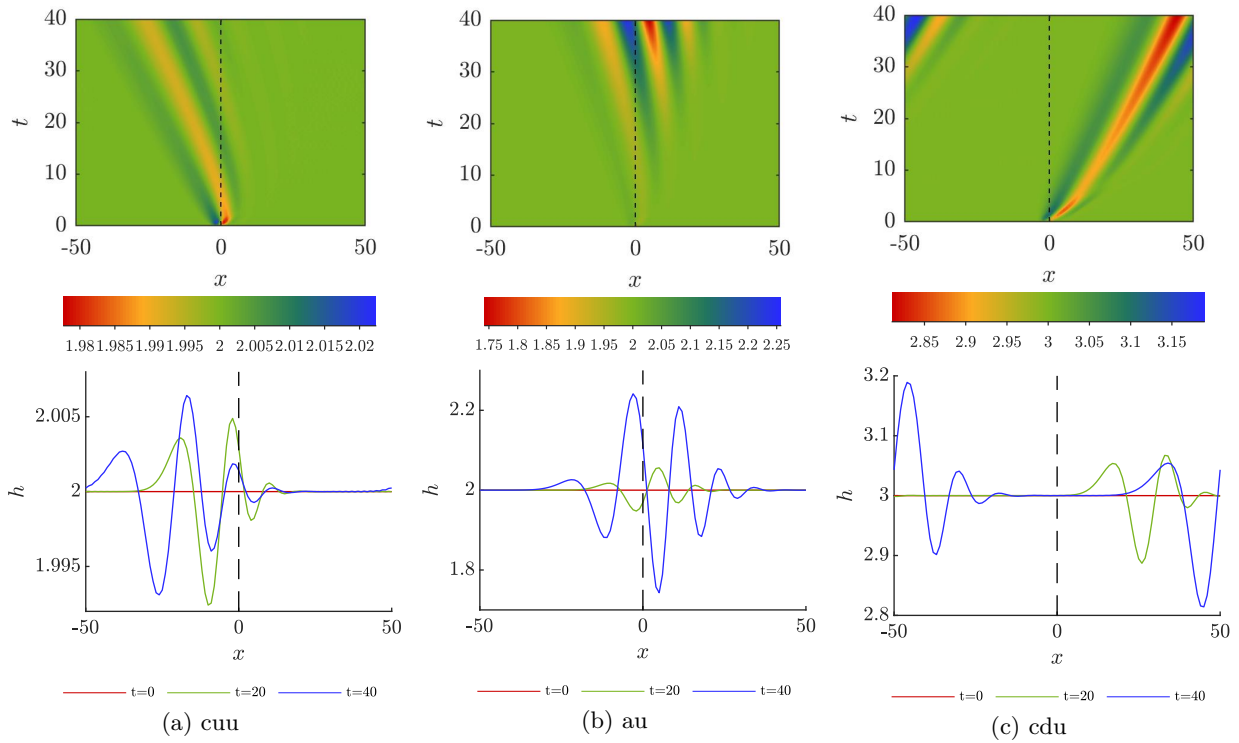


Figure 3: FLD (cf. Fig 5.16)

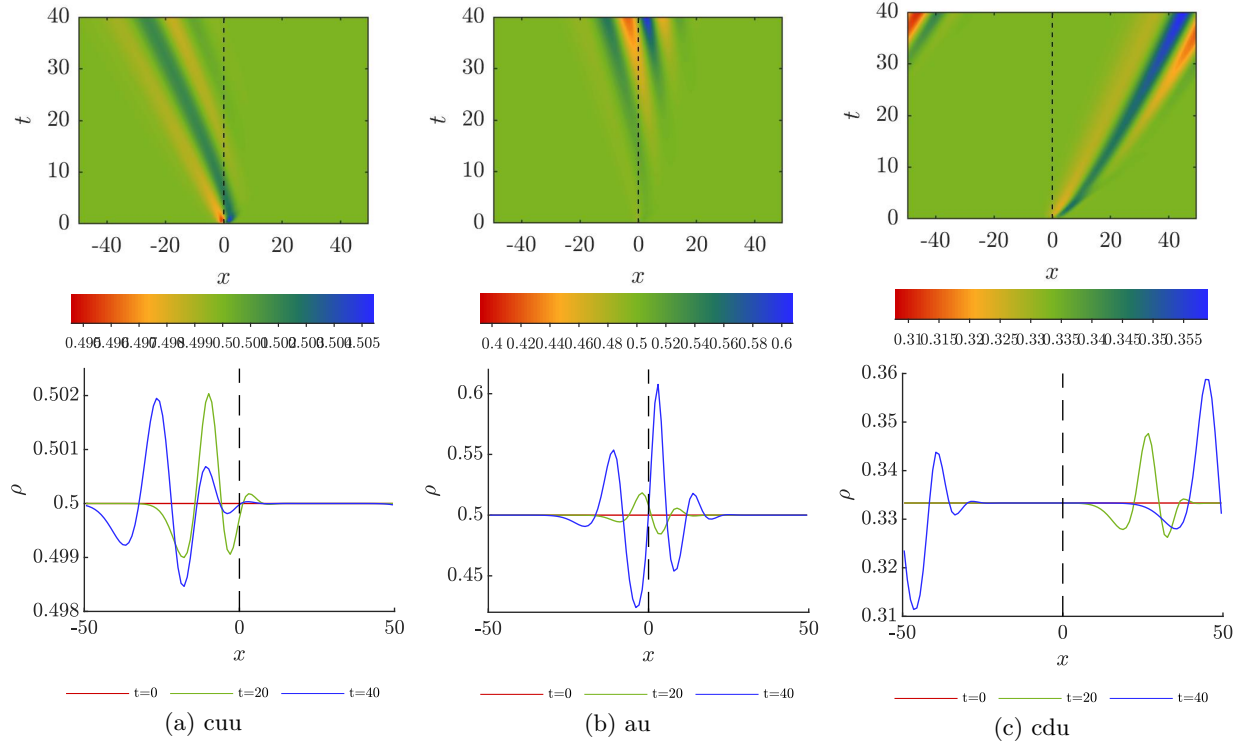


Figure 4: IHD, 2nd order (cf. Fig 5.18)

B Bifurcation analysis

B.1 Circular road

Locally, close to the bifurcation point, the stability of periodic solutions is determined by the sign of the first Lyapunov coefficient L_1^{ODE} (cf. KUZNECOV 1995):

$$L_1^{\text{ODE}} = \frac{1}{2\omega} \text{Re} \left[\langle p, \mathcal{C}(q, q, \bar{q}) \rangle - 2 \langle p, \mathcal{B}(q, \mathcal{A}^{-1} \cdot \mathcal{B}(q, \bar{q})) \rangle + \langle p, \mathcal{B}(\bar{q}, (2i\omega I - \mathcal{A})^{-1} \mathcal{B}(q, q)) \rangle \right], \quad (\text{B.1})$$

where q is an eigenvector to the critical pair of eigenvalues and p is an adjoint eigenvector, satisfying $\langle p, q \rangle = 1$. \mathcal{B} and \mathcal{C} are multilinear functionals, defined as

$$\mathcal{B}_i(\vec{x}, \vec{y}) = \sum_{j,k=1}^n x_j y_k \left. \frac{\partial^2 \tilde{f}_i(\xi)}{\partial \xi_j \partial \xi_k} \right|_{\xi=g(\vec{h}_c, \vec{v}_c)}, \quad \mathcal{C}_i(\vec{x}, \vec{y}, \vec{z}) = \sum_{j,k,l=1}^n x_j y_k z_l \left. \frac{\partial^3 \tilde{f}_i(\xi)}{\partial \xi_j \partial \xi_k \partial \xi_l} \right|_{\xi=g(\vec{h}_c, \vec{v}_c)}.$$

The nonlinear components of \tilde{f} are given by

$$\tilde{f}_j = \sum_{k=1}^N w_{j,k} f \left(\sum_{l=1}^{N-1} w_{l,k} y_l + \sqrt{N} h_e, \sum_{l=1}^N w_{l,k} z_l, \sum_{l=1}^N w_{l,k+1} z_l \right). \quad (\text{B.2})$$

Because of orthogonality, we have

$$\sum_{k=1}^N w_{j,k} w_{l,k} = \begin{cases} 1 & j = l \\ 0 & j \neq l \end{cases}$$

so if we arrange the coordinates \vec{y}, \vec{z} as $z_1, y_1, z_{N-1}, y_{N-1}, \dots, z_N, z_{N/2}, y_{N/2}$, \mathcal{A} is block-diagonal with $\lfloor N/2 \rfloor$ (4×4)-blocks, a scalar block (describing the evolution of the average velocity) and an additional (2×2)-block in the case that N is an even number.

Let now $\pm k^*$ denote the numbers of the critical eigenvalue pair. Where used as an index, $-k^*$ is meant as $N - k^*$.

From $\sum_{k=1}^N w_{l,k} w_{m,k} w_{n,k} = 0 \ \forall l, m, n \in \{\pm k^*\}$, we can deduce that the second term cancels,

$$\langle p, \mathcal{B}(q, \mathcal{A}^{-1} \cdot \mathcal{B}(q, \bar{q})) \rangle = 0. \quad (\text{B.3})$$

In a similar manner, we can use the double angle formula to show that only terms from the k^* , $2k^*$ and average velocity block can appear in the third term $\langle p, \mathcal{B}(\bar{q}, (2i\omega I - \mathcal{A})^{-1} \mathcal{B}(q, q)) \rangle$. Also, because of the block diagonal structure of matrix \mathcal{A} , the inversion is easily done analytically.

Ultimately, we see that L_1 can be expressed in terms of partial derivatives of f up to third order, evaluated at (h_e, v_e) .

For the Bando model on the circular road, the first Lyapunov coefficient was calculated in GASSER et al. (2004) as

$$L_1^{\text{ODE}} = \frac{s_1(c_1 + 1)}{2(5 - 3c_1)} \left(V'''(h_e) - \frac{(V''(h_e))^2}{V'(h_e)} \right). \quad (\text{B.4})$$

The sign depends on the chosen OVF. For $V(h) = \tanh(h - 2) + \tanh(2)$ it is positive, i.e. we have a supercritical bifurcation and initially stable periodic solutions. However, it was also shown in GASSER et al. (2004) that the stable region may be very small, so that numerical calculation of the Floquet multipliers is essential here.

B.2 Delay system

In order to calculate the first Lyapunov coefficient L_1^{DDE} for the Hopf bifurcation of equation (6.13) we use the respective formula for delay differential equations, stated in (FARIA and MAGALHAES 1995).

For this, we have to evaluate the Taylor expansion of

$$f(v(t)) = f \left(\int_0^{\Delta t} v(t + \theta) d\theta + \Delta x, v(t), v(t + \Delta t) \right)$$

for a critical pair of h_e and Δt with corresponding Δx and ω at a linear combination

$$v(t) = v_e + x_1 e^{i\omega t} + x_2 e^{-i\omega t} + x_3 + x_4 e^{2i\omega t}.$$

$$f(v(t)) = \underbrace{L(v(t) - v_e)}_{\text{linear part}} + \underbrace{B_{(2,0,0,0)} x_1^2 + B_{(1,1,0,0)} x_1 x_2 + B_{(1,0,1,0)} x_1 x_3 + B_{(0,1,0,1)} x_2 x_4 + \dots}_{\text{quadratic part}}$$

$$+ \underbrace{C_{(2,1,0,0)} x_1^2 x_2 + \dots}_{\text{higher order terms}} \quad (\text{B.5})$$

We may now use the coefficients $B_{(2,0,0,0)}, \dots, B_{(0,1,0,1)}$ and $C_{(2,1,0,0)}$ appearing in (B.5) and evaluate the linear operator L at $1, te^{i\omega t}$, and $e^{2i\omega t}$ to calculate the first Lyapunov coefficient as

$$L_1^{\text{DDE}} = \text{Re} \left(\frac{1}{1 - L(te^{i\omega t})} \left[C_{(2,1,0,0)} - \frac{B_{(1,1,0,0)} B_{(1,0,1,0)}}{L(1)} + \frac{B_{(2,0,0,0)} B_{(0,1,0,1)}}{2i\omega - L(e^{2i\omega t})} \right] \right). \quad (\text{B.6})$$

For the Bando model, we have with $v(t) = v_e + w(t)$

$$\begin{aligned} f(v(t)) &= V \left(\int_0^{\Delta t} v(t + \theta) d\theta + \Delta x \right) - v(t) = V \left(h_e + \int_0^{\Delta t} w(t + \theta) d\theta \right) - v_e - w(t) \\ &= \underbrace{V'(h_e) \cdot \int_0^{\Delta t} w(t + \theta) d\theta - w(t)}_{L(w(t))} + \underbrace{\sum_{j=2}^{\infty} \frac{V^{(j)}(h_e)}{j!} \left(\int_0^{\Delta t} w(t + \theta) d\theta \right)^j}_{\text{nonlinear part}}. \end{aligned} \quad (\text{B.7})$$

The coefficients in (B.6) are given by

$$\begin{aligned} L(te^{i\omega t}) &= -\frac{V'(h_e)}{\omega^2} \left(e^{i\kappa} (i\kappa - 1) + 1 \right), & L(1) &= V'(h_e) \Delta t - 1, \\ L(e^{2i\omega t}) &= -\frac{iV'(h_e)}{2\omega} \left(e^{2i\kappa} - 1 \right) - 1, & B_{(2,0,0,0)} &= -\frac{V''(h_e)}{2} \frac{(e^{i\kappa} - 1)^2}{\omega^2}, \\ B_{(1,1,0,0)} &= -\frac{V''(h_e)}{2} \frac{2(e^{i\kappa} - 1)^2}{\omega^2}, & B_{(1,0,1,0)} &= -\frac{V''(h_e)}{2} \frac{2i\Delta t (e^{i\kappa} - 1)}{\omega}, \\ B_{(0,1,0,1)} &= -\frac{V''(h_e)}{2} \frac{(e^{2i\kappa} - 1)(e^{i\kappa} - 1)}{\omega^2}, & C_{(2,1,0,0)} &= \frac{V'''(h_e)}{2} \frac{i(e^{i\kappa} - 1)^3}{\omega^3} \end{aligned}$$

and the first Lyapunov coefficient is

$$L_1^{\text{DDE}} = \text{Re} \left(\frac{a_1^2 a_2}{1 - L(te^{i\omega t})} \left(-\frac{V'''(b_c)}{2} - \frac{\Delta t (V''(b_c))^2}{-V'(b_c) \Delta t - 1} + \frac{\frac{1}{2} (V''(b_c))^2 a_4}{2i\omega - \frac{\beta}{2i\omega} (1 - e^{2ik}) + 1} \right) \right). \quad (\text{B.8})$$

C Summary of main results

As required by the Doctoral Degree Regulations for the Faculty of Mathematics, Informatics and Natural Sciences at Universität Hamburg from Dec. 01, 2010, §7 (5), we briefly summarise the main findings of this dissertation; see below for a translation to German.

- Links between microscopic and macroscopic traffic flow models were studied for different density definitions with special consideration of correction terms for the mass conservation equation (Sec. 3.3)
- A big class of linear microscopic traffic flow models can be described in terms of Toeplitz matrices and -operators (Sec. 4.1.1)
- The characteristic polynomials of the linearisations of “linked” macroscopic models converge to the characteristic function of the underlying microscopic model in the Eulerian frame in an appropriate sense (Sec. 4.2.2)
- The necessary criteria for convective and absolute instability for microscopic traffic models employed by MITARAI and NAKANISHI (2000a) and WARD and WILSON (2011) are equivalent (Sec. 5.2.2)
- The notions of transient and remnant instability were applied to microscopic traffic flow models (Sec. 5.3). It was demonstrated that this distinction may be more instructive than that between convective and absolute instability in a traffic flow context (Ex. 5.4)
- Boundaries between convective and absolute instability in parameter space for macroscopic traffic flow models were calculated and compared to the microscopic results for the Bando model (Sec. 5.4.2.2)
- A certain class of stop-and-go-waves was described as solutions to an associated delay differential equation. The ensuing singular eigenvalue problem can be avoided by formulation in terms of a integro-delay differential equation (Sec. 6.1)
- Periodic solutions on the infinite lane for the Bando model were numerically continued using the integro-delay differential equation (Ex. 6.4)
- Methods to determine (in-)stability (Sec. 7.1.2) and convective and absolute instability of periodic solutions on the infinite lane (Sec. 7.2) were discussed.

Zusammenfassung der Resultate

- Für verschiedene Definitionen der Dichte wurden aus einem mikroskopischen Verkehrsmodell unter besonderer Beachtung ggf. notwendiger Korrekturen der Massenerhaltungsgleichung entsprechende makroskopische Modelle abgeleitet (Sec. 3.3)
- Eine große Klasse linearer mikroskopischer Verkehrsmodelle konnte mit Hilfe der Theorie zu Töplitzmatrizen und -operatoren beschrieben und untersucht werden (Sec. 4.1.1)
- Die charakteristischen Polynome der Linearisierungen der makroskopischen Modelle konvergieren in geeignetem Sinne zur charakteristischen Funktion des zugrunde liegenden mikroskopischen Modells. (Sec. 4.2.2)
- Die in MITARAI and NAKANISHI (2000a) und WARD and WILSON (2011) aufgestellten notwendigen Kriterien zur Unterscheidung zwischen konvektiver und absolute Instabilität in mikroskopischen Verkehrsflussmodellen stellten sich als equivalent heraus (Sec. 5.2.2)
- Die Begriffe der “vorübergehenden” und “verbleibenden” Instabilität (remnant/transient instability) wurden auf mikroskopische Verkehrsflussmodelle angewandt (5.3); es konnte demonstriert werden, dass diese Unterscheidung unter gewissen Bedingungen der zwischen konvektiver und absoluter Instabilität vorzuziehen ist (Ex. 5.4)
- Die Grenzen zwischen konvektiver und absoluter Instabilität für makroskopische Verkehrsflussmodelle im Parameterraum wurden berechnet und mit den entsprechenden Ergebnissen für das zugrunde liegende mikroskopische Modell verglichen (Sec. 5.4.2.2)
- Eine gewisse Art von Stop-and-Go-Wellen konnte als Lösungen einer zugehörigen retardierten Differentialgleichung beschrieben werden. Das dabei auftretende Problems des singulären Eigenwertes der Linearisierung konnte durch Formulierung als integro-retardierte Differentialgleichung umgangen werden (Sec. 6.1)
- Periodischer Lösungen auf der Geraden für das Bando-Modell wurden mit dem Ansatz der integro-retardierte Differentialgleichung numerisch bestimmt (Ex. 6.4)
- Methoden zur Bestimmung der (In-) Stabilität (Sec. 7.1.2) und konvektiven bzw. absoluten Instabilität der gefundenen periodischen Lösungen auf der Geraden wurden diskutiert (Sec. 7.2)

D Publications derived from this dissertation

H. von Allwörden and I. Gasser. On a general class of solutions for an optimal velocity model on an infinite lane. *Transportmetrica A: Transport Science*, 2020

H. von Allwörden and I. Gasser. From circular road to infinite lane: Stability results for microscopic optimal velocity models. (in preparation)

E Eidesstattliche Versicherung / Declaration on oath

Hiermit erkläre ich an Eides statt, dass ich die vorliegende Dissertationsschrift selbst verfasst und keine anderen als die angegebenen Quellen und Hilfsmittel benutzt habe.

I hereby declare upon oath that I have written the present dissertation independently and have not used further resources and aids than those stated.

Ort, Datum | *city, date*

Unterschrift | *signature*